“Mechanics, Microstructure and Interfaces in Solid-State Batteries”

Von der Fakultät für Georessourcen und Materialtechnik der
Rheinisch-Westfälischen Technischen Hochschule Aachen

zur Erlangung des akademischen Grades einer

Doktorin der Ingenieurwissenschaften

genehmigte Dissertation

vorgelegt von

Lara Caroline Pereira dos Santos, M.Sc.

Berichter: Univ.-Prof. Dr. rer. nat. Robert Spatschek
Univ.-Prof. Dr. rer. nat. Michael Eikerling

Tag der mündlichen Prüfung: 28.04.2026

Diese Dissertation ist auf den Internetseiten der Universitätsbibliothek online verfügbar.

Dedication and Acknowledgements

I would like to acknowledge all the amazing people who supported me throughout this PhD journey. Special thanks to my supervisor, Robert, for his guidance, patience, flexibility and trust. To all colleagues and friends from IMD-1 and IMD-2: thank you for the good and bad times we shared. Thanks for fostering a positive attitude even in the face of challenges and obstacles. To the collaborators of the ALANO project and the BMW Group, who always respected and listened to me, treating me as an equal: thank you for promoting and encouraging a creative, honest and deeply collaborative environment where I could learn and grow as a professional. I started this journey as an unsure student but finish it as a confident and resilient researcher.

I would also like to thank all my personal friends and family members. Thank you for holding me up and for providing the humility to know when to listen, but also the courage to know when to speak. I am truly standing on the shoulders of giants, and it would never have been possible for me to achieve this without the support of all of you.

The most special thanks go to my partner, Luca, who believes in me even when I doubt myself; to my parents, Eliane and Adevailton; to my sisters, Gabriela and Lorena; to my goddaughter, Maria Clara; and to my grandmother, Joana, who passed away before seeing me become a doctor. I know it is painful to be far away, and maybe you never fully understood why I decided to reach for something that felt so high. So thank you for supporting me, even when you could not understand my choices, and for always reminding me that the most important thing in life is the people you love. I dedicate this work to you. My most loving and sincere: thank you!

Abstract

The development of Solid-State Batteries (SSBs) is a critical aspect in advancing technologies such as electric vehicles and renewable energy storage. This work investigates key scientific and engineering challenges related to the Lithium Metal Anode (LMA) and its interface with the Solid Electrolyte (SE).

Through atomistic simulations, we show that lithium exhibits strong mechanical anisotropy not only in elasticity but also in plasticity, with orientation and load type-dependent deformation mechanisms and clear size effects at the nanoscale. Meanwhile, experimental studies on anode foils find that the manufacturing process significantly influences microstructure and hardness. At the solid-solid interface between the LMA and SE, alloying lithium with sodium enables pressure-free stable cycling by forming new carbonate phases and a beneficial 3D microstructure through spinodal decomposition. Via thermodynamic modeling, we identify the sodium concentration thresholds for the onset of this spinodal instability.

Additionally, this thesis explores the use of Quantum Annealing (QA) as a valuable tool for energy materials simulations. We formulate mechanical deformations and interface energetics into Ising models and demonstrate the feasibility of modeling large-scale, complex systems using hybrid quantum-classical approaches. Particularly, we apply the model to lithium and predict deformation twinning in polycrystalline specimens, complementing the investigations of single crystals via atomistic simulations. The QA approach offers substantial speedups, highlighting quantum computing as a promising method in computational materials science.

Overall, this research addresses the mechanics, microstructure, interface chemistry and modeling strategies essential for the advancement of SSBs. It offers multi-physics insights across many scales, ranging from atomistic behavior and continuum simulations to micro-level experiments and cell-relevant performance.

Zusammenfassung

Die Entwicklung von Festkörperbatterien (SSBs) ist ein entscheidender Faktor bei der Weiterentwicklung von Technologien wie Elektrofahrzeugen und der Speicherung erneuerbarer Energien. Diese Arbeit untersucht zentrale wissenschaftliche und ingenieurtechnische Herausforderungen im Zusammenhang mit der Lithium-Metall-Anode (LMA) und ihrer Grenzfläche zum Festkörperelektrolyt (SE).

Durch atomistische Simulationen zeigen wir, dass Lithium nicht nur in der Elastizität, sondern auch in der Plastizität eine starke mechanische Anisotropie aufweist, mit orientierungs- und belastungsabhängigen Verformungsmechanismen und deutlichen Größeneffekten im Nanobereich. Gleichzeitig zeigen experimentelle Untersuchungen an Anodenfolien, dass der Herstellungsprozess die Mikrostruktur und Härte signifikant beeinflusst. An der Festkörper-Grenzfläche zwischen der LMA und dem SE ermöglicht die Legierung von Lithium mit Natrium einen druckfreien, stabilen Zyklusbetrieb, indem neue Carbonatphasen gebildet und durch spinodale Entmischung eine vorteilhafte dreidimensionale Mikrostruktur erzeugt werden. Mittels thermodynamischer Modellierung identifizieren wir die Natriumkonzentrationsgrenzen für den Beginn dieser spinodalen Instabilität.

Darüber hinaus untersucht diese Arbeit den Einsatz von Quantum Annealing (QA) als wertvolles Werkzeug für die Simulation von Energiematerialien. Wir formulieren mechanische Verformungen und Grenzflächenenergien in Ising-Modellen und demonstrieren die Machbarkeit der Modellierung großer, komplexer Systeme mit hybriden Quanten-Klassischen Ansätzen. Insbesondere wenden wir das Modell auf Lithium an und sagen Zwillingsverformungen in polykristallinen Proben voraus, was die Untersuchungen von einzelnen Kristallen durch atomistische Simulationen ergänzt. Der QA-Ansatz bietet erhebliche Geschwindigkeitsvorteile und unterstreicht das Potenzial der Quantentechnologie als vielversprechende Methode in der computergestützten Materialwissenschaft.

Insgesamt behandelt diese Arbeit die Mechanik, Mikrostruktur, Grenzflächenchemie

und Modellierungsstrategien, die für den Fortschritt von SSBs wesentlich sind. Sie liefert multiphysikalische Einblicke über viele Skalen hinweg, von atomistischem Verhalten und Kontinuumssimulationen bis hin zu mikroskaligen Experimenten und zellrelevanter Leistung.

Contents

Acronyms **i**

List of Figures **iii**

List of Tables **xiii**

1 Introduction **1**
1.1 Solid-State Batteries 1
1.2 Theoretical Background 5
1.2.1 Computational Modeling 6
1.2.2 Experimental Techniques 14
1.3 Objectives and Outline 15

2 Mechanical Properties of Metal Anodes **19**
2.1 Pure Lithium Metal 19
2.1.1 Microindentation Experiments 23
2.1.2 *Ab Initio* Simulations 32
2.1.3 Molecular Dynamics Simulations 37
2.1.4 Conclusions on Pure Lithium Mechanics 57
2.2 Pure Sodium Metal 59
2.2.1 *Ab initio* Simulations 59
2.2.2 Conclusions on Pure Sodium Mechanics 62
2.3 Lithium-Sodium Alloy 63
2.3.1 Theoretical Estimation via Reuss-Voigt Model 64
2.3.2 Microindentation Experiments 64
2.3.3 Conclusions on Lithium-Sodium Mechanics 69

3 Thermodynamics in Lithium-Sodium Systems **71**
3.1 Bulk Microstructure Formation 71
3.1.1 Methods 72
3.1.2 Results and Discussions 73
3.1.3 Conclusions 86
3.2 Carbonate Formation and Surface Effects 87
3.2.1 Methods 89
3.2.2 Results and Discussions 90
3.2.3 Conclusions 92

4 Quantum Annealing for Mechanics, Microstructures and Interfaces **95**
4.1 Deformation Twinning in Lithium Metal 96
4.1.1 Methods 98
4.1.2 Results and Discussions 99
4.1.3 Conclusions 117
4.2 Multi-Variant Description of Shear and Tetragonal Deformations 118
4.2.1 Methods 119
4.2.2 Results and Discussions 121
4.2.3 Conclusions 135
4.3 Conclusions on Quantum Annealing for Batteries 136

5 Conclusions **137**

Own Publications **141**

Bibliography **142**

Acronyms

BCC	Body-Centered Cubic
CV	Cyclic Voltammetry
DFT	Density Functional Theory
EIS	Electrochemical Impedance Spectroscopy
EMT	Effective Medium Theory
FEM	Finite Element Method
GBs	Grain Boundaries
GGA	Generalized Gradient Approximation
GND	Geometrically Necessary Dislocations
HM	Martens Hardness
ISE	Indentation Size Effect
KS	Kohn-Sham
LAMMPS	Large-scale Atomic / Molecular Massively Parallel Simulator
LC	lithium carbonate - Li_2CO_3
LDA	Local Density Approximation
LLZO	lithium lanthanum zirconium oxide - $Li_7La_3Zr_2O_{12}$
Li-ion	Lithium-Ion
LMA	Lithium Metal Anode
LNC	lithium-sodium carbonate - $LiNaCO_3$
MD	Molecular Dynamics
MFT	Mean Field Theory

NC	sodium carbonate - Na_2CO_3
PAW	Projector Augmented Wave
PBE	Perdew–Burke–Ernzerhof
PP	Pseudo-Potential
QA	Quantum Annealing
RVE	Representative Volume Element
SE	Solid Electrolyte
SEM	Scanning Electron Microscope
SSBs	Solid-State Batteries
TEM	Transmission Electron Microscope
VASP	Vienna *Ab Initio* Simulation Package
XC	Exchange-Correlation
XRD	X-ray Diffraction

List of Figures

1.1 Schematic description of a solid-state battery with a focus on the solid-solid interface between the lithium metal anode (LMA) and the solid electrolyte (SE), highlighting some of its main challenges. 3

1.2 Schematic representation of experimental (in orange) and computational methods (in blue) relevant to this work, positioned within their respective size and time scales. 6

2.1 Normalized force-displacement (left panel) and force-time (right panel) curves obtained from indentation experiments. Force and displacement (or time) values are normalized by their respective maximums. These examplary plots illustrate the characteristic loading behavior and temporal load evolution during the indentation experiments. 24

2.2 Average and standard deviation of HM (left) and maximum indentation depth (right) of 10 indents performed in pure lithium as-received foils. Different experimental parameters are investigated. In **(a)**, load application time and creep holding time (10 seconds) are kept constant, while the load is changed. In **(b)**, the load and creep holding time (10 seconds) as kept constant, while the load application time is changed. In **(c)**, the load and load application time are kept constant, while the creep holding time is changed. 26

2.3 **(a)** HM and **(b)** maximum indentation depth while changing the creep holding time are plotted. The creep tests are done with loading and unloading at F=15mN/10s and varying creep holding time. Statistical analyzes are done for 10 indents for each setting. Hardness values are higher than for the reference foil. Creep seems to not play an important role. 28

2.4 Average and standard deviation of E for the **(a)** Li reference foil and **(b)** Li 20x calendered foil. Tests are done with loading and unloading at F=15mN/10s, varying creep holding time and 10 indents for each setting. 29
2.5 Pole figures of the **(a)** reference foil and **(b)** 20x calendered foil. The reference foil is suggested to be a polycrystalline specimen with large grain sizes, while the calendered foil is a highly textured specimen with a $\langle 100 \rangle$ preferred orientation. 31
2.6 Comparison of the obtained results of equilibrium lattice constant (left panel) and bulk modulus (right panel) for pure BCC Li. 36
2.7 Comparison of the obtained results for Young's modulus (left panel) and shear modulus (right panel) for pure BCC Li. 37
2.8 Crystal structures for a $3 \times 3 \times 3$ supercell at 30 K, showing the difference between the two phases of Li, using the Nichol and Ackland EAM interatomic potential [150]. The top two crystal structures are the input geometry (perfect BCC unit cell), while the bottom two are the equilibrated structures at the end of the run, demonstrating the slight distortion of the BCC crystal structure. Atomic distances match the data by Dorrell and Partày [158]. . 40
2.9 Resulting stress free lattice constant as function of temperature using the Nichol and Ackland EAM interatomic potential [150]. 41
2.10 Sketch of the nanopillar geometry for tension-compression tests, together with the analyzed crystallographic planes. The BCC crystal structure is set so that the crystallographic plane of interest is initially perpendicular to the z axis (loading direction). Therefore, a [001] loading direction refers to a [001] oriented single crystal, by applying the load perpendicular to the (001) plane. 42
2.11 Stress-strain plots of free-standing Li nanopillars under tension and compression. These exemplary curves are from specimens with 6 nm radius and 30 nm height (left panel) and 20 nm radius and 100 nm height (right panel). A significant difference in the deformation behavior is observed for the different orientations. A change from sharp serrated to smooth wavy flow curves and a decrease in the yield point is observed between differently sized samples. 43
2.12 An exemplary evolution from a compression test of a single crystal with 3 nm radius and 15 nm height, loaded along [111]. Top row: stress strain curve, bottom row: corresponding atomic structure and dislocations with highlighted planes. Snapshots are taken at strains -0.047, -0.060 and -0.073, respectively, corresponding to first, second and third stress jumps. The $1/2\langle 111 \rangle$ dislocations appear in a variety of planes. 44

2.13 Top row: Exemplary evolution of a tensile test of a single crystal with 3 nm radius and 15 nm height loaded along [001], in which twinning takes place. The color coding indicates the orientation, with light green being the original orientation and dark green the re-oriented part. Bottom row: Pole figure representation of the orientation of the original (circles) and re-oriented (squares) part of the specimens loaded along [001] in tension (left) and loaded along [110] in compression (right) just after the onset of the partial re-orientation. Selected directions of the original (black) and the re-oriented (red) parts of the specimens are indicated. In both cases, the orientation relationship between both parts corresponds to twinning on {112} twin planes. 48

2.14 Yield strength for single crystals with different loading directions, sizes and load mode. The specimens are systematically increased in size maintaining a fixed radius over height ratio of 0.2. In order to get a statistical distribution, 5 runs are performed on each size using different random seeds. The average and standard deviation are reported. The left plot shows tension, while the right one shows compression. 49

2.15 Stress-strain curves for different strain rates on single crystals of 6 nm radius and 30 nm height. Compressive and tensile deformations are applied along [001] (left panel) and [110] (right panel). A change in strain rate does not influence the linear elastic past of the curve, but with increasing strain rate, a decrease in the yield strength is observed. 51

2.16 View of the single crystal under compression along [110]. Top row: snapshots of the lower strain rate test. First figure is the structure at strain 0, then the following figures highlighting the dislocations are at strains -0.03 (first strain drop) and -0.05 (second strain drop), respectively. Bottom row: snapshots of the higher strain rate test focusing on the evolution of twinning. At the bottom row the atoms are colored according to grain orientation, with light green being the original orientation and dark green the new orientation. 52

2.17 Exemplary crystal structures of the [001]/[111] bicrystal and polycrystals with average grain size, d, of 23.6 and 14.7 nm, respectively, calculated via Equation 2.15. 53

2.18 Young's modulus on the left panel and yield strength on the right panel of the polycrystalline specimens with same geometrical size, but different random grain structures. Trend lines are added in red for visualization purposes. In general, mechanical properties fall with decreasing grain size, despite a big variation between individual specimens. Polycrystals yield lower-than-expected values of E, which is approx. 19 GPa calculated from homogenization theory. 54

2.19 Left panel: Young's modulus highlighting the analyzed specimens. Right panel: Inverse pole figure representation of the respective grain orientations of the highlighted specimens with respect to the loading direction. The size of the circles is proportional to the grain size. All specimens present similar d, but distinct E values. For the harder specimens (H-1 in blue and H-2 in orange), their biggest grains are close to each other and lie near the direction presenting the higher E, which is $[111]$. For the softer specimens (S-1 in gold and S-2 in green), their biggest grains are also close to each other and lie near the direction presenting the lower E, which is $[001]$. . . . 55

2.20 Side view of exemplary evolutions from tensile (top row) and compression (bottom row) tests of a polycrystalline specimen with average grain size of 26 nm. The colors indicate different grains with random orientations. An apparent GB sliding at an inclined surface can be seen once the specimen is subjected to the mechanical tests. Snapshots are taken at the strain values of 0, 0.04 and 0.065. 56

2.21 Comparison of the obtained results of equilibrium lattice constant (left panel) and bulk modulus (right panel) for pure BCC Na. 62

2.22 Comparison of the obtained results for Young's modulus (left panel) and shear modulus (right panel) for pure BCC Na. 63

2.23 Average and standard deviation from different experimental parameters of HM in the four samples investigated. In **(a)**, the influence of load is analyzed. In **(b)**, the influence of load application time. In **(c)**, the influence of creep holding time. Additionally, in **(d)**, the maximum indentation depth is plotted across different creep holding times, showing the time-dependent plastic deformation of lithium metal. In **(e)**, the summary of the results from **(c)** is depicted, to evidence the difference between the foils. 67

2.24 Pole figures for the analyzed foils. Foils number **(a)** 1, **(b)** 2 and **(c)** 3 present a strong single-crystal-like texture, indicating that the manufacturing procedure generates a $\langle 100 \rangle$ preferred orientation. The measurements on foil number 4 (panels **(d)** and **(e)**) show no preferred orientation, indicating that the heat treatment dispose the strong foil texture. Panel **(d)** is the reflection from Li (110), while panel **(e)** is the reflection from Na (110). For foil number 4, due to overlapping with reflections of the Ni foil, some pole figures (e.g., Li (200)) cannot be measured. 68

3.1 Li-Na equilibrium phase diagram, calculated using the SGTE database in FactSage 8.3 and [190]. 72

3.2 *Ab initio* based formation energy of the Li-Na system. The low energy configurations in $x = 0.5$ correspond to partially ordered structures, where Li and Na are arranged in layers, in agreement with the energy reduction through phase separation. 74

3.3 Na solubility limit in Li in an Arrhenius representation, i.e., the Li rich side of the Li-Na phase diagram. The straight lines result from the low-concentration limit (3.6) for both the assessment by Zhang et al. [194] and the present work. They agree well with the full common tangent construction (squares) for each description in the entire temperature regime. 77

3.4 Li solubility limit in Na in an Arrhenius representation, i.e., the Na rich side of the Li-Na phase diagram. The straight lines result from the low-concentration limit (3.7) for both the assessment by Zhang et al. [194] and the present work. They agree well with the full common tangent construction (squares) for each description in the entire temperature regime. 78

3.5 Begin of the spinodal regime on the Li rich side. The plot compares for both the previous assessment [194] and the present description the analytical approximation (3.10) to the exact numerical solution (black squares). . . . 79

3.6 End of the spinodal regime on the Na rich side. The plot compares for both the previous assessment [194] and the present description the analytical approximation (3.11) to the exact numerical solution (black squares). The expansion is valid only at low concentrations, as shown in the magnification of this region in the inset. 80

3.7 Chemical and coherent binodals on the Li rich side, calculated both with the previous model [194] and the present description. The solid straight lines correspond to the new description, the dashed lines to [194], using the low-concentration approximations. The exact solutions from the common tangent constructions are shown as symbols, where the squares correspond to the chemical binodal (without elastic effects), and the open circles to the coherent binodals. 82

3.8 The same as Figure 3.7, but on the Na rich side. Notice that for the coherent binodals at higher temperatures the circles deviate slightly from the exponential asymptotic approximations. 83

3.9 Phase diagram of the Li-Na system up to the eutectic temperature, according to the *ab initio* based description in this work. In particular on the Li rich side, the solubility limit is very low, hence the chemical binodal appears on this scale as a vertical line. 84

3.10 Four Scanning Electron Microscope (SEM) images at different magnifications of the remaining sodium structure after complete lithium stripping of one side of a symmetrical half-cell with Li-Na anodes and LLZO separator (a, b): LLZO surface, while (c, d): Ni current collector surface. Images originally from [104] and licensed under CC BY 4.0. 85

3.11 FactSage equilibrium simulation with fixed partial pressure of the gases. Results show the formation of lithium carbonate and lithium-sodium carbonate. 91

3.12 **(a)** Relaxed bulk LNC structure in its low symmetry triclinic α phase. **(b)** Relaxed (001) surface on a 3 layers slab model and 4 unit cells, in which one layer is left fixed during the relaxations, but the other two layers are free to move. 92

3.13 An exemplary energy profile showing the interaction between a single lithium atom and the (001) surfaces of lithium sodium carbonate ($LiNaCO_3$, LNC) and lithium carbonate (Li_2CO_3, LC). The energy difference is plotted as a function of the lithium atom's distance from the surface with 1 Å resolution, indicating an attraction to LNC and a repulsion to LC. 93

4.1 Projection of the crystal structure of a twinned BCC crystal with lattice constant a onto the $(1\bar{1}0)$ plane. Black and red circles represent atoms that are on or above/below the projection plane, respectively. The red region corresponds to the original lattice (original orientation state), whereas the green region goes through the shear transformation (resulting in the transformed orientation state). The twin interface is a (112) plane, which is at the same time a twin mirror plane. The blue solid rectangle is sheared to the dashed one upon twinning. In the green region, the hollow circles mark the original positions of the atoms, and the full circles mark the new positions of atoms after twin formation. $ABCDEF$ refers to the stacking sequence, which is reversed by the twin transformation. 101

4.2 (a) Sketch of the twinned geometry, using periodic boundary conditions. The local coordinate system indicates the rotation of the crystal, $\hat{n}$ is the interface normal direction, as used in the subsequent polar plots. (b) Polar plot of the normalized elastic bulk energy for vanishing external strain, $\langle \epsilon_{ij} \rangle = 0$, with indicated normal directions of the twin interface. (c) The same for zero average stress, $\langle \sigma_{ij} \rangle = 0$. In both cases the Poisson ratio is chosen as $\nu = 1/4$. 103

4.3 Crystallographic visualization of the expected twin system with (112) interface generated by the shear transformation with a positive eigenstrain. . . 105

4.4 Crystallographic visualization of the unexpected $(\bar{1}\bar{1}1)$ interface generated by the shear transformation with a negative eigenstrain. 106

4.5 Sketch of the representation of interfaces through nearest neighbor interactions on the domain scale. 108

4.6 Orientation dependent interfacial energy. Left panel: Only horizontal and vertical nearest neighbor interactions are used, with equal magnitude ($\sigma_{-} = \sigma_{|}$). Center: The two values are chosen differently to enhance the anisotropy of the grain boundary energy, with the intention to suppress the crystallographically undesired $(\bar{1}\bar{1}1)$ interface orientation and the favor (112) twin boundaries. Right panel: Here, only diagonal nearest neighbor interactions are used, to reflect the interfacial energy anisotropy of crystals which are rotated by $\pm\pi/4$. In each figure, the values are scaled to the maximum value. The pictures illustrate the interface orientations in the polar plots. 109

4.7 Twin formation modeled in single crystals using quantum annealing. The horizontal direction corresponds to the $\hat{x}' \parallel [\bar{1}\bar{1}1]$ direction and the vertical direction to the $\hat{z}' \parallel [112]$ orientation. A tensile strain is applied in $[001]$ direction, and periodic boundary conditions are used in $\hat{x}'$ and $\hat{z}'$ directions. In the perpendicular $\hat{y}'$ direction a plane strain situation is assumed. The twin components in transformed orientation state are shown in green. From left to right the applied strains are $\langle \epsilon_{zz} \rangle = 0; 3/16, 3/8; 9/16; 3/4$. Notice that the domains are shown in the Lagrangian reference frame, i.e., not showing the actual shear deformation through the twinning. For these simulations, a weak anisotropic interfacial contribution is included, as discussed. 110

4.8 MD simulation of a lithium single crystal ($[001] \parallel z$) with 4 nm radius and 20 nm height. Tensile strain is applied along $[001]$. The original orientation state is colored in light green, while the transformed orientation state is colored in dark green. The polyhedral template matching and grain segmentation filters from Ovito are used [151, 161]. The snapshots are respectively from strains 0.118 (right before main twinning event), 0.123 (right after main twinning event). 112

4.9 Volume fraction of transformed twin lamellae as function of the applied tensile strain on single crystals. Without interfacial energy the twin formation starts at zero strain, and the volume fraction of transformed twin components increases linearly up to the upper limit $\langle \epsilon_{zz} \rangle = 3/4$, where the entire sample is transformed. With interfacial energy, first a nucleation barrier has to be overcome, both from the original and fully transformed side. The QA calculated transitions of twin formation agree with the analytical predictions (4.15) and (4.16), as marked by the vertical black lines. In these QA simulations, a decomposition into 1×32 grains is used in a quadratic system with edge length $L_{x'} = L_{z'}$, with the axes orientations as in Figure 4.7. The Poisson ratio is chosen as $\nu = 1/4$. 113

4.10 Deformation twinning in a polycrystal consisting of five grains. Here, the coordinate system is given by the basis set B', i.e., the horizontal axis corresponds to the $\hat{x}' \parallel [\bar{1}\bar{1}1]$ axis and the vertical axis to the $\hat{z}' \parallel [112]$ axis. Relative to these axis, the grains are rotated in the $x'z'$ plane in anti-clockwise direction, as indicated by the color coding. A tensile strain is applied in [001] direction, which is $\langle \epsilon_{zz} \rangle = 0$ in the left panel, $\langle \epsilon_{zz} \rangle = 0.1$ in the middle panel, and $\langle \epsilon_{zz} \rangle = 0.3$ in the right panel. The blue shading indicates the domains in transformed orientation state, i.e., the domains with Ising spin $+1$. Additionally to the tesselation by grains, the periodic system with plane strain boundary conditions is divided into 64×64 domains in the sense of the preceding discussion, hence altogether 4096 Ising spins are used. As third discretization level, a uniform mesh of size 2048×2048 is used for the Fourier transformation based self and domain interaction energy calculations, using $\nu = 1/4$. The simulation results include apart from elastic energy also a weak, anisotropic grain boundary energy to favor twinning on the (112) plane. 116

4.11 Visualization of the variants used in the present study. Spin s_1 corresponds to the shear deformation, s_2 to the tetragonal deformation, see Eq. (4.28). . 122

4.12 Equilibrium variant distribution with uniform grain orientation. The microstructure consist of 200 grains and a tensile strain is applied in horizontal (x) direction. The tensile strain is **(a)** $\langle \epsilon_{xx} \rangle / \epsilon_1 = 0$, **(b)** $\langle \epsilon_{xx} \rangle / \epsilon_1 = 0.25$, **(c)** $\langle \epsilon_{xx} \rangle / \epsilon_1 = 0.5$, **(d)** $\langle \epsilon_{xx} \rangle / \epsilon_1 = 0.75$, **(e)** $\langle \epsilon_{xx} \rangle / \epsilon_1 = 1.0$ and **(f)** $\langle \epsilon_{xx} \rangle / \epsilon_1 = 1.5$. In all figures $\epsilon_0 = \epsilon_1$ and the Poisson ratio is chosen as $\nu = 1/4$ (i.e., $\lambda = \mu$). 125

4.13 Orientation dependence of the normalized elastic energy for equal volume fraction stripes consisting of pairs of variants for $\langle \epsilon_{ij} \rangle = 0$ and $\epsilon_1 = \epsilon_0$. . . 126

4.14 2×2 supercell representation of Figure 4.12 to emphasize the microstructure patterns. The dashed yellow lines mark the boundaries or the simulation with periodic boundary conditions. In all figures $\epsilon_1 = \epsilon_0$ and $\nu = 1/4$. . . 127

4.15 Equilibrium variant distribution with uniform grain orientation. The microstructure consist of 200 grains and an average shear strain $\langle \epsilon_{xy} \rangle$ is applied. The strain is **(a)** $\langle \epsilon_{xy} \rangle / \epsilon_0 = 0$, **(b)** $\langle \epsilon_{xy} \rangle / \epsilon_0 = 0.25$, **(c)** $\langle \epsilon_{xy} \rangle / \epsilon_0 = 0.5$, **(d)** $\langle \epsilon_{xy} \rangle / \epsilon_0 = 0.75$, **(e)** $\langle \epsilon_{xy} \rangle / \epsilon_0 = 1.0$ and **(f)** $\langle \epsilon_{xy} \rangle / \epsilon_0 = 1.5$. In all figures $\epsilon_0 = \epsilon_1$, and the chosen Poisson ratio is $\nu = 1/4$ (i.e., $\lambda = \mu$). 128

4.16 2×2 supercell of the simulation domain for external shear $\langle \epsilon_{xy} \rangle / \epsilon_0 = 0.75$ from Figure 4.15(d) with $\epsilon_1 = \epsilon_0$. Apart from a negligible amount of the red variant three phases are present here. The sketch shows the geometrical explanation of the equilibrium pattern. 129

4.17 Equilibrium variant distribution with uniform grain orientation for $\langle \epsilon_{ij} \rangle = 0$. The microstructure consist of 200 grains and the dimensionless parameter ϵ_1/ϵ_0 is varied. The ratios are **(a)** $\epsilon_1/\epsilon_0 = 0.2$, **(b)** $\epsilon_1/\epsilon_0 = 1$ and **(c)** $\epsilon_1/\epsilon_0 = 5$. In all figures the chosen Poisson ratio is $\nu = 1/4$ (i.e., $\lambda = \mu$). . 130
4.18 Polar representation of the orientation dependence of the elastic energy (scaled to the maximum value) for mismatching pairs of variants. The calculations are for fixed strain boundary conditions $\langle \epsilon_{ij} \rangle = 0$. 132
4.19 2×2 supercell of the periodic solution Figure 4.17(a) with $\epsilon_1/\epsilon_0 = 0.2$. The structure's geometry is sketched and highlights the interface orientations between the variants. 133
4.20 Equilibrium variant distribution with random grain orientation. **(a)** Grain orientation map corresponding to the microstructure. The grain rotation angle in the color bar is given in radian (modulo π due to symmetry). The rotation axis is along the [001] direction. The microstructure consists of 200 grains and tensile strain in horizontal direction is **(b)** $\langle \epsilon_{xx} \rangle/\epsilon_1 = 0$ and **(c)** $\langle \epsilon_{xx} \rangle/\epsilon_1 = 2.5$. In all figures $\epsilon_0 = \epsilon_1$, and the chosen Poisson ratio is $\nu = 1/4$ (i.e., $\lambda = \mu$). The grains have a random orientation based on a uniform distribution. 134

List of Tables

2.1 Experimental settings used in the microindentation experiments of pure Li foils. 24

2.2 Elastic properties of BCC lithium metal. Li - PBE and Li - LDA are calculated at 0 K via *ab initio* simulations. Li - MD are computed using a $3 \times 3 \times 3$ supercell, at 0 and 300 K with the EAM interatomic potential by Nichol and Ackland [150]. Relevant literature data with its corresponding temperature ranges are added. 35

2.3 Summary of the plastic deformation mechanisms found for each set of single crystal orientations in the Li nanopillars mechanical tests. Simulations are carried out at 300 K and with a strain rate of 10^8 s^{-1}. For loading direction [001] in compression, both twinning and dislocation slip occur simultaneously as competitive mechanisms. 47

2.4 Elastic properties of BCC sodium metal. Na - PBE and Na - LDA are calculated at 0 K via *ab initio* simulations. Relevant literature data with its corresponding temperature ranges are added. 61

2.5 The calculated elastic modulus of Li-Na via Reuss-Voigt model. 64

2.6 Experimental settings used in the microindentation experiments of Li-Na foils. 65

3.1 α-LNC (001) surface energy and adsorption energies against one lithium and one sodium atom. From the 3 surface positions scouted, the average value is reported for both Li and Na, as mapping the entire surface energy landscape is computationally expensive. 91

Chapter 1

Introduction

Batteries are a key technology in modern society. They are present in almost all aspects of daily life, from appliances such as smartphones and laptops to implantable medical devices and vehicles [1]. Batteries have a long development history. They came into the spotlight when the first Lithium-Ion (Li-ion) cells were introduced by Sony to the market in the 90s [1]. Since then, they have been established as the top choice for electrochemical energy storage. Nowadays, several billions of Li-ion cells are manufactured every year, and the size of the Li-ion battery consumers' electronic market has been steadily increasing [1].

However, Li-ion batteries still suffer from a lack of safety, excessive costs and insufficient energy densities for certain applications, e.g., aircraft, renewable power plants and electric vehicles [1]. Due to the massive interest in building a greener economy, these applications became viable solutions to reduce global pollution. Nevertheless, they demand lightweight, high-energy-density batteries and the current cells need to be further improved to successfully meet these new requirements [1].

In this context, Solid-State Batteries (SSBs) are seen as an exciting and promising alternative to the established Li-ion batteries. They are therefore the focus of this PhD work. The introduction chapter starts with a motivation on SSBs in subsection 1.1, explaining how these work and diving deeper into their underlying phenomena. We move on to the theoretical background in subsection 1.2, which includes a description of the computational and experimental techniques used in this study. Then, we finish with a clear list of objectives and thesis outline in subsection 1.3.

1.1 Solid-State Batteries

Standard Li-ion batteries operate using the intercalation concept. Typically, during charging, lithium ions are extracted from the positive electrode (cathode) and intercalated into the layered structure of the negative electrode (anode). The process is then reversed during discharge and cyclically repeated [1]. During discharge, lithium ions move through the electrolyte, while electrons flow through the external circuit via the current collector, powering an electrical device [1]. A schematic description of a battery is shown in Figure 1.1. At the moment, the most used anode material in Li-ion batteries is graphite, with the

silicon-graphite composite anode gaining momentum in recent years [2]. The cathode is commonly either a lithium oxide or a lithium phosphate, and the electrolyte is usually an organic liquid [3].

However, the most ideal choice for the anode would be pure lithium metal, moving forward from the intercalation chemistry [1]. Metallic lithium possesses the lowest redox potential (-3.04 V vs. standard hydrogen electrodes), the lowest density (0.534 $g.cm^{-3}$), and consequently the highest theoretical capacity among all metals in the periodic table [4]. If the graphite electrode could be replaced by lithium metal, the cell's specific energy and energy density would increase by approximately 35% and 50%, respectively [5]. This rise would mean a wider application of such batteries, mainly in electric vehicles and power grids [5, 6].

The problem in this proposal relies mainly on reactions between the liquid electrolyte and the lithium metal. Lithium metal reacts with the liquid electrolyte resulting in growth of nano-sized whiskers, mossy lithium and dendrites, which could cause internal short circuits in the cell [7]. Furthermore, these reactions are highly exothermic, and as the liquid electrolytes are flammable, safety concerns against fire and explosions emerge [1, 6]. To solve such issues, the utilization of solid electrolytes has been suggested as an answer. It would reduce the safety hazard and also allow the use of lithium metal anodes to create higher voltage and higher energy density batteries [5, 6].

The Solid Electrolyte (SE) plays a vital role in SSBs, as the evolution of these cells is intrinsically attached to the development of SEs. The SEs enable the use of the Lithium Metal Anode (LMA), as well as high-voltage and high-capacity cathodes. Besides, they are praised for being safer, bearing almost no risk of thermal runaway. The SE operates transporting the Li-ions but blocking electrons. Thus, the main challenge for these materials is obtaining an electronic insulator combined with a high ionic conductivity within a solid structure that is mechanically and chemically stable at room temperature [4].

Many materials are currently being investigated for the application as SEs. In general, they are classified in two big groups: organic and inorganic electrolytes [4, 8, 9]. The organic SEs include polymers, while the inorganic SEs are mostly represented by oxides and sulfides. These two groups can also be combined, forming a hybrid solid electrolyte. Each class of materials has its pros and cons. For example, the polymers offer low cost, but also low ionic conductivity. Meanwhile, the oxides come with a high cost, but also a high ionic conductivity. The sulfides have an even higher ionic conductivity, but they are not stable against pure lithium metal, requiring an interface layer or protective coatings [4, 8–13]. In this work we focus on the lithium lanthanum zirconium oxide - $Li_7La_3Zr_2O_{12}$ (LLZO) as SE.

The individual features of the active materials are not the only thing to consider, as in SSBs the integration of different components is challenging, and extremely complex

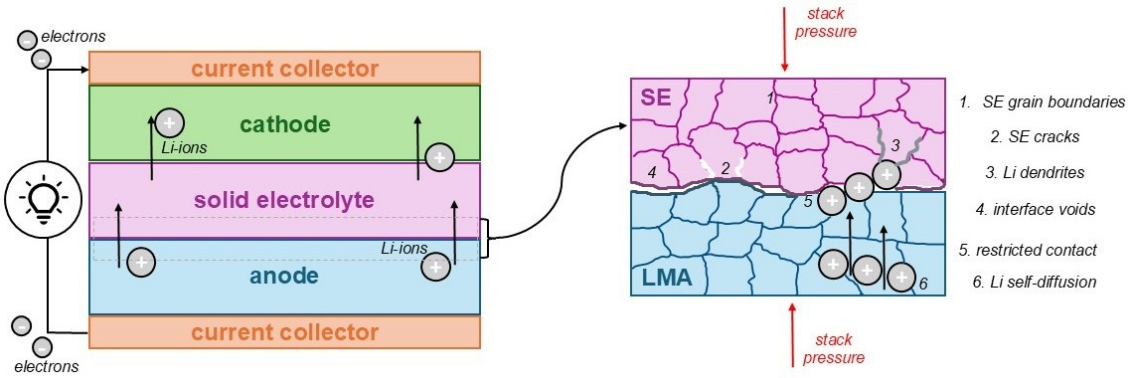

Figure 1.1: Schematic description of a solid-state battery with a focus on the solid-solid interface between the lithium metal anode (LMA) and the solid electrolyte (SE), highlighting some of its main challenges.

solid-solid interfaces emerge. These interfaces are highly-resistive, unstable and hinder obtaining high-performing and long-lasting cells. The interface degradation events are usually associated with either mechanical or electrochemical processes [4]. For instance, the interface between oxide SEs and LMA suffers from a loss of physical contact and a formation of lithium dendrites [4]. A schematic description is shown in Figure 1.1.

The lack of physical contact in oxide SEs is particularly troublesome. During cycling, the cell undergoes a series of volumetric changes. These changes, combined with low plasticity of the SE and limited lithium vacancy and self diffusion creates pores at the interface [14–16]. This phenomenon has several consequences for the battery. The most obvious one is a high interface impedance, since the physical contact is not sufficient to ensure low resistances. Apart from that, insufficient contact forces the current to pass via discrete spots, leading to current constrictions, which in turn, polarize the electrodes [14]. Besides, contrary to batteries with liquid electrolyte, which can partially accommodate mechanical stresses due to swelling, rather strong mechanical loads appear in these cells. To make the matters worse, often an external load (also named stack pressure) is applied to increase the real contact area in the cell [14]. The stack pressure plays a controversial role. At low pressures, the inadequate physical contact leads to high local current densities, which promote non-uniform lithium plating and dendrite initiation. Contrary, at high pressures, the SE cracks and lithium filaments can grow into the electrolyte's pores, cracks and grain boundaries, leading to eventual short circuiting [14, 17–19]. Ideally, the SSB should operate without a stack pressure [20].

The formation of lithium dendrites at the SE – LMA interface is a further critical issue. These lithium filaments usually initiate at the anode and propagate into the SE, causing

internal short circuits. Dendritic growth is strongly linked to the presence of structural defects at the SE, such as pores (both on the surface or internally), grain boundaries and cracks [14, 16, 21, 22]. Importantly, this phenomenon occurs in both polycrystalline and single-crystalline electrolytes [21]. In single-crystalline LLZO, the lithium depositions create a continuous accumulation of stresses, generating fracture of the SE at the dendrite tips [23]. In polycrystalline LLZO, the lithium dendrites are known to specially infiltrate through grain boundaries [23, 24]. In addition, the polycrystals are prone to intergranular fracture [25]. But generally, any pores and cracks of the LLZO induce the nucleation and penetration of Li dendrites [15]. A number of *in situ* experimental studies have visually characterized lithium filament growth and confirmed its correlation with factors such as SE defect density and size, current density and applied stack pressure [17, 18, 21, 26–28].

Another detrimental aspect in this interface is a poor surface contact between the SE and LMA. Many SEs exhibit lithiophobic behavior, characterized by high interfacial energy with molten lithium, resulting in low wettability and poor interfacial contact. In contrast, lithiophilic materials exhibit better wettability with molten lithium, facilitating stronger interfacial adhesion. Studies have employed the lithiophobic/lithiophilic framework to evaluate the surface of SEs, revealing a correlation between interfacial adhesion and interfacial resistance [29, 30]. Factors influencing wettability include temperature, surface roughness, electric potential and the presence of surface impurities [29, 30].

To investigate the electro-chemo-mechanical aspects of SSBs, numerous experimental and computational methods can be applied. On the experimental side, Scanning Electron Microscope (SEM) and Transmission Electron Microscope (TEM) are common imaging techniques for open or cross-cut cells [21, 22, 27]. For closed cell setup, X-ray tomography can be efficiently used [17, 26]. Meanwhile, for electrochemical characterization, the standard methods are Cyclic Voltammetry (CV) and Electrochemical Impedance Spectroscopy (EIS) [22]. On the modeling side, atomistic simulations and database-enabled thermodynamic calculations are important techniques [31]. Data-driven approaches can be used, e.g., to accelerate the atomistic simulations (e.g., [32]) or predict battery cycling data (e.g., [33]). Phase-field simulations have also already been applied within this context [34]. More recently, novel quantum computing techniques are gaining space [35, 36]. However, the majority of the studies still employ pure continuum formulations [37, 38].

Regarding the mechanical properties of the metal anodes, reliable and comprehensive research is still lacking. For instance, direct measurements of the elastic properties of Li such as Young's modulus (E), shear modulus (G) and Poisson's ratio (ν) are difficult to conduct due to its high reactivity and very low strength. Besides, Li has a low melting point, creeps at room temperature, and its mechanical properties are strongly anisotropic, which complicates the characterization even further. Various groups have invested significant efforts in characterizing lithium mechanics over a wide range of experimental techniques

and on different length-scales [39–47]. Even within published works, the mechanical data are widely scattered, depending on sample geometry, orientation and experimental procedures [46]. In a recent review, Kalnaus et al. [48] comprehensively summarized the current state-of-the-art. In general, the main findings indicate a strong anisotropy of lithium metal, with a high dependence on strain rate, temperature and length-scale. For instance, the Young's modulus can range from 3 to 21 GPa depending on the orientation [45]. Besides, the bulk hardness is found to be in the range of 6.5 to 14 MPa. However, for small indentation depths, the hardness increases significantly, reaching almost 300 MPa [44, 45].

Hence, to enable SSBs, it is of great importance to understand the mechanical behavior of the active materials involved. In this context, the metal anodes are specially lacking in-depth investigation of their deformation behavior. Besides, the solid-solid interfaces are regarded as one of the biggest challenges still to overcome in the SSBs. The interface between LLZO - LMA is particularly problematic and presents serious issues related to dendrite formation, pores generation (which leads to the need to apply a stack pressure), SE cracking and poor lithium wettability. At this interface, mechanical processes play a central role, alongside chemical / electrochemical reactions and surface effects.

1.2 Theoretical Background

In materials science, computational and experimental methods are often confined to specific size and time scales, each offering unique strengths, constraints and focal points. Depending on the scientific question, one might choose to delve deeply into a single method and scale, or instead adopt a multi-scale approach, where various techniques are combined to analyze the problem from multiple perspectives. In a multi-scale and multi-physics framework, the advantage lies in the diversity of viewpoints, enabling more comprehensive insights across a broader range. However, this approach also presents challenges, particularly in linking and benchmarking the results obtained from different methods. In this investigation, we adopt a multi-scale strategy to leverage the strengths of diverse techniques across different length and time scales, working towards the goal to develop an encompassing study of lithium and oxide-based SSBs. An overview of relevant methods is presented in Figure 1.2.

The theoretical background on the methods employed in this research work are explained in the following subsections. We start on the computational models on subsection 1.2.1, followed by the experimental techniques on subsection 1.2.2.

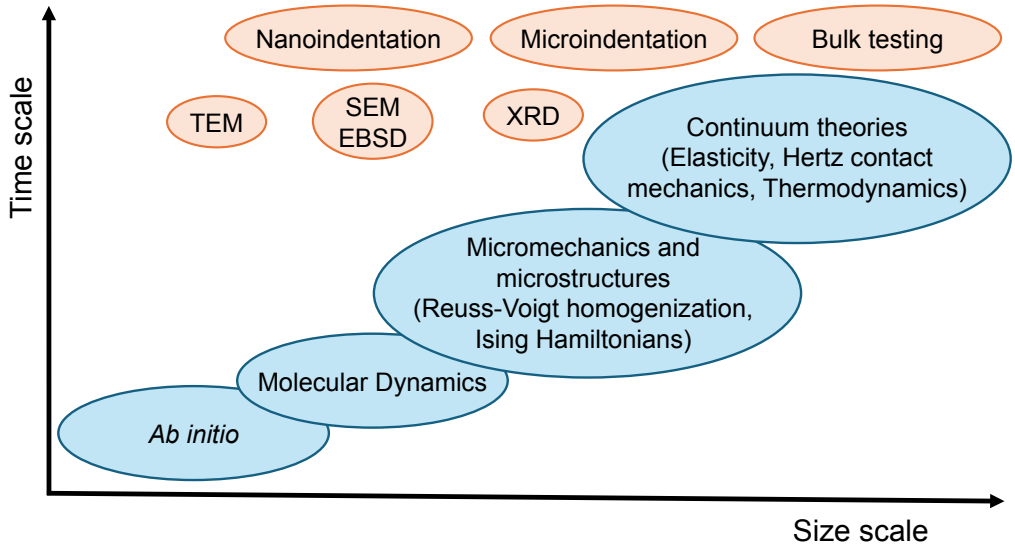

Figure 1.2: Schematic representation of experimental (in orange) and computational methods (in blue) relevant to this work, positioned within their respective size and time scales.

1.2.1 Computational Modeling

Linear Elasticity Theory

Linear elasticity theory is a fundamental framework in continuum mechanics that describes the mechanical behavior of solid materials under small deformations and stresses. It is based on two key assumptions. Firstly, that the relationship between stress and strain is linear in the form of the well-known Hooke's law. And secondly, that the material returns to its original shape when the load is removed, i.e., no permanent deformation is encountered. Several established works can be used as reference for grounding the equations, such as Timoshenko and Goodier [49], Nemat-Nasser and Hori [50] and Landau and Lifshitz [51].

When a body is deformed, a point in the undeformed (x_i) and deformed body (x_i') are linked via a displacement vector u_i defined as

$$u_i = x_i' - x_i. \tag{1.1}$$

Under the small strain approximation, the strain tensor ε_{ij} is defined as

$$\varepsilon_{ij} = \frac{1}{2}\left(\frac{\partial u_i}{\partial x_j} + \frac{\partial u_j}{\partial x_i}\right). \tag{1.2}$$

Because of the deformation, internal forces develop to resist deformation and an internal potential energy arises. This energy is analogous to, for example, the energy stored in a compressed spring, which seeks to restore itself to its initial shape. This elastic strain energy density F, for isotropic elastic materials, is denoted by

$$F = \frac{1}{2}\lambda\, {\varepsilon_{kk}}^2 + \mu\, {\varepsilon_{ij}}^2, \tag{1.3}$$

in which λ and μ are the Lamé coefficients, which directly relate to other mechanical properties such as Young's modulus and Poisson's ratio, ${\varepsilon_{kk}}^2$ follows Einstein notation and represents the squared sum of the diagonal components of the strain tensor (i.e., $(\varepsilon_{xx} + \varepsilon_{yy} + \varepsilon_{zz})^2$) and ${\varepsilon_{ij}}^2$ represents the sum of the squares of all the components (i.e., ${\varepsilon_{xx}}^2 + {\varepsilon_{yy}}^2 + {\varepsilon_{zz}}^2 + 2{\varepsilon_{xy}}^2 + 2{\varepsilon_{xz}}^2 + 2{\varepsilon_{yz}}^2$). Therefore, the free energy is a scalar value. In this formulation (Equation 1.3), it is possible to account for the eigenstrain (or stress-free strain), which refers to a deformation that a material would ideally undergo without developing internal stresses, arising from, e.g., thermal expansion or phase transformations.

The stress tensor σ_{ij} is derived from the strain energy density, yielding Hooke's law, via the formulation

$$\sigma_{ij} = \frac{\partial F}{\partial \varepsilon_{ij}} = \lambda \varepsilon_{kk}\delta_{ij} + 2\mu\varepsilon_{ij}, \tag{1.4}$$

where δ_{ij} is the Kronecker delta in the form of

$$\delta_{ij} = \begin{cases} 1 \text{ if } i = j\,, \\ 0 \text{ if } i \neq j\,. \end{cases} \tag{1.5}$$

For general anisotropic materials, Hooke's law is also expressed as

$$\sigma_{ij} = C_{ijkl}\varepsilon_{kl}, \tag{1.6}$$

where C_{ijkl} is the fourth-order stiffness tensor (with symmetries $C_{ijkl} = C_{jikl} = C_{ijlk} = C_{klij}$). For cubic crystals, the stiffness tensor reduces to three elastic constants (C_{11}, C_{12}, C_{44}), and from those, the other elastic properties can be obtained.

In simplified geometries, approximations may be adopted. If the strain tensor has vanishing components, a plane strain condition can be assumed. Meanwhile, if the stress tensor has a vanishing component, then plane stress condition can be assumed. Therefore,

often a reduction from a 3D problem to a 2D is possible when assuming a plane strain or plane stress situation.

Finally, linear elasticity allows for the application of the superposition principle, which states that the response of the system to multiple loads is the sum of the individual responses to each load applied independently. This is an important aspect, as the superposition principle makes linear elastic models suitable for use within a quantum annealer, which will be described in more details below.

Quantum Annealing

Quantum annealers represent a promising and accessible form of the quantum computing technology. They are built using qubits, much like general-purpose quantum computers. However, while fully scalable, general-purpose quantum computers with large numbers of qubits are still under development, Quantum Annealing (QA) devices with thousands of qubits and couplers are already available for use today [52–56]. Unlike universal quantum computers, QA systems are designed to efficiently solve a specific class of problems — namely, binary quadratic optimization problems [57]. The basic concept of QA is the initialization of its qubits in well-defined Hamiltonians, whose ground state is unique and known [58]. The Ising Hamiltonians describe a type of mathematical model used to represent systems of interacting spins. The QA utilizes superconducting loops to encode and manipulate information. The direction of current — either clockwise or counterclockwise — corresponds to distinct spin states. The qubits are influenced by external magnetic flux biases, shaping an energy landscape where the fluxes determine both energy differences and barrier heights [58]. The initial Hamiltonian is then changed adiabatically under cryogenic temperatures to the desired, final "problem Hamiltonian", ideally staying in the ground state throughout this transformation and, consequently, enabling efficient global energy minimizations [58, 59]. The Hamiltonians do not commute [57]. The time taken by the initial Hamiltonian to reach the low energy state is sufficiently large to establish the validity of the adiabatic theorem of quantum mechanics, which postulates that a system stays in its eigenstate during adiabatic changes [60]. QA uses quantum tunneling to escape local minima [52]. Besides, entanglement plays a critical role, with entangled states being central to the quantum processing unit [61].

The type of problems which can be addressed is limited. The QA technique is most adequate to solve problems in which the variables are binary, discrete and with strong interactions. The goal is to find the lowest energy configuration from a large but finite set of possibilities, i.e., a combinatorial optimization problem. It is required to map the question of interest to the minimization of an Ising model (with variables taking values of either +1 or -1) or of a Quadratic Unconstrained Binary Optimization (QUBO) model (with

variables taking values of either 0 or 1). These two models are mathematically equivalent and can be transformed into one another [62, 63].

In real-world applications, quantum annealing does not always guarantee the discovery of the absolute ground state, especially when nearby low-energy states exist. Therefore, the process is typically repeated multiple times, and the configuration with the lowest observed energy is selected as the ground-state [62]. The excited states can later be used, for example, to do a Monte Carlo sampling at low, but finite temperatures [63].

A pioneering company providing quantum annealing technology is D-Wave. Systems such as D-Wave's Advantage can handle problems involving up to 11,616 variables, and their software platform, Leap, allows users to directly formulate optimization tasks using an Ising Hamiltonian representation [64–66].

The application of QA in materials science is only starting to influence the opportunities and methodologies of modeling approaches. Research works have already been published in this regard (e.g., [36, 63, 67–78]). Often, the focus tends to lie on performance tests and benchmark against conventional approaches [79–82]. However, recently it is moving towards the application side [36, 78]. It can be expected that in future general-purpose quantum computing will have the potential to strongly accelerate materials science simulations and to enable completely new possibilities. Currently, we can explore the application of QA to materials science problems, provided the question of interest fits the formulation constraints.

Homogenization Techniques

Homogenization techniques are a group of theoretical methods used to predict the macroscopic behavior of materials by averaging the response of their individual phases. These approaches are particularly useful for analyzing composites, polycrystals and multiphase materials. In the case of polycrystals, they enable the estimation of bulk properties based on single-crystal elastic constants [50, 83].

Two widely adopted theoretical frameworks are Mean Field Theory (MFT) and Effective Medium Theory (EMT). Both aim to replace a macroscopically heterogeneous material with a homogeneous equivalent that reproduces its average mechanical behavior based on microscale characteristics. A key concept in this micro-to-macro transition is the Representative Volume Element (RVE), i.e., a microscale domain that statistically captures the material's local structure and provides the link between microscopic properties and macroscopic response [50, 83].

Among the earliest homogenization models are the Voigt and Reuss bounds. The Voigt model [84] assumes uniform strain across all phases (isostrain), similar to a parallel arrangement of phases. Meanwhile, the Reuss model [85] assumes uniform stress (isostress),

analogous to a series configuration of phases. These provide upper and lower bounds for the effective stiffness of the material. Later, Hill [86] proposed that the arithmetic mean of the Voigt and Reuss estimates offers a reliable approximation, now known as the Voigt–Reuss–Hill average, particularly applicable to randomly oriented polycrystals.

Thermodynamics

Thermodynamics is the study of the transformations of energy. Energy is the capacity of a system to do work. The internal energy is the total energy of a system. Thermodynamics is built upon three fundamental laws [87].

The first law of thermodynamics is essentially the principle of energy conservation. It states that the internal energy U of an isolated system is constant, and it only changes through heat transfer δQ or work δW. It is mathematically expressed as

$$\Delta U = \delta Q + \delta W. \tag{1.7}$$

The second law introduces entropy, a measure of disorder. It asserts that for any spontaneous process, the total entropy of an isolated system always increases, which imposes a directionality on natural processes, expressed as

$$\Delta S_{\text{tot}} \geq 0. \tag{1.8}$$

The third law states that as the temperature approaches absolute zero, the entropy of a perfect crystalline substance also approaches zero, providing an absolute reference for entropy values [87].

A central thermodynamic concept is the Gibbs free energy G formulated as

$$G = H - TS, \tag{1.9}$$

where H is enthalpy and T is temperature. At constant temperature and pressure, conditions which are very common in realistic settings, a chemical reaction is spontaneous if it leads to a decrease in the Gibbs free energy. The thermodynamic criterion for spontaneity is given by

$$\mathrm{d}G_{\mathrm{T,p}} \leq 0. \tag{1.10}$$

A negative change in G indicates that the forward reaction is thermodynamically favored. Conversely, if G increases during the reaction, the reverse process is spontaneous. Therefore, systems tend to evolve toward a state that minimizes the Gibbs free energy [87].

Graphs of Gibbs free energy versus temperature or composition are fundamental in constructing phase diagrams, allowing prediction of phase stability and transitions. Phase

diagrams are a map of, most commonly, the pressures, temperatures or concentrations at which each phase of a substance is the most stable. Here, it is important to introduce the concept of thermodynamic equilibrium. Equilibrium is reached at the minimum of the Gibbs free energy and there, the molar Gibbs energy, or chemical potential, of a substance is the same throughout a sample, regardless of how many phases are present [87].

To predict phase equilibria in multi-component systems, the CALPHAD (originally CALculation of PHAse Diagrams) method is extensively used [88]. Pioneered by Kaufman and Bernstein [89], CALPHAD combines experimental and first-principles data with thermodynamic models to construct self-consistent descriptions of entire systems. Each phase is modeled using Gibbs free energy minimizations. Once optimized, these models allow for the calculation of phase diagrams and thermodynamic properties over wide temperature and composition ranges. CALPHAD forms the theoretical basis of modern thermodynamic database software packages such as FactSage [88].

First Principles

The *ab initio* methods (also known as first principles) consider nuclei and electrons as the basic particles of a material, and it can obtain all properties via quantum mechanics given only the atomic numbers of the atoms to be simulated. Thus, the calculation is not based on any parameters from experimental data, but rather on the laws of physics [90].

To be able to formulate quantum mechanics as a simulation method and obtain results in reasonable computational times, Density Functional Theory (DFT) was developed. DFT is based on the idea that the ground-state properties of a many-electron system can be determined entirely by its electron density, rather than the full wave-function. It uses many approximations to deliver its results, such as the Born–Oppenheimer approximation (separating nuclear and electronic motion), the mean-field approximation (reducing many-body interactions), the Pseudo-Potential (PP) approach, the Exchange-Correlation (XC) functionals, the use of supercells and periodic boundary conditions and the energy cutoff and k-points sampling (which require convergence tests). The large majority of DFT calculations are carried out at the ground state at 0 K and do not consider the entropy terms [90].

From all these assumptions, the most relevant for us to understand is the PP approach. It divides the electrons into two groups: the core electrons (which are the ones closer to the nucleus) and the valence electrons. The approach freezes the nucleus and the core electrons together and leaves only the valence electrons to move. This leads to a significant reduction in the number of electrons and to a much easier description. From the computational point of view, the nucleus plus core electrons can be removed from the picture and only the active valence electrons can be dealt with. This is called the

frozen-core approximation [90].

With only the valence electrons being explicitly considered, the XC functionals reflect the electron-electron interactions. They are mainly defined by the Local Density Approximation (LDA), Generalized Gradient Approximation (GGA) or Hybrid Functionals. LDA is known to work fairly well in covalent systems and simple metals, but it tends to overestimate the bulk modulus and adsorption energies. GGA works very well with almost all systems, obtaining rather accurate physical properties, but it tends to slightly underestimate adsorption energies. One of the mostly used GGA potentials is the Perdew–Burke–Ernzerhof (PBE). The PBE has been proven to be highly accurate and computationally efficient, and it is the most frequently used functional. An improved accuracy can be obtained with the hybrid functionals, PBE0 for instance, but they are more expensive and can create a 10-fold increase in computational cost [90].

Once all the inputs are set, DFT is solved self-consistently and it involves two energy minimizations: electronic and ionic minimizations. To start the self-consistent calculations, firstly an initial guess for the electron density is made. Then, the Kohn-Sham (KS) equations are used to obtain the KS orbitals and KS Hamiltonian, which in turn calculate a new electron density. All these parameters are interdependent and must be solved iteratively until convergence. After the self-consistency loops are converged, the ionic forces are calculated and the ionic positions are updated, returning afterwards to the self-consistency loop. At the end, energy and other properties are calculated and output for further analyses [90]. A widely used software for first principles calculations is the Vienna *Ab Initio* Simulation Package, also known as VASP [91]. It performs *ab initio* quantum mechanical calculations with broad use in theoretical physics, materials science and quantum chemistry.

Molecular Dynamics

Molecular Dynamics (MD) is an atomistic modeling approach, which treats the involved atoms as classical particles interacting with one another. In its most elementary form, it solves Newton's equations of motion

$$F = ma, \tag{1.11}$$

with the force vector F acting on a particle with mass m, leading to an acceleration a. As the latter is related to the particle's position $x(t)$ via $a = \ddot{x}(t)$. This allows to integrate the equation of motion in time, e.g., via the Verlet or Velocity-Verlet algorithms, generating the simulated outputs [90].

The integration of Newton's equations of motion is done mostly via the Velocity-Verlet algorithm, which advances positions by Δt and velocities by $\Delta t/2$ of the particles while

conserving energy. Then neighbor lists are used to keep track of nearby particles within a radius r. The interaction between the particles is based usually on empirical potentials, which are designed to capture specific physical properties. Therefore, once the potential, the initial positions and initial velocities are known, the time evolution of the atoms can be revealed in a rather straightforward fashion. MD is a valuable simulation tool where quantum effects are negligible. This creates an advantage when dealing with bigger systems. Because, differently than *ab initio*, which is computationally expensive and can deal with at most a few hundred atoms, MD runs are significantly faster, and the system size can be easily increased to many millions of atoms [90].

MD supports a wide range of statistical ensembles through the appropriate combination of integration and control algorithms. These ensembles bridge microscopic atomic behavior (in the form of interacting particles) and macroscopic thermodynamic properties. The most commonly used are:

- The microcanonical ensemble (NVE): conserves the number of particles N, system volume V and total energy E. It represents an isolated system with no exchange of energy or matter with the surroundings.
- The canonical ensemble (NVT): fixes N, V and temperature T by allowing energy exchange with a thermal reservoir.
- The isothermal-isobaric ensemble (NPT): controls N, pressure P and T, allowing both volume and energy fluctuations.
- The isenthalpic-isobaric ensemble (NPH): maintains constant N, P and enthalpy H, with no direct temperature control.

The temperature control is typically handled using thermostats, which regulate the kinetic energy of atoms to maintain a desired temperature. The most commonly used thermostats are the Nosé-Hoover thermostat and the Langevin thermostat [92]. The Langevin thermostat is typically applied in conjunction with an NVE ensemble, acting as a stochastic heat bath by introducing random forces and frictional damping [92]. The Nosé-Hoover thermostat, on the other hand, maintains temperature by coupling the system to an extended set of variables directly related to the kinetic energy, allowing for realistic temperature fluctuations around the target value [92]. The Nosé-Hoover thermostat, sometimes together with a Nosé-Hoover barostat, is commonly used with NVT and NPT ensembles [92]. A commonly used software for MD calculations is Large-scale Atomic / Molecular Massively Parallel Simulator (LAMMPS) [92]. It is an open source package which performs flexible MD simulations with broad use in computational materials science.

1.2.2 Experimental Techniques

X-ray diffraction

X-ray Diffraction (XRD) on crystalline materials works based on two main principles. Firstly, when X-rays hit the atoms in a crystal, they reflect without losing their energy. This phenomenon is called elastic scattering and allow us to abstractly think of the flat layers of atoms in the crystal like mirrors reflecting light [93]. Secondly, X-rays have a wavelength on the same order of magnitude as the distance between atoms in a crystal, which is about 0.15 to 0.5 nm. This fact leads to X-rays interfering with each other, sometimes combining (constructive interference) and sometimes canceling (destructive interference). This interference pattern creates the measured diffraction effect [93].

Therefore, XRD serves as a fundamental method for investigating the structure of crystals. The angles and intensities of the diffracted X-rays are directly related to how atoms are arranged within the material. This relationship is described by the well-known Bragg's equation, which links the X-ray wavelength, the spacing between atomic layers and the angle at which the X-rays are incident on those layers [93].

XRD allows us then to measure the orientation and texture of samples. The orientation measurement works by maintaining the diffraction angle fixed and tilting and rotating the sample. In this way, the lattice planes which are not parallel to the surface are moved into the Bragg plane and the diffracted intensity is collected as function of the tilt and rotation angles [93, 94]. To obtain the full orientation distribution, it is often required to perform the analysis around several Bragg reflections [93]. After that, the intensity is normalized [94]. Finally, the resulting crystal orientation and texture can be expressed by a pole figure or inverse pole figure [94].

An advantage of measuring specimen texture and orientation via XRD is that the irradiation area is much larger than by EBSD and SEM techniques, making it ideal for thin films and foils [94]. Besides, light and reactive materials, such as lithium and sodium, are challenging to characterize via these latter methods and a complex sample preparation and transfer are necessary to access such information [95].

Indentation

An immensely useful technique to probe the mechanical properties of materials on small scales is indentation. From the indentation tests, load-displacement data can be measured continuously on a micro or nanoscale and afterwards it is used to derive the mechanical parameters of the tested specimens [96]. From these tests, usually two parameters are extracted, the elastic modulus E and hardness H. Hardness is typically defined as the resistance of a material to permanent penetration by another harder material. Indentation

hardness relates purely to plasticity, as it ignores the elastic recovery of the material to calculate the hardness. On the other hand, Martens Hardness (HM) includes the plastic and elastic deformation [97]. For materials with negligible elastic recovery, both hardness values output the same results. For a Vickers indenter, HM is evaluated according to the equation

$$HM = \frac{P_{max}}{A(h)} = \frac{P_{max}}{26.43 \times h^2}, \tag{1.12}$$

where P_{max} is the maximum testing load, A is the contact area of indentation and h is the indentation depth at the P_{max}. HM is expressed at N/mm² or MPa [97].

To evaluate the elastic modulus, the classic Oliver-Pharr method is commonly used [96, 98]. This method derives originally from the pioneering work of Hertz on elastic contact [99–101], which was extended by Sneddon [102], who generalized the relationship between load, displacement and contact area for arbitrary bodies. Oliver-Pharr observed that, in an indentation test, the diameter of the contact impression in the surface does not recover during unloading, but the depth does. Thus, they postulated that, to obtain the elastic modulus E of a material being penetrated by a hard indenter, the unloading curve shall be analysed [96, 98]. Therefore, a power-law function is fit to the unloading curve as

$$P = \alpha(h - h_f)^m, \tag{1.13}$$

where P is the applied load, h is the displacement, h_f is the final displacement, and α and m are fitting parameters. Then, the slope of this curve at the maximum load is defined as the stiffness S following the equation

$$S = \frac{dP}{dh} = \alpha m(h - h_f)^{m-1} = \frac{2}{\sqrt{\pi}} E_r \sqrt{A}, \tag{1.14}$$

where S is the experimentally measured stiffness of the unloading curve, A is the projected area of elastic contact and E_r is the reduced elastic modulus calculated as

$$\frac{1}{E_r} = \frac{(1 - \nu^2)}{E} + \frac{(1 - \nu_i^2)}{E_i}, \tag{1.15}$$

where E and ν are the elastic modulus and Poisson's ratio of the specimen, while E_i and ν_i are the same parameters of the indenter.

1.3 Objectives and Outline

Given the complexities of SSBs and the wide range of available methods, this study investigates the mechanics and microstructure of metal anodes, as well as the solid-solid

interface between LMA and LLZO. By bridging these perspectives through a multi-physics and multi-scale approach, we combine atomic-scale simulations, micromechanics, thermodynamic modeling, interfacial effects and continuum formulations. This integrated approach connects fundamental material behavior and practical cell-relevant aspects, developing a holistic understanding of SSBs. We can clearly state the objectives and goals of this thesis in the following research questions:

Research question 1: How does lithium behave mechanically? Do alloying and processing affect the mechanics of anode foils? Can we understand the correlation between processing, microstructure and mechanical properties?

Research question 2: What are the main aspects influencing the solid-solid interface between LMA and LLZO? How to improve this interface to obtain longer-lasting cells?

Research question 3: Is it possible to use quantum computing to simulate SSBs materials?

We start in chapter 2 by focusing on the mechanical properties and deformation behavior of the metal anodes. Here, we use a combination of theoretical and experimental methods to build a strong foundation in mechanics, while also looking into microstructural and properties changes induced by processing. On the pure lithium side, we start with microindentation experiments, which are then complemented by simulations. These simulations begin under highly controlled conditions and progressively incorporate complexity, culminating with nanopillar polycrystalline simulations. On the lithium-sodium side, the focus is on the influence of alloying and processing in the anode foils used for cell assembly.

Nonetheless, we note that mechanics are not the only factor to consider in SSBs. Therefore, in chapter 3, we broaden our investigation to include the thermodynamics of the lithium-sodium battery system, in conjunction with mechanical considerations. These thermodynamics studies aim to interpret observed experimental cell phenomena and offer deeper insights into the interfacial interactions between the LMA and the SE. Specifically, they support the understanding of this interface by revealing stability regimes, onset of phase separations, formation of new compounds and surface energies.

Finally, in chapter 4, we explore the use of quantum computing to augment the mechanics, microstructural and interface observations performed in chapter 2 and 3.

There, we investigate and discuss how emerging computational tools can complement classical methods on materials behavior prediction.

Subsequently, integrated discussions and conclusions are carried out in chapter 5, where we synthesize findings across all chapters, highlighting connections, summarizing the main contributions of this doctoral work and pointing future research directions.

Chapter 2

Mechanical Properties of Metal Anodes

In the past years, with the increasing interest in enabling Solid-State Batteries (SSBs), the investigation of mechanical properties of metal anodes gathered momentum. These alkali metals are usually considered as a simple, metallic, isotropic anode material [14]. However, this view is not justified. Lithium and sodium metals, for example, are far from being trivial, mainly regarding their mechanical properties, as we will discuss in this chapter. Even though other alkali metals can be used as anode materials in SSBs, here, we focus on pure lithium metal (subsection 2.1), pure sodium metal (subsection 2.2) and lithium-sodium alloys (subsection 2.3). We intend to build a comprehensive, multi-scale and fundamental understanding of lithium mechanics, as well as characterizing cell-relevant foils.

The simulation results from the subsection 2.1 are published in [103], while the main experimental results from subsection 2.3 are published in [104].

2.1 Pure Lithium Metal

The first main studies on lithium mechanics date back to the late 1950s and 1960s. These works were mainly experimental efforts to characterize mechanical parameters and their temperature dependence [105–110]. Nash and Smith [105] measured the bulk modulus and elastic constants of Li at 78, 155 and 195 K using an ultrasonic pulse-echo technique. Beg and Nielsen [106] also measured the temperature dependence of the equilibrium lattice constant and elastic constants of Li. The temperature was varied from 110 K to close to the melting point. Swenson [107] obtained pressure-volume-temperature data for Li using a piston-displacement technique. Temperature was changed between 350 and 20 K, and bulk modulus and other bulk properties were reported. Pichl [108] studied phase transitions of Li. The recrystallization temperature of Li was measured as 200 – 230 K, and a martensitic transformation was observed from Body-Centered Cubic (BCC) to a close-packed 9R structure at 70 K.

Recently, there has been a resurgence of experimental work on lithium mechanics. Two pioneering studies were published in 2017 by Wang and Cheng [39] and by Xu et al. [111]. Wang and Cheng [39] performed a nanoindentation study of the viscoplastic behavior of pure lithium at room temperature. It was found that the indentation

response of Li is dominated by viscoplastic deformation. The results showed that the elastic modulus has negligible influence on the indentation response of Li. The researchers concluded that the viscoplastic deformation is more relevant than the elastic deformation in designing Li metal electrodes operating at or near room temperature. Meanwhile, Xu et al. [111] performed the first experimental study to report on the scale-dependence and orientation-dependence of lithium mechanical properties. The authors conducted mechanical experiments on single crystal pillars in a scanning electron microscope. They showed that the compressive yield strength increases from 15 to 105 MPa as the pillar diameter decreases from 9.45 to 1.39 μm, unfortunately without specifying the crystallographic orientation of the specimens. This phenomenon is sometimes called the "smaller is stronger" effect, and it has been connected to a dislocation starvation mode within the pillars [112].

Further important works from the literature are by Herbert et al. [40, 41], in particular two publications on nanoindentation of pure lithium, and Masias et al. [42], who evaluated the bulk mechanical properties of Li, including stress-strain curves, creep in tension and creep in compression. Other key references in Li mechanics are LePage et al. [113] and Fincher et al. [44]. LePage et al. [113] investigated the deformation of bulk Li using tensile testing over a wide range of strain rates and temperatures. The results were used to calibrate a power-law creep model. No significant strain hardening was observed and creep was the dominating deformation mechanism. Fincher et al. [44] performed both bulk tensile testing and nanoindentation. From the bulk tests, the yield strength was measured for different strain rates. From the nanoindentation, hardness values decreased sharply from 43 MPa to 7.5 MPa as the indentation depth increased from 250 nm to 10 μm. All these works report a strong Indentation Size Effect (ISE) of lithium hardness values.

In addition, on the bulk scale, other studies have been published. Ding et al. [114] measured compressive creep deformation at varied temperatures and pressures from 0.6 to 3.6 MPa. Masias et al. [43] studied the dependence of Li flow stress in bulk compression by varying specimen geometry, temperature and strain rate. A variation of almost one order of magnitude was observed. On the mesoscale, Sedlatschek et al. [115] performed large-deformation plasticity and fracture experiments on pure lithium under various stress states. The examined length scale was around 150 μm to 1 mm. On the nanoscale, both Citrin et al. [116] and Zhang et al. [117] performed compression experiments on Li nanopillars and reported on Young's modulus and yield stress. Aspinall et al. [45] measured elastic and plastic properties of lithium using nanoindentation. The elastic constants and hardness were evaluated. Darnbrough et al. [46] measured elastic and plastic mechanical properties of lithium using nanoindentation as well. It was found that besides temperature and strain rate, anisotropy plays an important role. The elastic modulus does not show a significant size dependence, but hardness values do.

The ISE is specially worrying in the SSBs context, as the cells are built using thin Li foils. In addition, lithium dendrites are a common source of failure and these structures are much smaller than the usually tested bulk samples. It is widely accepted that the ISE for crystalline materials can be accurately modeled using the concept of Geometrically Necessary Dislocations (GND), published as the well-known Nix-Gao model [118]. According to this model, the strengthening appears when small volumes are plastically deformed. The scientists suggest avoiding the use the constitutive properties of bulk materials to make predictions about the mechanical behavior of thin film materials. The properties of the micro/nano-materials themselves must be used for such predictions.

In this context, in 2023, Lu et al. [47] published a nanoindentation study on Li. The researchers obtained load-displacement curves for different temperatures and indentation depths. They observed that the classical Nix-Gao ISE model based on the concept of GNDs was not sufficient to explain the ISE of Li. The model only showed improved results once effects from the surface energy were included. In a slightly different manner, Wang et al. [119] measured Young's modulus and creep in mossy Li. Mossy Li is porous lithium that forms close to the SE after some cycles. This structure showed a lower Young's modulus than bulk Li, however, a higher resistance to plastic flow and creep. Haslam et al. [120] examined the compression creep behavior of Li foil coupled with LLZO and Ni current collector. It was suggested that friction at the interfaces played a central role in Li deformation, and the level of deformation measured in compression was significantly different than predicted from tension experiments.

Besides experimental works, theoretical works were also recently published on lithium mechanics. From an atomistic perspective, Nagy and Siegel [121] computed the elastic properties of pure BCC Li via first-principles methods. Using the quasi-harmonic approximation, they reported data for finite temperatures. From a continuum perspective, the first relevant modeling studies are from Anand and Narayan [122–124]. In three consecutive publications, these researchers developed a continuum model for the mechanical deformation of lithium. Firstly, in 2018, Narayan and Anand [122], using microindentation data published by Wang and Cheng [39], simulated the elastic-viscoplastic deformation response of lithium with the Finite Element Method (FEM). The indenter was extended to function as the SE. Afterwards, in 2019, they proposed an elastic-viscoplastic model for lithium deformation, bench-marking the model against tensile and compressive bulk experiments [123]. Finally, in 2020, they extended their model to include lithium stripping and plating from a mechanistic point of view [124]. The numerical simulations were also carried out using FEM.

Previously, models have already been published for indentation of visco-elastic-plastic materials [125–128]. Creep, which is strongly observed in lithium, is specially problematic in this case, as the presence of the so-called nose in the load-displacement curves brings

complexities not fully covered by the classic methods [96, 98, 129]. Molecular Dynamics (MD) is a valuable tool to simulate the elastic and plastic effects in nanoindentation, including visualization of dislocation sourcing and movement [130–136]. However, given the MD simulation time constraints, it is not indicated for analyzing creep. FEM is more often used in these cases, as it can model power-law-creep [137]. Nevertheless, extending an FEM model to include effects of ionic transport is a non-trivial task.

So far, only few literature reviews on the mechanical properties of lithium exist. In 2021, Tang et al. [138] reviewed mechanical properties and dendrite growth of pure Li in SSBs. More recently, in 2023, Kalnaus et al. [48] published a long review on the role of mechanics in SSBs. A large fraction of the paper is dedicated to the discussion of Li mechanics.

Although major advancements have been done recently to unfold the complexities of lithium mechanics, the existing data are still sparse, resulting in an incomplete description, in which crucial gaps persist. Three remaining gaps are essential especially for battery applications:

1. *Size dependence of Li mechanical properties.* Even though a number of works have been carried out on various length scales, the full picture remains blurry. It is expected that lithium dendrites have a different deformation behavior compared to bulk lithium. Consequently, understanding Li mechanical properties on small scales, as well as bridging the scales, is a key element for modeling SSB failure [139].

2. *Orientation dependence of Li mechanical properties.* As it has been shown in this section, several papers conclude that Li has a strongly anisotropic behavior [46, 111, 121]. Thus, it is clear that Li mechanical properties vary widely depending on the texture and orientation of the tested foils and pillars. Investigating the orientation dependence is an essential requirement for understanding plasticity, cell cycling and dendrite formation.

3. *Fundamentals of plasticity on small scales and at high homologous temperatures.* As lithium is a soft metal, and batteries are often cycled at room temperature or above, the most relevant deformation will occur in the plastic and creep regime. Nevertheless, the irreversible deformation of pure BCC lithium metal has not been extensively investigated yet.

Here, we investigate the elastic and plastic properties of pure lithium metal with a combination of theoretical and experimental methods, providing a comprehensive view of the deformation behavior from different perspectives and supporting to close these remaining knowledge gaps.

2.1.1 Microindentation Experiments

Several complexities are involved in the mechanical testing of Li metal. Variables such as temperature, strain rate, foil texture and indentation depth can all influence the results. To investigate the deformation response of lithium from an experimental perspective, we perform a microindentation study on pure Li foils which are directly used for cell assembly. Two sets of 100 μm thick Li foils are used: industrial as-received foils, and the same foils after mechanical post-processing in-house. Martens hardness (HM), maximum indentation depth and elastic modulus (E) are evaluated for different experimental parameters. Pole figures analyzes via XRD are additionally performed. The main goal is to investigate the influence of foil orientation and strain hardening on the indentation results of cell-relevant foils.

Methods

As reference foil, the 100 μm thick lithium foils are supplied by Münster Electrochemical Energy Technology (MEET) are tested as-received. All experiments and sample preparation are conducted in an argon-filled glove-box, in which oxygen and water content are kept below 0.1 ppm. The experiments are performed using a Fischerscope H100 indenter (Helmut Fischer GmbH, Sindelfingen, Germany) equipped with a diamond Vickers tip. Square samples are cut from the original foil, which is protected by a plastic film to avoid specimen contamination. The plastic film is only removed right before testing. The squared samples are attached to a metal sample holder, to provide support and stability during indentation. All measurements are performed at room temperature.

HM and E are evaluated using the Equations 1.12, 1.14 and 1.15. The indentation experiments are load-controlled. The load is applied following $d\sqrt{F}/dt$. The influence of application force, creep holding time and application time in the results is systematically evaluated. The chosen settings as shown in Table 2.1. The average and standard deviation of 10 indents are calculated for each setting. The experiments are carried out with a space of at least 10 times the indentation depth in between each indent [140]. Exemplary normalized load-displacement and load-time curves are presented in Figure 2.1.

To investigate work hardening, the Li reference foil is folded and rolled 20x in-house in an argon-filled glove-box at room-temperature. The final foil thickness is kept at 100 μm. The 20x calendered foil is tested using the same settings as the reference one, so a proper comparison can be made. Additionally, XRD and pole figure analyzes are carried out on both specimens. These experiments are performed using a dome airtight sample holder, a diffractometer EMPYREAN (PANalytical) and Cu-Ka radiation.

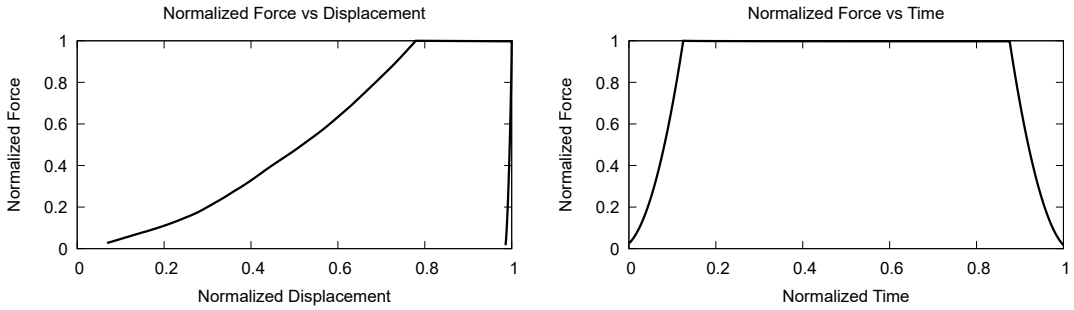

Figure 2.1: Normalized force-displacement (left panel) and force-time (right panel) curves obtained from indentation experiments. Force and displacement (or time) values are normalized by their respective maximums. These examplary plots illustrate the characteristic loading behavior and temporal load evolution during the indentation experiments.

Load (mN)	Creep holding time (s)	Load and unload application time (s)
10 / 15	10	5
10 / 15	10	10
10 / 15	10	15
10 / 15	10	20
5	10	15 / 20
10	10	15 / 20
15	10	15 / 20
20	10	15 / 20
15	1	10 / 20
15	5	10 / 20
15	10	10 / 20
15	15	10 / 20
15	20	10 / 20
15	25	10 / 20
15	30	10 / 20
15	35	10 / 20
15	40	10 / 20
15	45	10 / 20
15	50	10 / 20
15	55	10 / 20
15	60	10 / 20

Table 2.1: Experimental settings used in the microindentation experiments of pure Li foils.

Results and Discussions

Hardness and Maximum Indentation Depth of Li Reference Foil

Firstly, HM and maximum indentation depth of as-received, 100 μm thick, pure metallic lithium foils are experimentally investigated using microindentation. This foil is referred as reference foil. Application force, creep holding time and application time are systematically varied. The average and standard deviation of HM and maximum indentation depth of 10 indents are calculated for each setting and presented in Figure 2.2.

In Figure 2.2(a), the creep holding time is kept constant at 10 s, while the force is varied. The tests are done for two sets of specific load application times. That is total testing time of 40 s and 50 s, meaning that in the first case the load is applied faster, while for the second case the load is applied slowly. It can be observed that once the testing force is varied, the HM does not substantially change within the error bars. However, the indentation depth increases following a linear behavior. This means that the higher the force, the deeper the indentation mark. As these tests are done at the micro level, and not at the nano level, no ISE is expected at such depths. According to the experiments of Fincher et al. [44], the ISE on lithium is detrimental for indentation depths smaller than 5 μm.

From Figure 2.2(b), the creep holding time is kept constant at 10 s, while the load application time is varied. The tests are again done for two set of specific forces, 10 and 15 mN. When the load application time is changed, the maximum indentation depth does not significantly vary, but the HM changes. The main observation is that the faster the load is applied, the harder is the material response. This links with the strain rate sensitivity reported for lithium [39].

Finally, from Figure 2.2(c), the influence of the creep holding time is seen. The load application time and force are kept constant at 15mN/20s and 15mN/10s. As expected, given the strain rate sensitivity of lithium, the HM of these two settings are different, being that the faster load rate results in a harder material response. Nevertheless, the most striking feature is the strong creep behavior present in these reference foils. The maximum indentation depth increases non-linearly with the creep holding time, until reaching a plateau, indicating a strong influence of time-dependent plasticity in the indentation response of these foils.

When comparing the results obtained in these tests and what is already reported in the literature for lithium hardness, similarities are found. The load displacements curves look closely to the ones published by Wang and Cheng [39]. Besides, Fincher et al. [44] reported an indentation hardness of approximately $6.5 \sim 11.5$ MPa for indentation depths higher than 5 μm. These values match with our findings. In the case of Li, given the insignificant elastic recovery, Martens and indentation hardness are comparable.

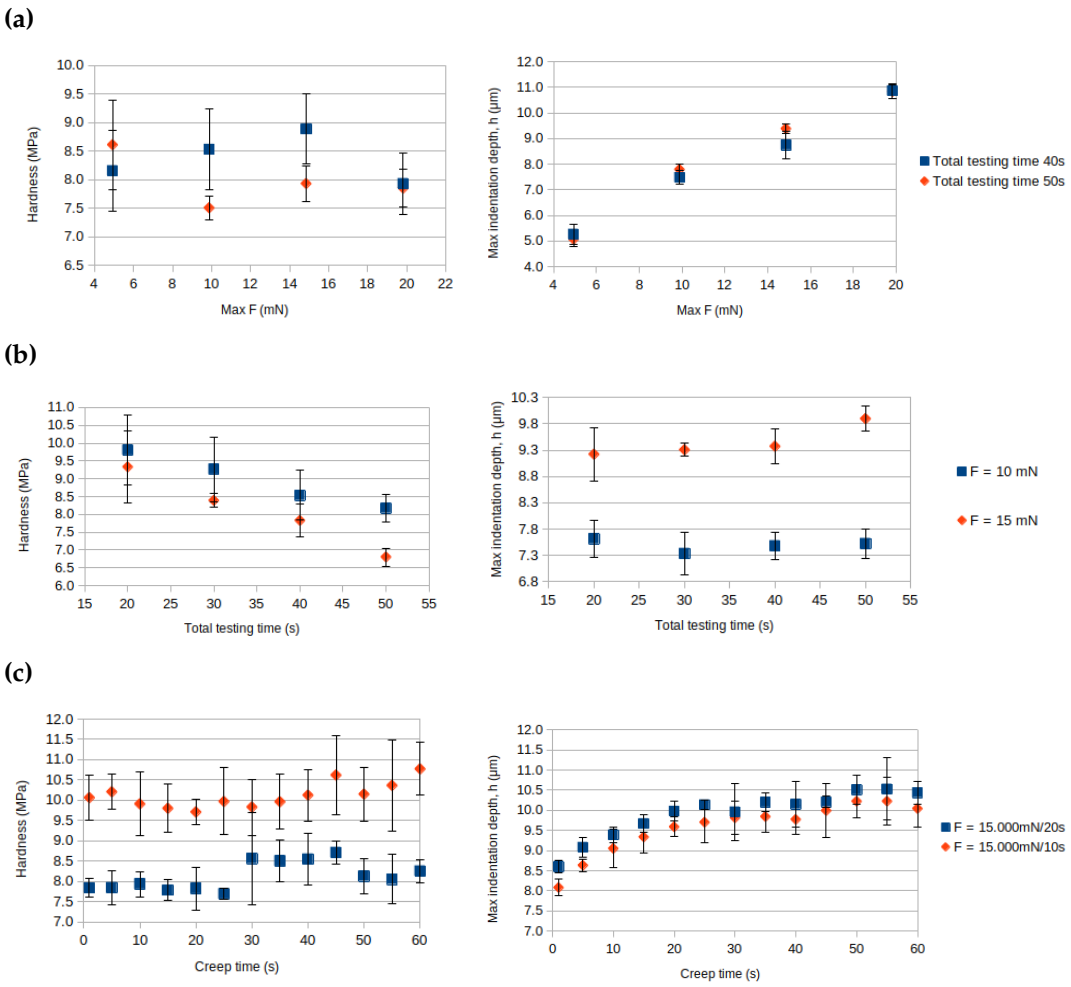

Figure 2.2: Average and standard deviation of HM (left) and maximum indentation depth (right) of 10 indents performed in pure lithium as-received foils. Different experimental parameters are investigated. In **(a)**, load application time and creep holding time (10 seconds) are kept constant, while the load is changed. In **(b)**, the load and creep holding time (10 seconds) as kept constant, while the load application time is changed. In **(c)**, the load and load application time are kept constant, while the creep holding time is changed.

Indentation Modulus of Li Reference Foil

The indentation modulus of the Li reference foils is analyzed following the Oliver-Pharr method [96]. As here we are dealing at larger length scales and not indenting single grains, the isotropic assumption most likely holds true. The classic analysis is done by retrieving the elastic recovery of the material at the initial part of the unloading curve. This means measuring the inclination of the unloading curve at the maximum load. It is already known for materials with a strong creep behavior, that the indentation creep will mostly affect the measured modulus when the load hold is too brief and when the unloading rate is too slow [129]. Therefore, the E is measured for the indents from Figure 2.2 sub-picture f, using the setting F=15mN/10s and creep holding time larger than 30s. Results are depicted in Figure 2.4.

From Figure 2.4, it can be seen that the measured indentation modulus of the lithium reference foil lies in between 2.5 and 6.0 GPa. This value is lower than the reported literature values. But for the case of materials with strong creep and anisotropic effects, elastic modulus measurements via indentation techniques are known to be specially challenging [141]. Fincher et al. [44] reports an indentation modulus of around 10 GPa. Herbert et al. [40] obtained values between 8.2 and 9.8 GPa, depending on the thickness of the foil. Besides, lithium has very low levels of elastic recovery, which complicates even further the analysis of the unloading curve, as the latter appears almost as a straight line. However, as discussed by Wang and Cheng [39], the elastic modulus has negligible influence on the indentation response of Li, which is dominated by viscoplasticity.

Work Hardening Effect

Given the low melting point of lithium, at room-temperature the material is already at high homologous temperature. Thus, it is thought that Li would continuously anneal itself at room-temperature mechanical tests, ruling out the possibility of strain hardening [48]. The only experimental demonstration of strain hardening on Li specimens is published by LePage et al. [113], in which bulk lithium tests showed strain hardening only at high strain rates and low temperatures. This has not yet been investigated for thin foils at the microscale.

To assess the effect of work hardening on the indentation results, the Li reference foil is folded and rolled 20x in-house in an argon-filled glove-box at room-temperature. The final foil thickness is kept at 100 μm. This foil is referred as "20x calendered". Microindentation tests with the same settings as the ones performed to the reference foil are carried out. When comparing the reference foil and the 20x calendered foil depicted in Figure 2.3, a robust and significant increase of hardness is observed. The HM jumps from around 10 to approximately 23 MPa once the foil is work-hardened. In addition, when analyzing

the maximum indentation depth in function of creep holding time, it becomes clear that the influence of the holding time is not as extreme as for the reference foil. Furthermore, the load application time does not appear to have a strong influence in the results. This indicates that once the Li foil goes through work hardening, the material becomes less sensitive to time-dependent plastic deformation.

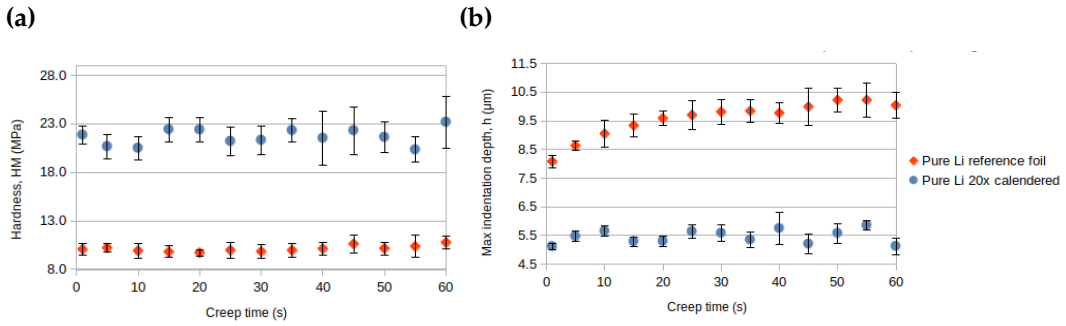

Figure 2.3: (a) *HM* and **(b)** maximum indentation depth while changing the creep holding time are plotted. The creep tests are done with loading and unloading at F=15mN/10s and varying creep holding time. Statistical analyzes are done for 10 indents for each setting. Hardness values are higher than for the reference foil. Creep seems to not play an important role.

The indentation modulus of the Li 20x calendered foil is analyzed following the classic Oliver-Pharr method, similarly to what is done for the reference foil [96]. As this foils is less susceptible to creep, E measurements are analyzed starting from 1 s creep holding time. Average and standard deviation of E are done for 10 indents for each setting. Tests are performed with loading and unloading at F=15mN/10s and varying creep holding time. The experiments indicate an E in between 0.7 and 3.2 GPa for the 20x calendered foil. This value is fairly smaller than the one indicated for the reference foil. However, given the low elastic recovery of lithium and high influence of creep in this material, the quantification of E via indentation experiments is not accurate.

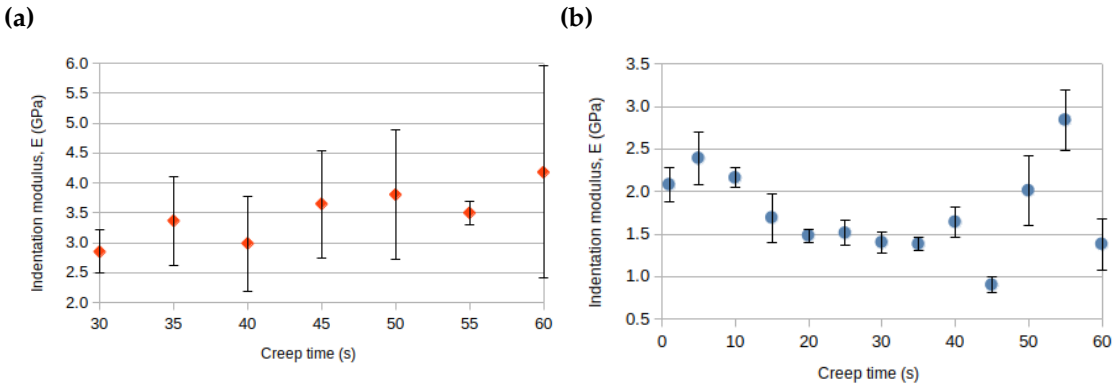

Figure 2.4: Average and standard deviation of E for the **(a)** Li reference foil and **(b)** Li 20x calendered foil. Tests are done with loading and unloading at F=15mN/10s, varying creep holding time and 10 indents for each setting.

Pole Figures and Texture Analysis

XRD, pole figures and texture analysis are carried out in both foils. The results can be seen in Figure 2.5. For the reference foil no preferred orientation can be recognized in the pole figures. It seems to be a randomly oriented polycrystalline structure with large grain sizes, actually leading to insufficient orientation statistics. For the 20x calendered foil, the pole figures demonstrate a highly textured foil. This foil has clear a $\langle 100 \rangle$ preferred orientation. As the only difference between the two foils is the rolling step, it becomes clear that the mechanical processing induced the formation of this strong $\langle 100 \rangle$ texture.

It is already known that lithium presents a high degree of anisotropy, with the $\langle 100 \rangle$ orientation resulting in the lowest elastic modulus of all directions [111, 121]. Therefore, the discreet reduction in indentation modulus of the 20x calendered sample in comparison with the reference sample can be explained via this texture analysis, even though it is important to point out that the creep behavior negatively influences the quantification of the elastic parameter. In a one-of-a-kind study, Aspinall et al. [45] indicated a similar hardness value for the $\langle 100 \rangle$ and $\langle 011 \rangle$ orientations. Meanwhile, the $\langle 111 \rangle$ orientation presented a higher resistance to penetration. However, the difference of hardness in between the orientations was found to be only 5 MPa, with the hardness values ranging from 8.5 at $\langle 011 \rangle$ to 14 MPa at $\langle 111 \rangle$. We obtain a hardness of 23 MPa for the 20x calendered specimen, which is significantly higher.

As the literature does not suggest that orientation strongly influence the hardness of lithium foils [45], we attribute the increased resistance to plastic deformation after rolling to strain hardening. Following the mechanical treatment, the hardness increases from

approximately 10 MPa to around 23 MPa. The lowest value match with numbers reported in the literature [44]. This treatment also modifies the crystallographic texture, producing a dominant ⟨100⟩ orientation. Notably, this specific orientation corresponds to the lowest directional Young's modulus for lithium [111, 121]. As a result, the measured indentation modulus decreases from an average of 3.48 GPa to 1.76 GPa. It is important to note, however, that the presence of creep during unloading complicates precise determination of the elastic modulus. As a consequence, we suggest mechanical treatments as a possible method to increase the hardness and decrease the creep rates of thin Li foils used for battery assembly. As long as a melting does not take place, which would revert the mechanical behavior back to the starting point, this could be an inexpensive approach to improve the mechanical stability of metal anodes.

However, the orientation dependence of the mechanical properties is not fully clarified via these experiments. Furthermore, they do not provide insight into the size dependence of mechanical parameters, which is particularly relevant for battery applications. Hence, we complement our experimental investigation with computational simulations. We begin with *ab initio* calculations at 0 K, which allow for controlled analysis with relatively few atoms. Subsequently, we perform MD simulations at 300 K to explore behavior in more complex, larger and thermally active systems.

(a)

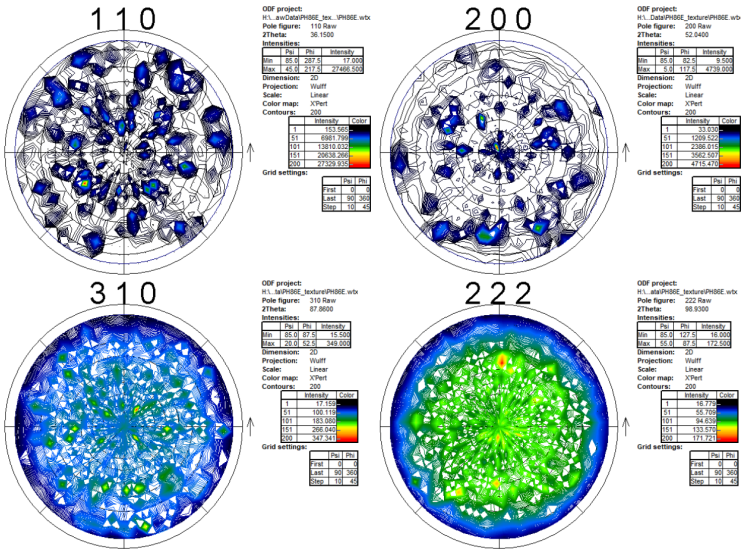

(b)

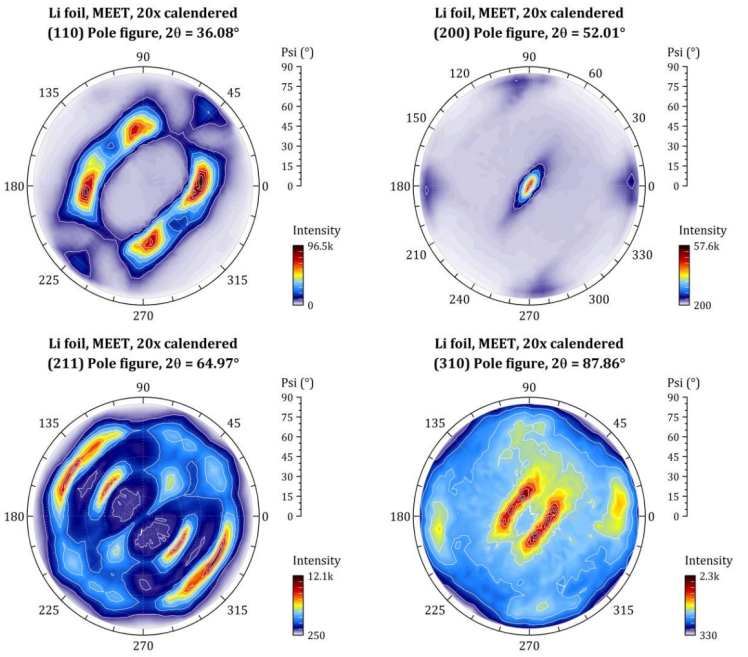

Figure 2.5: Pole figures of the **(a)** reference foil and **(b)** 20x calendered foil. The reference foil is suggested to be a polycrystalline specimen with large grain sizes, while the calendered foil is a highly textured specimen with a ⟨100⟩ preferred orientation.

2.1.2 *Ab Initio* Simulations

To support the experimental observations and obtain reference numbers for the elastic mechanical properties, we begin our computational investigation from a highly controlled framework. Specifically, we perform *ab initio* simulations on systems containing a small number of atoms and in the absence of thermal excitations (0 K). This approach allows for precise evaluation of fundamental mechanical properties without the complexities introduced by temperature or large system size. This method allows us to extract elastic mechanical parameters that serve as benchmarks for both the previous experiments and the subsequent molecular dynamics investigations.

Methods

Mechanical parameters of pure BCC Li metal are computed using the Vienna *Ab Initio* Simulation Package (VASP), which uses a plane wave basis set and the Projector Augmented Wave (PAW) method [91, 142–144]. The exchange-correlation energy is determined via two different potentials: the Perdew-Burke-Ernzerhof (PBE) Generalized Gradient Approximation (GGA) and the Local Density Approximations (LDA). In both cases, the pseudopotential that includes the valence state *1s* for Li is used. The electronic self-consistency loop uses an energy accuracy condition of 10^{-6} eV. Ionic relaxation is carried out with an energy accuracy of 10^{-5} eV between two ionic steps. For all ab initio calculations, systematic convergence checks concerning the energy cutoff and the k-space sampling are performed. We select an energy cutoff for the plane-wave basis set of 800 eV for the LDA potential and 500 eV for PBE. For the k-space sampling, we use a $40 \times 40 \times 40$ Monkhorst-Pack discretization, as the convergence requires a fine mesh, in particular for symmetry reducing shear transformations [121, 145]. Different deformations are applied to a BCC unit cell, so that the cubic elastic constants C_{11}, C_{12} and C_{44} are obtained, according to [146–148]. Specific strains are applied at the unit cell, while keeping the volume constant. The stiffness tensor of a cubic system is determined by three elastic constants, C_{11}, C_{12} and C_{44}. C_{11} and C_{12} are defined by applying a distortional orthorhombic deformation (D_{ortho}) and a volumetric cubic deformation (D_{cubic}). While for C_{44}, a distortional monoclinic deformation (D_{monoc}) is applied. The deformations are defined as

$$D_{\text{ortho}} = \begin{pmatrix} 1+e & 0 & 0 \\ 0 & 1-e & 0 \\ 0 & 0 & \frac{1}{1-e^2} \end{pmatrix}, \tag{2.1}$$

$$D_{\text{cubic}} = \begin{pmatrix} 1+e & 0 & 0 \\ 0 & 1+e & 0 \\ 0 & 0 & 1+e \end{pmatrix}, \tag{2.2}$$

$$D_{\text{monoc}} = \begin{pmatrix} 1 & e & 0 \\ e & 1 & 0 \\ 0 & 0 & \frac{1}{1-e^2} \end{pmatrix}. \tag{2.3}$$

In these matrices, e refers to the applied strain, which is very small, as the intention is to remain in the elastic regime.

Then, from the three elastic constants of a cubic cell, elastic mechanical properties are obtained using an homogenization model. The development of the equations shown below started originally with Voigt [149] and they are for the case of free-standing structures. In this work, we also refer to the equations published by Nagy and Siegel [121] and Yu et al. [146] and are explicitly shown below.

The bulk modulus, B, is defined as

$$B = \frac{1}{3}(C_{11} + 2C_{12}), \tag{2.4}$$

and the Zener ratio, A, is defined as

$$A = \frac{2C_{44}}{C_{11} - C_{12}}. \tag{2.5}$$

The directional values of Young's modulus, E, and shear modulus, G, are calculated as

$$E_{[100]} = \frac{(C_{11} - C_{12})(C_{11} + 2C_{12})}{(C_{11} + C_{12})}, \tag{2.6}$$

$$E_{[110]} = \frac{4(C_{11} - C_{12})(C_{11} + 2C_{12})C_{44}}{2C_{11}C_{44} + (C_{11} - C_{12})(C_{11} + 2C_{12})}, \tag{2.7}$$

$$E_{[111]} = \frac{3(C_{11} + 2C_{12})C_{44}}{C_{11} + 2C_{12} + C_{44}}, \tag{2.8}$$

$$G_{[100]} = C_{44}, \tag{2.9}$$

$$G_{[110]} = \frac{2(C_{11} - C_{12})C_{44}}{C_{11} - C_{12} + 2C_{44}}, \tag{2.10}$$

$$G_{[111]} = \frac{3(C_{11} - C_{12})C_{44}}{C_{11} - C_{12} + 4C_{44}}, \tag{2.11}$$

enabling the quantification of anisotropy in the elastic properties. In a polycrystalline

structure, however, given the high number of randomly oriented grains, the values are averaged isotropically. Thus, for a polycrystalline structure, we use the Voigt-Reuss-Hill averaging approach [86] as

$$G = \frac{1}{2}\left[\frac{C_{11} - C_{12} + 3C_{44}}{5} + \frac{5C_{44}(C_{11} - C_{12})}{4C_{44} + 3(C_{11} - C_{12})}\right] \tag{2.12}$$

for the shear modulus and

$$E = \frac{9GB}{3B + G} \tag{2.13}$$

for the Young's modulus. Finally, for determination of the Poisson's ratio, ν, keeping the isotropic assumption, we use the formula

$$\nu = \frac{3B - 2G}{2(3B + G)}. \tag{2.14}$$

Results and Discussions

Firstly, the equilibrium lattice constant and bulk modulus (B) are estimated. Then, further elastic constants and other mechanical parameters, such as Young's modulus (E), shear modulus (G) and Poisson's ratio (ν) are calculated. The elastic parameters of single crystals are computed for loading along different crystallographic directions, or as homogenized values for polycrystalline materials, following Equations from 2.4 to 2.14. The calculated values and relevant literature data are shown in Table 2.2.

Property	Li - PBE (0 K)	Li - LDA (0 K)	Li - MD (0 K)	Li - MD (300 K)	Ref. [105] (78 - 195 K)	Ref. [106] (110 - 424 K)	Ref. [107] (20 - 350 K)	Ref. [42] (RT)	Ref. [121] (150 - 450 K)	Ref. [45] (RT)
a_0 (Å)	3.441	3.361	3.510	3.5783		3.490 - 3.537				
B (GPa)	13.877	14.483	13.244	18.667	13.3 - 12.0		12.3 - 10.9		13.1 - 11.9	11.9
C_{11} (GPa)	15.708	15.921	14.739	22.600	14.81 - 13.42	17.7 - 16.2			14.9 - 13.6	13.34
C_{12} (GPa)	12.961	13.764	12.496	16.700	12.48 - 11.25	13.2 - 11.9			12.2 - 11	11.19
C_{44} (GPa)	11.480	11.709	10.733	13.300	10.77 - 9.60	10.8 - 7.4			11.2 - 10.7	8.83
$E_{[100]}$ (GPa)	3.988	3.157	3.272	8.407						3.1
$E_{[110]}$ (GPa)	11.054	9.407	9.435	18.869						
$E_{[111]}$ (GPa)	26.996	27.670	25.351	32.242						21.2
E (GPa)	13.807	13.241	12.503	19.485				7.89	13.5 - 12.8	
$G_{[100]}$ (GPa)	11.480	11.709	10.733	13.300						
$G_{[110]}$ (GPa)	2.453	1.975	2.031	4.829						
$G_{[111]}$ (GPa)	1.944	1.546	1.599	3.983						
G (GPa)	5.174	4.913	4.656	7.347				2.82	5.1 - 4.9	
ν	0.334	0.348	0.343	0.326				0.381		
Zener ratio	8.360	10.858	9.570	4.508						8.21

Table 2.2: Elastic properties of BCC lithium metal. Li - PBE and Li - LDA are calculated at 0 K via *ab initio* simulations. Li - MD are computed using a $3 \times 3 \times 3$ supercell, at 0 and 300 K with the EAM interatomic potential by Nichol and Ackland [150]. Relevant literature data with its corresponding temperature ranges are added.

The Zener ratio is a measure for the anisotropy of a material (see Equation 2.5 for definition). A perfect isotropic material has Zener ratio equal to 1. The higher its value, the more anisotropic the materials behaves. According to our calculations, lithium has a Zener ratio close to 9 at 0 K, which indicates an extremely anisotropic behavior. In fact, Young's modulus for the [111] direction is approximately 27 GPa, while in [100] direction does not even reach 4 GPa.

From Table 2.2, small differences are found when the properties are calculated using either the PBE or the LDA potentials. The comparison of the bulk modulus and equilibrium lattice constant are depicted in Figure 2.6. For the comparison, the theoretical work of Nagy and Siegel [121] and the experimental works of Nash and Smith [105] and Beg and Nielsen [106] are used. From the plots, it can be seen that both potentials provide a reliable bulk modulus estimation, but the PBE lattice constant is closer to the reference values.

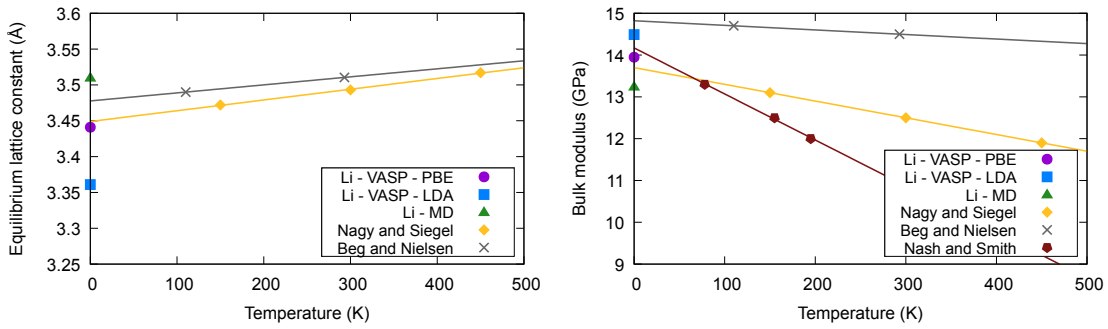

Figure 2.6: Comparison of the obtained results of equilibrium lattice constant (left panel) and bulk modulus (right panel) for pure BCC Li.

In Figure 2.7 a benchmark of the calculated polycrystalline values of Young's and shear modulus following the homogenization formulas are shown. Again, theoretical and experimental work from the literature are used for comparison [105, 121]. Both PBE and LDA potentials reproduce accurate values for these mechanical properties. For a complete description of the calculated elastic parameters, please refer to Table 2.2.

Focusing on the Young's modulus, the ⟨100⟩ orientation is confirmed to exhibit the lowest value among all crystallographic directions, in the range of approximately 4 GPa. In contrast, a polycrystalline specimen, averaging over multiple orientations, shows a significantly higher modulus, around 13 GPa. Experimentally, we observe values ranging from 2.5 to 6.0 GPa for polycrystalline lithium and from 0.7 to 3.2 GPa for samples exhibiting a dominant ⟨100⟩ texture (Figure 2.4). These experimental results are indeed lower than predicted by the *ab initio* simulations, even considering the temperature dependence (Figure 2.7). Consequently, we conclude that the very low elastic recovery of

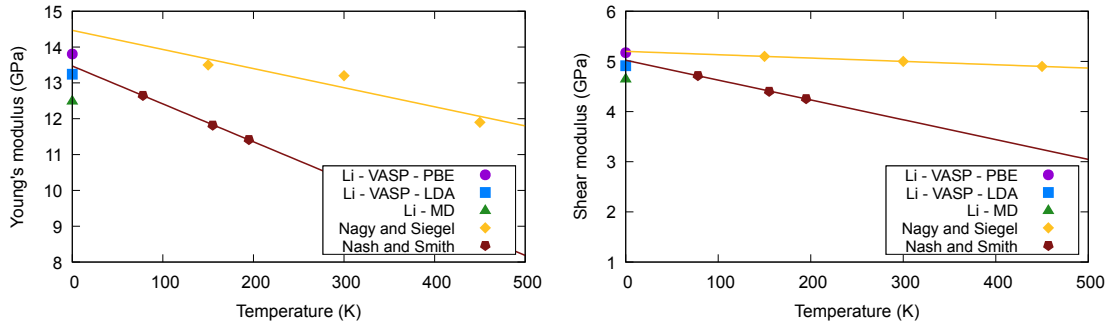

Figure 2.7: Comparison of the obtained results for Young's modulus (left panel) and shear modulus (right panel) for pure BCC Li.

lithium in the experiments limits the accuracy of the elastic modulus measurements and introduces additional uncertainty in interpreting the elastic mechanical response via the experimental method.

2.1.3 Molecular Dynamics Simulations

We continue our investigation of lithium mechanics using MD simulations, which enable the study of larger atomic systems and incorporate finite temperature effects. This approach allows for the gradual introduction of complexity and thermal fluctuations. We aim to get a deep understanding of the size, orientation and load type dependence of lithium metal mechanics. Our MD analysis proceeds in several stages: we begin with small systems comparable in size to the *ab initio* simulations to establish a consistent baseline. Next, we simulate nanopillar single crystal compression and tension tests to probe the mechanical response under different loading conditions and specimen sizes. Finally, we analyze polycrystalline structures to determine how grain size influences the mechanical behavior of nanopillars.

Methods

The deformation behavior of lithium is studied using MD via the Large-scale Atomic / Molecular Massively Parallel Simulator (LAMMPS) [92]. Analysis and visualization are carried out with the support of OVITO [151] and Gnuplot [152]. The empirical embedded atom model (EAM) inter-atomic potential for lithium metal developed by Nichol and Ackland [150] is used. For the volumetric thermal expansion tests, different MD simulations are run with increasing temperature from 10 to 450 K. A Nosé-Hoover thermostat and barostat are used in an NPT ensemble. The pressure is fixed to 1 bar unless a mechanical

load is applied. The final equilibrium lattice constant is calculated from averaging over 1 million time steps for each temperature. The size of the supercell is systematically varied between $1 \times 1 \times 1$ and $10 \times 10 \times 10$ to capture internal lattice reconstructions. For estimation of the elastic constants, a $3 \times 3 \times 3$ supercell at 300 K is simulated. For these computations, an NVE ensemble coupled with a Langevin thermostat is used. The change in average stress tensor when the cell volume undergoes a finite deformation is captured and averaged over one million time steps [92, 153]. Equations 2.1 - 2.14 are applied to calculate the mechanical parameters.

For tensile and compressive Li nanopillar simulations, single crystals with the orientation [001], [110] and [111] parallel to the loading direction are tested in both tension and compression. Simulations are run with periodic boundary conditions in z direction (long, central axis of the nanopillar and loading direction), but non-periodic in x and y direction, with free boundary conditions at the mantle of the pillar. The specific orientations of the crystallographic directions with respect to the x, y and z coordinate axes are: [001] single crystal with [001] $\parallel z$, [100] $\parallel x$ and [010] $\parallel y$; [110] single crystal with [110] $\parallel z$, $[00\bar{1}] \parallel x$ and $[\bar{1}10] \parallel y$; and [111] single crystal with [111] $\parallel z$, $[10\bar{1}] \parallel x$ and $[\bar{1}2\bar{1}] \parallel y$. For all simulations, a time step of 0.005 ps is used. The specimens are first temperature equilibrated at 300 K using an NVT ensemble for 40,000 time steps. Afterwards, a fixed strain rate is applied in z direction, using also an NVT ensemble at 300 K. These conditions are not changed unless explicitly mentioned.

To generate stress-strain curves, the force in z direction is normalized to the initial cross sectional area and the strain is calculated as engineering strain. We define positive stresses and strains for tension, and negative stresses and strains for compression. The linear elastic moduli are defined through the slope of the stress-strain curve near the origin. For most curves, a big drop in stress is observed when the deformation behavior changes from elastic to plastic. The stress reached at the peak of the curve, or just before the big drop, is considered the yield strength, similar to [154, 155]. For the mechanical tests of the elastic regime, the nanopillar size is fixed with a radius of 20 nm and height of 100 nm. An engineering strain rate of 10^6 s^{-1} is applied. For the mechanical tests of the plastic regime, the specimen size is systematically changed. Five runs with different random seeds are performed for each geometrical size. For all tests including plasticity (single crystal and polycrystal), the strain rate is fixed to 10^8 s^{-1}, unless when the influence of the strain rate on the results is specifically investigated.

For a bicrystal with [001]/[111] parallel to the loading direction z, a flat surface of a grain with [111] $\parallel z$ is placed on top of a grain with [001] $\parallel z$, with both grains having a similar number of atoms. For polycrystalline samples, the software Atomsk is used to create the structures [156]. Atomsk uses a Voronoi tessellation to construct a random, polycrystalline 3D microstructure. For both bicrystal and polycrystalline specimens,

free-standing cylinders with 20 nm radius and 100 nm height are simulated. Atoms which are too close to each other (significantly below the equilibrium lattice constant) are removed from the initial setup to avoid instabilities due to too high forces. To study the effect of grain size on the results, simulations of polycrystalline specimens with the same geometrical size but different random grain structures are carried out following the same procedure as described before. In total 20 different polycrystals simulations are performed, with varying number of randomly oriented grains. The grain size d is estimated as

$$d = \left(\frac{N_{\text{grain}} \times V_{\text{total}}}{N_{\text{total}}} \right)^{1/3}, \tag{2.15}$$

where N_{total} is the total number of atoms in the specimen, V_{total} is the total volume of the cylindrical specimen at the start of the simulation and N_{grain} is the average number of atoms per grain as estimated via a grain segmentation analysis in OVITO [151]. The grain size information is taken at the end of the equilibration period.

Results and Discussions

Structural Information

At ambient pressure and room temperature, the equilibrium lattice structure of lithium is BCC. However, lithium undergoes a phase transition at around 75 K to a complex 9R phase. Therefore, the low-temperature low-pressure phase is a different, intricate one [157], and in the preceding section single unit cell calculations with enforced BCC structure were performed. An established interatomic potential for MD simulations of lithium metal is published by Nichol and Ackland [150]. We note that this empirical potential was fitted against properties of BCC lithium at 0 K. Thus, to capture the phase transition, the researchers fitted the energy difference between BCC and the FCC structure to be very low. As a consequence, the equilibrium lattice constant at finite temperatures is higher than the experimental room temperature value. And given the low energetic difference between the BCC and FCC phases, transformations are easily triggered.

Dorrell and Partày [158] created phase diagrams of lithium using three different EAM interatomic potentials and a nested sampling technique. They observed that the potential from Nichol and Ackland shows the lithium phase transition at around 100 K from the room-temperature-stable BCC to a wide range of structures and recovered several properties best.

Here, volumetric thermal expansion tests are performed to determine the equilibrium lattice constant. A $1 \times 1 \times 1$ cell, which enforces a perfect BCC structure, is simulated first. Afterwards, the size of the supercell is systematically increased until $10 \times 10 \times 10$. The energy gap in between the $1 \times 1 \times 1$ and larger and less constrained supercells at

different temperatures indicates that the aforementioned phase transition is naturally triggered. As a result, the equilibrium lattice constant at 300 K is approximately 3.5783 Å and corresponds to a slightly distorted BCC structure, with atomic distances matching the data by Dorrell and Partày [158]. This value is used in the following simulations. In Figure 2.8 the resulting crystal structures, showing the difference between the two phases, are plotted. In Figure 2.9, the resulting stress free lattice constants as function

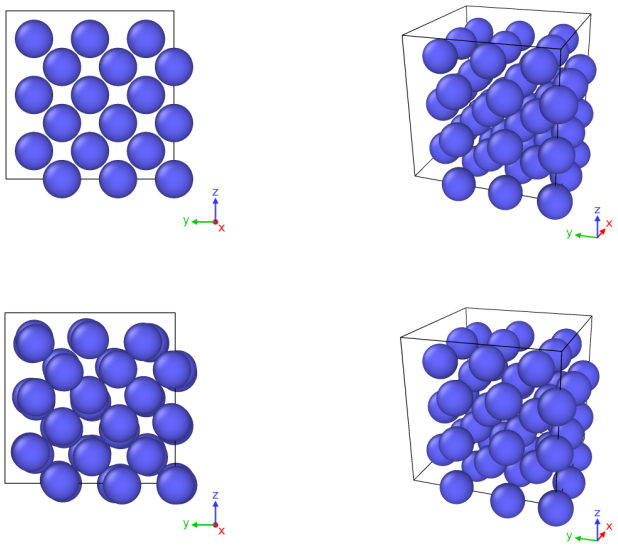

Figure 2.8: Crystal structures for a $3 \times 3 \times 3$ supercell at 30 K, showing the difference between the two phases of Li, using the Nichol and Ackland EAM interatomic potential [150]. The top two crystal structures are the input geometry (perfect BCC unit cell), while the bottom two are the equilibrated structures at the end of the run, demonstrating the slight distortion of the BCC crystal structure. Atomic distances match the data by Dorrell and Partày [158].

of temperature are plotted. From these data, the linear thermal expansion coefficient of lithium metal can be calculated. At 300 K, we compute $33 \times 10^{-6} K^{-1}$ for the BCC cell and $21 \times 10^{-6} K^{-1}$ for the larger, slightly distorted cell. Comparing with experimental literature values also at 300 K of $46 \times 10^{-6} K^{-1}$ from [159], we find a reasonable agreement with the computed BCC data.

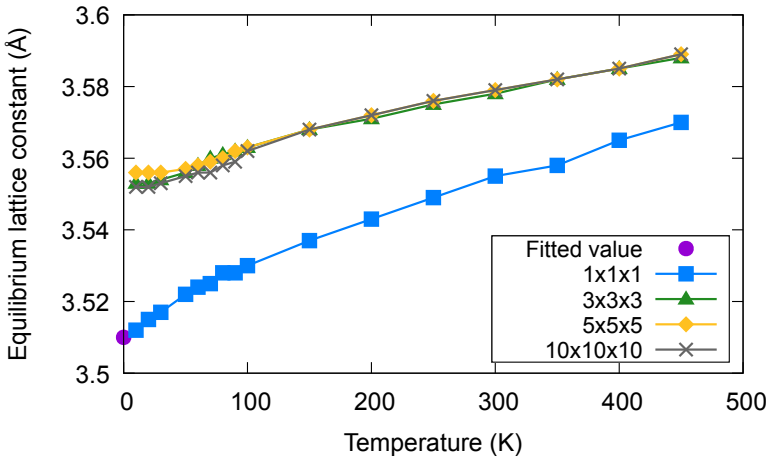

Figure 2.9: Resulting stress free lattice constant as function of temperature using the Nichol and Ackland EAM interatomic potential [150].

Single Crystal: Linear Elasticity

To study linear elasticity, the elastic constants of BCC lithium are computed first, following the same principles as for the *ab initio* methods. The results for 0 and 300 K are shown in Table 2.2. The agreement is particularly good for the 0 K case, as these data were originally fitted in the MD potential. However, the elastic properties obtained at 300 K are overestimated, with exception to the Zener ratio. The values for shear modulus are closer to the *ab initio* numbers, but the Young's moduli are all higher than expected. Despite this drawback, the EAM potential correctly indicates the order for the directional elastic properties, i.e., $E_{[100]} < E_{[110]} < E_{[111]}$ and $G_{[111]} < G_{[110]} < G_{[100]}$. As discussed in the preceding section, the first-principles and MD simulations operate using different potentials, with phase stability and definition of ground-state structure being an exceptionally complex challenge. This explains such divergences found at the 300 K simulations.

Moreover, virtual mechanical tests in both tension and compression are performed for single-crystal Li nanopillars. A sketch of the geometry, which is also applied in the further investigations, is given in Figure 2.10. The Young's modulus is calculated as the slope of the linear part of the stress-strain curve, as the mantle of the pillar is stress-free in the simulations [154].

The values for the elastic moduli, as obtained separately from the small strain tensile and compression regime, consistently match the output from the preceding elastic constant analyzes.

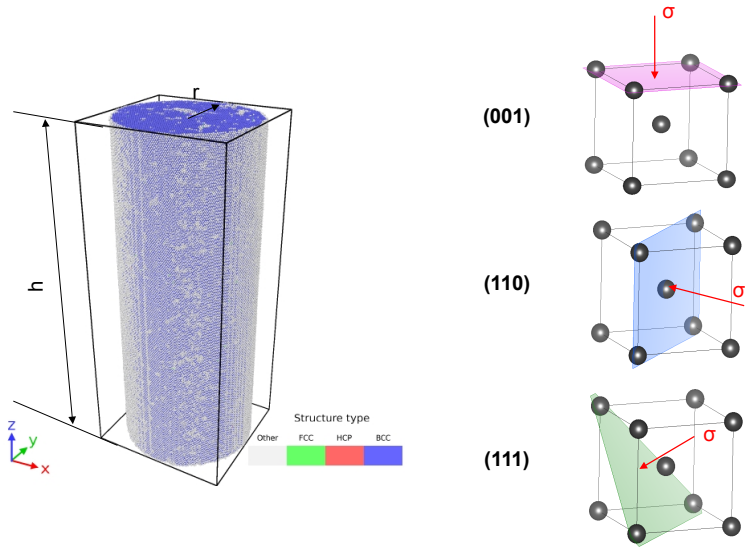

Figure 2.10: Sketch of the nanopillar geometry for tension-compression tests, together with the analyzed crystallographic planes. The BCC crystal structure is set so that the crystallographic plane of interest is initially perpendicular to the z axis (loading direction). Therefore, a [001] loading direction refers to a [001] oriented single crystal, by applying the load perpendicular to the (001) plane.

Single Crystal: Plasticity

In order to look into plasticity, virtual mechanical tests on free-standing, single crystal, cylindrical nanopillar specimens are performed at 300 K. As the melting point of lithium is low (454 K from [160]), 300 K is already a high homologous temperature. The MD tests have a duration of only a few nanoseconds. Thus, in these simulations creep does not play a role, but only time-independent plastic deformations. The effects of orientation, size and strain rate dependence are discussed, as well as the details regarding dislocation, slip planes and crystallographic re-orientations. The analyzes are done using the common neighbor analysis, polyhedral template matching and grain segmentation methods [161].

Orientation Dependence

Free-standing, single crystal cylindrical nanopillars are tested in both tension and compression along [100], [110] and [111] direction, with a focus on the orientation dependence. Exemplary stress-strain curves are shown in Figure 2.11. It can be observed that the curves change considerably when comparing the three different orientations. Beyond the yield

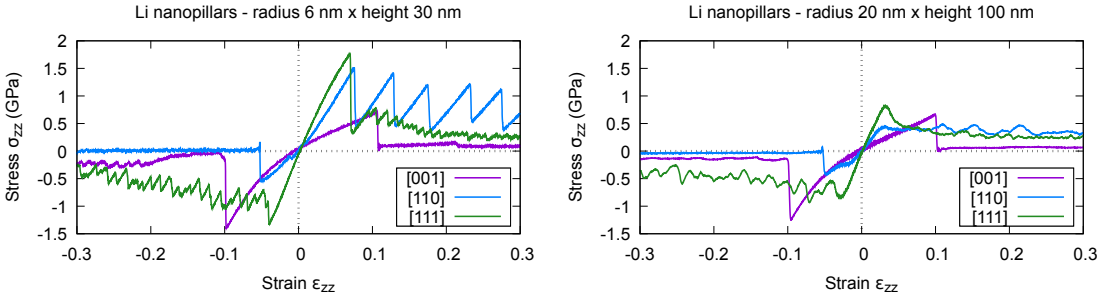

Figure 2.11: Stress-strain plots of free-standing Li nanopillars under tension and compression. These exemplary curves are from specimens with 6 nm radius and 30 nm height (left panel) and 20 nm radius and 100 nm height (right panel). A significant difference in the deformation behavior is observed for the different orientations. A change from sharp serrated to smooth wavy flow curves and a decrease in the yield point is observed between differently sized samples.

point, in tension, a serrated plastic flow is present when the crystal is loaded along the [111] and [110] directions, while for loading along [100] the stress level remains constant at a low value. In compression, serrated plastic flow is observed for loading along [111], while the curves for loading along [110] and [001] remain constant at low stresses.

Serration in the flow curves are related to avalanches of deformation processes. These stress drops or strain jumps are found in a variety of materials, such as high-entropy alloys, shape-memory alloys, TWIP and TRIP steels, and more generally, in nanostructures [162]. However, there is no universal model or theory explaining such behavior. In experiments carried out on 200 – 900 nm Nb nanopillars, the compressive flow curves contained numerous discrete segments with intermittent strain bursts, which were associated with dislocation glide occurring predominantly in the (110), (112) and (123) planes [163].

BCC plasticity is rather atypical, particularly at low temperatures and high strain rates. BCC metals are known to disobey the Schmid law, slipping along dense $\langle 111 \rangle$ directions, but the potential slip planes vary [164, 165]. A general fact is that dislocations with $1/2\langle 111 \rangle$ Burgers vector are predominantly observed in almost all cases of BCC plastic deformation. However, cross-slip is relatively easy. Therefore, $1/2\langle 111 \rangle$ screw dislocations can slip and also cross-slip onto a large number of possible lattice planes [164, 165].

In our simulation results, for the specimens with serrated flow, namely those loaded along [110] in tension and [111] in tension and compression, the primary source of plasticity is indeed dislocation formation with a $1/2\langle 111 \rangle$ Burgers vector. The dislocation analyzes

are done using the Dislocation Extraction Algorithm (DXA) [166, 167]. Each stress drop is connected with an abrupt formation of a dislocation. However, the dislocations appear in different planes. Figure 2.12 visualizes the evolution of the dislocation movement in a specimen with 3 nm radius and 15 nm height, which is compressed along the [111] direction. Dislocations abruptly appear and are detected when a stress jump occurs. In this example, at the first stress jump, the corresponding dislocation shows up at the $(\bar{1}\bar{1}3)$ plane, followed by a dislocation at the $(3\bar{1}\bar{6})$ plane at the second stress jump. Then, at the third stress jump, the dislocation is at the $(\bar{1}21)$ plane. No dislocation is found between the stress drops.

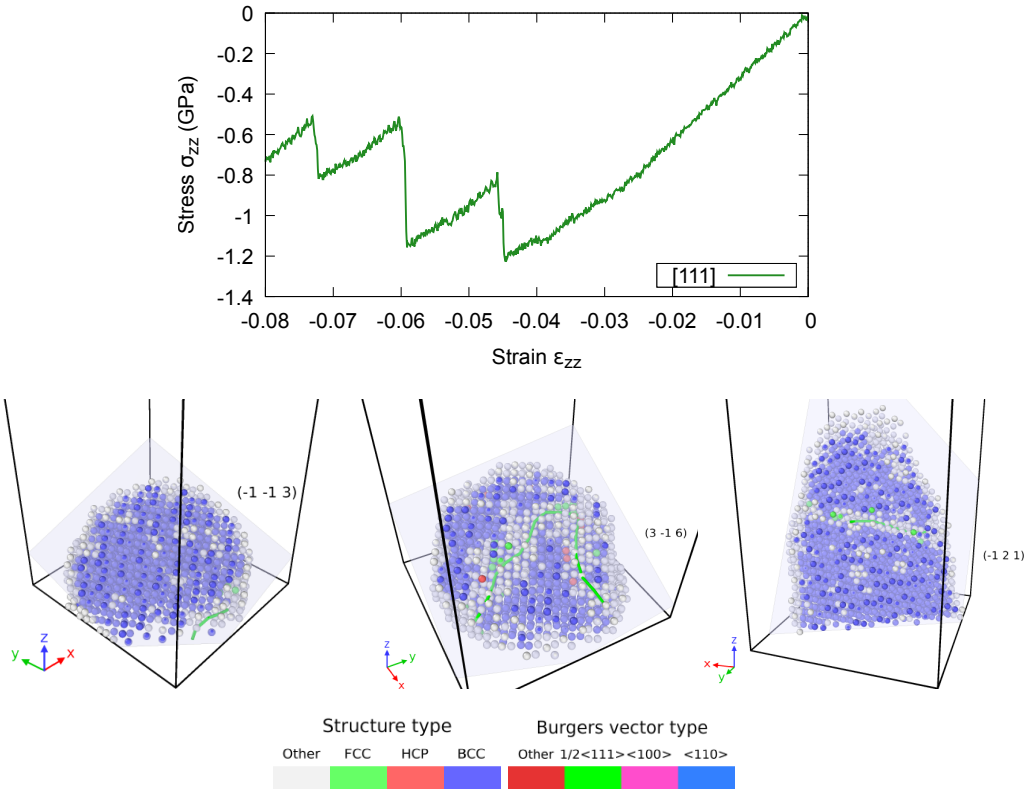

Figure 2.12: An exemplary evolution from a compression test of a single crystal with 3 nm radius and 15 nm height, loaded along [111]. Top row: stress strain curve, bottom row: corresponding atomic structure and dislocations with highlighted planes. Snapshots are taken at strains -0.047, -0.060 and -0.073, respectively, corresponding to first, second and third stress jumps. The $1/2\langle 111\rangle$ dislocations appear in a variety of planes.

Interestingly, the specimens that remain flowing constantly at low stresses, namely for

loading in [001] direction both for tension and compression, and for [110] in compression, a partial re-orientation of the crystal takes place in the plastic regime and no dislocations are detected. The crystallographic orientation relationships involved in this re-orientation are analyzed using the MTEX toolbox [168]. The average orientations of the original and re-oriented parts of the pillars are determined by the OVITO software. For the first case, the initial orientation $[001] \parallel z$, $[100] \parallel x$ and $[010] \parallel y$ re-orients locally to $[22\bar{1}] \parallel z$, $[\bar{1}22] \parallel x$ and $[2\bar{1}2] \parallel y$. Meanwhile, for the second case, the initial orientation $[110] \parallel z$, $[00\bar{1}] \parallel x$ and $[\bar{1}10] \parallel y$ re-orients to $[11\bar{4}] \parallel z$, $[221] \parallel x$ and $[1\bar{1}0] \parallel y$. It should be noted that the crystal directions that were precisely aligned with the coordinate axes in the beginning of the MD simulation become slightly misaligned during the plastic deformation. This happens because the deformation results in bending or tilt of the sample (where the tilt axis is perpendicular to the slip plane normal and the slip direction). This tilt causes the twin or slip plane to turn towards the loading direction as deformation progresses, which can also be seen in the pole figures as a deviation of the crystallographic directions from their initial positions (e. g., [001] in the tensile case that is misaligned by 6° in the deformed state shown in Figure 2.13).

These specific re-orientations are observed for all investigated pillar sizes and are caused by deformation twinning. Pictures of this phenomenon are seen in Figure 2.13 for the specimen loaded along [001] in tension and in Figure 2.16 for the specimen loaded along [110] in compression. In Figure 2.13 a pole figure representation of the crystallographic orientation of the original and re-oriented parts of the specimens loaded along [001] in tension and loaded along [110] in tension is shown. In both cases, the coincidence between major lattice planes suggests that the orientation relationship corresponds indeed to twinning. Analyzing the orientation relationship in detail, it turns out that the original and re-oriented parts of the pillar form reflection twins with $\{112\}$ twin planes and common $\langle 111 \rangle$ axes in both cases, tensile and compressive loading. This is the most common twin system observed in BCC metals [169]. It is also the system with the highest Schmid factor, corresponding to 0.496 for tensile loading along [001] and 0.483 for compression along [110] in our simulations. For tension in the [001] direction and compression in the [110] direction, pure twinning is detected without signs of dislocation slip. For compression along [001], twinning is still the dominating mechanism, however, slip simultaneously occurs after the main twinning event.

The main twin formation event occurs almost instantaneously at the big stress drop of the stress-strain curve. Afterwards, the twin is evolved re-orienting layer by layer and growing continuously. We can interpret that the applied deformation is absorbed by the cooperative atomic movements, accommodating strain without a significant change in stress. This explains the plateau at low stress levels observed in the stress-strain curves, similar to discussions in [170, 171].

Regarding twin formation, in MD simulations, twinning in BCC iron has been extensively studied [155, 171–174]. It was shown that at low temperatures, iron tends to deform via twinning, while at high temperatures, the dominating mechanism is slip [172]. In BCC niobium, it was found that twins in simulations only appear under high pressures, and depending on the empirical interatomic potential used [175]. For lithium, Gröger et al. [169] showed in small scale, low-temperature molecular statics simulations, that the formation of Li twins on the $\{112\}$ planes in the $[111]$ direction is associated with a local energy minimum. The formation of deformation twins with $\{112\}$ twin planes can therefore be expected, which is in agreement with our results.

Another point worth highlighting is the tension-compression asymmetry present in these samples. Experimentally, it has already been found that Li is softer in compression than in tension [120]. In our results, the yield stresses are indeed generally lower for compression than for tension, as seen in Figures 2.11 and 2.14. In addition, the specimens loaded along $[001]$ and $[110]$ exchange their positions as the lowest yield when comparing tension and compression. A similar asymmetry had previously been reported for MD simulations of BCC iron nanowires [155]. In the case of the iron nanowires, as in our simulations, the loading directions $[110]$ and $[001]$ show the asymmetry regarding tensile and compressive loading.

This tension-compression asymmetry is linked with a twinning/anti-twinning anisotropy and is inherent to BCC plastic deformation [169, 170]. In BCC metals, twinning occurs mostly in one way along the $\langle 111 \rangle$ direction. This favorable direction is called the twinning (T) direction, while the reverse is called the anti-twinning (AT) direction. A plastic T/AT anisotropy is interpreted as resulting from slip on $\{112\}$ planes, as these planes are not symmetrical with respect to shear along the $\langle 111 \rangle$ direction [164, 165, 170]. The T/AT plastic anisotropy has been previously found for lithium [169]. As shown in Figures 2.12 and 2.13 and extensively discussed here, the slip (or twin) system $\{112\}\ \langle 111 \rangle$ is active in our simulations, leading therefore to the observed plastic T/AT anisotropy. Similarly to the results from [155], when loading along the $[110]$ direction, the specimens deform by slip in tension and by twinning in compression. On the other hand, differently than [155], when loading along the $[001]$ direction, the dominating mechanism in both tension and compression is twinning. It is expected to observe only slip in this $[001]$ compression case. Indeed dislocation slip is present, but as a competitive mechanism occurring simultaneously with twinning after the main stress drop, indicating an anti-twin formation.

A summary of the deformation mechanisms observed in the reported plastic flow simulations is given in Table 2.3. The present observations are valid for all sizes investigated at this specific strain rate. Given the higher number of atoms, the flow curves tend to only move from a very sharp serration behavior to a smoother flow line, as it is depicted in

Load direction	Load mode	Flow curve behavior	Deformation mechanism
[001]	tension	plateau at low stresses	twinning
[001]	compression	plateau at low stresses	twinning/dislocation slip
[110]	tension	serrated	dislocation slip
[110]	compression	plateau at low stresses	twinning
[111]	tension	serrated	dislocation slip
[111]	compression	serrated	dislocation slip

Table 2.3: Summary of the plastic deformation mechanisms found for each set of single crystal orientations in the Li nanopillars mechanical tests. Simulations are carried out at 300 K and with a strain rate of 10^8 s^{-1}. For loading direction [001] in compression, both twinning and dislocation slip occur simultaneously as competitive mechanisms.

Figure 2.11. Nevertheless, the values for yield strength do change considerably. This size dependence is discussed in more details in the next paragraph.

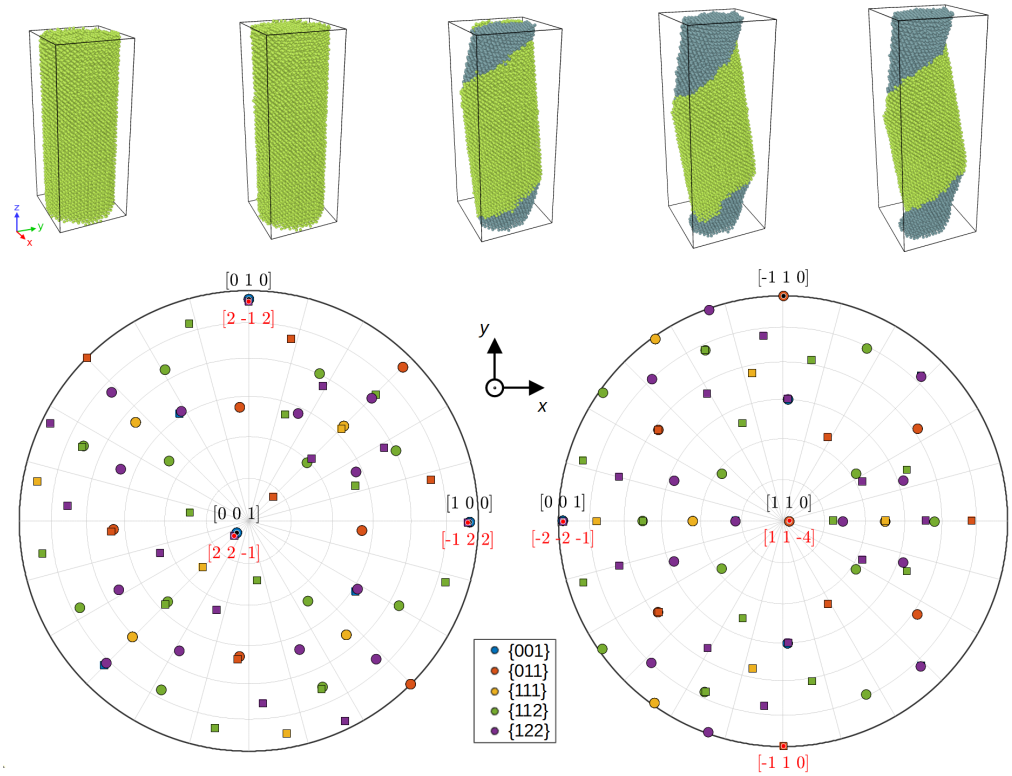

Figure 2.13: Top row: Exemplary evolution of a tensile test of a single crystal with 3 nm radius and 15 nm height loaded along [001], in which twinning takes place. The color coding indicates the orientation, with light green being the original orientation and dark green the re-oriented part. Bottom row: Pole figure representation of the orientation of the original (circles) and re-oriented (squares) part of the specimens loaded along [001] in tension (left) and loaded along [110] in compression (right) just after the onset of the partial re-orientation. Selected directions of the original (black) and the re-oriented (red) parts of the specimens are indicated. In both cases, the orientation relationship between both parts corresponds to twinning on {112} twin planes.

Size Dependence

As observed in Figure 2.11, a change from sharp serrated to smoother wavy flow curves and a decrease in the yield point is observed between differently sized samples. The first phenomenon is due to the increasing number of atoms, which leads to the stress fluctuations becoming less abrupt. The change in yield point, however, requires a closer look.

To address the size dependence of the yield point, cylindrical specimens of different geometrical sizes are simulated. The specimens are systematically increased in size maintaining a fixed radius over height ratio of 0.2. As before, the three main loading directions are inspected. The average and standard deviation of the yield strength of 5 runs for each set-up are calculated and reported. The results are plotted in Figure 2.14.

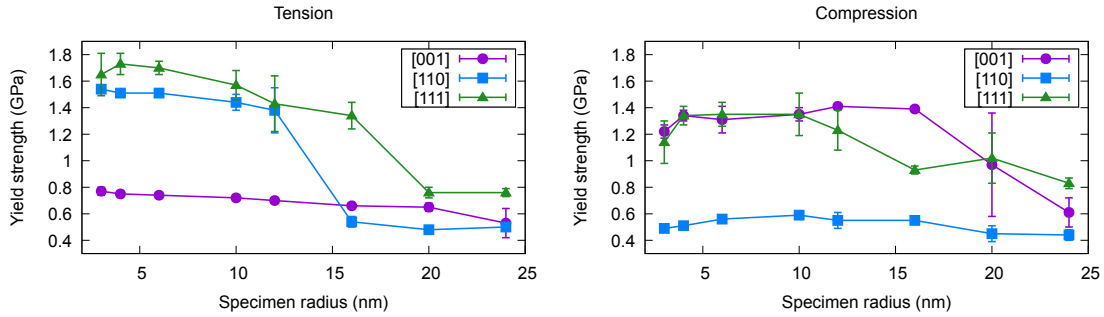

Figure 2.14: Yield strength for single crystals with different loading directions, sizes and load mode. The specimens are systematically increased in size maintaining a fixed radius over height ratio of 0.2. In order to get a statistical distribution, 5 runs are performed on each size using different random seeds. The average and standard deviation are reported. The left plot shows tension, while the right one shows compression.

As explained in the methods section, we define yield strength as the maximum stress reached just before the main stress drop, as done in [154, 155]. For the cases of dislocation slip based plasticity, that corresponds to the formation of the first dislocation in the structure. For the cases of twin based plasticity, that correspond to the formation of the first twin event. For the directions and loading modes with slip, we see the "smaller is stronger" effect, meaning that the yield strength falls significantly when the specimens grow in size, with a transition from "harder" to "softer" occurring predominantly in the range from 16 to 24 nm pillar radius. Whereas in the case of twinning, the maximum stress level remains essentially constant, and no extreme variation is observed. In general, as the specimen size increases, the anisotropy in the yield point tends to reduce, with the loading directions with slip-based plasticity reaching similar yield point as the twinning-based

plasticity.

A case to highlight here is the [001] loading direction in compression. As discussed in the preceding section, it is expected that these specimens would experience purely dislocation slip. Nevertheless, we observe twin (here as anti-twin) and slip present competitively. In smaller samples, twinning is more pronounced, while slip is more obscured. In contrast, in larger samples, the behavior is reversed: twinning is discreet, and slip plays a more central role. This aspect is particularly strong in the largest samples analyzed, i.e., 24 nm radius and 120 nm height, in which slip dominates twinning. The samples with a 20 nm radius and 100 nm height present a transitional behavior, therefore leading to the significantly sized error bar and reduction of the maximum stress levels (see Figure 2.14).

Hence, we can interpret that the observed "smaller is stronger" trend is a result of dislocation slip, since the specimens with twinning-based plasticity are rather insensitive to the size effect. In smaller volumes, the dislocations have less space to move and interact, traveling only very small distances before annihilating at free surfaces, as clarified by the dislocation starvation concept [112]. Furthermore, as introduced in the section 2.1, the generation of geometrically necessary dislocations coupled with surface effects (e.g., surface-to-volume ratio) are additional concepts that shed light into these size-dependent behaviors [47].

Strain Rate Dependence

To evaluate the influence of the strain rate on the plastic response, single crystals of a specific geometrical size (6 nm radius and 30 nm height) are investigated, using three different strain rates, 10^8 s^{-1}, 10^7 s^{-1} and 10^6 s^{-1}. Both tension and compression simulations are performed. The results can be seen in Figure 2.15. As expected, changing the strain rate does not influence the linear elastic part of the curve. However, a higher strain rate leads to higher yield strength in all single crystals of the three orientations investigated. That means that the faster the nanopillar is deformed, the harder the material behaves.

In addition to the change in the yield point, the flow curve of the single crystal under compression along [110] shows a distinct difference at the lowest strain rate compared to higher strain rates. This difference indicates a shift of deformation mechanism from twinning to dislocation slip. Pictures depicting this phenomenon are shown in Figure 2.16. Because twinning involves small, coordinated atomic movements, it can occur much more rapidly than slip. It is therefore encouraged under higher strain rate conditions, and it is more probable to occur in single crystals [176]. Thus, it is important to emphasize that the summary of deformation mechanisms presented in Table 2.3 may depend on the chosen strain rate, being that a critical factor to consider when investigating Li plasticity.

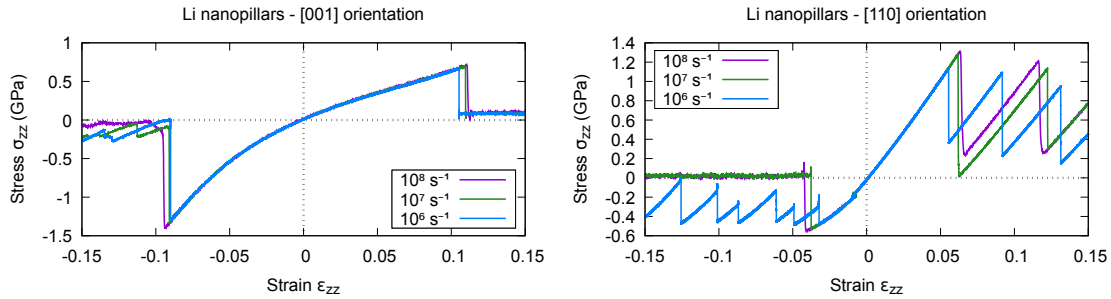

Figure 2.15: Stress-strain curves for different strain rates on single crystals of 6 nm radius and 30 nm height. Compressive and tensile deformations are applied along [001] (left panel) and [110] (right panel). A change in strain rate does not influence the linear elastic past of the curve, but with increasing strain rate, a decrease in the yield strength is observed.

The strain rate sensitivity of Li had already been reported at the literature for bulk samples [42, 44, 113]. This can also explain why our numbers for the yield point are considerably higher than the ones reported for experiments. To directly compare our yield strength data with literature values, one would have to extrapolate the timescale, as well as the length-scale, since nanostructures have considerable orders of magnitude higher yield stress than bulk structures [44, 111, 113]. Given that MD simulations are conducted at extremely high strain rates and the entire virtual test spans only a few nanoseconds, the computed resulting yield point values are in an expected range.

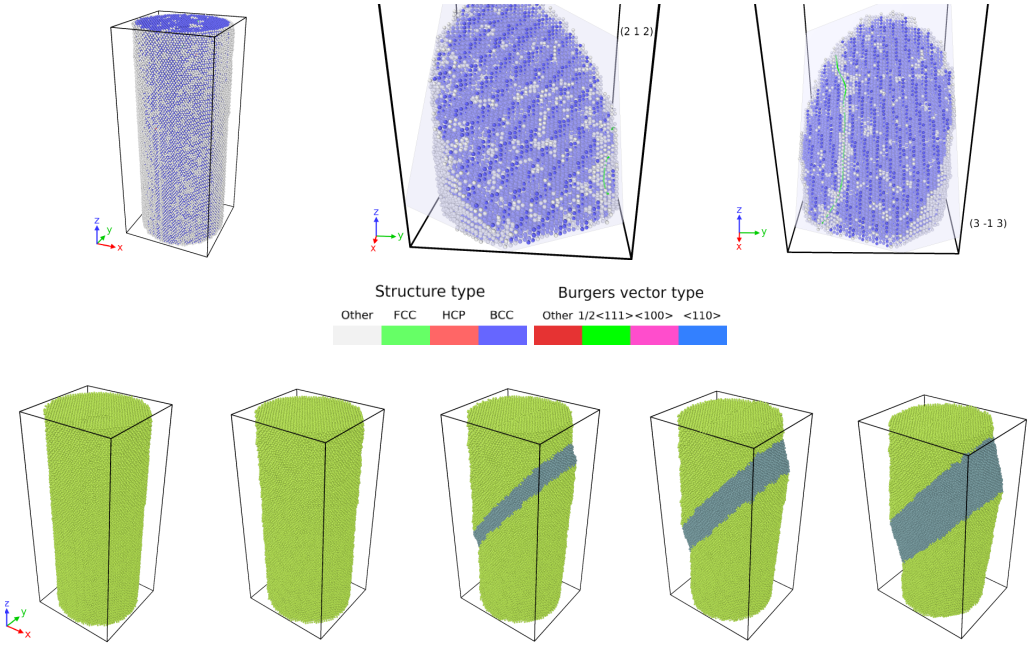

Figure 2.16: View of the single crystal under compression along [110]. Top row: snapshots of the lower strain rate test. First figure is the structure at strain 0, then the following figures highlighting the dislocations are at strains -0.03 (first strain drop) and -0.05 (second strain drop), respectively. Bottom row: snapshots of the higher strain rate test focusing on the evolution of twinning. At the bottom row the atoms are colored according to grain orientation, with light green being the original orientation and dark green the new orientation.

Polycrystals

To systematically transfer the results from the single crystal investigations to texture-dependent polycrystal mechanics, the next step is to look into bicrystal setups. Focusing firstly on elasticity, exemplarily a bicrystal with [001]/[111] parallel to the loading direction with equal volume fractions of the grains and a planar interface is simulated. The structure can be visualized in Figure 2.17. To estimate the expected value of Young's modulus in the linear elastic regime, the Reuss and Voigt equations are applied [84, 85, 149]. They provide upper and lower bounds to the effective elastic constants, using axial equal strain loading as upper bound (Voigt model) and transverse equal stress loading as lower bound (Reuss model). The equations can be used as

$$E_{Voigt} = f_1 E_1 + f_2 E_2, \tag{2.16}$$

$$E_{Reuss} = \frac{E_1 E_2}{f_1 E_1 + f_2 E_2}, \tag{2.17}$$

where f_1 and E_1 refer to the fraction and value of elastic modulus of one compound, while f_2 and E_2 refer to the same respective characteristics of the other compound.

In this case, the specimen geometry corresponds to the lower bound (Reuss model), and accordingly, the expected effective Young's modulus should obey

$$E_{\text{Reuss}} = \frac{E_{[111]} E_{[001]}}{f_{[111]} E_{[111]} + f_{[001]} E_{[001]}}, \tag{2.18}$$

where f refers to the volume fractions of the constituents with the given orientation, therefore here $f_{[111]} = f_{[001]} = 0.5$, while $E_{[111]}$ and $E_{[001]}$ are the elastic moduli of the specimens loaded along $[111]$ and $[001]$, respectively.

With the above, single crystal values from the previous sections are applied to Eq. (2.18), leading to an $E_{\text{Reuss}} \approx 12.2\,\text{GPa}$. Then, tensile and compressive tests are performed in the bicrystal and the Young's modulus is extracted from the stress-strain graphs, computing approx. 12.4 GPa, and matching the expected value from the Reuss equation.

Finally, simulations of 20 polycrystalline specimens under tensile and compressive loads are carried out. We keep the same geometrical pillar size constant (same radius and height), while changing the grain size d. Some exemplary structures are visualized in Figure 2.17. In Figure 2.18 the Young's modulus and yield strength versus grain size

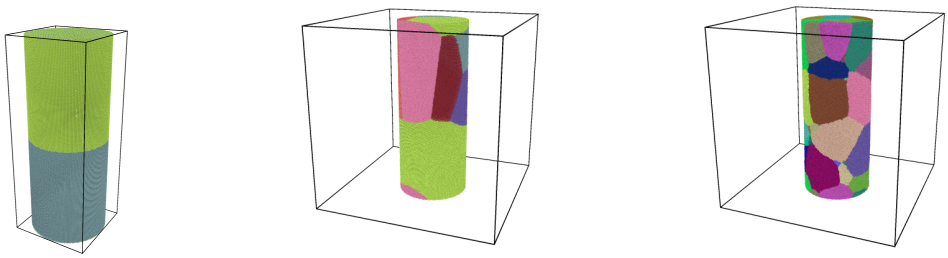

Figure 2.17: Exemplary crystal structures of the $[001]/[111]$ bicrystal and polycrystals with average grain size, d, of 23.6 and 14.7 nm, respectively, calculated via Equation 2.15.

are plotted for the analyzed specimens. Unlike the bicrystal, whose elastic modulus aligns well with predictions from homogenization theory, the polycrystals yield lower-than-expected values of E, which is approximately 19 GPa (see Table 2.2 and Figure 2.18). Here, the large scatter of the data is explained by the still small number of grains, where the homogenization model assumes that for large grain numbers the orientation

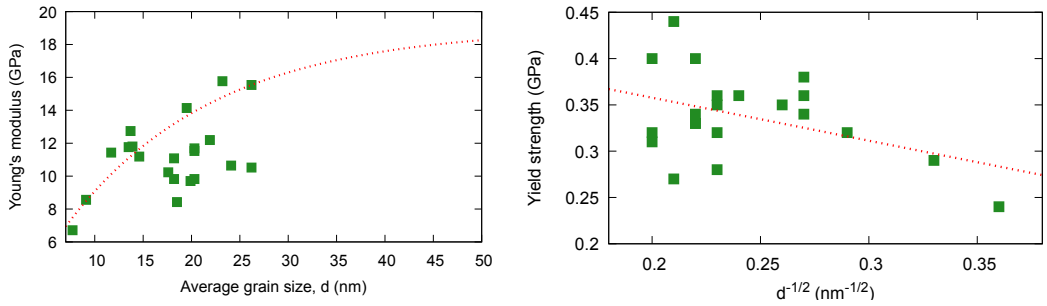

Figure 2.18: Young's modulus on the left panel and yield strength on the right panel of the polycrystalline specimens with same geometrical size, but different random grain structures. Trend lines are added in red for visualization purposes. In general, mechanical properties fall with decreasing grain size, despite a big variation between individual specimens. Polycrystals yield lower-than-expected values of E, which is approx. 19 GPa calculated from homogenization theory.

dependence averages out. In fact, we can assign the strong variations in the effective Young's modulus to the orientation of abnormally large grains. As the number of grains in the specimens is still rather low, abnormally large grains can have a stronger influence on the computed properties. As a result, given the extreme anisotropy of lithium metal, individual grains have a considerable variation regarding the Young's modulus. For example, when comparing the specimens with d = 26, 24 and 23 nm, we see that the specimens with higher E have their larger grains close to the directions with higher directional Young's modulus, while the specimens with lower E present the majority of their grains close to the direction with lower directional Young's modulus. These data are plotted in Figure 2.19, and elucidates the large scatter observed in the data.

Lithium has a natural tendency to crystallize into large grains, mostly in the micrometer range [45, 177]. We can then infer that if such small pillars were experimentally manufactured, they would only contain a few grains, with one, two or a maximum of three grains being a reasonable number. Thus, also in an experimental case, a large scatter in the E data would be expected. On the other hand, if the polycrystalline structures were larger and the number and size of grains big enough, the reference isotropic values should be reached.

The second effect is that the purely macroscopic homogenization model does not account for contributions from the Grain Boundaries (GBs), which play a significant role for the present, ultra fine grains [178]. From the obtained results we can therefore conclude that the GBs act as soft layers, which lead to smaller Young's moduli for small grain sizes. In turn, we expect the convergence of the effective modulus to the macroscopic

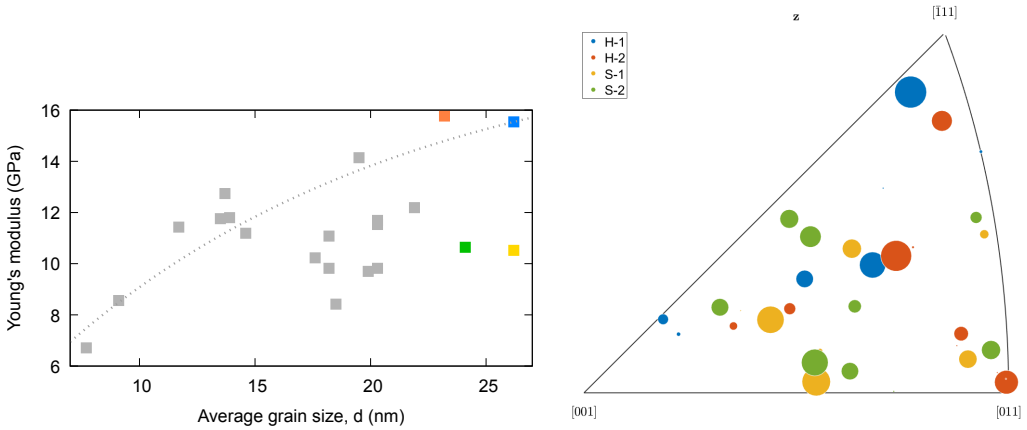

Figure 2.19: Left panel: Young's modulus highlighting the analyzed specimens. Right panel: Inverse pole figure representation of the respective grain orientations of the highlighted specimens with respect to the loading direction. The size of the circles is proportional to the grain size. All specimens present similar d, but distinct E values. For the harder specimens (H-1 in blue and H-2 in orange), their biggest grains are close to each other and lie near the direction presenting the higher E, which is $[111]$. For the softer specimens (S-1 in gold and S-2 in green), their biggest grains are also close to each other and lie near the direction presenting the lower E, which is $[001]$.

homogenization prediction for large numbers and sizes of the grains, as sketched in Figure 2.18. This interpretation is indeed confirmed by systematic bicrystal simulations with increasing number of grains at a fixed pillar size.

Moving on to plasticity, the yield strength of the polycrystalline specimens are lower than of the single crystals tested in this study. Opposite to the single crystal findings, in which smaller crystals signify higher yield strength, here we see that the smaller the crystals, the lower the yield strength. This is also contrary to what one would expect from the well-known Hall-Petch relationship, which states that a finer grain structure leads to higher yield point, as the GBs act as barriers for dislocation movement. However, it has been found that this is valid until a certain grain size. When the grains become too small, for instance on the nanoscale, the Hall-Petch relationship can be either stopped or inverted [179–181]. Indeed, an inverse Hall-Petch relationship describes well the phenomenon observed in our simulations, despite the non-negligible scatter. Work on the explanations and models of the inverse Hall-Petch effect has been discussed in the literature, see e.g. [182, 183]. To evaluate the Hall-Petch relationship, the results are plotted as yield strength vs grain size to the power of $-1/2$, as done in Figure 2.18. The data usually falls within a straight line with a slope m. The slope m is positive for big grain sizes (for

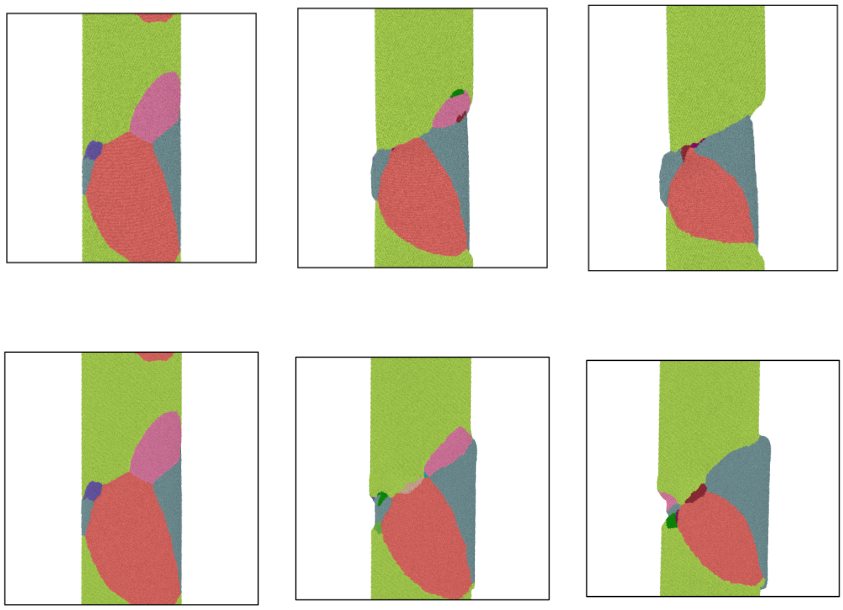

Figure 2.20: Side view of exemplary evolutions from tensile (top row) and compression (bottom row) tests of a polycrystalline specimen with average grain size of 26 nm. The colors indicate different grains with random orientations. An apparent GB sliding at an inclined surface can be seen once the specimen is subjected to the mechanical tests. Snapshots are taken at the strain values of 0, 0.04 and 0.065.

instance in the micrometer ranges), but negative for small grain sizes (for example in the nanometer ranges) [179]. Studies indicate that in the range of the inverse Hall-Petch the dominating deformation mechanism is GB sliding, as opposed to dislocation slip [183]. In all specimens simulated, the root cause of deformation appears indeed to be GB sliding, which happens at an inclined surface. This holds true even for specimens with similar grain size, but a big discrepancy in mechanical parameters. Snapshots of the deformation evolution can be seen in Figure 2.20. It can be understood that the GBs in our structures, instead of hindering dislocation movement, are acting as a soft zone, by sliding and easing deformation. To fully comprehend the mechanics of polycrystalline nanopillars, it is essential to clarify not only the behavior within single crystals but also the phenomena occurring at GBs, as they have the greatest influence on elastic and plastic results, which is beyond the scope of the present study.

2.1.4 Conclusions on Pure Lithium Mechanics

Lithium mechanical behavior is complex, but we successfully develop a deeper understanding of its deformation process. Our conclusions and contributions can be summarized as:

1. *Size dependence of Li mechanical properties.* From MD simulations of nanopillars, clear length-scale effects are found in the yield point of single crystals, showing a "smaller is stronger" trend for the specimens with dislocation slip-based plasticity. In general, a change from harder to softer occurs for pillars between 16 and 24 nm radius. In specimens deforming purely by twinning, the size effects are less prominent. Contrary to the single crystal findings, the mechanical parameters of the polycrystals tend to fall with decreasing grain size. Thus, the finer the grain structure, the softer is the polycrystalline response. This suggests a case of an inverse Hall-Petch relationship. Polycrystalline structures also show lower elastic modulus than expected from homogenization theory. This effect is attributed to the softening through GBs. In the plastic regime, the primary deformation mechanism appears to be GB sliding.

2. *Orientation dependence of Li mechanical properties.* It is noteworthy that even for a task usually considered straightforward, such as analyzing the elasticity of a pure metal, discrepancies arise among simulation methods, experimental results and literature values. As demonstrated in these sections, the pronounced anisotropy of lithium is a consistent observation and should not be overlooked. However, quantifying its elastic properties remains challenging, mainly due to the intricacy of the system and inherent methodological assumptions. The elastic properties output via *ab initio* simulations agrees with literature data and emphasize the strong anisotropy of Li metal. They serve as reference for the following investigations. The MD results on small atomic supercells and nanopillars, although overestimating the elastic properties at room-temperature, are consistent and accurately capture the expected anisotropy, in particular $E_{[100]} < E_{[110]} < E_{[111]}$ and $G_{[111]} < G_{[110]} < G_{[100]}$. Moreover, the MD results on nanopillars indicate that anisotropy plays a central role not only in elasticity but also in plasticity, with single crystals of different orientations showing significant variations in yield strength, plastic flow and deformation mechanisms.

3. *Fundamentals of plasticity on small scales and at high homologous temperatures.* We have showed that at 300 K the Li single crystal nanopillars are either deforming by slip or by twinning depending on the orientation, load mode (tension/compression) and strain rate. For the slip cases, dislocations with Burgers vector $1/2\,\langle 111\rangle$ are the

predominant carriers of deformation, appearing in a variety of planes, such as {112} and {113}. For the twinning cases, reflection twins occur singularly on {112} that exhibit a twinning/anti-twinning anisotropy. This anisotropy leads to a pronounced orientation and loading mode dependence of the occurrence of twinning. Besides, the experimental indentation results indicate that even at room temperature Li foils have the ability of being strain-hardened and afterwards are less susceptible to plastic deformations. As a consequence, we suggest mechanical treatments as a possible method to increase the hardness and mechanical stability of thin Li foils used for battery assembly.

We believe this work provides valuable insights into the deformation behavior of lithium metal, particularly in the context of battery applications, helping to bridge the existing knowledge gaps.

2.2 Pure Sodium Metal

The low reserves and inflated cost of lithium, combined with an increasing demand for the material, has induced concerns about the availability of this element [184]. Hence, alternatives to lithium have been intensively studied. In the context of SSBs, sodium (Na) gained much interest, due to low cost and high abundance of its resources [184, 185]. Apart from that, Na-based batteries can exhibit comparative performances with Li-based cells [184].

However, Na is even softer than Li, has a lower melting point and it is significantly more prone to creep. Research has already been done focusing on its mechanical behavior (see, e.g., [121, 186–189]). Nevertheless, mechanical tests with Na are even more complex to perform than tests with Li. Besides, Na is also a BCC metal at room temperature. Thus, we can infer that much of its deformation behavior is influenced for the inherent characteristics also present in the Li deformation mechanisms. Therefore, here we focus only in the simulations of elastic mechanical properties via *ab initio*.

2.2.1 *Ab initio* Simulations

Methods

Mechanical parameters of pure BCC Na metal are computed using the Vienna Ab initio Simulation Package (VASP), which uses a plane wave basis set and the projector augmented wave (PAW) method [91, 142–144]. The exchange-correlation energy is determined via two different potentials: the Perdew-Burke-Ernzerhof (PBE) Generalized Gradient Approximation (GGA) and the Local Density Approximations (LDA). In both cases, the pseudopotential that includes the valence state p for Na is used. The electronic self-consistency loop uses an energy accuracy condition of 10^{-6} eV. Ionic relaxation is carried out with an energy accuracy of 10^{-5} eV in between two ionic steps. For all ab initio calculations, systematic convergence checks concerning the energy cutoff and the k-space sampling are performed. We select an energy cutoff for the plane-wave basis set of 500 eV for both the LDA and PBE potentials. For the k-space sampling, we use a $40 \times 40 \times 40$ Monkhorst-Pack discretization for LDA and $50 \times 50 \times 50$ for PBE, as in particular for symmetry reducing shear transformations of the unit cell the convergence requires a fine mesh [145]. Different deformations are applied to a BCC unit cell, so that the cubic elastic constants C_{11}, C_{12} and C_{44} are obtained, according to [146, 147] and shown in Equations 2.1 - 2.3. Then, the homogenization Equations 2.4 - 2.14 are applied to calculate the mechanical parameters. The obtained data are compared against both theoretical and experimental literature works.

Results and Discussions

Following the same procedure as for lithium metal, firstly, the equilibrium lattice constant and bulk modulus (B) are estimated. Then, further elastic constants and other mechanical parameters, such as Young's modulus (E), shear modulus (G) and Poisson's ratio (ν) are calculated. The elastic parameters of single crystals are computed for loading along different crystallographic directions, or as homogenized values for polycrystalline materials. The calculated values and relevant literature data are shown in Table 2.4.

Property	Na - PBE (0 K)	Na - LDA (0 K)	Ref. [190] (298 K)	Ref. [121] (150 - 300 K)	Ref. [187] (78 - 195 K)	Ref. [188] (195 - 299 K)	Ref. [189] (RT)
a_0 (Å)	4.192	4.052	4.2906	4.236 - 4.286			
B (GPa)	7.668	9.142		7.2 - 6.6	7.3 - 6.82	7.75 - 6.88	
C_{11} (GPa)	8.359	10.020		7.9 - 7.1	8.26 - 7.71	8.13 - 7.69	
C_{12} (GPa)	7.322	8.703		6.9 - 6.3	6.87 - 6.45	6.8 - 6.468	
C_{44} (GPa)	6.009	7.052		5.9 - 5.5	5.78 - 5	5.1 - 4.34	
$E_{[100]}$ (GPa)	1.521	1.929					
$E_{[110]}$ (GPa)	4.612	5.741					
$E_{[111]}$ (GPa)	14.294	16.828					
E (GPa)	6.717	8.037		6.5 - 6.0			4.6
$G_{[100]}$ (GPa)	6.009	7.052					
$G_{[110]}$ (GPa)	0.955	1.204					
$G_{[111]}$ (GPa)	0.746	0.944					
G (GPa)	2.480	2.969		2.4 - 2.2			1.7
ν	0.354	0.353					0.41
Zener ratio	11.591	10.710					

Table 2.4: Elastic properties of BCC sodium metal. Na - PBE and Na - LDA are calculated at 0 K via *ab initio* simulations. Relevant literature data with its corresponding temperature ranges are added.

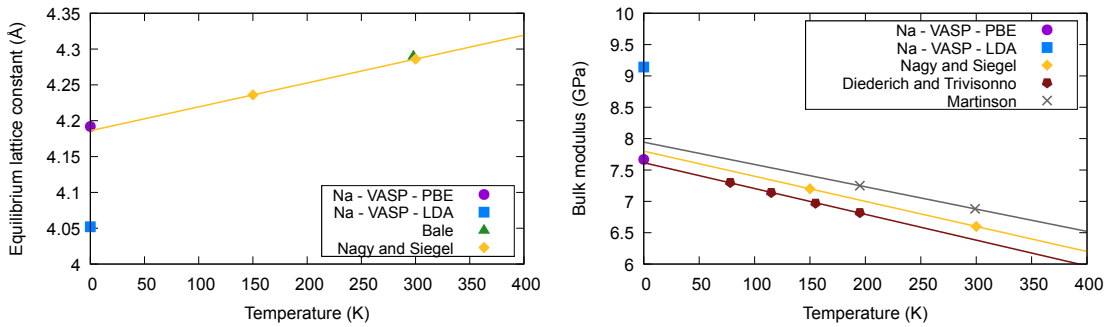

Figure 2.21: Comparison of the obtained results of equilibrium lattice constant (left panel) and bulk modulus (right panel) for pure BCC Na.

As discussed in the previous section, lithium has a Zener ratio close to 9 at 0 K, indicating an extremely anisotropic behavior. According to our simulations, sodium has a Zener ratio of approximately 12 at 0 K, which is even higher than on Li. Therefore, it can be expected that Na mechanical properties has a strong dependence on specimen orientation and loading direction. Besides, the Young's modulus for Na is around 15 GPa at the [111] direction, while in [100] direction does not even reach 2 GPa. These values are also lower than the ones from Li.

From Table 2.4, differences are found when the properties are calculated using either the PBE or the LDA potentials. For the comparison, the theoretical work of Nagy and Siegel [121] and the experimental works of Bale [190], Diederich and Trisonno [187] and Martinson [188] are used. The comparison of the bulk modulus and equilibrium lattice constant are depicted in Figure 2.21. From the plots, it can be seen that the PBE potential provides a significant closer bulk modulus and lattice constant to the reference values. In Figure 2.22 a benchmark of the calculated polycrystalline values of Young's and shear modulus following the homogenization formulas are shown. In this case, both PBE and LDA potentials reproduce accurate values for these mechanical properties, with LDA being slightly overestimated, and PBE slightly underestimated.

2.2.2 Conclusions on Pure Sodium Mechanics

In general, these are similar findings as for lithium. Sodium presents an even higher orientation dependence of the elastic properties than lithium and lower mechanical properties, making it softer and more elastically anisotropic. The PBE potential outputs values closer to the references. Here, we suggest that the elastic mechanical properties depicted in Table 2.4 are complete, reliable and can be used as benchmark for future studies.

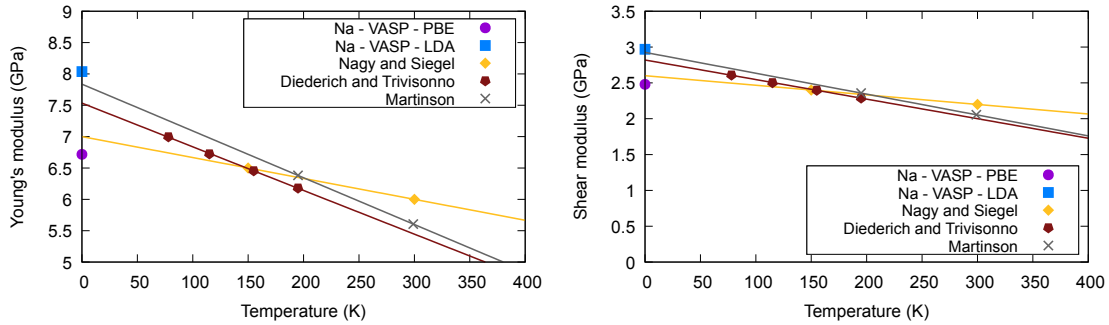

Figure 2.22: Comparison of the obtained results for Young's modulus (left panel) and shear modulus (right panel) for pure BCC Na.

2.3 Lithium-Sodium Alloy

In [104], we present a simple, scalable and innovative approach, that consists in mixing solid-state lithium (Li) and sodium (Na) metals to create a meta-stable, homogeneous Li-Na anode foil for use with lithium lanthanum zirconium oxide - $Li_7La_3Zr_2O_{12}$ (LLZO) separators. In order to achieve a good distribution of Na in the Li host structure, physical mixing is chosen over in-melt mixing, as the latter usually leads to segregation of Na in large clusters (demixing), especially in the region of mutual immiscibility of Li- and Na-rich melt phases [191]. During mechanical mixing, Li and Na metal are weight in the desired amounts, mixed and calendered to obtain a thin, flat foil of roughly combined metals. This foil is then cut into multiple pieces, folded and calendered to the same thickness as before. This process is repeated at least 20 times to ensure a homogeneously, finely dispersed Na in Li metal which could then be applied to the LLZO pellets. We then melt-quench the Li-Na foils directly onto the LLZO surface. The symmetric cells prepared in this way are operated without external pressure (0.1 MPa) and show record electrochemical performance, cycling stability of over 1200 cycles, and a total stripping capability of up to 100 µm Li metal. Most remarkably, our approach results in a very low impedance of the Li-Na/LLZO interface, which remained constant even at high stripping/plating rates.

Here we characterize the mechanical properties and microstructure of the Li-3mol%Na (Li-Na) anode foils used in these cells and make a comparison against pure lithium to investigate the influence of alloying and processing in the anode foils. Firstly, the elastic properties are theoretically estimated using the Reuss-Voigt model. Secondly, Martens Hardness (HM) is determined using microindentation. X-ray Diffraction (XRD), texture and pole figure analyzes are carried out on all specimens.

2.3.1 Theoretical Estimation via Reuss-Voigt Model

According to the phase diagram, the Li-Na system does not form either alloys or an intermetallic compound [190]. When mixed, both metals retain their original crystal structure and tend to a phase separation, which is explored in detail at the next chapter (subsection 3.1). Therefore, the use of the Reuss-Voigt theories (also known as rule of mixture) is an appropriate estimation of the elastic parameters [84, 85, 149]. So, we apply the Equations 2.16 and 2.17 for 97% lithium and 3% sodium using reference values of elastic modulus from both literature and our own *ab initio* data. The obtained results are summarized in Table 2.5, which shows that the upper and lower bounds are close to each other and the elastic properties of Li-Na are similar to the properties of the pure lithium.

E_{Li} (GPa)	E_{Na} (GPa)	Method (refs.)	$E_{LiNa\text{-}Voigt}$ (GPa)	$E_{LiNa\text{-}Reuss}$ (GPa)
7.82	4.60	Pulse-echo [42, 189]	7.72	7.66
9.40	3.90	Nano-indentation [44, 186]	9.24	9.02
13.81	6.72	VASP-PBE (this work)	13.59	13.38

Table 2.5: The calculated elastic modulus of Li-Na via Reuss-Voigt model.

Here, the equations are applied to the elastic modulus. The same can be done for any other elastic mechanical property, such as shear modulus or bulk modulus. Nevertheless, the mechanical properties of Na and Li are not drastically different from each other and they phase separate keeping their individual crystal structures. Consequently, as long as the fraction of Na remains low, the rule of mixture is not expected to output significant changes for any elastic mechanical property of this anode.

2.3.2 Microindentation Experiments

HM and texture of pure lithium and Li-Na foils are experimentally determined using microindentation and XRD.

Methods

All experiments and sample preparation are conducted in an argon filled glove-box. The indentation experiments are performed using a Fischerscope H100 indenter (Helmut Fischer GmbH, Sindelfingen, Germany) equipped with a diamond Vickers tip. Square samples are cut from the original foil. The squared samples are attached to a metal sample holder, to provide support and stability during indentation. All measurements are performed at room temperature. The indentation experiments are load-controlled. The load is applied following $d\sqrt{F}/dt$, with loading and unloading at the same rate. The application force, creep holding time and application time are systematically varied. The

details are shown in Table 2.6. At least 10 indents are done for each setting, from which average and standard deviation are calculated. The individual measurements are carried out with a space of at least 10 times the indentation depth in between each indent [140].

Load (mN)	Creep holding time (s)	Load and unload application time (s)
15	10	5
15	10	10
15	10	15
15	10	20
5	10	20
10	10	20
15	10	20
20	10	20
15	1	10
15	5	10
15	10	10
15	15	10
15	20	10
15	25	10
15	30	10
15	35	10
15	40	10
15	45	10
15	50	10
15	55	10
15	60	10

Table 2.6: Experimental settings used in the microindentation experiments of Li-Na foils.

HM is evaluated according to the Equation 1.12. To decouple the influence of the anode preparation procedure in the hardness results, four sets of samples are prepared:

- Foil 1: conventional pure Li foil. Mechanically rolled in-house from Li pellets. Minimally calendered.
- Foil 2: 20x calendered pure Li foil: same as foil 1, but 20x calendered.
- Foil 3: 20x calendered Li-Na foil: same as 2, but with the addition of 3mol% Na into the Li matrix.
- Foil 4: Li-Na foil after heat treatment: same as 3, but after heated at 300°C for 5 minutes and quenched in between two Ni foils. Foil used in the cells in which the improved performance is obtained.

Therefore, by analyzing the foils in this scheme, it is possible to attribute the variation of hardness to the individual manufacturing steps of the final anode. Additionally, XRD, texture and pole figure analyzes are carried out on all specimens. These experiments are performed using a dome airtight sample holder, a diffractometer EMPYREAN (PANalytical) and Cu-Ka radiation.

Results and Discussions

The results from the indentation can be seen in Figure 2.23 and the ones from the texture analyzes in Figure 2.24. It can be seen from Figure 2.23(a), that the choice of load does not seem to systematically influence the hardness results. Nonetheless, from Figure 2.23(b), it becomes clear that in general, the faster the load is applied, the harder is the material response. This strain-rate sensitivity of lithium metal has already been reported and characterized in more details [44]. From Figure 2.23(c), a robust measurement of hardness is performed across different creep holding times. The creep holding time should not influence the hardness, but rather the maximum indentation depth, as it is depicted in Figure 2.23(d). The longer the indent is hold at the maximum load, the deeper is the indentation mark. That is a clear consequence of the high creep rates of lithium, which at room-temperature is already at elevated homologous temperatures. Nevertheless, from all these analyzes it becomes obvious that the foil number 1 tends to have a systematically softer behavior as the other foils.

Hence, a summary of the results is presented in Figure 2.23(e), which shows the average from the indents of panel c (fixed load and load rate, while changing creep time). It can be observed that foil 1 has a lower hardness. This is the foil which has been minimally calendered. Afterwards, foil 2 already shows an increase of hardness. The only difference between foil number 1 and 2 is the 20x calendering step, as both foils are manufactured from pure lithium pellets. Thus, the calendering step seems to have a clear influence in the mechanical properties of the thin lithium foils.

The influence of addition of sodium can be seen when comparing foil number 2 and 3. These two sets of samples are manufacturing following exactly the same procedure, so 20x folding and calendering, but foil 3 carries 3mol%Na within the Li matrix. These both foils behave extremely alike in the mechanical tests.

A final remark regarding hardness must be done for foil 4, which is the main specimen of interest, as the improved cycling is obtained with such sample. The average hardness of this foil is slightly lower than the 20x calendered samples, but still higher than the reference foil. The melting step theoretically should remove all traces of mechanical processing, such as texture and high dislocation density. So it would be expected that, in turn, this would reduce the hardness of the foil to the initial levels. However, one point

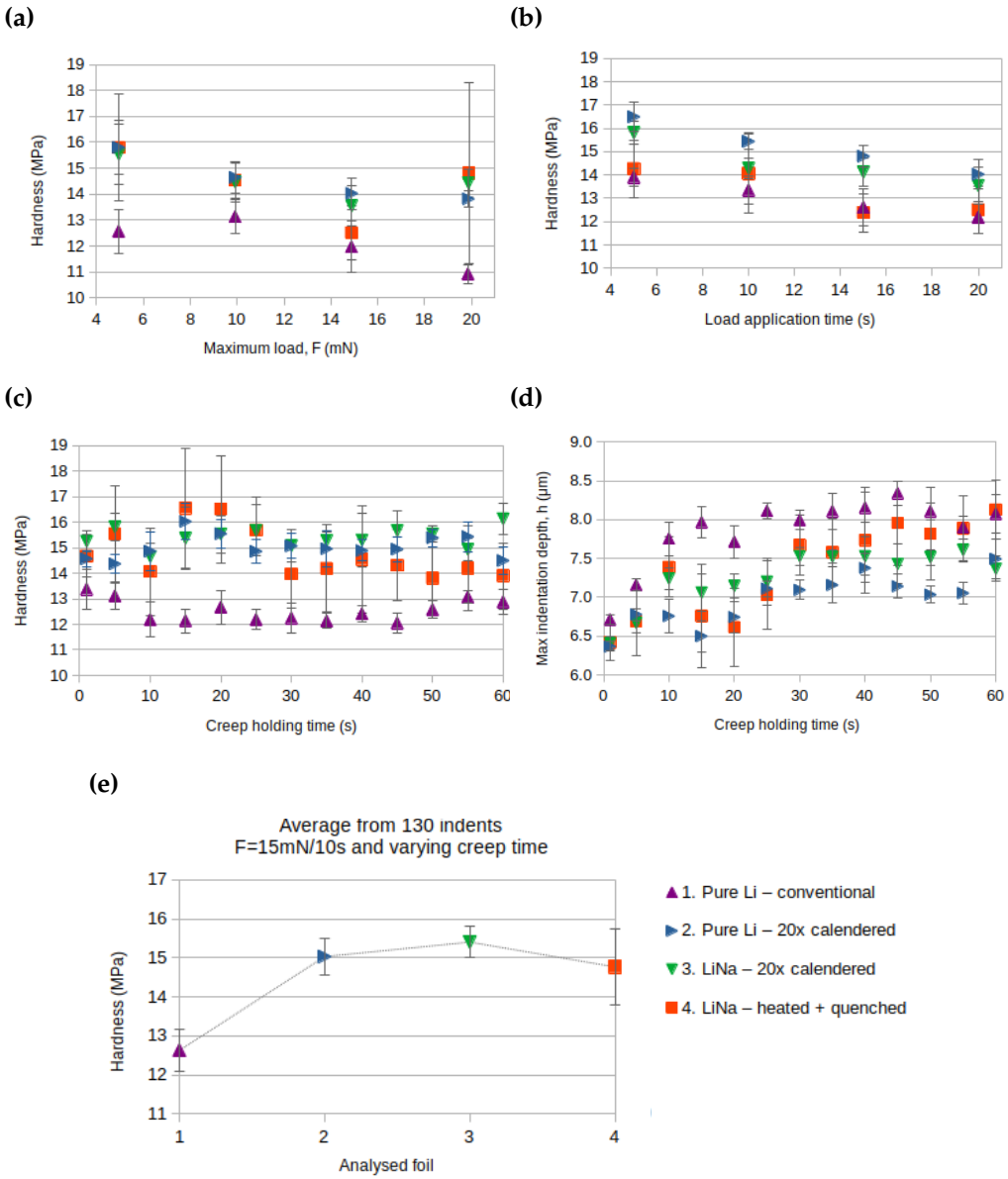

Figure 2.23: Average and standard deviation from different experimental parameters of *HM* in the four samples investigated. In **(a)**, the influence of load is analyzed. In **(b)**, the influence of load application time. In **(c)**, the influence of creep holding time. Additionally, in **(d)**, the maximum indentation depth is plotted across different creep holding times, showing the time-dependent plastic deformation of lithium metal. In **(e)**, the summary of the results from **(c)** is depicted, to evidence the difference between the foils.

to be highlighted is that, given the heat treatment, the sodium in small concentration is evenly distributed through the lithium matrix, as in a solid solution, which could lead to the observed hardness result (see chapter 3). Another point is that this foil is produced in between two Ni foils. At least one of these Ni foils must the removed in order to expose fresh Li-Na for the indentation experiments. The fierce removal of one of the Ni foils can damage the surface, influencing the micro-hardness results.

To further investigate the foils, XRD, texture and pole figure analysis are carried out. The XRD data does not indicate any unusual feature, simply the individual peaks of the pure metals. On the other hand, the pole figures provide an interesting observation into the texture of the foils. Selected pole figures for the four foils can be seen in Figure 2.24.

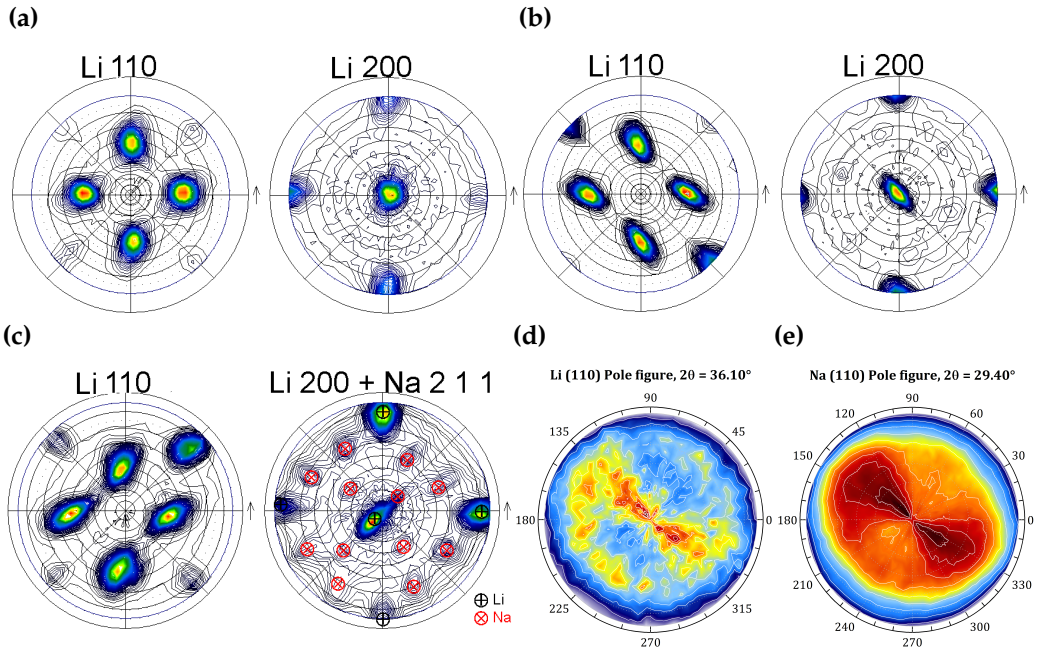

Figure 2.24: Pole figures for the analyzed foils. Foils number **(a)** 1, **(b)** 2 and **(c)** 3 present a strong single-crystal-like texture, indicating that the manufacturing procedure generates a $\langle 100 \rangle$ preferred orientation. The measurements on foil number 4 (panels **(d)** and **(e)**) show no preferred orientation, indicating that the heat treatment dispose the strong foil texture. Panel **(d)** is the reflection from Li (110), while panel **(e)** is the reflection from Na (110). For foil number 4, due to overlapping with reflections of the Ni foil, some pole figures (e.g., Li (200)) cannot be measured.

The pictures depicted in Figure 2.24 show that the mechanically rolled foils are highly textured. As the pole figures demonstrate, it is not just a $\langle 100 \rangle$ preferred orientation. It

rather looks like an almost perfectly aligned single crystal with one ⟨100⟩ pole perpendicular to the sample surface and coincidentally one at a rotation angle 0°. The extreme texture is found for the foils number 1, 2 and 3. The foil number 4, after the heat treatment, does not present the strong texture, confirming that the melting took place and erased the traces of the rolling.

2.3.3 Conclusions on Lithium-Sodium Mechanics

Succinctly, all analyzed anode foils show creep behavior and a slight strain rate dependence. The manufacturing step that provides the largest increase in hardness is the mechanical mixing with folding and rolling 20x. Therefore, here we confirm that mechanical treatments increase the hardness and decrease the creep rates of thin Li foils. This is found for both pure Li and Li-Na foils, which originated from different suppliers, but go through the same mechanical post-processing in house. The experiments indicate that the addition of small quantities of sodium does not influence the mechanical behavior, agreeing with the theoretical expectations from the Reuss-Voigt Model.

Regarding texture, all rolled foils present a strong single-crystal-like ⟨100⟩ texture. The heat treatment removes this texture and likely also the traces of strain hardening, but it does not lead to a significant variation in hardness, probably due to the formation of a meta-stable solid solution from the physical mixing with subsequent melt and quenching of the Li and Na metals, which will be explored in more details at the next chapter.

When comparing the four specimens in this study, it can be said that no large difference is found between the analyzed foils. Mainly if we compare foil number 1 and foil number 4, which are the ones used for cell assembly, a difference of a few MPa cannot explain the improved cell performance and notable increase in dendrite tolerance obtained experimentally. Therefore, we cannot attribute this electrochemical improvement to changes in mechanical properties. It is possible that other effects are playing a role, such as the lithium-sodium phase separation or formation of new compounds at the interface, which will be investigated at the following chapter.

This Li-Na experimental results are published together with the electrochemical characterization of the Li-Na anodes in [104].

Chapter 3

Thermodynamics in Lithium-Sodium Systems

Recently, Li-Na metal anodes have attracted attention by developments of cells with beneficial electrochemical performance [104, 191, 192]. But, as we see from the previous chapter, the addition of small quantities of sodium does not alter significantly the mechanical properties of the lithium metal anode. The results also do not suggest that the manufacturing procedure is the root cause for the improved cell performance. Consequently, some other effects must be playing a role.

Besides mechanical properties, chemical and surface aspects are essential to help explain Solid-State Batteries (SSBs) behavior, mostly regarding the solid-solid interfaces. It was experimentally observed by Mann et al. [104] that during Li stripping, the Li-Na anode forms a self-organized 3D microstructure that significantly improves the LMA/LLZO interface. The cell was operated very stably without external applied pressure. In addition, Fu et al. [192] also experimentally observed that Li, when doped with small quantities of Na, presents higher wettability, lower interface resistance, less dendrite formation and longer cycle life than pure Li. The authors hypothesized that this happened due to interactions between Na and a carbonate phase.

Therefore, in order to get a deeper understanding of this interface, we investigate the thermodynamics of the lithium and sodium system, focusing on their relevance for these remarkable Li-Na/LLZO cells [104, 192]. Here we investigate bulk microstructure formation (subsection 3.1), as well as carbonate formation and surface effects (subsection 3.2). The content of subsection 3.1 is published in [193].

3.1 Bulk Microstructure Formation

Li-Na, as a binary system, has been previously investigated, with its phase diagram detailed in [194], building upon earlier descriptions in [195]. These authors have developed a comprehensive thermodynamic modeling, based on existing experimental work and the SGTE data [196], leading in particular to the phase diagram shown in Figure 3.1.

Li-Na is a monotectic alloy, hence it exhibits phase separation in the melt phase [197]. Additionally, it has a lower temperature eutectic point on the Na rich side. It is therefore

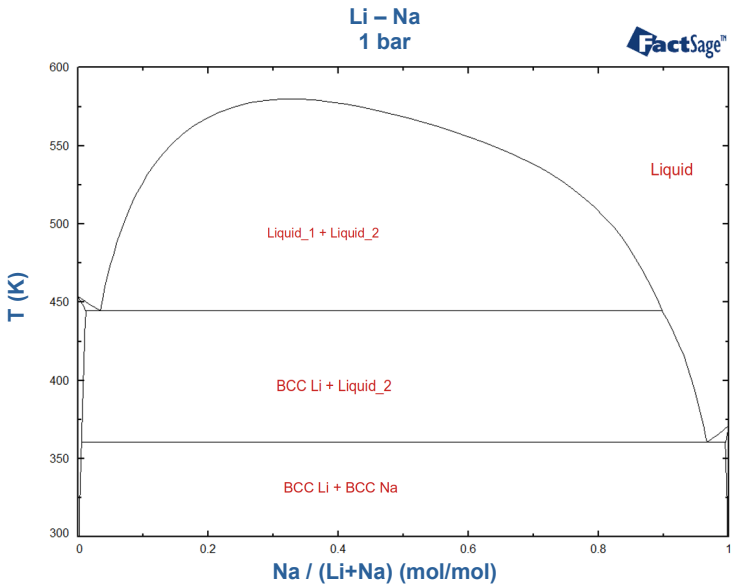

Figure 3.1: Li-Na equilibrium phase diagram, calculated using the SGTE database in FactSage 8.3 and [190].

obvious that the focus of these investigations was on the high temperature regime of the phase diagram, to capture the behavior in the vicinity of these invariant points [198–206]. In contrast, less attention has been paid to the low-temperature regime below the eutectic temperature ($\approx$ 350 K), where Li and Na form essentially immiscible body-centered cubic (BCC) phases.

Therefore, we revisit the low-temperature regime of the Li-Na phase diagram, using *ab initio* techniques, as these low solubility regimes are difficult to access experimentally. Based on these investigations, we suggest an improved thermodynamic description of the BCC phases at low temperatures. We extract system energetics and predict the low-temperature phase diagram, where Li and Na are practically immiscible. Apart from phase stability, also spinodal decomposition is investigated, as it is relevant for the microstructure formation at the Li-Na anodes. The onset of spontaneous phase separation is determined both with and without considering elastic mechanical effects, providing a theoretical composition range where such microstructures are expected to form. The consequences of the new assessment are discussed from the perspective of battery applications.

3.1.1 Methods

All *ab initio* simulations are performed with the Vienna *Ab Initio* Simulation Package (VASP), which uses a plane wave basis set and the projector augmented wave (PAW)

method [91, 142, 143]. Different supercell sizes ranging from $2 \times 2 \times 2$ to $4 \times 4 \times 4$ are used, where one or more Na atoms replace Li atoms on the BCC positions. A full ionic relaxation is performed with an energy accuracy of 10^{-5} eV in between two ionic steps. The electronic self-consistency loop has a global break condition of 10^{-6} eV. The exchange-correlation energy is determined via the Perdew-Burke-Ernzerhof (PBE) generalized gradient approximation (GGA) using the harder pseudopotentials that include the valence states *s* for Li and *p* for Na [144]. An energy cutoff for the plane-wave basis set of 500 eV and a $10 \times 10 \times 10$ Monkhorst-Pack k-point mesh are selected for the simulations [145].

3.1.2 Results and Discussions

Low-temperature Thermodynamics

For the application as anode material, mainly the low-temperature phases of Li-Na are of interest. As obvious from the phase diagram, the mutual solubility of Na in Li and vice versa is rather low. Consequently, data on this regime is limited, and the thermodynamic modeling in [194] has presumably only reduced accuracy. Therefore, we perform *ab initio* calculations at 0 K to obtain the energetics of the Li-Na system.

The results of the density functional theory computations are summarized in Figure 3.2. It shows the energy of formation (per atom), using the definition

$$E_f(N_{\mathrm{Li}}, N_{\mathrm{Na}}) = E(N_{\mathrm{Li}}, N_{\mathrm{Na}}) - N\left[(1-x)E_{\mathrm{Li}} + xE_{\mathrm{Na}}\right], \tag{3.1}$$

where $N = N_{\mathrm{Li}} + N_{\mathrm{Na}}$ is the total number of atoms in the substitutional alloy, in analogy to the definition in [207]. Here, $E(N_{\mathrm{Li}}, N_{\mathrm{Na}})$ denotes the energy of a system consisting of N_{Li} lithium and N_{Na} sodium atoms, and $E_{\mathrm{Li}} = E(N, 0)/N$ is the energy per (pure) lithium atom (similarly $E_{\mathrm{Na}} = E(0, N)/N$). Furthermore, $x = N_{\mathrm{Na}}/N$ is the sodium concentration. By definition, the energy of formation difference equals zero for both pure Li and pure Na. Alloys which contain both elements have a higher formation energy E_f, indicating that at $T = 0\,\mathrm{K}$ no solid solution phase is formed, and instead a decomposition into pure Li and pure Na takes place, which is in agreement with the experimental phase diagram. Eq. (3.1) can be interpreted as total energy of the system, from which a linear function in concentration is subtracted. Such a subtraction affects neither the common tangent construction for identifying phase coexistence nor the condition for the onset of spinodal decomposition, which will be discussed below.

Due to the equivalence of BCC lattice positions, the energy is unique for setups with only a single impurity. For two such defects, the energy depends on their relative position, which leads to a slight scatter in the data. This effect is most pronounced for an equal amount of Li and Na atoms ($x = 0.5$), where the highest energy configurations correspond

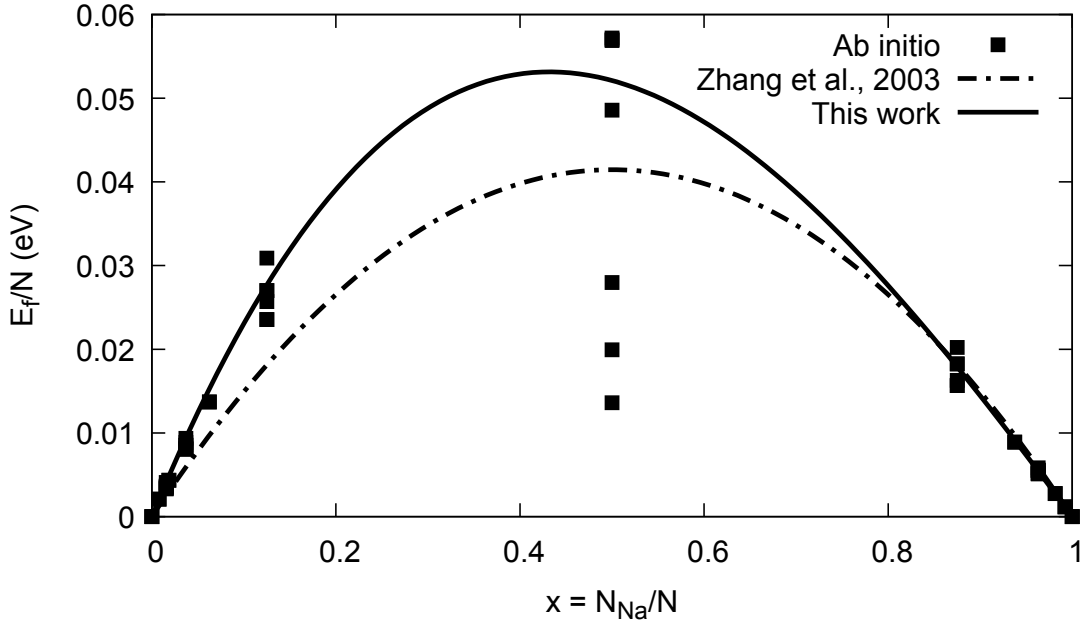

Figure 3.2: *Ab initio* based formation energy of the Li-Na system. The low energy configurations in $x = 0.5$ correspond to partially ordered structures, where Li and Na are arranged in layers, in agreement with the energy reduction through phase separation.

to irregular "solid solution" configurations, whereas the lower ones to arrangements, where the different atom types are organized in layers or blocks. This energy reduction relative to the solid solution configurations indicated the system's tendency for phase separation. As we treat the phase separation on the continuum level, we mainly focus here on the randomly arranged high energy configurations; further improvements using special quasirandom structures are possible [208]. However, we point out that the focus of the present investigations is on solubility limits and spinodal decomposition, which occur at low concentrations, and therefore only these essentially unique branches of the energy matter and are considered for the determination of an optimized thermodynamic description in the following. Moreover, in the present investigations, only $T = 0\,\mathrm{K}$ energies from the *ab initio* simulations are used. For higher temperatures closer to the eutectic temperature, next to configurational entropy contribution, which are discussed below, also thermal vibrations should be considered. The focus of the present work is formally on low-temperature phase separation, where vibrational modes are not yet excited. Especially on the Li rich side, such an approximation is reasonable due to the higher Debye temperature of Li as compared to Na [209]. This simplification is in line with

existing thermodynamic descriptions, but an extension to quasiharmonic descriptions is possible, similar to discussions, e.g., in [210].

Finite temperature configurational entropy is added via the ideal solution model, in agreement with the Calphad description. We note that not all lattice configurations are energetically equivalent, thus the use of the ideal model, which assumes equal probability for all states, is strictly speaking not appropriate. However, as we are here mainly interested in the low-concentration regimes, only small amounts of Na in the BCC Li lattice (and vice versa) are relevant. As all lattice positions in the BCC lattice are equivalent, as discussed above, and the distance between Na atoms is large for low concentrations, the assumption is appropriate. For higher concentrations, deviations are captured in the Calphad framework in the excess Gibbs energy expression, as defined below.

From a thermodynamics perspective, the finite temperature Gibbs energy is modeled as

$$G_{\mathrm{m}}^{\Phi} = \sum_i x_i {}^0G_i^{\Phi} + RT \sum_i x_i \ln x_i + {}^{\mathrm{xs}}G_{\mathrm{m}}^{\Phi} \tag{3.2}$$

within the Calphad framework. Here, the molar Gibbs energies ${}^0G_i^{\Phi}$ of the pure element i with structure Φ as described in [196], and R is the ideal gas constant, in agreement with the usual normalization as Gibbs energy per mole. The non-ideal, excess contribution is expressed through the Redlich-Kister polynomials as

$${}^{\mathrm{xs}}G_{\mathrm{m}}^{\Phi} = \sum_i \sum_{j>i} x_i x_j \sum_{k=0}^{n} {}^kL_{i,j}^{\Phi}(x_i - x_j)^k. \tag{3.3}$$

Zhang et al. [194] truncates the expansion after the leading term for the BCC Li-Na phase, using ${}^0L_{\mathrm{Li,Na}}^{\mathrm{BCC}} = 16000\,\mathrm{J/mol}$. For $T = 0\,\mathrm{K}$ the excess contribution ${}^{\mathrm{xs}}G_{\mathrm{m}}^{\Phi}$ corresponds to the formation energy E_f (apart from the normalization per mole), i.e., ${}^{\mathrm{xs}}G_{\mathrm{m}}^{\Phi} = N_A E_f / N$, and the expression from [194] is depicted in Figure 3.2. Although the agreement with the *ab initio* data is reasonable, it does not capture well the apparent asymmetry between the Li and Na rich sides. Therefore, we suggest including also the next order term in the Redlich-Kister expansion.

To this end, an analysis of the low-concentration and low-temperature regime of the common tangent construction yields for the solubility limit of Na in Li

$$x \simeq \exp\left(-\frac{{}^{\mathrm{xs}}G_{\mathrm{m}}^{\Phi\,\prime}(x=0)}{RT}\right), \tag{3.4}$$

where the prime denotes differentiation with respect to the Na concentration x, see [211].

On the Na rich side, one gets similarly

$$1 - x \simeq \exp\left(\frac{{}^{\mathrm{xs}}G_{\mathrm{m}}^{\Phi\,\prime}(x=1)}{RT}\right). \tag{3.5}$$

An expansion up the second term in Eq. (3.3) yields on the Li rich side

$$x \simeq \exp\left(-\frac{{}^{0}L_{\mathrm{Li,Na}}^{\mathrm{BCC}} + {}^{1}L_{\mathrm{Li,Na}}^{\mathrm{BCC}}}{RT}\right) \tag{3.6}$$

and similarly on the Na rich side

$$1 - x \simeq \exp\left(-\frac{{}^{0}L_{\mathrm{Li,Na}}^{\mathrm{BCC}} - {}^{1}L_{\mathrm{Li,Na}}^{\mathrm{BCC}}}{RT}\right). \tag{3.7}$$

These expressions show that for a description of the low-concentration regimes the coefficients ${}^{0}L_{\mathrm{Li,Na}}^{\mathrm{BCC}}$ and ${}^{1}L_{\mathrm{Li,Na}}^{\mathrm{BCC}}$, as well as the solubility limits, are directly related to the slope of the *ab initio* computed formation energy at $x = 0$ and $x = 1$. As the computed energies with one Na or Li defect are unique, the coefficients therefore follow directly from a finite difference expression,

$${}^{0}L_{\mathrm{Li,Na}}^{\mathrm{BCC}} + {}^{1}L_{\mathrm{Li,Na}}^{\mathrm{BCC}} = N_A\Big[E(N-1;1) - (N-1)E_{\mathrm{Li}} - E_{\mathrm{Na}}\Big], \tag{3.8}$$

$${}^{0}L_{\mathrm{Li,Na}}^{\mathrm{BCC}} - {}^{1}L_{\mathrm{Li,Na}}^{\mathrm{BCC}} = N_A\Big[E(1;N-1) - (N-1)E_{\mathrm{Na}} - E_{\mathrm{Li}}\Big], \tag{3.9}$$

using here the results from the largest calculated $4 \times 4 \times 4$ system, which contains $N = 128$ atoms. Solving the above linear system yields ${}^{0}L_{\mathrm{Li,Na}}^{\mathrm{BCC}} = 20109.8\,\mathrm{J/mol}$ and ${}^{1}L_{\mathrm{Li,Na}}^{\mathrm{BCC}} = 5772.6\,\mathrm{J/mol}$, leading to the new formation energy curve shown in Figure 3.2, which agrees well with the *ab initio* data also in the intermediate concentration regime.

Figures 3.3 and 3.4 show the low-temperature solubility limits both on the Li and Na rich side in an Arrhenius representation. Obviously, the exact expressions, as obtained from the common tangent construction, agree well with the low-temperature asymptotics (3.6) and (3.7). The graphs also contain the predictions from the previous assessment [194]. Whereas on the Na rich the two descriptions lead to very similar results, the new assessment leads to a significantly lower solubility limit on the Li rich side. We note that the phase equilibrium between the two BCC phases plays a role only below the eutectic temperature $T_e \approx 370\,\mathrm{K}$.

Beyond the thermodynamic phase stability we can also use the description to evaluate the onset of spinodal decomposition. The spinodal regime is in between the inflection

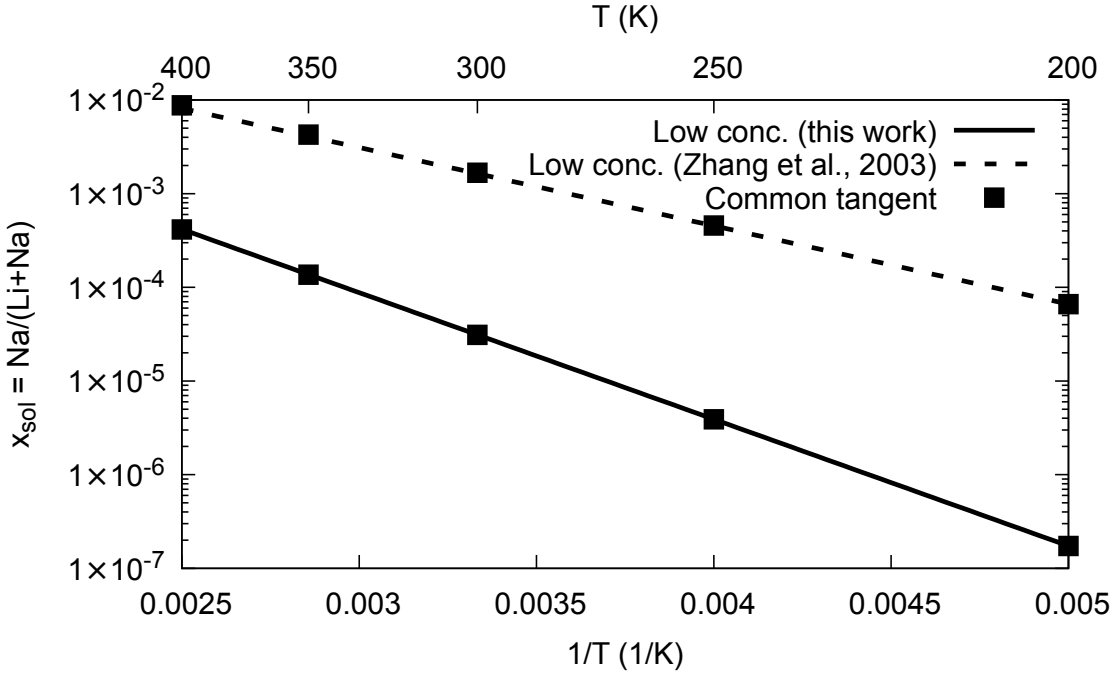

Figure 3.3: Na solubility limit in Li in an Arrhenius representation, i.e., the Li rich side of the Li-Na phase diagram. The straight lines result from the low-concentration limit (3.6) for both the assessment by Zhang et al. [194] and the present work. They agree well with the full common tangent construction (squares) for each description in the entire temperature regime.

points of the Gibbs energy curve, $G_{\mathrm{m}}^{\Phi\prime\prime}(x) = 0$. Apart from a numerical solution of this condition, also analytical approximations in the low-concentration regime (either $x \ll 1$ or $1 - x \ll 1$) can be worked out easily. For the Li rich side, we can neglect the configurational term $(1-x)\ln(1-x)$, and then the condition for the inflection point becomes approximately

$$x_{\mathrm{spin}} \approx -\frac{RT}{{}^{\mathrm{xs}}G_{\mathrm{m}}^{\Phi\prime\prime}(x=0)} = \frac{RT}{2 \times {}^{0}L_{\mathrm{Li,Na}}^{\mathrm{BCC}} + 6 \times {}^{1}L_{\mathrm{Li,Na}}^{\mathrm{BCC}}}, \tag{3.10}$$

hence the onset of spinodal decomposition increases linearly with temperature. An

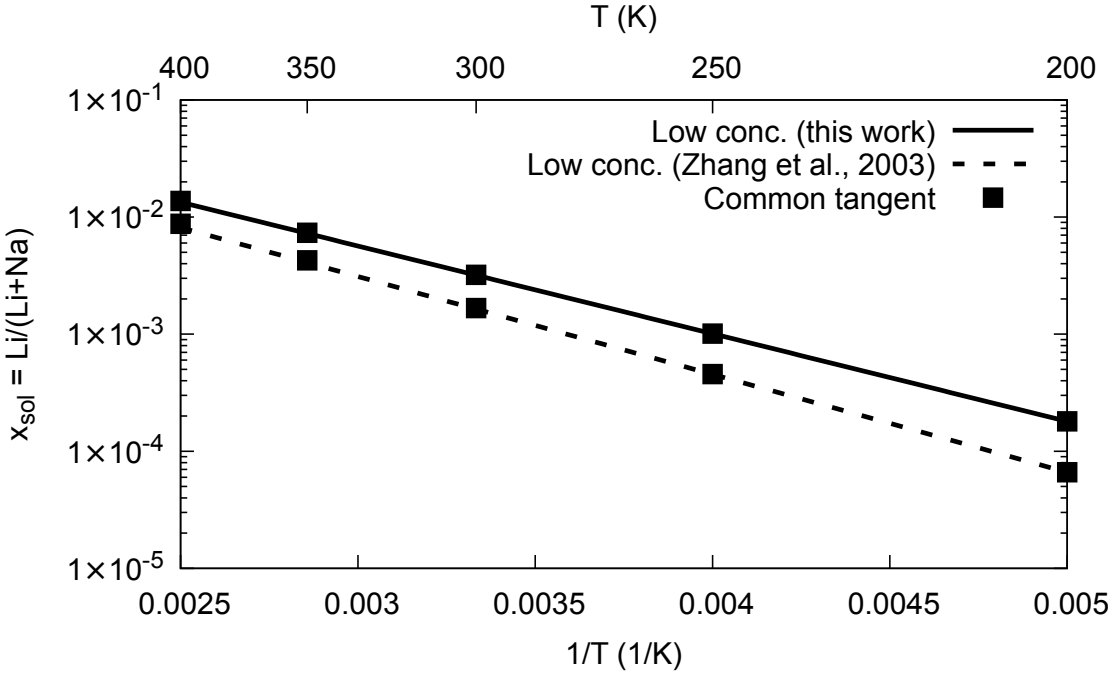

Figure 3.4: Li solubility limit in Na in an Arrhenius representation, i.e., the Na rich side of the Li-Na phase diagram. The straight lines result from the low-concentration limit (3.7) for both the assessment by Zhang et al. [194] and the present work. They agree well with the full common tangent construction (squares) for each description in the entire temperature regime.

analogous analysis on the Na rich side yields

$$\begin{aligned} 1 - x_{\text{spin}} &\approx -\frac{RT}{{}^{\text{xs}}G_{\text{m}}^{\Phi\prime\prime}(x=1)} \\ &= \frac{RT}{2 \times {}^{0}L_{\text{Li,Na}}^{\text{BCC}} - 6 \times {}^{1}L_{\text{Li,Na}}^{\text{BCC}}}. \end{aligned} \tag{3.11}$$

Figures 3.5 and 3.6 compare the analytical approximations (3.10) and (3.11) to the numerically determined onset of spinodal decomposition. Especially on the Li rich side that agreement is excellent, as the required concentrations for spinodal decomposition are still small. Nevertheless, the difference between the present and the previous description [194] is significant, since the old description leads roughly to twice as high critical concentration of Na to trigger spinodal decomposition. On the Na rich side, the analytical approximation (3.11) delivers reliable estimates only at very low temperatures, as at around 50 K the spinodal concentration is already high. This invalidates the assumptions used for the

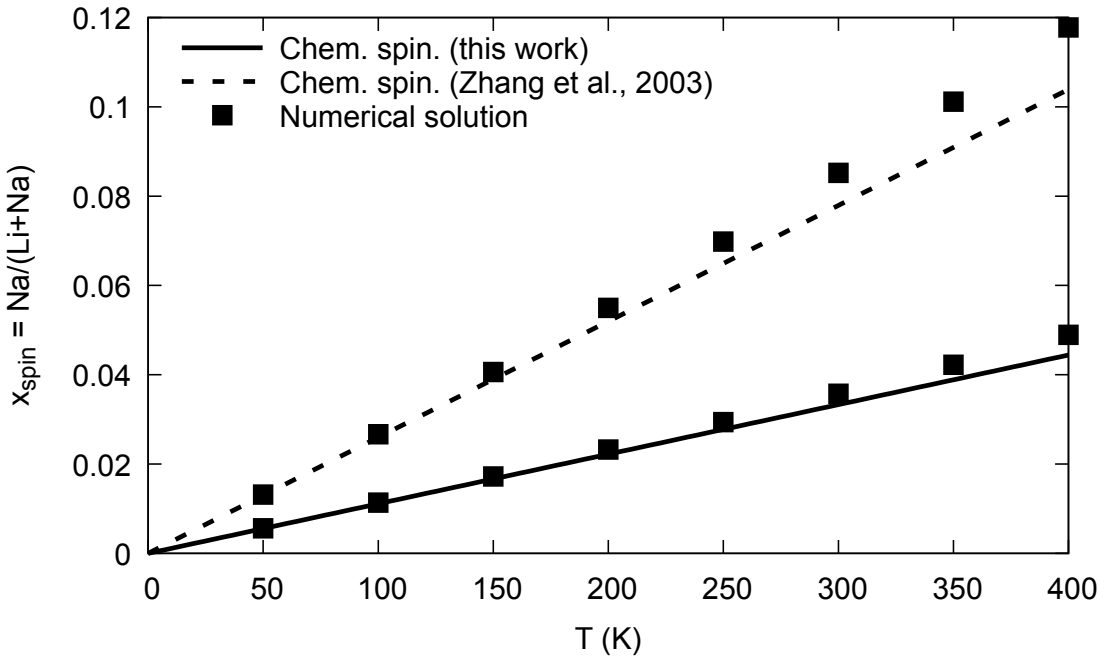

Figure 3.5: Begin of the spinodal regime on the Li rich side. The plot compares for both the previous assessment [194] and the present description the analytical approximation (3.10) to the exact numerical solution (black squares).

derivation of Eq. (3.11), which can therefore serve only as an order of magnitude estimate.

Elastic Effects

The considerations so far neglect elastic effects, as usually done for thermodynamic descriptions. This assumes that in case of phase separation the two phases are separated such that they cannot deform each other. In many applications, however, the phases stick together, and if then different lattice constants emerge, they mutually deform one another, which leads to an additional elastic energy contribution. This contribution always makes the phase separation less favorable, as in a single phase material without external mechanical constraints all macroscopic stresses can relax.

At this point it is instructive to compare the above *ab initio* predictions to simulations without ionic relaxation, where all atoms are forced to remain on the equilibrium positions of the pure Li lattice. As sodium has a larger equilibrium lattice constant than lithium, this leads to compressed states if Li is replaced by Na. From the computed energies we then get a negative formation energy, which indicates that in this case no phase separation would occur and instead a solid solution should form. This improper prediction is a consequence

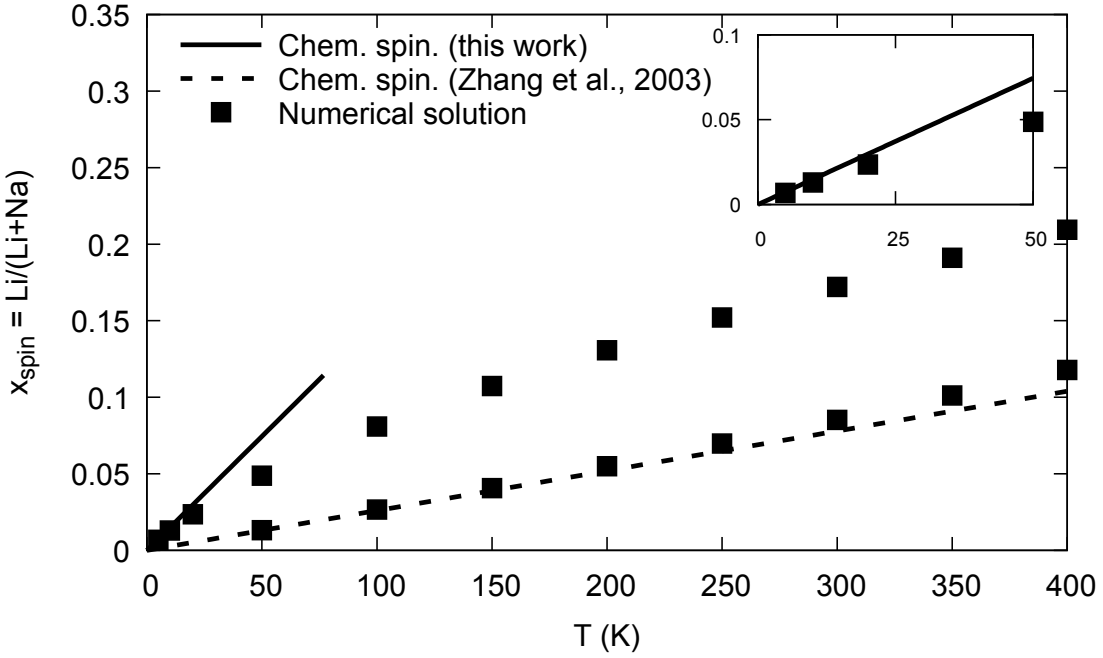

Figure 3.6: End of the spinodal regime on the Na rich side. The plot compares for both the previous assessment [194] and the present description the analytical approximation (3.11) to the exact numerical solution (black squares). The expansion is valid only at low concentrations, as shown in the magnification of this region in the inset.

of the artificially strong internal elastic deformations, which make the phase separation energetically unfavorable, as the emerging sodium phase is strongly compressed. However, from this result we conclude that elastic effects can have a substantial influence on phase coexistence in Li-Na.

A more realistic description is based on the assumption of coherent precipitation of the second phase. In contrast to the above perspective, elastic relaxation is permitted, such that the total elastic energy, which arises due to lattice mismatches, is minimized. This perspective gives an upper bound to the influence of elastic effects, as additional relaxation effects, e.g., due to plasticity, creep or interface slip are not considered. Therefore, we follow a similar approach as in [212, 213], where mechanical effects are taken into account using a mean field description. Such approaches are further elaborated and justified in [211], also with the extension towards the inclusion of elastic relaxation near free surfaces [214]. The calculation is based on the assumption of forming coherent interfaces between the emerging phases and linear elasticity. Further major assumptions are the isotropy of the elastic constants and the lattice expansion through the increase of the sodium

concentration. In this case, the Bitter-Crum theorem [215] applies in infinite or periodic systems, and therefore the elastic energy becomes a function of the volume fractions of the two involved phases alone and does not depend on their spatial arrangement. As suggested by Cahn [216], the elastic effects can effectively be described by adding an elastic contribution (with dimension energy per mole)

$$G_{\mathrm{el}} = \frac{E\chi^2\Omega_0 N_A}{N_0(1-\nu)}x^2 \tag{3.12}$$

to the existing description. An explicit proof for this result is given in [211]. In the above expression, E is Young's modulus, ν the Poisson ratio, χ the Vegard coefficient of lattice expansion, Ω_0 the volume of a unit cell and N_0 the number of atoms per unit cell. It is assumed that both phases have the same elastic constants, and that they differ only by a concentration dependent isotropic eigenstrain $\epsilon_{ij}^{(0)} = \delta_{ij}\chi x$. With pure lithium as reference phase we use $\Omega_0 = a_{\mathrm{Li},0}^3$ with $a_{\mathrm{Li},0} = 3.42\,\text{Å}$ being the $T = 0\,\mathrm{K}$ lattice constant of BCC Li and $N_0 = 2$ for a BCC lattice. The Vegard coefficient is approximated as $\chi = (a_{\mathrm{Na},0} - a_{\mathrm{Li},0})/a_{\mathrm{Li},0}$, using $a_{\mathrm{Na},0} = 4.19\,\text{Å}$. Here, we use as upper bound Young's modulus of lithium in isotropic approximation as $E = 13.8\,\mathrm{GPa}$ and a Poisson ratio of $\nu = 0.33$.

As derived in detail in [211] an analogous low-temperature Arrhenius behavior can be obtained from the generalized common tangent construction, which reads on the Li rich side

$$x \simeq \exp\left(-\frac{{}^{\mathrm{xs}}G_{\mathrm{m}}^{\Phi\,\prime}(x=0) + \Delta G_{\mathrm{el}}}{RT}\right) \tag{3.13}$$

with

$$\Delta G_{\mathrm{el}} = -\frac{E\chi^2\Omega_0 N_A}{N_0(1-\nu)}. \tag{3.14}$$

An analogous description can be obtained for the Na rich side. Results for the low-concentration regime for the coherent binodals both for the description [194] and the present one are shown in Figures 3.7 and 3.8. As expected, the coherent phase separation can occur only inside the chemical binodal regime, hence elastic effects increase the solubility limits. The reason is that elastic coherency contributions appear only in two phase configurations, which are therefore energetically less favorable. Similar to the above approach, also the coherent spinodals can be calculated [216]. It turns out that the description based on [194] leads to a critical temperature around 205 K, which is significantly below the eutectic temperature, contrary to the new assessment. Here, one has to keep in mind that rather an upper bound for the elastic effects has been calculated. Also, the non-ideal Gibbs energy contribution (3.3) is optimized to deliver

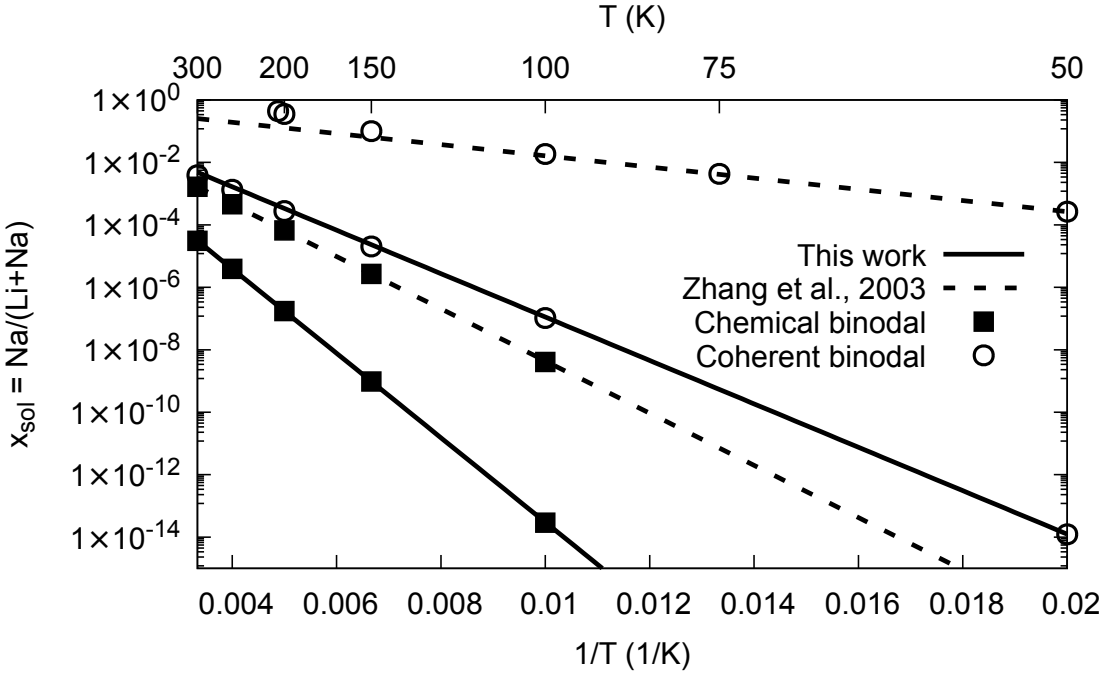

Figure 3.7: Chemical and coherent binodals on the Li rich side, calculated both with the previous model [194] and the present description. The solid straight lines correspond to the new description, the dashed lines to [194], using the low-concentration approximations. The exact solutions from the common tangent constructions are shown as symbols, where the squares correspond to the chemical binodal (without elastic effects), and the open circles to the coherent binodals.

reliable predictions in the dilute regime, and therefore the behavior near a possible critical point may not be captured well. All results can be combined, leading to the new phase diagram below the eutectic temperature, see Figure 3.9. The coherent phase diagram becomes very asymmetric, whereas the previous description leads to a symmetric phase diagram. Compared to the previous description, the Na solubility limit in Li is therefore reduced, whereas more Li is soluble in Na.

Relevance for Li-Na Anodes

Enabling lithium metal as electrode in all-solid-state batteries is a key step for enhanced energy density and safety. However, it is frequently reported that the limited self diffusion of Li and the morphological instability of the lithium metal anode restrict the rate capability of these cells. During lithium stripping, pore formation takes place at the interface due to the slow diffusion kinetics of vacancies in the lithium metal, see, e.g., [217]. These authors

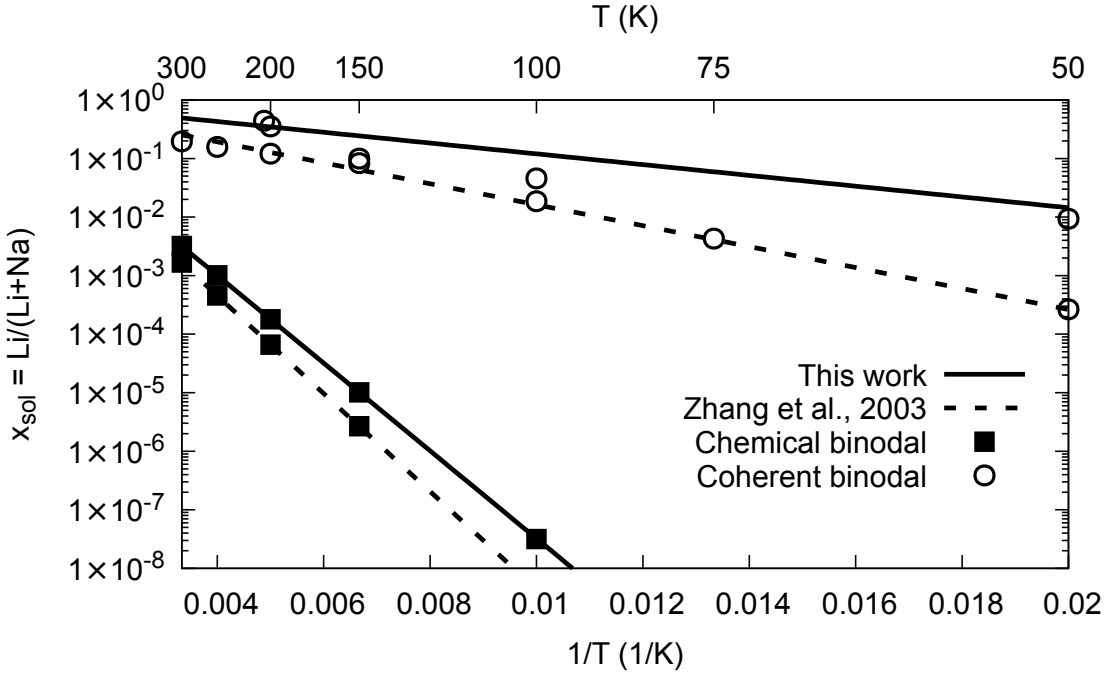

Figure 3.8: The same as Figure 3.7, but on the Na rich side. Notice that for the coherent binodals at higher temperatures the circles deviate slightly from the exponential asymptotic approximations.

report that alloying with Mg leads to stable solid solution phases which can stabilize the interface and lead to better performance.

Recently, a complementary approach was presented, which is based on the mechanical mixing with small amounts of sodium to lithium [104]. This approach differs strongly from the Mg alloying, as Li-Na are essentially immiscible at low temperatures, as discussed in the preceding sections. Therefore, phase separation is an immediate consequence of equilibrium thermodynamics. However, by alloying Li with 3at% Na via mechanical mixing, heating above the melting point and quenching to room temperature sufficiently fast, a metastable solid solution or fine dispersed structures emerge. Only during a formation step at the first cycles a 3D scaffold structure establishes, consisting of Li and Na rich regions, which form a complex three-dimensional network with characteristic pattern scale of the order 10 μm (see Figure 3.10). As there were no indications for the formation of such a microstructure already from the liquid state during quenching, the question of a possible mechanism for the origin of this pattern arises through a solid-state reaction. During the initial formation step, the Li concentration in the anode is reduced during stripping, and therefore the alloy is quenched isothermally deeper into the two

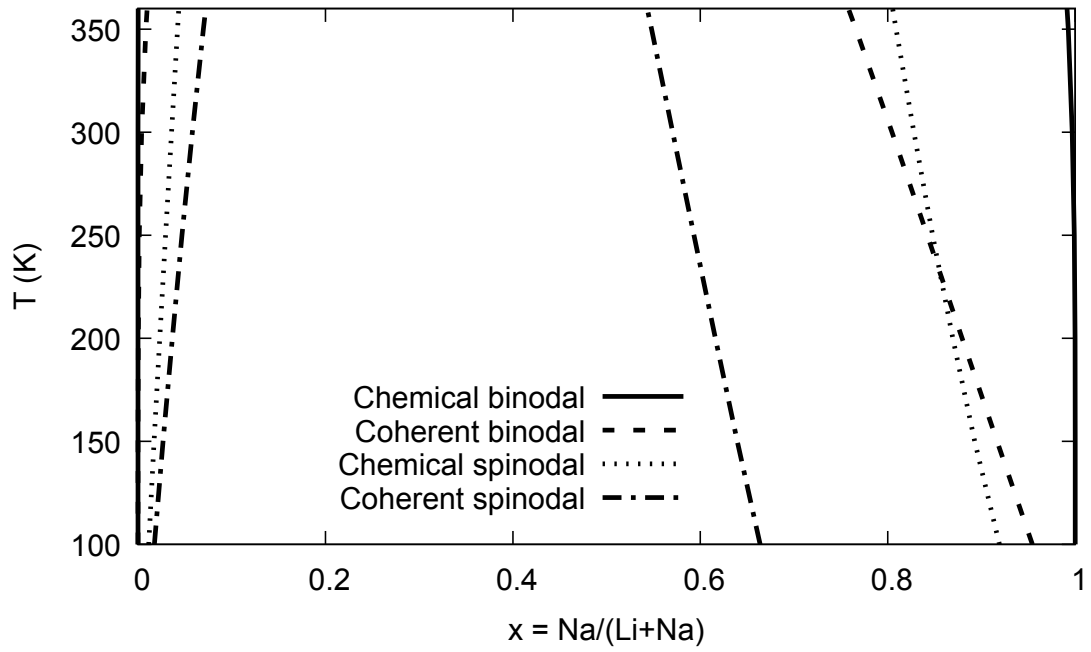

Figure 3.9: Phase diagram of the Li-Na system up to the eutectic temperature, according to the *ab initio* based description in this work. In particular on the Li rich side, the solubility limit is very low, hence the chemical binodal appears on this scale as a vertical line.

phase region. An appealing mechanism for the emergence of a Na rich phase would be by nucleation and growth. Nonetheless, inspection of the microstructure indicates that the scaffold structures are spatially rather uniform, whereas nucleation as a thermally activated random event and subsequent fast growth would rather suggest the emergence of irregular structures. Instead, the scaffold structure shows similarities to evolving structures from spinodal decomposition, which raises the question whether this barrierless transformation process may at least initiate or support the scaffold formation.

Due to the small amount of Na, the low-temperature eutectic point on the sodium rich side is only indirectly relevant, whereas the monotectic point on the Li rich side turns out to be an important feature for composition and process design. In a first step, Li and Na at the monotectic composition are mechanically mixed at room temperature. This mechanical mixing, which can be handled in advance in the sense of a industrial processing, is mainly intended as a pre-mixing step, whereas direct alloying would lead to immediate phase separation, which turns out to be less suitable [191]. Then, the temperature of the assembled symmetrical cell is raised above the monotectic temperature, such that a homogeneous Li-Na melt phase can form. Due to the mechanical mixing, the required

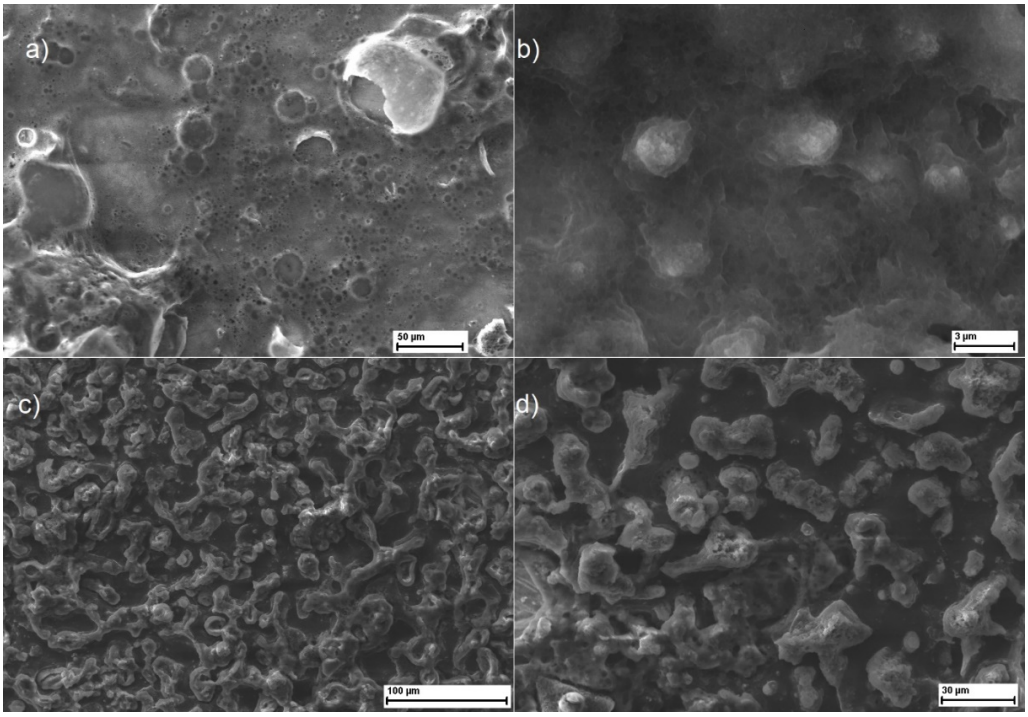

Figure 3.10: Four Scanning Electron Microscope (SEM) images at different magnifications of the remaining sodium structure after complete lithium stripping of one side of a symmetrical half-cell with Li-Na anodes and LLZO separator (a, b): LLZO surface, while (c, d): Ni current collector surface. Images originally from [104] and licensed under CC BY 4.0.

holding time for this homogenization is rather short. With the chosen composition, the melting temperature is minimized, and similarly it is avoided to bring the alloy neither into the low-concentration miscibility gap nor into the range of the monotectic demixing. As in both cases phase separation involving at least one liquid phase with fast diffusion would result, rather rapid microstructure formation would take place, e.g., by monotectic solidification [218]. This would be detrimental for the anode performance, and is indeed not observed [104]. We can indirectly conclude that through the choice of the monotectic composition and sufficiently fast quenching, the alloy is maintained in a metastable state with at most nanoscale sized precipitates.

This perspective is plausible from the description developed in the previous sections. Although at room temperature the solubility limit of Na (chemical binodal) is only around $x \approx 3 \cdot 10^{-5}$ and therefore below the nominal composition of 3 at%, spinodal decomposition sets in at around 3.6 at%. Coherency effects can further stabilize the metastable solid solution to a solubility limit of $x \approx 3.8 \cdot 10^{-3}$ with coherent spinodal decomposition

starting at 5.8 at%. During the formation step of the symmetric Li-Na/LLZO/Li-Na cell the sodium concentration is increased due to stripping of lithium, and the alloy definitely enters the spinodal regime, which can trigger the observed scaffold formation. Moreover, inside the electrode a concentration gradient emerges during stripping of lithium due to the finite diffusivity of Li. This explains the observation in Figure 3.10 that the Li-Na/LLZO interface consists essentially of Na only, as the lithium is depleted there. In contrast, the Li-Na alloy remains in the solid solution regime for a longer time near the current collector before phase separation is triggered, and therefore there a finer scaffold structure is observed.

We point out that spinodal decomposition alone will presumably not be able to entirely explain the scaffold formation due to kinetic reasons. The kinetics of this process are usually described by the Cahn-Hilliard equation, which is a fourth order equation, and is directly related to the original discrete treatment by Hillert [219]. It describes the initial rapid development of concentration fluctuations and the following phase separation into essentially depleted local equilibrium phases. After this initial growth regime, coarsening is driven by the reduction of interfacial energy. Quantitatively, the coarsening regime was investigated in [220]. The authors show that for a phase independent kinetic coefficient the coarsening is in line with classical Ostwald ripening [221, 222]. Hence, it shows a scaling of the characteristic length scale of the patterns as $R \sim (d_0 D t)^{1/3}$, as for interface controlled diffusion, the scaling obeys $R \sim t^{1/4}$. Using characteristic values for Li and Na diffusion coefficients, which are of the order $\sim 10^{-10}\,\mathrm{cm}^2/\mathrm{s}$ in the relevant temperature regime (from room temperature to $\sim 60\,^\circ\mathrm{C}$) and a capillary length d_0, which is typically on atomic scales, it leads even after extended times to patterns which are on the submicron scale and thus below the scaffold pattern size experimentally observed [104]. Consequently, we believe that an additional acceleration through the ionic transport during stripping will ultimately form these structures, which are possibly initiated by the spinodal instability. In turn, the slow curvature driven coarsening in absence of electrical fields implies that the self-organized scaffold structure is rather robust against curvature driven coarsening even on extended lifetimes of batteries.

3.1.3 Conclusions

We have calculated the phase stability of BCC Li and Na in the low-temperature regime, where both elements show only low mutual solubility. By performing *ab initio* simulations to calculate the formation energy, which is used together with a configurational entropy expression for predicting the low-temperature phase coexistence, we revisit the Li-Na phase diagram and improve the current description. An asymmetry in the non-ideal interaction term calls for the inclusion of higher order terms in the Redlich-Kister expan-

sion, therefore extending the work from [194]. Based on the new thermodynamics, we find a reduced solubility limit of Na in Li, compared to the previous study, which is in line with a theoretical Arrhenius description. Beyond phase stability, we also considered spinodal decomposition, which is expected to start at 3.6 at% at room temperature. The inclusion of mechanical coherency stresses rises the Na solubility limit and pushes the onset of coherent spinodal decomposition to higher Na concentrations (up to 5.8 at%). For all-solid-state batteries, we suggest that spinodal decomposition may trigger the formation of a scaffold microstructure in Li-Na anodes during Li stripping, when the Na content is effectively increased. However, spinodal decomposition alone will not fully explain the microstructure formation due to sluggish coarsening kinetics.

3.2 Carbonate Formation and Surface Effects

Besides the bulk microstructure formation at the Li-Na anodes, side reactions and phase formation of sodium rich compounds could also help to explain such low interface resistance of these cells, mainly at the early stages, before the phase separation takes place. A possible reason is that Na could react with any resistive impurities on the LLZO surface such as lithium oxides or carbonates, thereby helping to clean the interface and reducing the interface resistance. Moreover, Na remains electrochemically inert at the potentials applied during electrochemical cycling but provides electronic conductivity, which can provide a morphologically stable contact between the LLZO pellet, current collector and the metal anode [104].

In SSBs, it is thought that the presence of carbonates can negatively impact the cell performance [223]. For example, in oxide-based SSBs, the LLZO decomposes as LiOH and lithium carbonate - Li_2CO_3 (LC), and LC does not have a good affinity with Li metal [224]. In fact, researchers showed that the higher the degree of contamination on the LLZO, the higher the Li/LLZO interface resistance [224]. Therefore, finding a way of removing the LC from the interface or exchanging LC for a lithiophilic carbonate is detrimental to achieve high-energy-density cells.

In the work of Fu et al. [192], the authors hypothesized that Na served as a reagent to remove LC from the surface to create a carbonate free interface. However, the *ab initio* simulations performed in their work are not sufficiently convincing to confirm the hypothesis.

Both Li and Na are highly reactive metals. Lithium, for example, will not react with oxygen or carbon dioxide in air in the complete absence of water, but even trace amounts of moisture cause it to react with nitrogen, oxygen and carbon dioxide at room temperature. Therefore, even in the inert fluids in which it is stored, these metals react readily with traces of water, oxygen, carbon, nitrogen and hydrogen [225, 226].

Within this context, lithium-sodium carbonate - $LiNaCO_3$ (LNC) is a compound that still has not been in-depth investigated. The formation of LNC is indicated from a phase diagram upon the reaction of LC and sodium carbonate - Na_2CO_3 (NC) [227]. LNC has a low symmetry triclinic phase at room temperature (α phase) and a hexagonal phase at higher temperatures (β phase). The phase transition from the α phase to the β phase is indicated to happen at 175 °C. At 415 °C another phase transition occurs, but the hexagonal β phase to another hexagonal γ phase with different lattice parameters [228, 229].

The first simulation work on LNC was conducted by Ricca et al. [230] in 2016. The researchers investigated the structural, electronic and surface properties of LNC via *ab initio*. The bulk properties of α, β and γ phases were obtained. All three phases were found to be strong electronic insulators. In addition, the (001) and (110) surfaces of the γ phase were simulated. Since no experimental or theoretical surface study was previously available, the authors referred to the work of Bruno and Prencipe [231]. Bruno and Prencipe [231] modelled the most important terminations of LC, that being the (001), $(\bar{1}01)$ and (110) surfaces. The LC and LNC structures indeed show similarities. Therefore, to reduce computational effort, it was suggested to focus on these surfaces. Using the slab model, surface energy values were computed and reported.

Besides pure surface energy towards the vacuum, the affinity of, e.g., lithium towards the carbonate surface can be quantified via the adsorption energy. The attachment of particles to a surface is called adsorption. Molecules and atoms can attach to surfaces in two ways. The first way is called physisorption (or physical adsorption). In this case, there is a long range but weak van der Waals interaction. The energy released by physisorption is small and not sufficient to lead to bond breaking, so a physisorbed molecule retains its identity, although it might be distorted. The second way is via chemisorption (or chemical adsorption), in which the atoms stick to the surface by forming a stronger chemical bond. The enthalpy of chemisorption is much greater than that for physisorption, with the distance between the surface and the closest adsorbed atom being typically shorter. Chemisorption is always exothermic, with the spontaneous process requiring $\Delta G < 0$ [87].

Therefore, based on these works, we hypothesize that instead of leaving the surface, as proposed by [192], Na stays at the cell interface and consumes the LC, forming sodium rich compounds that can decrease the interface impedance. One of these compounds could be LNC. The presence of LNC was so far overlooked, as little is known about this carbonate. However, this might be a key aspect to improve the contact between Li-Na and LLZO. To investigate such hypothesis, we perform thermodynamic database calculations to assess the formation of new compounds, as well as *ab initio* simulations to determine their surface energy and affinity with Li and Na metals.

3.2.1 Methods

In order to determine possible reactions and compounds to be formed, we simulate via FactSage 8.1 the equilibrium conditions inside the glove-box. The commercial database SGPS and an internal database PCMJ are used [232]. The initial conditions inside the glove-box are assumed as:

- Ar (Vol.-%) = 99.999
- O_2 = 0.5 ppm
- N_2 = 5 ppm
- H_2O = 0.5 ppm
- CO_2 = 0.5 ppm

These conditions are realistic for the glove-box used in the experiments. The numbers are chosen based on the water and oxygen contents measured inside the glove-box and nitrogen and carbon contents from the argon specifications [233]. In total, 0.97 mol of Li and 0.03 mol of Na, together with the gases, are added to the equilibrium simulation. Fixed partial pressure of the gases is assumed.

Then, to investigate the surface energy and surface affinity of the new carbonate phase towards lithium and sodium, we perform *ab initio* simulations with the Vienna *Ab Initio* Simulation Package (VASP), which uses a plane wave basis set and the projector augmented wave (PAW) method [91, 142, 143]. The exchange-correlation energy is determined via the Perdew-Burke-Ernzerhof (PBE) generalized gradient approximation (GGA) using the harder pseudopotentials that include the valence states *s* for Li, *p* for Na and *2s* and *2p* for both O and C [144]. The electronic self-consistency loop has a global break condition of 10^{-6} eV. The ionic relaxation steps are performed until the norms of all the forces are smaller than 0.01 eV. First, the bulk structure of the α phase of the LNC is fully relaxed. Then, a slab with 3 layers and 4 unit cells is created from the (001) surface with a sufficiently large vacuum on top. According to [231], 3 slab layers are adequate to reach surface energy convergence. One layer is left with fixed atomic positions, while in the other two layers the atoms are free to relax. Given the high number of atoms, large cell sizes and low symmetry of the systems, the structure optimizations are run with 520 eV and 1 Gamma k-point.

Surface energy E_s of this (001) surface is calculated as

$$E_s = \frac{E_n - nE_{bulk}}{2A}, \tag{3.15}$$

where E_n is the total energy of the slab with n layers, E_{bulk} is the energy of the bulk system per unit cell and A is the area of the slab unit cell [230, 231, 234].

The adsorption energy E_{ads} is calculated as

$$E_{ads} = E_{surface+adsorbate} - E_{surface} - E_{adsorbate}, \tag{3.16}$$

where $E_{surface+adsorbate}$ is the total energy of the system after adsorption, $E_{surface}$ is the energy of the clean surface and $E_{adsorbate}$ is the energy of the isolated adsorbate. A negative E_{ads} value indicates an exothermic and stable adsorption process, while a positive value suggests the adsorption to be unfavorable. If the E_{ads} values are negatively small, it indicates the physisorption process. Whereas if the values are negatively large, it indicates the chemisorption process [87, 235]. Therefore, starting from the relaxed surface, we place additional Li and Na atoms in different sites, relax the system again with the same parameters as for the clean surface and calculate its adsorption energy.

To compare the behavior of LNC and LC (001) surfaces regarding lithium attraction, we perform static *ab initio* calculations without ionic relaxation, in which a single lithium atom is incrementally moved from the vacuum towards the surface in 1 Å steps. At each position, the total energy of the system is computed and the energy difference within the vacuum is calculated. This is repeated for various places within the surfaces.

3.2.2 Results and Discussions

We perform thermodynamic database simulations using FactSage 8.1, replicating the conditions inside the glovebox to predict the most stable compounds under realistic conditions. The results (Figure 3.11) indicate the formation of LC and LNC.

A different scenario can be suggested, which consists in assuming that LC is already present at the interface, which is realistic, as often the solid electrolyte or anode foil presents some level of contamination or passivation [223, 224]. In this case, the database also indicates the formation of LNC, similarly to Figure 3.11. Thus, it is highly likely that carbonates are found at the interface between solid electrolyte and metal anode and we can safely assume that the LNC carbonate phase is formed.

The α-LNC is then simulated using *ab initio* methods. The relaxed bulk structure and (001) surface slab model can be seen in Figure 3.12. On the surface structure, Li and Na atoms are placed on three different positions along the surface, as mapping the entire surface energy landscape would be extremely expensive, and the full structure is once more relaxed. These calculations are used to obtain the bulk, surface and adsorption energies according to Equations 3.15 and 3.16. The results are seen in Table 3.1.

The surface energy of the α phase of LNC has never been calculated before, which complicates the benchmark of the results. If we compare our data to numbers from

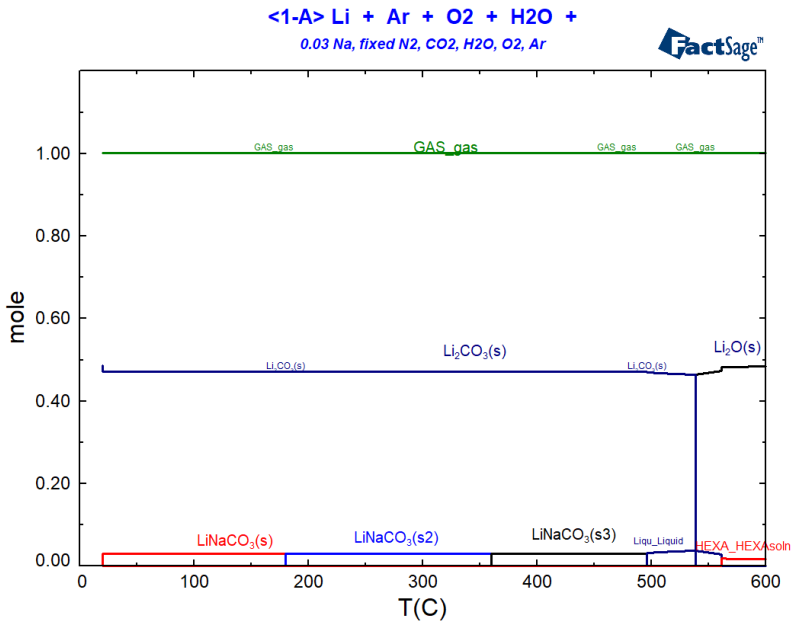

Figure 3.11: FactSage equilibrium simulation with fixed partial pressure of the gases. Results show the formation of lithium carbonate and lithium-sodium carbonate.

[230] on the (001) γ-LNC, which is approximately 0.5 J/m^2, and from [231] on the (001) LC, which is approximately 0.2 J/m^2, we see that the value hereby obtained is higher, indicating a higher wettability. Therefore, the α-LNC seems to have a more active surface that is more easily wet than the other structures investigated in the literature.

Concerning the adsorption energies, these values indicate a chemisorption process, whose typical numbers lie in the range of -200 kJ/mol [87]. The adsorption energy for lithium is higher than for sodium, suggesting that lithium has a higher affinity to the LNC surface than sodium. However, sodium also possesses a negative value of adsorption

Property	Value
Surface energy	1.231 J/m^2
Adsorption energy of Li	-487.06 kJ/mol
Adsorption energy of Na	-366.41 kJ/mol

Table 3.1: α-LNC (001) surface energy and adsorption energies against one lithium and one sodium atom. From the 3 surface positions scouted, the average value is reported for both Li and Na, as mapping the entire surface energy landscape is computationally expensive.

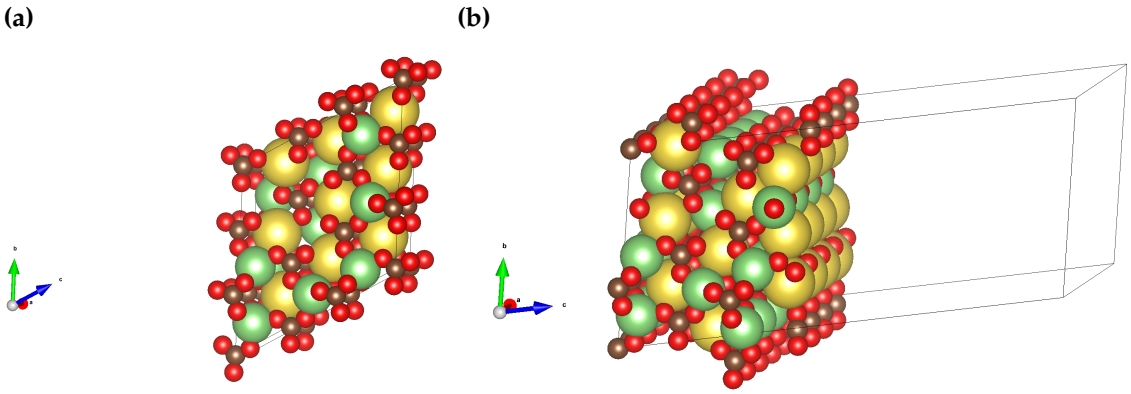

Figure 3.12: (a) Relaxed bulk LNC structure in its low symmetry triclinic α phase. **(b)** Relaxed (001) surface on a 3 layers slab model and 4 unit cells, in which one layer is left fixed during the relaxations, but the other two layers are free to move.

energy. This means that, although at lower levels than Li, Na is also attracted to the LNC surface. Hence, regarding the improved electrochemical performance of Li-Na metal anodes on LLZO separators from [104], it is possible that LNC is present at the cells interface, helping to promote a good interface contact of the LLZO and the metal anode.

To further investigate surface affinity, we perform static *ab initio* calculations without ionic relaxation, in which a single lithium atom is incrementally moved from the vacuum towards the surface in 1 Å steps. At each position, the total energy of the system is computed. This is repeated for various places within the surfaces. Figure 3.13 presents an exemplary energy difference as a function of the lithium atom's distance from the (001) surfaces of LNC and LC. In the case of LNC, the energy decreases as the lithium atom approaches the surface, indicating an attractive interaction. On the other hand, the energy increases near the LC surface, revealing a repulsive interaction. This suggests that the LNC surface is more favorable for lithium adsorption compared to LC. As discussed, the repulsion of lithium from the LC surface had already been indicated in previous works [223, 224].

Therefore, we can infer that LNC has the potential to replace LC as a lithiophilic passivation layer, as this structure has a better affinity with lithium metal. This proposal could promote the protection of lithium foils, as well as the improvement of the interface contact in solid-state batteries.

3.2.3 Conclusions

Here we investigate the surface energy and affinity of the (001) α phase LNC against lithium and sodium metals via theoretical methods. Our results suggest that this carbonate

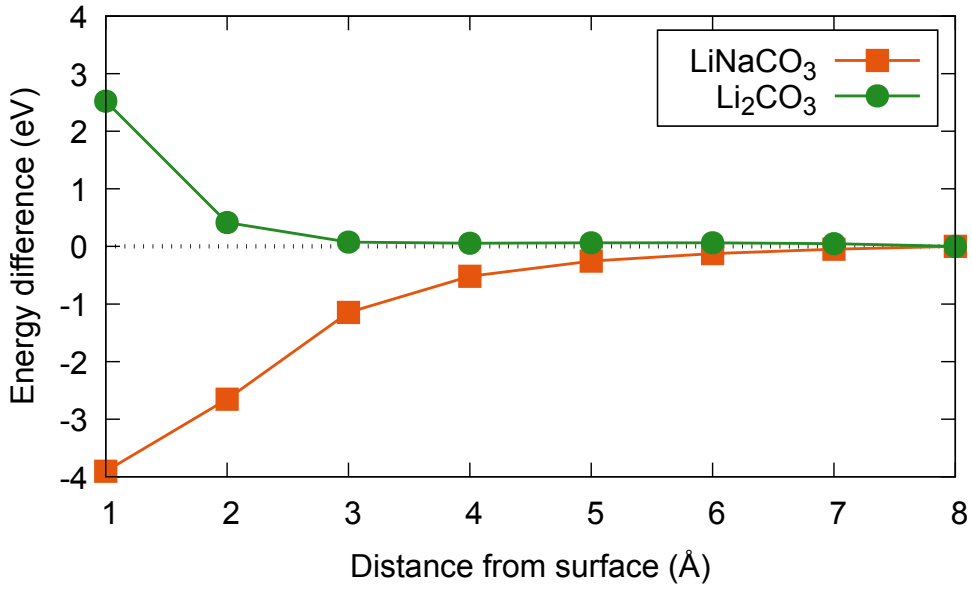

Figure 3.13: An exemplary energy profile showing the interaction between a single lithium atom and the (001) surfaces of lithium sodium carbonate ($LiNaCO_3$, LNC) and lithium carbonate (Li_2CO_3, LC). The energy difference is plotted as a function of the lithium atom's distance from the surface with 1 Å resolution, indicating an attraction to LNC and a repulsion to LC.

possesses an active surface with high wettability properties. Besides, both lithium and sodium seem to be attracted to the surface, outputting high negative values of adsorption energies. Therefore, we suggest that LNC could potentially replace LC as a lithiophilic passivation layer on solid-state batteries. This proposal would not only protect the lithium foils, but also decrease the interface impedance of assembled cells.

Regarding the improved performance of Li-Na metal anodes on LLZO separators observed in [104], it is possible that both hypothesis investigated in this chapter are partly true and work together to generate the good electrochemical results. The combination of surface-cleaning properties of the Na metal with the formation of a 3D Na microstructure enhances the cell performance. A small content of sodium would be enough to react with the LC present at the setup, for example at the grain boundaries of the LLZO, form the LNC and decrease the interface impedance. The remaining sodium would phase separate from the lithium to create the scaffold microstructure observed, process likely triggered by the spinodal instability. The LNC and scaffold microstructure provide sufficient interfacial contact between the cell components, even when the anode is completely stripped of Li. Furthermore, the 3D Na structure could distribute electrons and ions evenly and serve as

nucleation site, likely increasing the surface area and surface diffusion.

Chapter 4

Quantum Annealing for Mechanics, Microstructures and Interfaces

A critical challenge in modeling lithium mechanics (chapter 2) is predicting their long-term deformation behavior and microstructure evolution under near-equilibrium conditions. Classical Molecular Dynamics (MD) struggles with these timescales, while continuum methods often lack the atomic-scale resolution needed to capture crystallographic details. In particular, deformation twinning in BCC metals has so far been overlooked. Meanwhile, atomistic simulations with complex structures and large number of atoms (chapter 3) suffer from a slow optimization of lattice positions. Often, an extremely high number of repeated, expensive simulations is needed to get a full description of the system. Surface simulations are specially sluggish in this regard. Novel Quantum Annealing (QA) models can substantially support closing these gaps.

QA has been used to optimize ionic configurations in battery materials [36] and high entropy alloys [78], laying a foundation for fast lattice equilibration in complex systems. This application of QA is promising, as it could dramatically accelerate simulations that seek the lowest energy lattice configuration. On the microstructure side, Sandt et al. [62] succeeded to map shear transformations to a QA formulation. This approach builds on earlier works from [236–239]. In an additional publication, Sandt et al. [35] extended the shear description to obtain the equilibrium microstructure of the lithium lanthanum zirconium oxide - $Li_7La_3Zr_2O_{12}$ (LLZO), demonstrating how to include interfacial effects into the QA approach. Although this conceptual progress demonstrates well the benefits of quantum annealing for microstructure modeling, the chosen example was limited in particular by the restriction to just two variants, whereas, e.g., typical materials microstructures posses many more variants [240–243].

We focus here on the microstructure question, by developing a continuum approach solvable via QA, which reformulates the mechanical energy minimization as an Ising Hamiltonian and predicts equilibrium microstructures. Our approach builds on previous work of Sandt et al. [62]. We adapt their QA framework to BCC Li twinning, describing the phenomenon in terms of shear transformations and interfacial energies, leveraging crystallographic theory of twinning (chapter 2) and linear elasticity with interfacial energy contributions (introduced in chapter 1). The fundamental concept of our approach treats

mechanical twinning as a coherent phase transformation, where the twinned region exhibits a characteristic stress-free strain that mirrors the original crystal lattice. This description allows us to frame the prediction of equilibrium twinned microstructures as a mechanical energy minimization problem, transforming continuum mechanics into a discrete optimization task solvable via the quantum annealer.

The BCC twinning formulation is explored in subsection 4.1. However, for realistic microstructural predictions, not only two but often various possibilities must be considered, e.g., multiple twin systems, phases or grain variants. Thus, we show how to include tetragonal transformations in the previous shear-only approach, and generalize the microstructural equilibrium problem to a multi-variant description (subsection 4.2).

The content of the subsection 4.1 is published in [244], and the content of the subsection 4.2 is published in [245].

4.1 Deformation Twinning in Lithium Metal

BCC metals primarily deform either by dislocation motion or by deformation twinning, depending on the conditions (see, e.g., Table 2.3). We have explored the BCC, in particular lithium, mechanics in chapter 2 in detail. This topic is relevant and has remained as a widely studied field persisting until these days [155, 165, 169, 170, 173, 176, 246–248]. In close-packed metallic structures, deformation twins are well understood and have been extensively used to design materials with exceptional mechanical properties [249–251]. However, in BCC metals, deformation twinning endures as an elusive and intricate phenomenon [170, 173]. Achieving a deeper insight into the twinning mechanisms in BCC structures, as well as simulating it in larger scales, could open up new possibilities to enhance these materials' performance, applicability and understanding.

Not only deformation twins, but also growth and annealing twins can occur within metals [170, 252]. Growth twins are formed far from equilibrium mostly during initial crystal growth [170]. Annealing twins happen during recrystallization of previously deformed metals, and there is no deformation associated with their formation. Instead, they occur as a result of minimization of interfacial energy and grow diffusionally [253, 254]. On the other hand, deformation twins minimize elastic strain energy and there is a clear deformation associated to their formation. Deformation twins occur as a result of a large deformation of a single grain and have a lenticular morphology, since the small thickness to length ratio minimizes the long-range elastic strain [253].

As discussed in subsection 2.1.3, deformation twinning in BCC metals occurs by shearing the crystal on $\{112\}$ planes along the $\langle 111 \rangle$ directions, and it is associated with a twinning / anti-twinning anisotropy [169]. In BCC transition metals, such as α-iron and niobium, deformation twinning has been studied frequently [155, 171–175]. However, in

BCC alkali metals, such as lithium and sodium, the deformation behavior is still largely under-reported due to the difficult handling. Nevertheless, with the advance of solid-state batteries and the prospect of using full metal anodes, specific knowledge about these materials became a necessity [48, 139]. While it is reasonable to infer that the alkali metals exhibit similar characteristics as the other BCC structures, direct confirmation is necessary to assert it definitively. Recently, Molecular Statics simulations of all BCC metals showed that deformation twinning in the alkali metalss indeed occurs only on $\{112\}$ planes, but with a lower likelihood of anti-twin formation compared to the transition metals [169].

Generally, atomistic simulations contain a relatively small number of atoms and single crystals setups, since the simulation of large-scale and polycrystalline samples is computationally demanding via these methods. To address twinning in polycrystalline materials, continuum-based modeling approaches (see, e.g., [255]) and phase-field models (see, e.g., [256]) have been developed. Despite their differences in scale and methodology, these approaches have a common goal to predict the dynamics of the system, either based on interatomic potentials or crystal plasticity slip laws [169, 255]. Thus, a relaxation to the equilibrated twin structures may require extended simulation times, which typically exceed the capabilities of atomistic simulations.

Here, we propose an alternative continuum picture, which directly determines the ground state configuration of the system under mechanical loads. Our approach minimizes the mechanical energy with respect to both the elastic degrees of freedom (i.e., displacements) and the evolving twinning microstructure, aligning with the fundamental definition of deformation twinning [253]. In this way, the description neither relies on empirical interatomic potentials nor on constitutive kinematic relations. Instead, it can be considered as a minimum model, based just on well established concepts of elasticity and crystallography. In addition, twin interface energies are incorporated into the formulation. The elastic deformations are handled conventionally using classical computing. However, at each material point, an additional discrete variable is introduced to represent whether this region belongs to a twin or to the matrix. In this way, the direct determination of twin distributions becomes a hard combinatorial problem, as one needs to calculate the total energy of all possible arrangements of twins. This is the point at which quantum annealing gives a substantial benefit and efficiently optimizes the total energy of the system. The model is built on our previous work on shear transformations, where we have mapped the spatial arrangement of martensite variants to an Ising Hamiltonian, which is efficiently minimized using quantum annealing [35, 62]. As the quantum annealing simulations are extremely fast, the ground state configuration is obtained very quickly, as compared to the aforementioned modeling approaches, offering new opportunities for simulating deformation twinning.

4.1.1 Methods

We pursue a continuum description of deformation twin formation, to extend atomistic descriptions to larger scales using well established concepts only. The description is based on linear elasticity. For simplicity, we use a reduced two-dimensional description assuming a plane strain setup, i.e., all deformations reside in-plane, which will be justified later. Furthermore, we use isotropic elasticity, to keep the number of parameters small, but most of the presented concepts work equally for anisotropic systems. The formation of twins is expressed through a local stress free strain or eigenstrain, ϵ^{twin}. For a given twin distribution inside the material, the elastic (free) energy is an extension of Equation 1.3 given as

$$F_{\text{el}} = \int dV \left(\frac{1}{2}\lambda(\epsilon_{kk} - \epsilon_{kk}^{\text{twin}})^2 + \mu(\epsilon_{ik} - \epsilon_{ik}^{\text{twin}})^2 \right), \tag{4.1}$$

where the integration is performed over the volume V of the sample; μ and λ are shear modulus and Lamé coefficient, respectively. The strains are derived from the displacement field components u_i as in Equations 1.1 and 1.2. Mechanical equilibrium is obtained, for a given twin eigenstrain, through the minimization of the elastic energy with respect to displacements,

$$\frac{\delta F_{\text{el}}}{\delta u_i} = 0, \tag{4.2}$$

which is performed here using Fourier transformation approaches (Khachaturyan method) [257]. The Khachaturyan method is based on a continuum description of linear elasticity and employs Fourier spectral techniques to solve mechanical equilibrium equations under periodic boundary conditions. The Fourier approach transforms field variables into reciprocal space, where spatial derivatives become algebraic operations. This enables efficient and highly accurate solutions for periodic microstructures, making it suited for simulating materials with internal eigenstrains [257].

In addition to the elastic solver, we use the QA approach, which determines the equilibrium deformation state and finds the energetically most favorable distribution of twins in the entire system of investigation. Therefore, we discretize the system into small domains. This tesselation can be done through a regular lattice as well as irregular regions, as discussed in [62]. We point out that the size of these domains does not have to coincide with an underlying grid or mesh size for solving the elastic problem. In fact, we usually use far less of these domains than grid points for the elastic solver. We assign to each of these domains a discrete indicator ("spin") s_i, where $s_i = -1$ corresponds to the original crystal (not twinned) and $s_i = +1$ to a domain after twinning. In analogy to [62], the elastic energy can then be exactly expressed as Ising Hamiltonian in the framework of

linear elasticity,

$$E(\{s_\nu\}) = E_0 + \sum_{\nu=1}^{N_\nu} \tilde{H}_\nu s_\nu + \sum_{\nu,\eta=1}^{N_\nu} \tilde{J}_{\nu\eta} s_\nu s_\eta, \tag{4.3}$$

with a quadratic, symmetric matrix $\tilde{J}_{\nu\eta}$. The coefficients E_0, $\tilde{H}_\nu$ and $\tilde{J}_{\nu\eta}$ can be expressed directly in terms of the Fourier transformation solution, or alternatively be calculated using any elastic solver, which delivers the total elastic energy $E(\{s_\nu\})$ for a given spin configuration $\{s_\nu\}$. In other words, for a given microstructure (i.e., knowledge of the spin states of all domains), the elastic energy consists of terms which are linear in the spin value plus additionally pairwise spin-spin interactions between the domains only. The interactions between domains are long-ranged, and therefore the ground state of such a spin glass Hamiltonian is nontrivial. It turns out that the interaction coefficients have to be calculated with very high accuracy to obtain the correct equilibrium microstructure. In particular, the introduction of a cutoff for the range of the interactions is not recommended [62].

Therefore, we obtain the reference state when all domains are not twinned. Next, we perform calculations where all spins but one flips to being twinned. From that, we can extract the self energies. Finally, to calculate the interaction coefficients, we perform elastic calculations with two twinned spins $s_i = s_j = 1$ and we determined the pairwise interactions. To run the QA calculations, we use the D-Wave Quantum Annealer Advantage^{TM} system.

For benchmarking, we use as reference the Li nanopillar MD simulations carried out in subsection 2.1.3. Here we focus on single crystals with the orientation $[001]$ parallel to the loading direction tested in tension. For the technical details on the MD simulations, we refer to subsection 2.1.3.

4.1.2 Results and Discussions

Crystallography and Elasticity

According to the crystallographic definition [258], a twin is an intergrowth of two or more individuals of the same crystal species with a well-defined crystallographic orientation relationship. This orientation relationship is given by the twin law, which comprises the set of symmetry operations and elements that transform the lattice of one individual into the lattice of the other one. The individuals that form the twin are called twin components or domains, while their individual orientation corresponds to one out of two orientation states. The contact plane between two individuals is called twin interface or domain boundary. Although the term domain is commonly used describing twins composed of lamellar twin components, we rather use the term twin component in order to avoid

confusion with the discretization domains used for the QA description. It should be noted, however, that a discretization domain corresponds to the smallest possible twin component. Furthermore, in the literature on metallurgy and especially in studies of deformation twinning, the term "twin" is ascribed to twin components formed by the deformation twinning, while the part of the grain that remains in its original orientation state is designated "matrix", see the examples presented in [170]. In this work we refer to twin components characterized by their respective orientation state — transformed or original —, as the size or volume fraction of the transformed twin components may exceed that of twin components with the original orientation state.

In the case of the BCC crystal structure, the commonly observed twin interfaces are the $\{112\}$ planes [169, 170], and the orientation states of adjacent twin components are related by a reflection on this plane. The corresponding twin law is the so-called *spinel law*, which is associated with a $\Sigma = 3$ coincidence site lattice; i.e., the twin interfaces are $\Sigma 3$ boundaries.

To express the transformation strain through the twinning, we consider twinning on a (112) plane specifically and introduce a local coordinate system spanned by orthogonal unit vectors $\hat{x}' \parallel [\bar{1}\bar{1}1]$, $\hat{y}' \parallel [1\bar{1}0]$ and $\hat{z}' \parallel [112]$. Here, $\hat{y}'$ is the in plane direction of translational invariance in the sense of a plane strain description, while $\hat{x}'$ is the twinning direction and $\hat{z}'$ the twin interface normal, as indicated in Figure 4.1. All Miller indices designating crystallographic planes or directions refer to the original orientation state unless stated otherwise. The BCC crystal structure can be built by stacking layers of atoms situated on (112) planes (dashed lines in Figure 4.1). Each layer is shifted relative to the previous one by $a/(2\sqrt{3})$ along $[\bar{1}\bar{1}1]$, with a being the lattice constant. The stacking sequence repeats every six layers ($\ldots ABCDEF \ldots$ stacking sequence, note that the atoms on every second layer are located above/below the projection plane). Twinning can then be described by additional shifts of the (112) planes by $a/(2\sqrt{3})$ for the first layer (green arrow), $2 \times a/(2\sqrt{3})$ for the second layer (twice the green arrow), etc., such that the stacking sequence is reversed (into $\ldots FEDCBA \ldots$) and the upper part of the crystal becomes mirror symmetric to the lower one. Anti-twinning, which will not be considered in this study, could be described by additional shifts of the (112) planes by $-a/\sqrt{3}$ for the first layer, $-2 \times a/\sqrt{3}$ for the second layer, etc., resulting in the same atomic arrangement as twinning. Deformation twinning of the crystal can therefore be understood as a shear of the original lattice, as illustrated by the transition from the solid to the dashed blue rectangle in Figure 4.1. With the lateral shift by $\Delta u_{x'} = a/2\sqrt{3}$ per interplanar distance $\Delta z' = a/\sqrt{6}$, the shear strain therefore becomes in the rotated reference frame

$$\epsilon^{\text{twin}}_{x'z'} = \frac{1}{2}\left(\frac{\partial u_{x'}}{\partial z'} + \frac{\partial u_{z'}}{\partial x'}\right) = \frac{1}{2\sqrt{2}}. \tag{4.4}$$

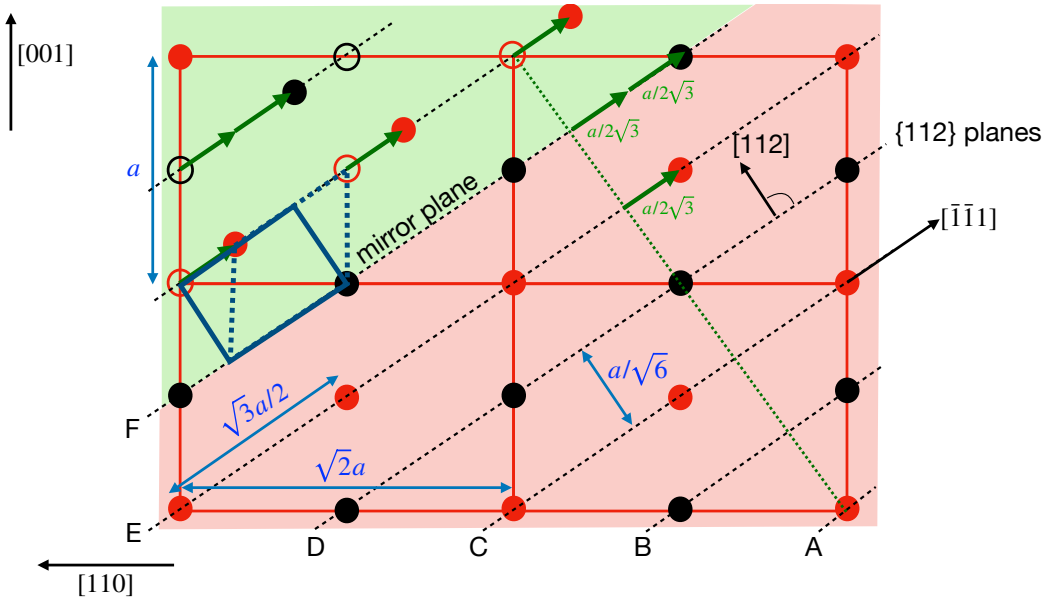

Figure 4.1: Projection of the crystal structure of a twinned BCC crystal with lattice constant a onto the $(1\bar{1}0)$ plane. Black and red circles represent atoms that are on or above/below the projection plane, respectively. The red region corresponds to the original lattice (original orientation state), whereas the green region goes through the shear transformation (resulting in the transformed orientation state). The twin interface is a (112) plane, which is at the same time a twin mirror plane. The blue solid rectangle is sheared to the dashed one upon twinning. In the green region, the hollow circles mark the original positions of the atoms, and the full circles mark the new positions of atoms after twin formation. $ABCDEF$ refers to the stacking sequence, which is reversed by the twin transformation.

For an orthonormal, right handed basis set $B' = \{\hat{x}', \hat{y}', \hat{z}'\}$, the symmetric twin eigenstrain tensor therefore becomes

$$\epsilon^{\text{twin}'} = \begin{pmatrix} 0 & 0 & 1/(2\sqrt{2}) \\ 0 & 0 & 0 \\ 1/(2\sqrt{2}) & 0 & 0 \end{pmatrix} = {}_{B'}[\epsilon^{\text{twin}}]_{B'}. \tag{4.5}$$

In particular, the direction $\hat{y}'$ remains invariant under the transformation.

Whereas a local analysis of the twinning process is easier in this rotated reference frame, for an inspection from the laboratory system a transformation to a basis set $B = \{\hat{x}, \hat{y}, \hat{z}\}$ is desirable, using unit vectors $\hat{x} \parallel [\bar{1}\bar{1}0]$, $\hat{y} \parallel \hat{y}' \parallel [1\bar{1}0]$ and $\hat{z} \parallel [001]$. We note that we keep the 45° rotation in the xy plane relative to the conventional basis vectors, as this allows to

keep a reduction to a two-dimensional (xz) plane strain description.

With these definitions, we have

$$\hat{x}' = \frac{1}{\sqrt{3}} \begin{pmatrix} -1 \\ -1 \\ 1 \end{pmatrix} = \sqrt{\frac{2}{3}}\hat{x} + \frac{1}{\sqrt{3}}\hat{z}, \tag{4.6}$$

$$\hat{z}' = \frac{1}{\sqrt{6}} \begin{pmatrix} 1 \\ 1 \\ 2 \end{pmatrix} = -\frac{1}{\sqrt{3}}\hat{x} + \sqrt{\frac{2}{3}}\hat{z}. \tag{4.7}$$

Therefore, the coordinate transformation matrix from basis set B to B' is given by

$${}_B[\mathrm{id}]_{B'} = \begin{pmatrix} \sqrt{2/3} & 0 & -\frac{1}{\sqrt{3}} \\ 0 & 1 & 0 \\ \frac{1}{\sqrt{3}} & 0 & \sqrt{2/3} \end{pmatrix}, \tag{4.8}$$

which maps the unit vectors from set B to B'. In the laboratory frame B the twin transformation strain tensor becomes

$${}_B[\epsilon^{\mathrm{twin}}]_B = {}_B[\mathrm{id}]_{B'}\, {}_{B'}[\epsilon^{\mathrm{twin}}]_{B'}\, {}_{B'}[\mathrm{id}]_B{}^{\dagger} \tag{4.9}$$

$$= \begin{pmatrix} -1/3 & 0 & 1/(6\sqrt{2}) \\ 0 & 0 & 0 \\ 1/(6\sqrt{2}) & 0 & 1/3 \end{pmatrix}. \tag{4.10}$$

We focus here only this single BCC twinning system, but the generalization to more systems is possible. From point of view of continuum elasticity, the microstructure is therefore defined by the knowledge of whether at any given location the crystal has undergone the shear transformation, leading to either an eigenstrain 0 (reference state indicating the original lattice orientation, i.e., a twin component with original orientation state) or a finite eigenstrain ϵ^{twin} (indicating the lattice after the shear transformation, i.e., a twin component with transformed orientation state). In conjunction with given boundary conditions, i.e., typically given strain or given stress, the problem is then well-posed in the framework of linear elasticity. We can in particular determine for a given microstructure the displacements, strains and stresses everywhere, as well as the stored elastic energy in the system. We use Fourier transformation methods for solving the elastic problem (Khachaturyan method), which assumes periodic conditions. Alternatively, other solving procedures can be used like FEM, provided that the elastic energy is obtained with very high accuracy.

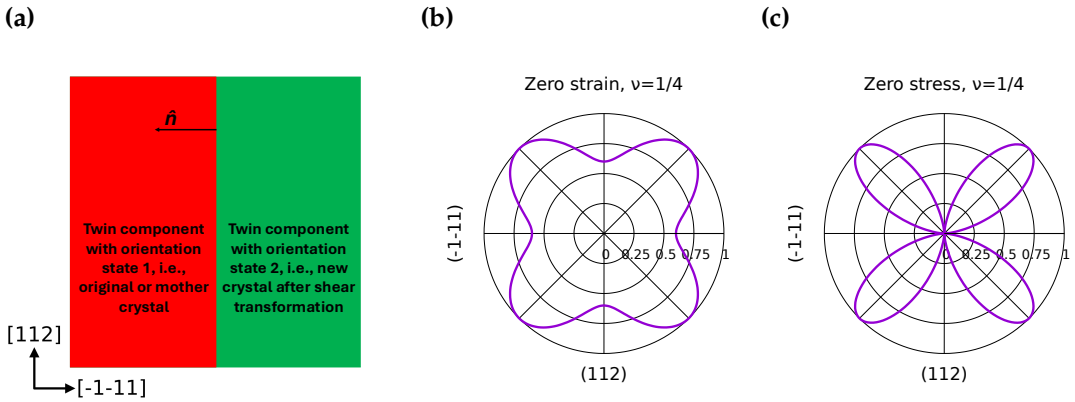

Figure 4.2: (a) Sketch of the twinned geometry, using periodic boundary conditions. The local coordinate system indicates the rotation of the crystal, $\hat{n}$ is the interface normal direction, as used in the subsequent polar plots. (b) Polar plot of the normalized elastic bulk energy for vanishing external strain, $\langle \epsilon_{ij} \rangle = 0$, with indicated normal directions of the twin interface. (c) The same for zero average stress, $\langle \sigma_{ij} \rangle = 0$. In both cases the Poisson ratio is chosen as $\nu = 1/4$.

For the purpose of illustration, we use a two-dimensional plane setup. This is legitimate if the out-of-plane direction coincides with the $\hat{y}'$ direction, as according to the transformation strain no deformation is induced in this direction for suitable boundary conditions. In the used isotropic approximation, the Young's modulus scales out of the description, and only a weak dependence on the Poisson ratio remains, which it is not critical here.

Twin Interface Orientations

The above formulation allows for a continuum description of twinned structures, as the orientation states of their twin components differ only by the eigenstrain expressions, with a coherent interface in between them. To understand the role of the elastic energy on the twin interface, we set up an array of straight lamellae using a periodic setup, as sketched in Figure 4.2a. For determining the lowest energy configuration with a planar interface between these regions, it is sufficient to calculate the elastic energy in a system consisting of two equally sized layers, and vary their crystallographic orientation. The following results are obtained from an isotropic elasticity calculation using a Poisson ratio of $\nu = 1/4$.

Figure 4.2a sketches the setup of the calculations, where the twin components have the same volume fractions. Both parts of the crystal initiate from the same crystallographic

orientation, and the twin eigenstrain shear tensor is applied to half of the setup. With the use of periodic boundary conditions, the system consists of a stripe pattern with alternating sheared (transformed) and not sheared (original) regions, i.e., a twinned crystal with lamellar twin components. Then, the entire crystal structure is rotated (rotation axis $[1\bar{1}0]$) while keeping the interface vertically, so that the energy of different interfaces can be calculated. We note that in the absence of external stresses or strains this approach is equivalent to keeping the lattice orientations fixed, but rotating the interface normal of the dividing plane between the original and shear regions.

Figures 4.2b and c show the elastic energy of the system for both zero average strain and stress boundary conditions in polar representation. In the polar plots, the normal orientation of the interface is shown relative to the lattice orientation, as defined in Figure 4.2a. The energy is always scaled to the maximum value, which depends on the chosen boundary condition. Obviously, these two cases differ significantly, as for the stress free case the elastic energy is cusped, as further discussed below.

In both cases, the energy reaches its minimum in particular for (112) interface orientations, hence the continuum description – which is ignorant of the underlying crystallography – correctly captures the expectation that (112) is a favorable interface orientation. However, a second spurious preferred interface orientation appears, $(\bar{1}\bar{1}1)$, which is not a twin interface from a crystallographic perspective. We must emphasize that up to this point only bulk elasticity for coherent interfaces is taken into account, but other possible energy contributions, such as interfacial energies, are neglected so far. As a consequence, pure elasticity is not sufficient to select the desired (112) orientation, as rotations of the crystal by 90° also lead to such preferred orientations. This effect is discussed in more detail in the next subsection.

We point out that this effect, which may seem at a first glance as an artifact of the chosen description, should appear similarly in phase-field models of twin formation, which use a corresponding elastic energy based description using eigenstrains for the twin formation [256, 259]. For instance, in [259], an anisotropic interfacial energy, which is much lower for the twin interface than for other grain boundaries, is used. Therefore, also here it is important to include an interfacial contribution which gives preference to the expected twin interface.

From the bulk elastic perspective alone, for the zero stress boundary conditions, internal coherency stresses do not arise if the interfaces are oriented such that a pure shear arises in the tranformed twin components (as expressed through the eigenstrain tensor (4.5)), as then the original twin component is not deformed. This is the case if the interface between the two components coincides with either the (112) or $(\bar{1}\bar{1}1)$ planes. For other orientations tangential stresses appear at the interface due to the rotation of the eigenstrain tensor, and then the elastic energy is increased. We note that in both cases, zero

external strain and stress, the elastic energy of a single, non-twinned crystal is zero, and therefore twinning always increases the energy in here, apart from the specific orientations mentioned above for the stress-free case. Consequently, twinning is expected to appear only under the presence of an external shear load.

As a consequence, pure elasticity is not sufficient to select the desired (112) orientations, as rotations of the crystal by 90° also lead to such preferred orientations, although they do not correspond to twin interfaces from a crystallographic perspective.

Elastically Preferred Interface Orientations

To make the four fold symmetry of the elastic energy more transparent, we first consider a (112) twin interface. There, the half of the grain undergoes a shear transformation with strain $\epsilon^{\text{twin}}_{x'z'} = 1/2\sqrt{2}$, whereas the diagonal components vanish. This transformation is sketched in Figure 4.3.

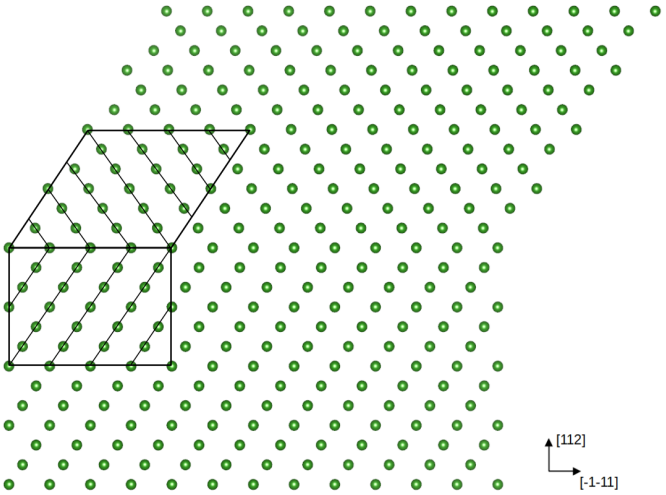

Figure 4.3: Crystallographic visualization of the expected twin system with (112) interface generated by the shear transformation with a positive eigenstrain.

In the first step, both grains are assumed to have the same crystal orientation. Then, the twin operation takes place in half of the grain, which leads to a macroscopic shear transformation of the outer contour of the grain (depicted in the deformed, Eulerian frame). As the transformation strain is a pure shear, the common interface remains unaffected, and both grains are stress free, if a vanishing mean stress is assumed as macroscopic boundary condition, obviously minimizing the elastic energy. In particular, the interface remains a perfect twin from a crystallographic perspective.

Next, we consider the case that the crystal structure is rotated by 90°, corresponding to a $(\bar{1}\bar{1}1)$ interface (Figure 4.4). With the 90° lattice rotation the transformed eigenstrain

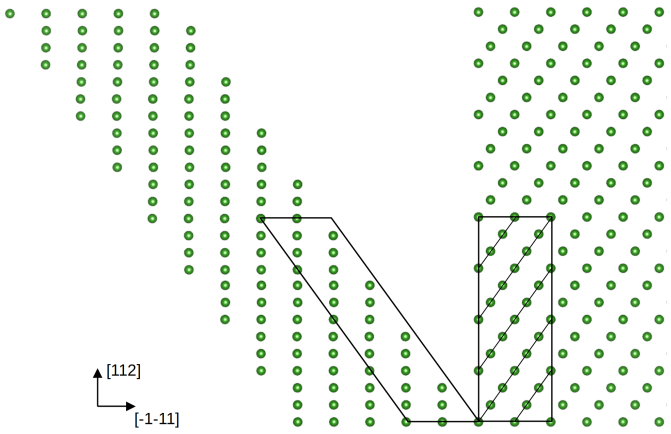

Figure 4.4: Crystallographic visualization of the unexpected $(\bar{1}\bar{1}1)$ interface generated by the shear transformation with a negative eigenstrain.

tensor becomes $\epsilon^{\text{twin}}_{x'z'} = -1/2\sqrt{2}$, and the diagonal components vanish, hence it still reflects a shear transformation, but this time with opposite orientation. However, this shear operation — applied in the sense of moving layers parallel (112) along $[11\bar{1}]$ — leads to disconnected twin components. Notably, this discontinuity is not compatible with a coherent interface, as an additional (non strain inducing) rigid body rotation is required to re-establish contact between the grains. Again, both grains are then in a stress free state, which explains the vanishing elastic energy also for this cusp in the polar plot of Figure 4.2c.

However, from a crystallographic perspective, the 90° rotation would lead to a $(\bar{1}\bar{1}1)$ boundary which is not a twin interface, in agreement with common knowledge of deformation twinning in BCC. As this example demonstrates, continuum elasticity cannot be aware of this small scale effect. It should be emphasized that this not a deficit of the continuum description, which is intended to capture the behavior beyond atomic scales, and supports the need to penalize improper non-twin boundaries by a higher interfacial energy for capturing the crystallographic aspect. Still, on larger scales, when the original and transformed regions become wide, such that a bulk elastic energy dominates over interfacial contributions, $(\bar{1}\bar{1}1)$ interface configurations have a relatively low total energy.

For any other rotation angle of the crystal structure, the diagonal components of the eigenstrain are nontrivial, and therefore merging the two grains requires application of tensile or compressive tangential stresses, which increases the bulk elastic energy, therefore making these interfaces unfavorable also from a mechanical perspective.

In conclusion, it is worthwhile to mention the role of interface coherency. From a continuum mechanics perspective, we consider an interface with continuous normal and shear stresses as well as elastic displacements across the interface as coherent. However, this continuum description does not possess knowledge of the underlying crystal structure, and therefore such interfaces does typically not consist of twin boundaries but rather arbitrary grain boundaries. This analysis shows the limitations of continuum elasticity alone for describing the mechanical response of twin configurations, even though such approaches are also commonly used in, e.g., phase-field models [256, 259]. However, these limitations can be accounted for by introducing anisotropic interfacial energies as an additional part of the model that is based on crystallographic knowledge.

It should be noted, that the common twin interfaces in the face-centered cubic (FCC) structure are $\{111\}$ planes, and deformation twinning in FCC crystals involves shear of adjacent $\{111\}$ planes along $\langle 112\rangle$. The twinning eigenstrain tensor of the FCC structure is the same as the transformed eigenstrain tensor of the BCC structure (after the 90° rotation of the interface), $\epsilon^{\text{twin}}_{x'z'} = -1/2\sqrt{2}$, when the same coordinate system is used and twinning with $(\bar{1}\bar{1}1)_{\text{FCC}}$ twin interface is considered.

Interfacial energy

We use a simple approach for modeling the interfacial energy between domains. At these boundaries, we have a different spin value on both sides of the interface. Therefore, the approach is to use an additional energy contribution

$$H_s = \sum_{i<j} J_{ij} s_i s_j + H_0 = \sum_{i<j,\text{n.n.}} \sigma(\theta) A_{ij} \frac{1 - s_i s_j}{2} s_i s_j \tag{4.11}$$

with only quadratic interaction terms, with $\sigma(\theta)$ denoting an orientation dependent interaction energy and A_{ij} as area of the common interface between the domains. In the simplest case, only nearest neighbor interactions (n.n.) in horizontal ($\sigma(\theta = \pi) = \sigma_|$) and vertical direction ($\sigma(\theta = 0) = \sigma_-$) are considered, see Figure 4.5. We note that a horizontal nearest neighbor spin pair of different orientation corresponds to vertical interface, hence the subscript of the interfacial energy σ indicates the corresponding interface orientation. On the domain discretization level, inclined interfaces consist of steps (see Figure 4.5), which allows to calculate the effective macroscopic interfacial energy in large systems. In the case of equal values $\sigma_| = \sigma_-$, the energy for horizontal and vertical interfaces coincide, but the angular dependence shows a weak anisotropy, see left panel of Figure 4.6. Choosing σ_- and $\sigma_|$ differently allows to suppress the non-twin grain boundaries with $(\bar{1}\bar{1}1)$ orientation, see Figure 4.6 (center) for a case with $\sigma_| = 2\sigma_-$. Here, a vertical interface, which is assumed to coincide with the crystallographically undesired orientation, becomes

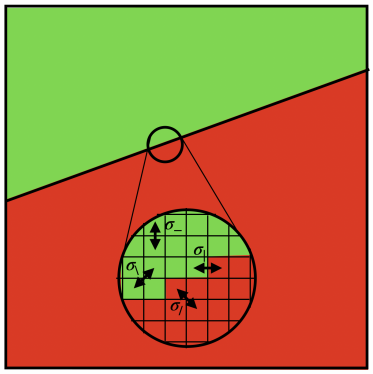

Figure 4.5: Sketch of the representation of interfaces through nearest neighbor interactions on the domain scale.

unfavorable. For the present simulations, we use this formulation of the anisotropic interfacial energy to exemplarily demonstrate the suppression of the undesired grain boundary and splitting of twins into smaller lamellae.

For polycrystalline simulations, where also the lattice orientations are rotated, the interfacial energy needs to be adjusted. The simplest case of a 90° rotation is reflected through the choice $\sigma_- = 2\sigma_|$ (Figure 4.6 center). For a rotation by $\pi/4$ we need to involve diagonal nearest neighbor interactions, $\sigma_/$ and $\sigma_\backslash$. In comparison to σ_- and $\sigma_|$ they need to be renormalized by $1/\sqrt{2}$ to account for the "staircase representation" of a tilted interface, and the increased number of diagonal interactions, to be equivalent to the non-rotated crystal (Figure 4.6 right panel). For arbitrary grain orientations we use here for simplicity the interfacial energy representation of one of the cases discussed above, which is closest in orientation. We note that more accurate expressions for the interfacial energy are possible and will be discussed separately.

Prediction of Twin Formation in Single Crystals Through Quantum Annealing

So far, we have used a given twinned microstructure with fixed sizes of the original and transformed twin components to investigate the agreement of the continuum description with crystallographic expectations concerning the selection of the preferred twin interface orientation. In this section, we add the quantum annealing framework for selecting the distribution of twin components based on the global minimization of the elastic energy. Therefore, we discretize the studied sample into small "domains", to which we assign one Ising spin variable $s_i = \pm 1$ each. We use here the convention that $s_i = -1$ and $s_i = +1$ correspond to the original and transformed orientation state of the respective domain.

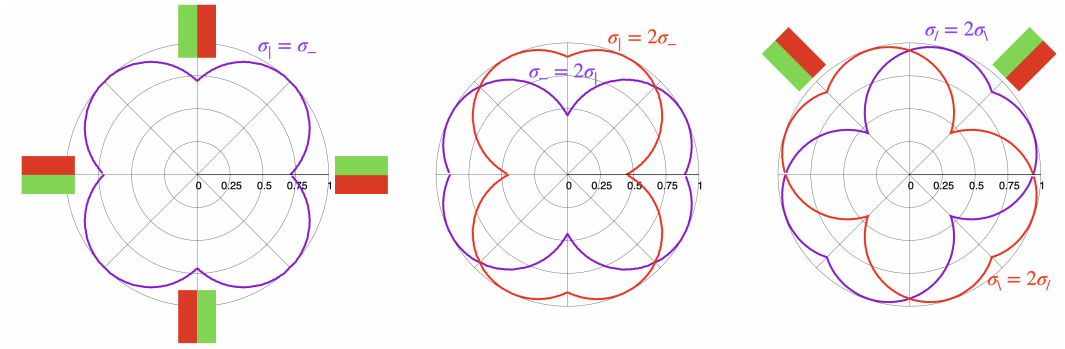

Figure 4.6: Orientation dependent interfacial energy. Left panel: Only horizontal and vertical nearest neighbor interactions are used, with equal magnitude ($\sigma_- = \sigma_|$). Center: The two values are chosen differently to enhance the anisotropy of the grain boundary energy, with the intention to suppress the crystallographically undesired $(\bar{1}\bar{1}1)$ interface orientation and the favor (112) twin boundaries. Right panel: Here, only diagonal nearest neighbor interactions are used, to reflect the interfacial energy anisotropy of crystals which are rotated by $\pm\pi/4$. In each figure, the values are scaled to the maximum value. The pictures illustrate the interface orientations in the polar plots.

By choosing a sufficiently fine domain decomposition, arbitrary arrangements of twin components can be described. According to the formalism which describes the elastic state from a continuum perspective with coherent interfaces between the domains with different eigenstrain, the mechanically equilibrated (in the sense of Equation 4.2) elastic energy can be written as Ising Hamiltonian, see Equation 4.3. This transformation has been derived in [35, 62]. The Ising coefficients can be computed through a series of elastic calculations, where only one or two domains are in the transformed orientation state. The determination of the microstructure then turns into a discrete global minimization of the Ising Hamiltonian with respect to the spin variables s_i.

We demonstrate the approach using a discretization which is adapted ideally to the symmetries of the twinning, using a description in the coordinate system B', as then small simulations with only a minimum number of domains are sufficient. In particular, the $[1\bar{1}0]$ (y') direction has a vanishing eigenstrain contribution, and the use of a plane strain description is appropriate. Tensile strain $\langle\epsilon_{zz}\rangle$ in $[001]$ (z) direction translates in the rotated frame B' to prescribed average strains of $\langle\epsilon_{x'x'}\rangle = 1/3\langle\epsilon_{zz}\rangle$, $\langle\epsilon_{x'z'}\rangle = \sqrt{2}/3\langle\epsilon_{zz}\rangle$ and $\langle\epsilon_{z'z'}\rangle = 2/3\langle\epsilon_{zz}\rangle$. We note that only the shear component $\langle\epsilon_{x'z'}\rangle$ triggers the formation of twins, as the other components lead to tensile contributions, as expressed through the transformation tensor (4.5).

Due to the chosen problem adapted coordinate system, one can use a rather coarse

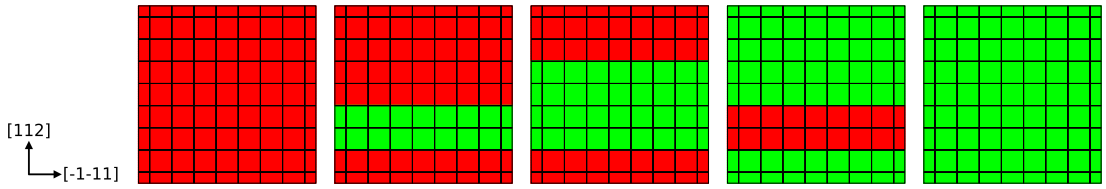

Figure 4.7: Twin formation modeled in single crystals using quantum annealing. The horizontal direction corresponds to the $\hat{x}' \parallel [\bar{1}\bar{1}1]$ direction and the vertical direction to the $\hat{z}' \parallel [112]$ orientation. A tensile strain is applied in $[001]$ direction, and periodic boundary conditions are used in $\hat{x}'$ and $\hat{z}'$ directions. In the perpendicular $\hat{y}'$ direction a plane strain situation is assumed. The twin components in transformed orientation state are shown in green. From left to right the applied strains are $\langle \epsilon_{zz} \rangle = 0; 3/16, 3/8; 9/16; 3/4$. Notice that the domains are shown in the Lagrangian reference frame, i.e., not showing the actual shear deformation through the twinning. For these simulations, a weak anisotropic interfacial contribution is included, as discussed.

domain decomposition, as twin lamellae are expected to form parallel to the coordinate axes. For illustrational purposes, we use the decomposition on 8×8 quadratic domains in the $x'z'$ plane, as shown in Figure 4.7. This sequence of figures shows the layer-by-layer growth of the twin, in agreement with the atomistic simulations from [169]. The green regions correspond to the transformed twin components. From a pure bulk elastic perspective, the twin growth must not necessarily happen in a strictly ordered layer-by-layer sense, as it is energetically equivalent to form thicker twin lamellae or several smaller ones, as long as their volume ratio is the same once again. This reflects the importance of a twin interface energy contribution.

The undesired energetic degeneracy of (112) and $(\bar{1}\bar{1}1)$ interfaces from a bulk elastic perspective alone, where the latter does not correspond to a twin interface, is cured immediately by the use of an anisotropic interfacial energy between the twin components. These observations are important as they differ from time dependent computations using, e.g., crystal plasticity on the growth of twins. In such simulations, the orientation of a twin is typically fixed by the initial "nucleus", which grows subsequently in the given direction. In contrast, the QA simulations are independent simulations for each applied external strain, reflecting quasistatic transitions between ground state configurations. Therefore, without the anisotropic interface contribution, lamellae can spontaneously break into smaller ones or change their orientation by 90° due to energetic degeneracy of the bulk mechanical energy.

In absence of an external strain, $\langle \epsilon_{zz} \rangle = 0$, the entire material is in the original orientation state, but as soon as a tensile strain is applied, twinning occurs, and the volume fraction of transformed twin components increases with strain. In the shown simulations,

the growth occurs rather step-wise due to the chosen coarse discretization, but for smaller and more domains, the growth becomes more and more continuous. In the end, we arrive at a volume fraction, which increases linearly above $\langle \epsilon_{zz} \rangle > 0$, until the entire sample has undergone the transformation. Although these finding agree with atomistic simulations of deformation twinning in [169] at a first glance, still discrepancies remain, which are discussed in detail in the following section.

Furthermore, we can understand the twin growth in the present simulations analytically for an infinitely fine domain discretization. In this case, the stress $\sigma_{x'z'}$, induced by the transformation strain (4.5) remains strictly zero. With the volume fraction v of transformed twin components we have the average eigenstrain $v/2\sqrt{2}$, which has to match the prescribed value $\langle \epsilon_{x'z'} \rangle = \sqrt{2}/3 \langle \epsilon_{zz} \rangle$, therefore leading to

$$v = \frac{4}{3} \langle \epsilon_{zz} \rangle. \tag{4.12}$$

This prediction is indeed in agreement with the findings in Figure 4.7.

Benchmarking Against Atomistic Simulations

It is instructive to qualitatively compare the predictions from the continuum model, as it is developed up to this point, to atomic scale simulations. We use a description which is close to the tensile tests of free standing nanowires and nanopillars using MD simulations in [155, 171–175]. Results are shown in Figure 4.8, which depicts an exemplary simulation of a tensile test of a BCC lithium single crystal nanopillar with crystallographic directions as $[001] \parallel z$, $[100] \parallel x$ and $[010] \parallel y$. When the specimen is strained along the $[001]$ direction, the pillar forms reflection twins with $(\bar{1}12)$ twin interfaces and common $[\bar{1}1\bar{1}]$ axes (discussed in more details in section 2.1.3). Upon twinning, the crystal only deforms in the (110) plane, in agreement with the discussion in section 4.1.2. There is no deformation along $[110]$. Contrary to the continuum prediction, as expressed through Equation 4.12, the twinning requires a minimum strain to appear in the sense of a nucleation event due to the need to overcome a Peierls-Nabarro barrier for the formation of a stacking fault. Only after this nucleation event, the twin fraction increases linearly with strain, which is the result of a layer-by-layer reorientation of the original crystal, similar to discussions in [170, 171].

The discrepancy between the two different behaviors can be resolved through an interfacial energy in the continuum description. Additionally, it prevents splitting of twins into smaller lamellae, which have the same bulk elastic energy as a single bigger lamella. Most importantly, as discussed previously in subsection 4.1.2, the anisotropic interfacial grain boundary energy is needed to suppress the formation of unexpected $(\bar{1}\bar{1}1)$ grain

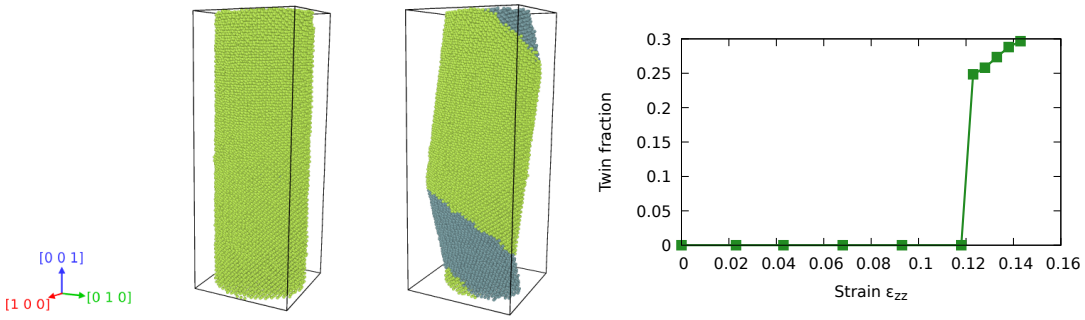

Figure 4.8: MD simulation of a lithium single crystal ($[001] \parallel z$) with 4 nm radius and 20 nm height. Tensile strain is applied along $[001]$. The original orientation state is colored in light green, while the transformed orientation state is colored in dark green. The polyhedral template matching and grain segmentation filters from Ovito are used [151, 161]. The snapshots are respectively from strains 0.118 (right before main twinning event), 0.123 (right after main twinning event).

boundary orientations.

All effects can be overcome through the consideration of nearest neighbor spin-spin interactions, as demonstrated in [35] and explaned in subsection 4.1.2. In fact, different spin states in neighboring domains indicate the presence of a twin interface in between them, to which we attribute an interfacial energy σ. We use here a weakly anisotropic interfacial energy, favoring the crystallographically expected (112) twin boundaries. The actual amount of anisotropy is not significant at this point, as it is sufficient to simply break the symmetry between the formerly energetically equivalent configurations. To this end, we add to the Ising Hamiltonian an additional pair interaction term of the type $-s_i s_j \sigma(\theta) A_{ij}/2$ for nearest neighbors i and j (Equation 4.11). The reason for this term is that $(1 - s_i s_j)/2$ equals one for distinct orientation states $s_i = -s_j$, whereas it vanishes inside the bulk phases. Additionally, A_{ij} is the area of the common interface of these two domains (interface length in two dimensions), and $\sigma(\theta)$ represents the anistropic interfacial energy, with θ being the local interface normal.

As confirmed in Figure 4.7, we find that the addition of a small interfacial energy $\sigma > 0$ is also sufficient to prevent the splitting into micro-lamellae, which is unfavorable from the perspective of interfacial energy. To further investigate the influence of the twin interface energy on the onset of deformation twinning, we performed a series of simulations similar to Figure 4.7, but with a finer discretization in the $[112]$ direction, using 1×32 rectangular domains. Figure 4.9 shows the volume fraction of transformed twin components as function of the applied tensile strain in z direction. In agreement with the preceding investigations and Equation 4.12, the volume fraction of transformed twin

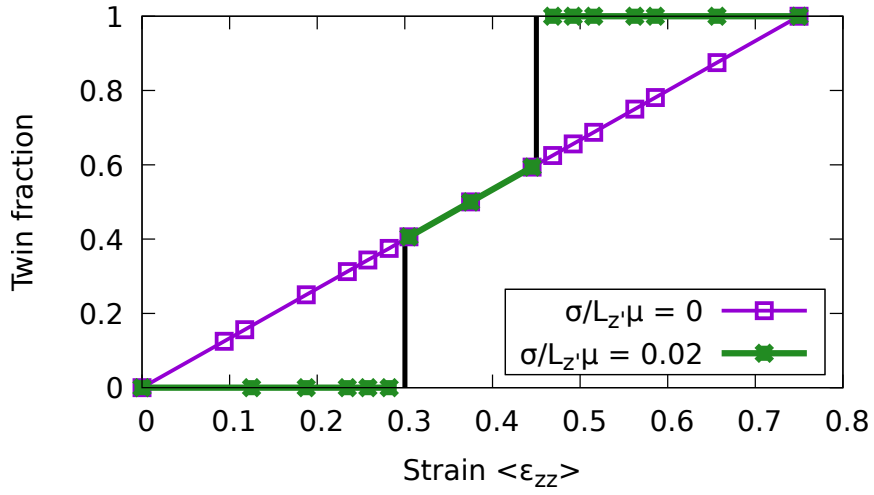

Figure 4.9: Volume fraction of transformed twin lamellae as function of the applied tensile strain on single crystals. Without interfacial energy the twin formation starts at zero strain, and the volume fraction of transformed twin components increases linearly up to the upper limit $\langle \epsilon_{zz} \rangle = 3/4$, where the entire sample is transformed. With interfacial energy, first a nucleation barrier has to be overcome, both from the original and fully transformed side. The QA calculated transitions of twin formation agree with the analytical predictions (4.15) and (4.16), as marked by the vertical black lines. In these QA simulations, a decomposition into 1×32 grains is used in a quadratic system with edge length $L_{x'} = L_{z'}$, with the axes orientations as in Figure 4.7. The Poisson ratio is chosen as $\nu = 1/4$.

components increases linearly with the applied strain in the absence of interfacial energy. With twin interface energy, it requires a finite activation barrier to form the twin. Notice that this behavior happens symmetrically coming from the fully transformed state, as then for the appearance of domains with the original orientation state again a nucleation barrier has to be overcome. In general, the twin formation becomes hysteretic due to this new energy term. As discussed, the quantum annealing finds the absolute minimum of the energy landscape, it does not follow metastable branches. However, close to the transition the QA does not always find the true ground states directly, and the number of required readout repetitions increases in this regime. Overall, the behavior now agrees with the MD simulations of twinning at nanopillars (Figure 4.8), where first a strain needs to be built up, before the release of this strain is sufficient to overcome the nucleation barrier of the twin interface energy.

The behavior in the QA simulations can also be understood analytically. From the elastic energy (4.1) in the system only the shear related part is relevant here, as due to the

transformation strain in the frame B' the diagonal parts of the strain tensor are not affected. Below the threshold of twinning, the uniform shear leads to a free energy contribution

$$F_{\text{shear}} = 2\mu\langle\epsilon_{x'z'}\rangle^2 L_{x'}L_{z'}, \tag{4.13}$$

per length in y' direction, where $L_{x'}$ and $L_{z'}$ are the system lengths in the respective directions. From the strain rotation we have $\langle\epsilon_{x'z'}\rangle = \sqrt{2}\langle\epsilon_{zz}\rangle/3$. Beyond the onset of twinning, the shear strain is fully compensated by the eigenstrain in a lamella of suitable width, as discussed in the previous section. Therefore, here only the interfacial energy (per length in y' direction) remains, which reads

$$F_s = 2L_{x'}\sigma. \tag{4.14}$$

Therefore, the twin will nucleate above the threshold strain

$$\langle\epsilon_{zz}^{\text{crit},1}\rangle = \frac{3\sqrt{\sigma}}{\sqrt{2L_{z'}\mu}}. \tag{4.15}$$

This threshold is marked as vertical line in Figure 4.9 and coincides with the annealer results.

An analogous analysis can be carried out in the high strain result, where a twin component with original orientation state has to nucleate. In this case the threshold strain reads

$$\langle\epsilon_{zz}^{\text{crit},2}\rangle = -3\sqrt{\frac{\sigma}{2L_{z'}\mu}} + \frac{3}{4}, \tag{4.16}$$

which is also marked in the plot. Again, the QA results agree with this prediction, which are in line with the MD results. Furthermore, we note that the threshold strain for twin formation, $\langle\epsilon_{zz}^{\text{crit}}\rangle \sim 1/\sqrt{L_{z'}}$, due to the interplay of interfacial and bulk mechanical effects, is analogous to the well-known Hall-Petch equation, which states a relationship of yield strength with grain size to the power of $-1/2$ [260, 261]. In fact, for most twinning cases the Hall-Petch relation is indeed obeyed, but with a higher slope than for slip [176].

Twinning in Polycrystals

With the investigations of planar twins on single crystals and the understanding of twin interface energetics from the preceding sections, we are now equipped to perform larger scale simulations of polycrystals.

In polycrystals, it is difficult to predict which arrangement of twin components leads to a global minimum of the mechanical and interfacial energy. Although it is possible to perform also dynamical atomistic or continuum simulations, they can get stuck in local

energetic minima, and the relaxation to the ground state can be prohibited or take a long time.

Even at the QA level, a larger number of domains is required to properly discretize the polycrystalline system. The drawback of this step is that more domain-domain interactions for computing the Ising coefficients are required, and the overall computation time increases.

As a consequence, for computational reasons, the number of domains should be not too large. However, one has to keep in mind that periodic boundary conditions can affect the selection of the twins. With planar twins, the periodicity does not have an effect, as twin lamellae appear parallel or perpendicular to the axis (as shown in Figure 4.7). On the other hand, if the choice of coordinate system leads to the appearance of inclined twins (as shown in Figure 4.8), the periodicity, in combination with the externally applied load, can instead enforce them to appear at other orientations rather than (112). We note that this effect similarly appears in other simulations, is not specific to the present model and has been discussed before in a similar context in [62].

In the QA framework, we can independently vary the eigenstrain in each domain to represent different grain rotations. A technical difference between these polycrystalline simulations and the ones performed in [245] is that in the latter each grain was connected to one spin, while here an additional subdivision of the grains into domains is necessary, as the transformed twin components typically occupy only a small amount of entire grains, and therefore multiple spins per grain are used. In the example shown in Figure 4.10 we use a setup consisting of five grains with different, randomly chosen orientations, subjected to periodic boundary conditions.

Each grain contains approximately 800 domains, and the grain orientation is shown as color code. The reference system is chosen to coincide with the preceding computations which used the basis B'. So, for a grain with orientation $\theta = 0$ (shown in red in the plot) the horizontal axis corresponds to the lattice orientation $[\bar{1}\bar{1}1]$ and the vertical axis to $[112]$. As before, a tensile strain is applied in $[001]$ direction. Results are shown in Figure 4.10.

Although the overall behavior is significantly more complex than in the single crystals cases studied above, there are a few general conclusions which can be drawn:

i) Twinning happens preferentially in grains without rotation, as the driving force for the transformation is maximized. Therefore, most of the red grains are twinned. Also, the twin orientations are close to the predictions.

ii) In the light blue grain, which is rotated by around $3\pi/4$, also the twin interfaces are rotated accordingly, as the (112) twin boundaries are energetically favorable. Still, this does does not exclude the formation of transformed domains without a twin interface, if strongly favored by bulk relaxation (orange grain). We note that the anisotropic interfacial energy contribution in the example is rather small.

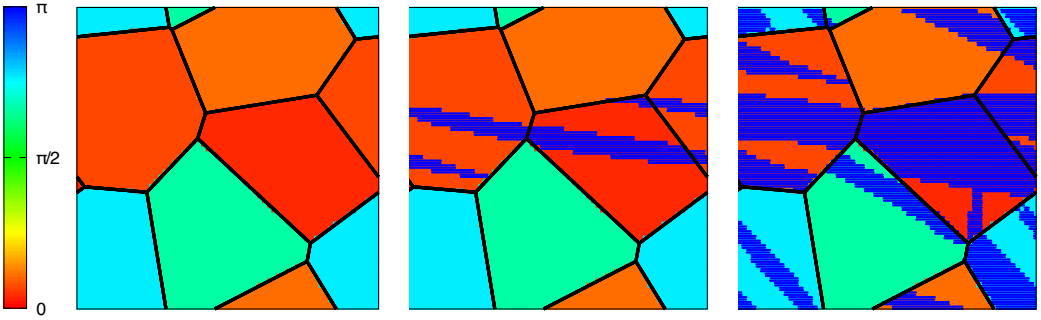

Figure 4.10: Deformation twinning in a polycrystal consisting of five grains. Here, the coordinate system is given by the basis set B', i.e., the horizontal axis corresponds to the $\hat{x}' \parallel [\bar{1}\bar{1}1]$ axis and the vertical axis to the $\hat{z}' \parallel [112]$ axis. Relative to these axis, the grains are rotated in the $x'z'$ plane in anti-clockwise direction, as indicated by the color coding. A tensile strain is applied in $[001]$ direction, which is $\langle \epsilon_{zz} \rangle = 0$ in the left panel, $\langle \epsilon_{zz} \rangle = 0.1$ in the middle panel, and $\langle \epsilon_{zz} \rangle = 0.3$ in the right panel. The blue shading indicates the domains in transformed orientation state, i.e., the domains with Ising spin $+1$. Additionally to the tesselation by grains, the periodic system with plane strain boundary conditions is divided into 64×64 domains in the sense of the preceding discussion, hence altogether 4096 Ising spins are used. As third discretization level, a uniform mesh of size 2048×2048 is used for the Fourier transformation based self and domain interaction energy calculations, using $\nu = 1/4$. The simulation results include apart from elastic energy also a weak, anisotropic grain boundary energy to favor twinning on the (112) plane.

iii) Twinning usually stops at high angle grain boundaries (green to red or blue to red), whereas low angle boundaries (red to red) are permeable to twin progression.

iv) Twin domains can be "attracted" by grain boundaries, leading to deviations from the crystallographically expected orientation. This is the case in the green colored grain.

v) Qualitatively, the microstructure is similar to those observed in experiments with polycrystalline bcc metals (see, e.g., [262, 263]) and close-packed structures (see, e.g., [249, 264]) which deform primarily by twinning. Important features regarding twin transmission through grain boundaries and formation of lamellar twins can be identified in both experimental and our pictures.

vi) The characteristic lenticular shape of deformation twins is partly observed in the present simulations as a consequence of minimization of mechanical energy. This effect becomes screened if a twin traverses the entire sample, as then the strain is reduced homogeneously.

v) Interfacial energy contributions lead to the appearance of a nucleation barrier, and therefore promotes less, but wider twin components with a high release of mechanical

energy, which are properly aligned to the external mechanical load.

Overall, the presented continuum approach for describing deformation twins has the potential to support simulations of this deformation mechanism, complementing atomistic approaches, like Molecular Statics and Dynamics, as well as continuum methods, like Crystal Plasticity based Finite Element Simulations. The detailed interplay between microstructure, the crystallography of twinning and complex mechanical effects will be elucidated in future investigations.

4.1.3 Conclusions

Modeling deformation mechanisms and microstructure formation is critical for many materials science applications, and efficient simulation approaches to predict equilibrium microstructures in large systems are highly desired. Mainly BCC metals remain intricate to model due to their complex deformation behavior, while their importance in, e.g., battery technologies, grows consistently. In this work, we extend insights of deformation twinning in BCC metals from an atomistic level to a continuum scale using quantum annealing (QA). We have developed a framework to bridge the scales by bringing crystallography and theoretical knowledge into a QA formulation and simulate deformation twinning in large systems. We have compared the continuum descriptions to MD simulations of lithium due to its relevance for battery research. Still, the approach is not material-specific and it applies to all systems in which twinning is a relevant deformation mechanism.

Building on an existing QA framework that captures shear transformations via an Ising model, we have added crystallographic knowledge specific to BCC deformation twinning and twin interface energetics. This enables accurate simulations of deformation twinning for given external mechanical load. In single crystals, the QA predictions agree conceptionally with MD simulation results of deformation twinning. In polycrystals, the QA model makes it feasible to scale up the predictions to larger and more complex microstructures, which are closer to reality, delivering deformation twin arrangements comparable to experimental observations. As such, the QA complements available modeling techniques by outputting directly the equilibrium ground structure of large systems extremely fast, while classic techniques, such as MD, FEM, Monte Carlo simulations and phase-field modeling, typically follow the temporal evolution and can suffer from slow convergence. In particular, MD simulations typically require unrealistically high strain rates due to time constraints, while the QA approach represents the opposite with an infinitely slow straining, i.e., a quasistatic process.

Altogether, this novel framework shows that the use of quantum annealing is a promising approach for obtaining ground-state configurations in mechanically strained systems, which experience stress relaxation through deformation twinning. A particular advantage

is that the time consuming computations of the mutual domain interactions could be calculated only once, whereas changes in the externally applied stress or strain can be treated analytically. The QA simulations are very fast, with actual computation times in the microsecond range for pure QA simulations, and runtimes at the order of seconds for larger hybrid simulations. In addition, variations of the interfacial energy are treated on the annealer level, and therefore these calculations are very fast. At the same time, one should be aware of potential limitations of the approach in the present form, including the assumption of homogeneous and linear elasticity to preserve superposition and restrict the effective interactions between the domains to pairwise terms, which can be handled with the quantum annealer. Deviations from these assumptions can lead to many-body terms, which could possibly be treated through perturbation approaches.

We point out that the present energy minimization based description of deformation twinning, which is complementary to stress based considerations, is a valuable concept also independent of quantum computing implementation. In fact, digital annealears, which are also based on Ising Hamiltonians, are an alternative to quantum annealing and could instead be used. Moreover, if such dedicated hardware options are not available, conventional discrete optimization methods, probably tuned to the particular problem for performance optimization, could still be used with the same workflow.

Potentially, future model extensions could include anisotropic elastic responses and multiple grain variants, as well as other mechanical loadings, which can occur, e.g., during tribological applications, paving the way for realistic, fast and accurate predictions of microstructures of technologically critical materials.

4.2 Multi-Variant Description of Shear and Tetragonal Deformations

The formation of microstructures is critical for many applications, as it strongly impacts the properties of materials. It was recently presented an approach to predict equilibrium microstructures by separating discrete from continuous degrees of freedom, and solving the problem via QA [62]. Specific applications are stress or strain driven transformations in, e.g., deformation twinning, as explored in the previous subsection 4.1, or shape memory alloys and martensitic transformations, as discussed in [62, 245]. In [62], it is assumed that a grain can be in one out of two variant states, which differ by their eigenstrain, i.e., their stress-free configuration. Specifically in the previous subsection 4.1, to describe the deformation twinning process, the two possible variant states were defined as either the transformed or the original twin orientation states. By application of external stresses and the presence of internal stresses, the grains can flip between the two variants, and

these transitions are driven by a reduction of the overall elastic energy.

As discussed, this new simulation approach complements the well-known phase-field picture and other classical methods, such as MD and FEM. However, some questions remain open. A first question, emerging from the goal of extending prior work, is how to generalize the previously studied two-variant-only QA framework to accommodate microstructure equilibration involving multiple grain variants in the form of, e.g., different phases, twin variants or grain rotations. A second question, which arises generally in the context of materials science, is how this multi-variant grain optimization can be solved efficiently via QA. Therefore, here we extend the previous description from a single variant selection to multiple ones, while efficiently solving it via a hybrid QA approach.

4.2.1 Methods

The overall concept of the investigations is that we assume that in a microstructure each grain is allowed to select between different variants, such that the overall elastic energy is minimized in equilibrium. As the grains are coherently connected to each other, a variant flip, as sketched in Figure 4.11, leads possibly to an energetically unfavorable distortion of the surrounding grains, and therefore the discrete optimization of the variants is a nontrivial problem.

To achieve a description in the framework of continuum elasticity, we consider eigenstrain (stress-free strain) expressions of the form

$$\epsilon_{ij}^{(0)}(\mathbf{r}) = \sum_{n=1}^{N} \theta_n(\mathbf{r}) \sum_{k=1}^{K} s_\nu \epsilon_{ij}^{(0,n,k)}. \tag{4.17}$$

Here, the function $\theta_n(\mathbf{r})$ is equal to one inside grain n and vanishes everywhere else. The eigenstrain in each grain with index n can be a superposition using K "spin variables" $s_\nu = s_{n,k} = \pm 1$ with the total number of spins $N_\nu = N \cdot K$, which weight eigenstrain tensor components $\epsilon_{ij}^{(0,n,k)}$. Therefore, we have altogether 2^K variants in each grain by suitable selection of the parameters $\epsilon_{ij}^{(0,n,k)}$.

To determine the thermodynamic equilibrium state (minimum elastic energy), first the elastic problem has to be solved for a given eigenstrain. This can be expressed through the minimization of the elastic energy with respect to the displacement field u_i in combination with suitable mechanical boundary conditions. In case of isotropic linear elasticity, the elastic energy functional reads as in Equation 4.1, which is simply an extension of Equation 1.3, and the strain tensor as in Equation 1.2.

Contrary to the optimization of the displacement and strain fields as continuous variables, the variant selection becomes a discrete problem on top of the preceding step.

Following the Fourier transformation approach outlined in [62], we can calculate the elastic energy $E(\{s_\nu\})$ of the microstructure for a given "spin configuration" $\{s_\nu\}$. We note that the approach does not necessarily require using Fourier transformation methods, but, e.g., also finite element methods can be used, provided that the elastic interactions can be computed with sufficient accuracy, as discussed in [62].

As the expression for the elastic energy is quadratic in the framework of the linear theory of elasticity, the final expression for the elastic energy can be expressed as Equation 4.3. We note that the above form of the energy holds for arbitrary values of the spin variables and does not apply only to the special case $s_\nu = \pm 1$ (as done for the twinning case). Therefore, we obtain directly

$$E_0 = E(\{s_\nu \equiv 0\}), \tag{4.18}$$

where all spins have the value 0, which we also denote as the reference state. Next, we perform calculations where all spins but one vanish, and the selected one has either the value $+1$ or -1. From that we get

$$E(\{s_i = \pm 1, \text{all others } 0\}) = E_0 \pm \tilde{H}_i + \tilde{J}_{ii}. \tag{4.19}$$

Therefore, we can extract the diagonal element for the self-interactions as

$$\begin{aligned} \tilde{J}_{ii} = \frac{1}{2} \quad \Big[\quad & E(\{s_i = +1, \text{all others } 0\}) \\ + \quad & E(\{s_i = -1, \text{all others } 0\} - 2E_0 \Big] \end{aligned} \tag{4.20}$$

and consequently

$$\begin{aligned} \tilde{H}_i = \frac{1}{2} \quad \Big[\quad & E(\{s_i = +1, \text{all others } 0\}) \\ - \quad & E(\{s_i = -1, \text{all others } 0\}) \Big]. \end{aligned} \tag{4.21}$$

Finally, to calculate the interaction coefficients $\tilde{J}_{ij}$ for $i \neq j$ we perform elastic calculations with two nonvanishing spins $s_i = s_j = 1$. With

$$E(\{s_i = s_j = 1, \text{others } 0\}) = E_0 + \tilde{H}_i + \tilde{H}_j + 2\tilde{J}_{ij} + \tilde{J}_{ii} + \tilde{J}_{jj}, \tag{4.22}$$

where we can directly calculate $\tilde{J}_{ij}$ using the expressions obtained above

$$\begin{aligned} 2\tilde{J}_{ij} &= E(\{s_i = s_j = +1, \text{all others } 0\}) \\ &- E(\{s_i = +1, \text{all others } 0\}) \\ &- E(\{s_j = +1, \text{all others } 0\}) + E_0. \end{aligned} \tag{4.23}$$

For zero stress boundary conditions, we get for the eigenstrain of the type (4.17) the simplification $E_0 = 0$ and $\tilde{H}_i = 0$ for all i.

For the use of the quantum annealer, we restrict the allowed spin values to $s_v = \pm 1$ and we also have to rewrite the expression (4.3) in a slightly different way, which excludes in particular self interactions of the type $s_i s_i$. The classical Hamiltonian reads

$$H = H_0 + \sum_{i=1}^{N_v} H_i s_i + \sum_{i=1}^{N_v} \sum_{j=i+1}^{N_v} J_{ij} s_i s_j, \tag{4.24}$$

where the offset H_0 only affects the energy value but not the spin configuration minimizing the energy, and therefore it can be dropped for the desired Ising type of the QA "problem Hamiltonian". Physically, it corresponds to the elastic energy of a microstructure as reference state, see Figure 4.11. Comparison with the expression (4.3) above gives

$$H_0 = E_0 + \sum_{i=1}^{N_v} \tilde{J}_{ii}, \tag{4.25}$$

$$H_i = \tilde{H}_i, \tag{4.26}$$

$$J_{ij} = 2\tilde{J}_{ij} \quad \text{for } i < j. \tag{4.27}$$

This general formulation has the advantage that it decouples the approach for setting up the Ising coefficients for the annealer from the specific linear elastic energy solver. Nevertheless, one has to keep in mind that the formulation (4.3) relies on the assumption of equal elastic constants in all phases and variants and coherent boundary conditions.

For larger systems, hybrid quantum annealing utilizes classical algorithms and the interplay with quantum annealing to address areas with high computational demands using a QPU coprocessor working with generic parameters for up to 11616 spin variables on the D-Wave Advantage system [64–66].

4.2.2 Results and Discussions

To illustrate the workflow, we consider a case with four variants per grain, i.e., two spins per grain. Similar to [62], we use here specific cases of shear and tetragonal distortions,

which are now combined and lead to eigenstrains

$$\epsilon_{ij}^{(0,n)} = s_{n,1} \begin{pmatrix} 0 & \epsilon_0 & 0 \\ \epsilon_0 & 0 & 0 \\ 0 & 0 & 0 \end{pmatrix} + s_{n,2} \begin{pmatrix} \epsilon_1 & 0 & 0 \\ 0 & -\epsilon_1 & 0 \\ 0 & 0 & \epsilon_1 \end{pmatrix}, \tag{4.28}$$

where n numerates the grains. For the first application we assume that the individual tensors of the shear (involving the strain parameter ϵ_0) and tetragonal deformations (associated with ϵ_1) are the same in all grains; later we will also discuss the case of grain rotations, where the tensors differ from grain to grain. Figure 4.11 visualizes the different strain variants and illustrates the color codings used for the following plots.

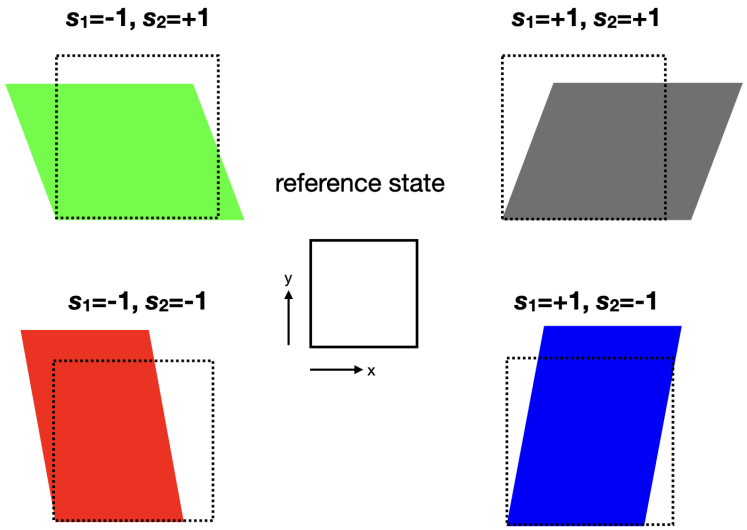

Figure 4.11: Visualization of the variants used in the present study. Spin s_1 corresponds to the shear deformation, s_2 to the tetragonal deformation, see Eq. (4.28).

The grain structure is generated using a Voronoi tesselation in two dimensions, and we assume plane strain conditions, using isotropic linear theory of elasticity with periodic boundary conditions. According to the above approach, first the self energies related to each spin are calculated, followed by a computation of spin-spin interactions, from which the Ising vector components H_n and interaction parameters J_{ij} are extracted.

Apart from the self generated internal stresses due to the different variants, also a homogeneous external (average) strain field $\langle \epsilon_{ij} \rangle$ can be superimposed, which leads to an additional contribution to the magnetic field vector H_n, which couples the external strain

$\langle \epsilon_{ij} \rangle$ to the $\mathbf{k} = 0$ mode of the Fourier transform of the eigenstrain tensor. This means that a change of the external strain leaves the coupling constants J_{ij} invariant and only modifies a contribution to H_n, which can be treated analytically, therefore minimizing the computational cost for repeated calculations with different external boundary conditions.

Figure 4.12 shows a sequence of equilibrium microstructures and their response to a tensile strain in horizontal (x) direction for $\epsilon_1 = \epsilon_0$. Here, the computer generated, random 2D microstructure consists of 200 grains. Each grain selects its optimum variant state $(s_{n,1}, s_{n,2})$ to minimize the total energy. In panel (a) the fixed external strain vanishes, which implies that in the ground state the volume fractions of the blue and green (resp. red and grey) variants should be close to each other, as then the positive and negative contributions to the shear and tetragonal (eigen)strain cancel each other to minimize the elastic energy. The arrangement of the differently coloured patches is then a result of the mutual spin-spin interactions. We can observe in panel (a) a structure of horizontal stripes with alternating layers of shear strain (blue-grey and red-green). Such stripes with (100) orientation have been discussed already in [62], as the formation of these structures minimizes the overall shear deformation. Additionally, tilted stripe pairs red-blue and green-grey correspond to the same tetragonal strain and annihilating shear strain, similar to the patterns for pure tetragonal eigenstrain discussed in [62].

The patterns formed by several variants can be better understood by analyzing the elastic anisotropy of the transformation. Specifically, the normal to the interface between two variants must be close to a direction that minimizes the elastic kernel of the transformation from one variant to the neighboring one. This can be demonstrated for plate-like domains [257], but is also very commonly observed in complex microstructures whose anisotropy is of elastic origin, such as cuboidal microstructures in superalloys [265], Widmanstätten structures [266] or chessboard structures in Co-Pt alloys [267]. The elastic kernel can be obtained analytically in Fourier space [257] or can be calculated in real space, using a regular stripe pattern of both variants. Indeed, in this geometry, only Fourier modes perpendicular to the stripes remain, and the elastic energy is proportional to the elastic kernel. In the following, the orientation dependence of the pattern is analyzed by considering successively each pair of variants. We assume fixed vanishing average strain and equal volume fractions of the two involved variants. The angular dependence of relevant combinations of stripe pairs is shown in Figure 4.13.

In these pole figures the angle 0° corresponds to vertical stripes, and positive angles to anticlockwise rotations of the pattern. From this figure, one can conclude that both green-grey and red-blue interfaces are preferred either at 0° or 90°, and this is in agreement with the observed interface orientation between these variant pairs in Figure 4.12(a).

Both green-red and grey-blue pairs have preferred orientations around $\pm 38^\circ$. Due to constraints of the chosen system sizes and the used periodic boundary conditions,

typically deviations from the analytical prediction for infinite system sizes are expected, as discussed in detail in [62]. In the equilibrium microstructure in Figure 4.12(a) we indeed find inclined interfaces between green-red and grey-blue pairs, which are in line with the theoretical expectation.

Finally, green-blue and red-grey interfaces show a very pronounced anisotropy with a strong cusp at either 17° and -62° (green-blue) or 62° and -17° (red-grey). Due to this strong orientation dependence these interfaces either have to appear at these preferred angles or they are strongly suppressed. In fact, the corresponding interface lengths in Figure 4.12(a) are much shorter than the other interfaces.

We note for the subsequent panels of Figure 4.12 that the elaborated anisotropy of the interactions is not affected by a homogeneous external strain, and therefore the polar plots in Figure 4.13 remain valid also in these cases. In these pictures, the applied tensile external strain in horizontal direction is incrementally increased. This favors the variants with a positive "tetragonal spin value", and consequently the fraction of green and grey grains increases. They form more and more pronounced bands in the (100) directions, as explained above, partly interrupted by disappearing inclined red/blue bands with unfavorable tetragonal strain contribution. Finally, only grains with $s_{n,2} = +1$ remain, and the volume fractions with positive and negative shear are essentially the same, as much as the irregular grain sizes permit.

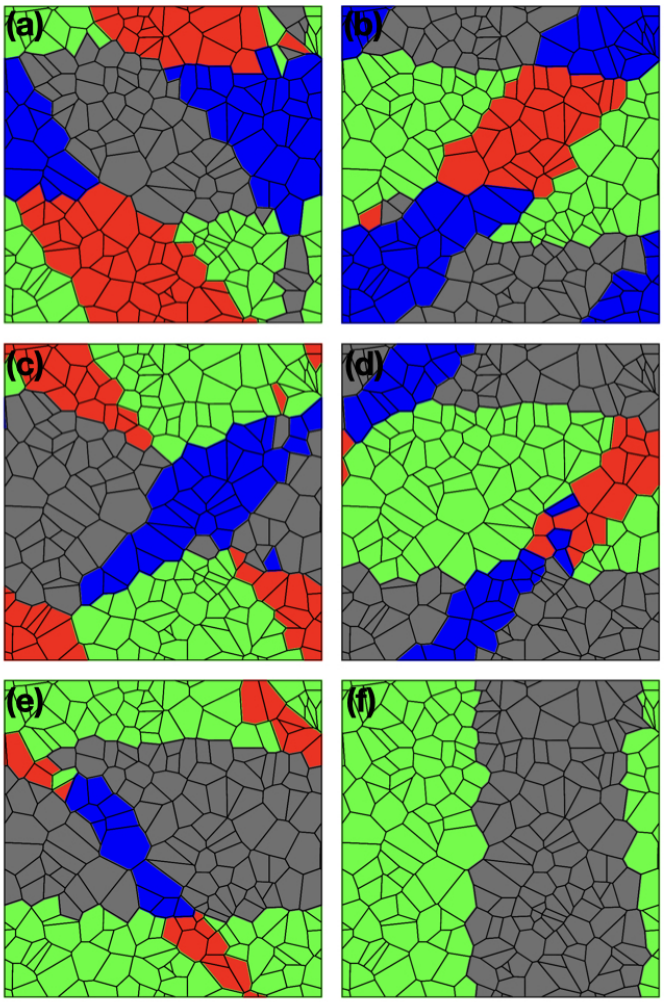

Figure 4.12: Equilibrium variant distribution with uniform grain orientation. The microstructure consist of 200 grains and a tensile strain is applied in horizontal (x) direction. The tensile strain is **(a)** $\langle\epsilon_{xx}\rangle/\epsilon_1 = 0$, **(b)** $\langle\epsilon_{xx}\rangle/\epsilon_1 = 0.25$, **(c)** $\langle\epsilon_{xx}\rangle/\epsilon_1 = 0.5$, **(d)** $\langle\epsilon_{xx}\rangle/\epsilon_1 = 0.75$, **(e)** $\langle\epsilon_{xx}\rangle/\epsilon_1 = 1.0$ and **(f)** $\langle\epsilon_{xx}\rangle/\epsilon_1 = 1.5$. In all figures $\epsilon_0 = \epsilon_1$ and the Poisson ratio is chosen as $\nu = 1/4$ (i.e., $\lambda = \mu$).

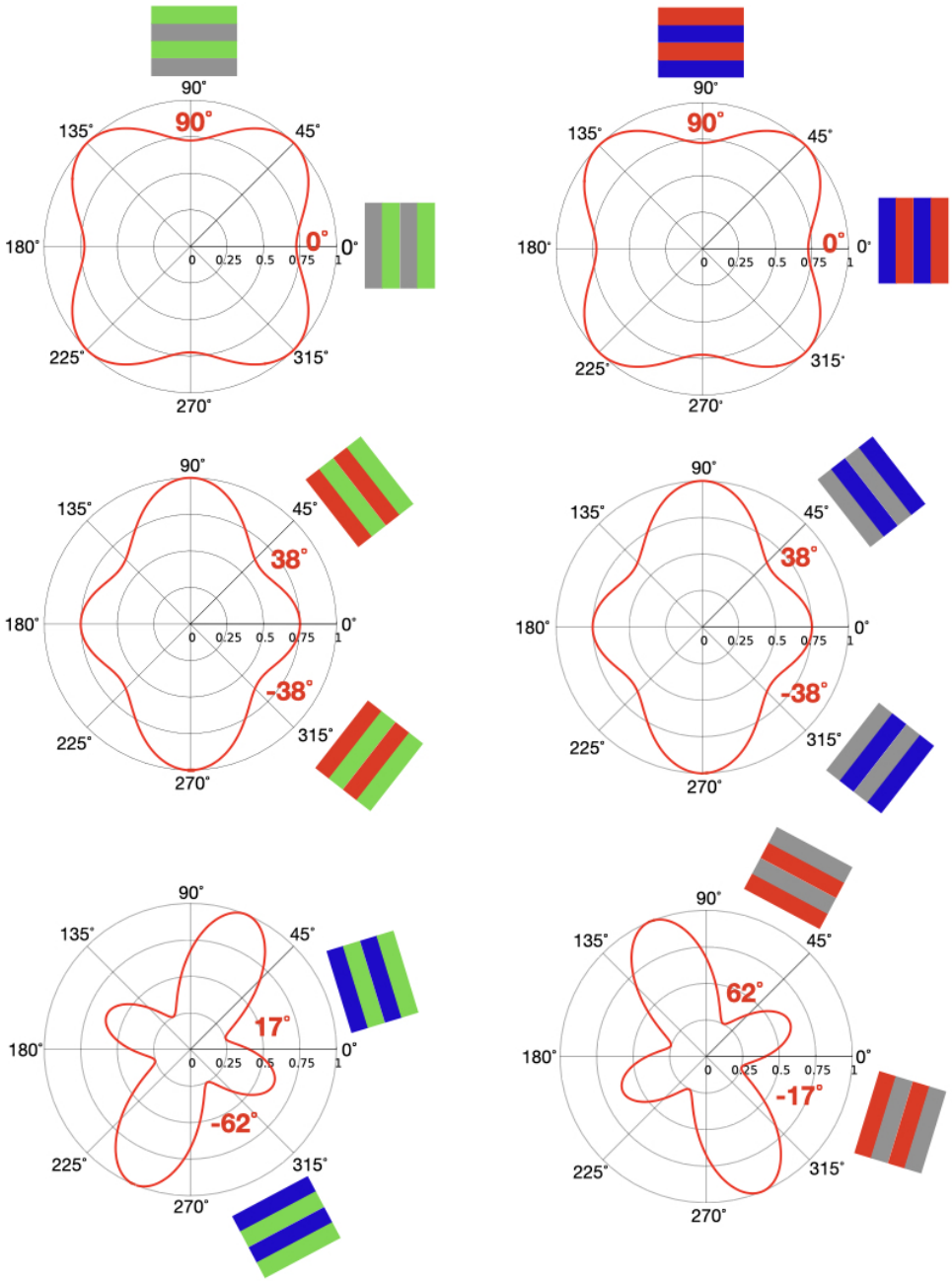

Figure 4.13: Orientation dependence of the normalized elastic energy for equal volume fraction stripes consisting of pairs of variants for $\langle \epsilon_{ij} \rangle = 0$ and $\epsilon_1 = \epsilon_0$.

It is useful to emphasize the periodicity of the patterns by looking at a 2×2 supercell of the simulation domain, as shown in Figure 4.14.

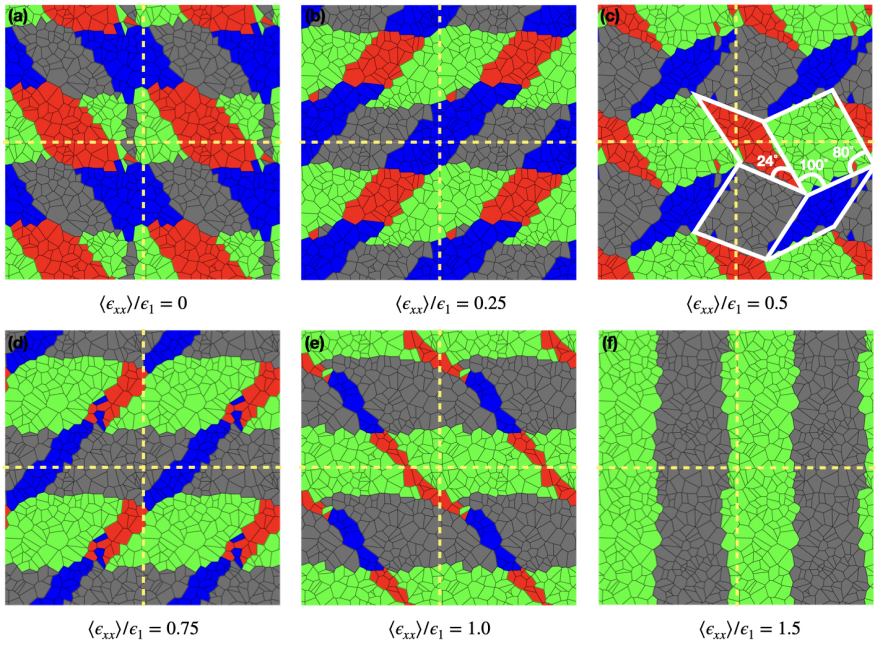

Figure 4.14: 2×2 supercell representation of Figure 4.12 to emphasize the microstructure patterns. The dashed yellow lines mark the boundaries or the simulation with periodic boundary conditions. In all figures $\epsilon_1 = \epsilon_0$ and $\nu = 1/4$.

The first striking observation is that the pattern in panel (c) for $\langle\epsilon_{xx}\rangle/\epsilon_0 = 0.5$ differs significantly from the other cases. These latter cases show both horizontal and tilted stripes, as analyzed above. There, grey-green and red-blue interfaces appear at 0° or 90°, and green-blue as well as red-grey interfaces play at most a minor role, as discussed above. The red-green and grey-blue interfaces are roughly at $\pm 45^\circ$ as a compromise between the preferred analytical predictions for infinite systems and the constraints by the periodic boundary conditions.

The special case $\langle\epsilon_{xx}\rangle/\epsilon_0 = 0.5$ shows a remarkable topological change, as now interfaces between green-blue, green-red, grey-blue and grey-red appear, whereas the previously important red-blue and green-grey interfaces are absent. Moreover, the newly appearing interfaces are at their preferred orientations. For example, the marked 24° angle inside the red lozenge is the difference between the 62° minimum energy orientation for the red-grey interface and the 38° orientation for the red-green pattern. This leads to the geometry sketched in Figure 4.14(c), from which the overall periodic pattern is constructed.

According to the equilibrium angles, this demands that the joint volume fraction of the diamond-shaped green and grey domains is $\sin(80°)/[\sin(24°)+\sin(80°)] \approx 0.7$, and therefore this exceptional pattern is only observed close to a specific external strain value. We note that this chessboard structure is very similar to the one observed in Co-Pt and $(CuAu)_{1-x}$-Pt_x systems [267]. However, the symmetry is lower in the present case because the green and grey regions are not tetragonal.

The same microstructure as in Figure 4.12 is subjected to a shear strain $\langle\epsilon_{xy}\rangle$ in (110) direction, and the results of the energy minimization are shown in Figure 4.15.

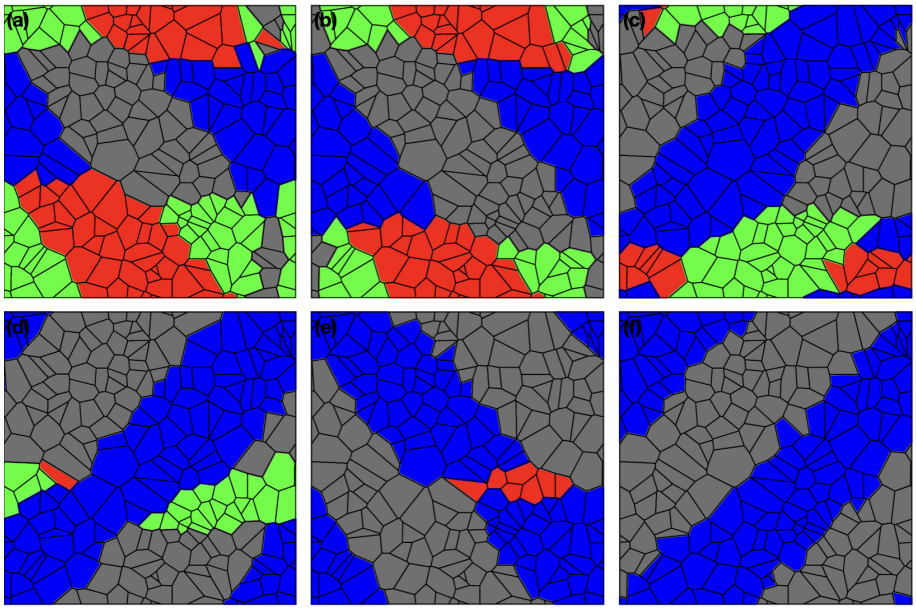

Figure 4.15: Equilibrium variant distribution with uniform grain orientation. The microstructure consist of 200 grains and an average shear strain $\langle\epsilon_{xy}\rangle$ is applied. The strain is **(a)** $\langle\epsilon_{xy}\rangle/\epsilon_0 = 0$, **(b)** $\langle\epsilon_{xy}\rangle/\epsilon_0 = 0.25$, **(c)** $\langle\epsilon_{xy}\rangle/\epsilon_0 = 0.5$, **(d)** $\langle\epsilon_{xy}\rangle/\epsilon_0 = 0.75$, **(e)** $\langle\epsilon_{xy}\rangle/\epsilon_0 = 1.0$ and **(f)** $\langle\epsilon_{xy}\rangle/\epsilon_0 = 1.5$. In all figures $\epsilon_0 = \epsilon_1$, and the chosen Poisson ratio is $\nu = 1/4$ (i.e., $\lambda = \mu$).

The starting configuration without external strain (panel (a)) is therefore identical to Figure 4.12(a). An increase of the shear strain favors variants with positive $s_{n,1}$, as they accommodate the given external strain to a large amount. Therefore, for large positive shear strain $\langle\epsilon_{xy}\rangle/\epsilon_0$ values only grey and blue patches remain. As they differ by the tetragonal eigenstrain only, they align as inclined bands to minimize the total elastic energy, as discussed in detail in [62].

In particular, grey-green and red-blue interfaces are at 0° or 90°, as predicted in

Figure 4.13. Similarly, blue-green and red-grey interfaces have orientations close to the expected ones ($\pm 17°, \pm 62°$). For blue-grey and red-green interfaces the periodicity constraint enforces orientations close to 45°.

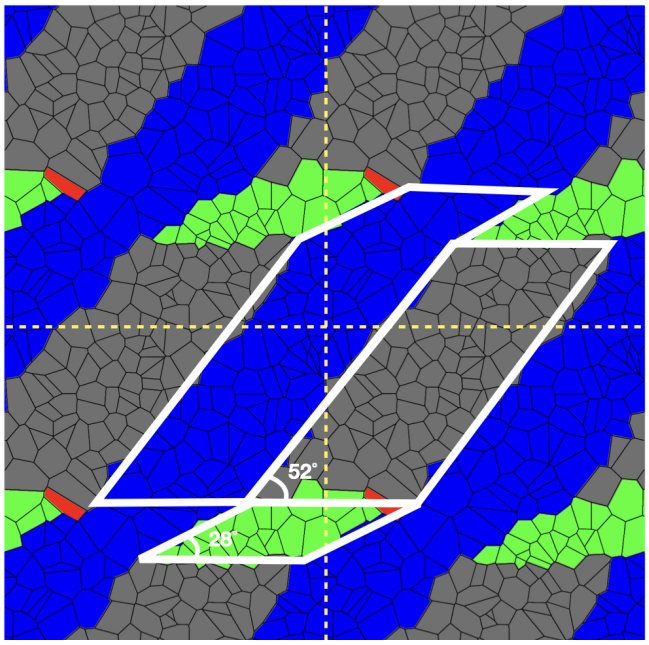

Figure 4.16: 2×2 supercell of the simulation domain for external shear $\langle \epsilon_{xy} \rangle / \epsilon_0 = 0.75$ from Figure 4.15(d) with $\epsilon_1 = \epsilon_0$. Apart from a negligible amount of the red variant three phases are present here. The sketch shows the geometrical explanation of the equilibrium pattern.

An interesting case is the three-variant configuration in Figure 4.15(d) (apart from a negligible fraction of the red variant). A 2×2 supercell of the equilibrium microstructure is shown in Figure 4.16. The overall 45° alignment is imposed by periodic boundary conditions. The green domain slightly changes the orientation of the blue-grey interfaces so that they are rotated closer to the optimal orientation $90° - 38° = 52°$. This configuration would not be favorable at $-45°$ (instead of the 45°) because the blue-grey interfaces would be rotated away from the optimal orientation. Instead, for $-45°$, red domains appear in the blue platelets (see Figure 4.15(e)).

For the present four variant setup, the response of the microstructure does not only depend on the ratio $\langle \epsilon_{ij} \rangle / \epsilon_0$, but also on the relative relevance of shear and tetragonal deformations, as expressed through the dimensionless parameter ϵ_1 / ϵ_0. Whereas in the above investigations we have fixed this ratio to $\epsilon_1 / \epsilon_0 = 1$, Figure 4.17 shows the influence

of this parameter for fixed external strain. Here, we note that a change of $\epsilon_0 \to a\epsilon_0$ and $\epsilon_1 \to b\epsilon_1$ does not require to repeat the entire computations for the interaction parameters J_{ij} and the external magnetic field H_i. Instead, it follows from the theory of linear elasticity that the coupling constants J_{ij} are quadratic in the rescaling factors a, b, and H_i scales linearly with them. In detail, for a spin pair (i, j), where both of them refer to shear transformations, the coupling constants are rescaled according to $J_{ij} \to a^2 J_{ij}$, and similarly for two "tetragonal spins" as $J_{ij} \to b^2 J_{ij}$. For mixed interactions between a tetragonal and a shear degree of freedom, the rescaling obeys $J_{ij} \to abJ_{ij}$. The "magnetic" terms H_n scale linearly with either a or b, depending on the spin type.

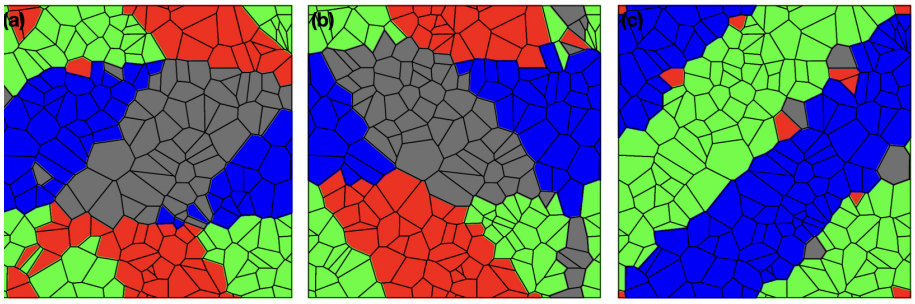

Figure 4.17: Equilibrium variant distribution with uniform grain orientation for $\langle \epsilon_{ij} \rangle = 0$. The microstructure consist of 200 grains and the dimensionless parameter ϵ_1/ϵ_0 is varied. The ratios are **(a)** $\epsilon_1/\epsilon_0 = 0.2$, **(b)** $\epsilon_1/\epsilon_0 = 1$ and **(c)** $\epsilon_1/\epsilon_0 = 5$. In all figures the chosen Poisson ratio is $\nu = 1/4$ (i.e., $\lambda = \mu$).

The starting case (center panel in Figure 4.17) is again the already discussed reference situation with $\epsilon_1 = \epsilon_0$. In all three pictures, the boundary conditions are fixed to vanishing average strain, $\langle \epsilon_{ij} \rangle = 0$. The right panel shows the equilibrium microstructure for $\epsilon_1/\epsilon_0 = 5$, which means that the weight of the tetragonal deformations is significantly larger than that of the shear. Here, the variants select essentially diagonal bands, as discussed in [62], in order to match the periodic boundary conditions. The blue and green variants have cancelling tetragonal and shear eigenstrains, such that for equal volume fractions the zero strain boundary conditions are met best. We can expect that also the opposite colour pair (red-grey) can lead to an energetically equivalent solution, and therefore a weak, locally "noisy" pattern, which mixes these two configurations, may appear. We expect this effect to be more pronounced in larger systems. One may expect that the opposite case with $\epsilon_1/\epsilon_0 = 0.2$, which is dominated by the shear eigenstrain, should similarly lead to bands with alternating shear in $\langle 100 \rangle$ direction, as discussed for the two-variant case in [62]. However, as can be seen from the left panel of Figure 4.17, this is not the case. Instead, each horizontal stripe consists of blue and grey (or red and

green) patches, which share the same shear eigenstrain but have opposite tetragonal strain. The reason for this assymetry — as compared to the tetragonal dominated case discussed above — is that a small, but nonvanishing tetragonal eigenstrain leads also to a tangential mismatch strain at the interfaces between the $\langle 100 \rangle$ bands. Therefore, a purely blue horizontal band would lead to a contraction in tangential direction, whereas the compensating green horizontal band would expand in the same direction, hence leading to large mismatch coherency stresses. Therefore, it is energetically favorable to generate $\langle 100 \rangle$ structures with an additional zigzag substructure, such that all four variants are present with equal volume fraction, and only the irregularity of the microstructure adds some minor noise.

It is again instructive to look at the angular dependence of the elastic energy for infinite stripe patterns (again for zero mean strain boundary conditions), as it depends on the ratio ϵ_1/ϵ_0, see Figure 4.18.

Here, one can clearly see that the interaction becomes very anisotropic for green-grey interfaces at low ratios ϵ_1/ϵ_0 and essentially isotropic at high values, with minimum energetic cost at 0° and 90°. For the green-red interfaces, the trend is opposite. Green-red (and similarly grey-blue) interfaces have preferred interface orientations $\pm 38^\circ$. The green-blue and similarly grey-red interfaces have the strongest dependence on ϵ_1/ϵ_0 and therefore the overall energy minimization clearly favors the optimal orientations for these interfaces. From this perspective, Figure 4.17(a) is particularly interesting, and its zigzag structure becomes obvious in the 2×2 supercell representation in Figure 4.19.

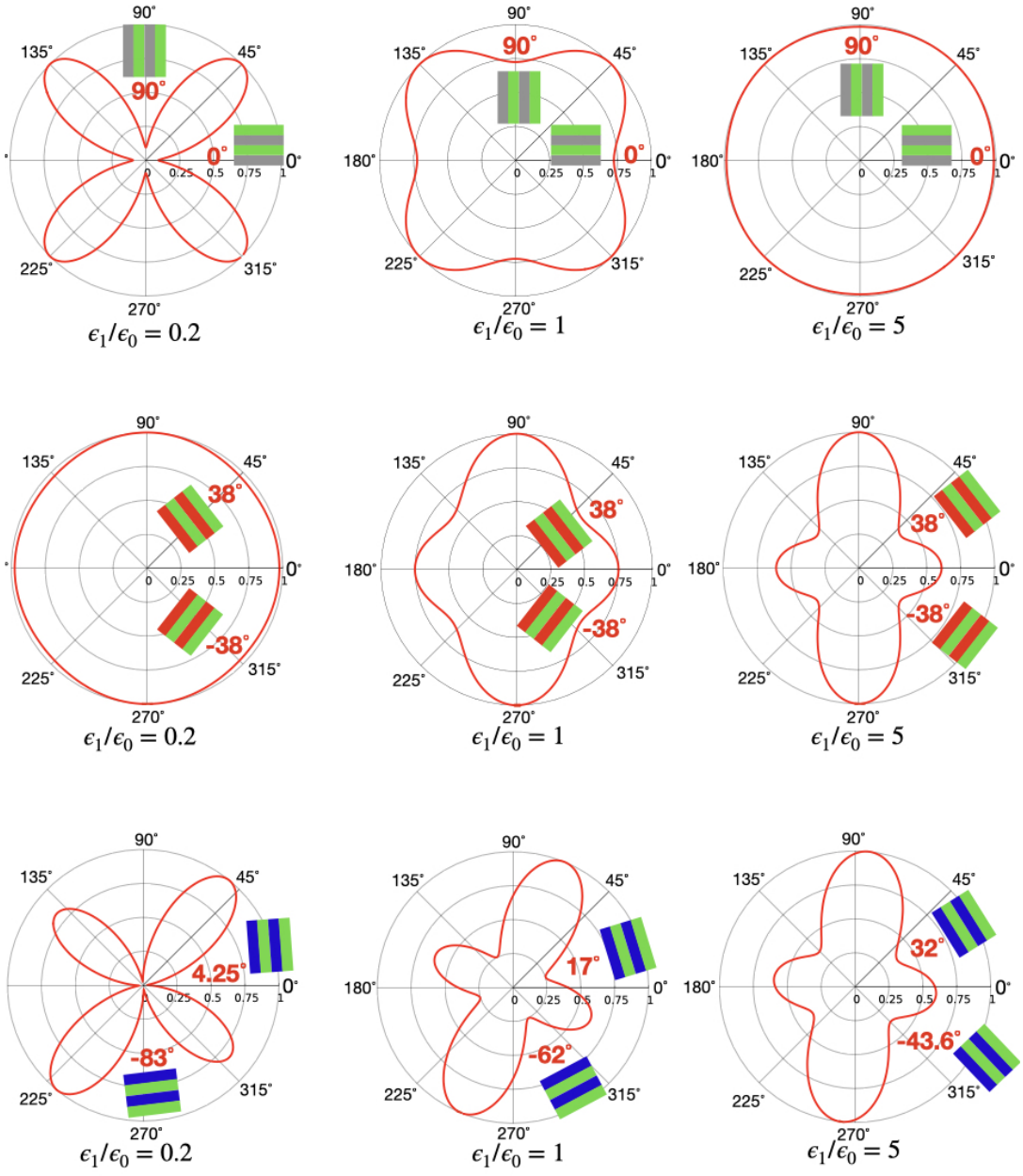

Figure 4.18: Polar representation of the orientation dependence of the elastic energy (scaled to the maximum value) for mismatching pairs of variants. The calculations are for fixed strain boundary conditions $\langle \epsilon_{ij} \rangle = 0$.

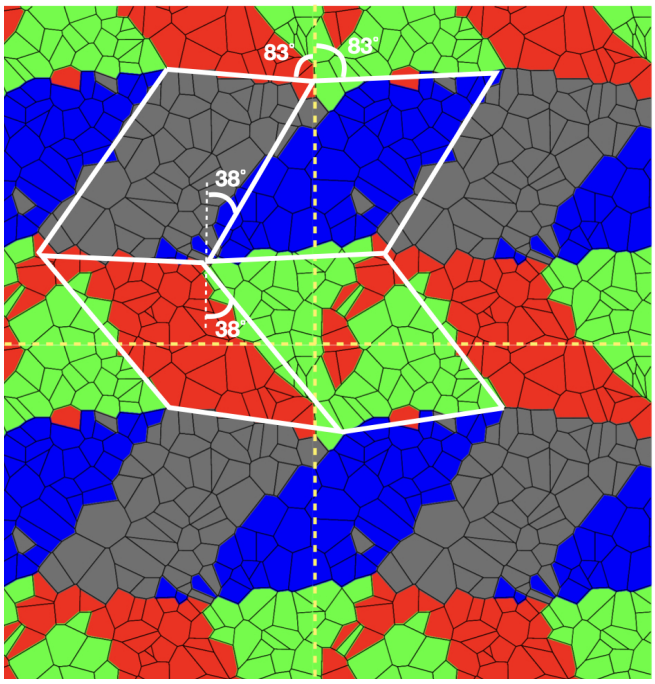

Figure 4.19: 2×2 supercell of the periodic solution Figure 4.17(a) with $\epsilon_1/\epsilon_0 = 0.2$. The structure's geometry is sketched and highlights the interface orientations between the variants.

The white lines emphasize the structure and illustrate that for this microstructure all interface orientations are optimal and not affected by periodicity constraints.

The last example concerns a case where the grains are oriented randomly, i.e., rotated around the [001] axis, as depicted in the left panel of Figure 4.20. Like in the previous publication [62], the response to an uniaxial strain $\langle \epsilon_{xx} \rangle$ is less pronounced than in the cases with uniform grain orientation above. The center panel shows the equilibrium microstructure for vanishing mean strain, whereas the right panel is for a rather high tensile strain $\langle \epsilon_{xx} \rangle / \epsilon_1 = 2.5$.

For a clockwise rotation of a grain by an angle α around the [001] axis, the relevant components of the eigenstrain tensor become

$$\begin{aligned}
\epsilon^{(0)\prime}_{xx} &= \cos^2\alpha\, \epsilon^{(0)}_{xx} + 2\cos\alpha \sin\alpha\, \epsilon^{(0)}_{xy} + \sin^2\alpha\, \epsilon^{(0)}_{yy} && (4.29)\\
\epsilon^{(0)\prime}_{xy} &= -\sin\alpha\cos\alpha\, \epsilon^{(0)}_{xx} + (\cos^2\alpha - \sin^2\alpha)\, \epsilon^{(0)}_{xy} \\
&\quad + \sin\alpha\cos\alpha\, \epsilon^{(0)}_{yy} && (4.30)\\
\epsilon^{(0)\prime}_{yy} &= \sin^2\alpha\, \epsilon^{(0)}_{xx} - 2\cos\alpha\sin\alpha\, \epsilon^{(0)}_{xy} + \cos^2\alpha\, \epsilon^{(0)}_{yy}. && (4.31)
\end{aligned}$$

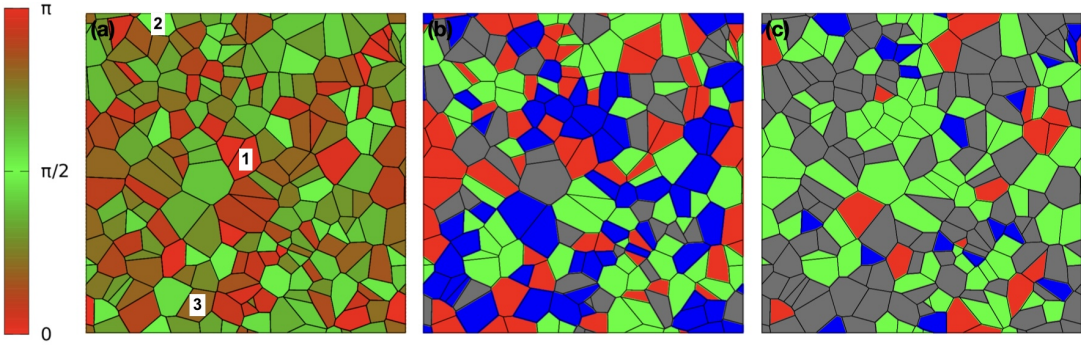

Figure 4.20: Equilibrium variant distribution with random grain orientation. **(a)** Grain orientation map corresponding to the microstructure. The grain rotation angle in the color bar is given in radian (modulo π due to symmetry). The rotation axis is along the [001] direction. The microstructure consists of 200 grains and tensile strain in horizontal direction is **(b)** $\langle\epsilon_{xx}\rangle/\epsilon_1 = 0$ and **(c)** $\langle\epsilon_{xx}\rangle/\epsilon_1 = 2.5$. In all figures $\epsilon_0 = \epsilon_1$, and the chosen Poisson ratio is $\nu = 1/4$ (i.e., $\lambda = \mu$). The grains have a random orientation based on a uniform distribution.

Therefore, for the chosen example, a rotation by $\pi/4$ converts the tetragonal deformation to a shear transformation (and vice versa), apart from the eigenstrain contribution in z direction, which only affects the energetic cost but not the strain distribution. Therefore, we expect for a tensile load in [100] direction, that grains with orientation close to 0 or π (the response is π-periodic), to have a tetragonal spin preferentially being in state $+1$; for a rotation near 90°, the tetragonal contribution prefers the $s = -1$ state. For both of these orientations (and nearby values), the shear contributions are indifferent, as they have only a vanishing or small contribution $\epsilon_{xx}^{(0)'}$, which is sensitive to the tensile strain. As explained above, for rotations by approximately $\pi/4$ (or $3\pi/4$) the role of shear and tetragonal deformations is exchanged, but the original tetragonal transformation has an energy penalty due to the contribution in z direction for the used plane strain setup.

For some selected grains in Figure 4.20 the change of the variant states is discussed in the following. Grain 1 has an orientation close to 0 (or π). In the zero strain state, it is marked in red, hence the shear spin equals -1 and the tetragonal component is also -1. Under stronger tensile load it turns grey, hence both spins flipped their sign, leading to a stronger alignment with the external field. Grain 2 has an orientation close to 90°, is originally red (shear: -1, tetragonal -1) and becomes blue in the right panel. In this case, the dominant effect is to have a negative tetragonal spin values, as discussed above. Finally, for grain 3, which has a mixed orientation, we have effectively a transition from blue to grey, where the positive shear spin is relevant due to the orientation near $\pi/4$,

whereas the flipping tetragonal spin component is less relevant.

4.2.3 Conclusions

Here we demonstrate that the selection of multiple grain variants can be mapped to an Ising problem for specific conditions and how the energy minimization can be performed efficiently via quantum annealing. The superiority of QA compared to classical computing has been shown in previous publication [62]. The multiplicity of the domains together with the long-range, anisotropic and shape-dependant character of the elastic interactions make the determination of the ground state a particularly difficult problem, and therefore QA opens completely new possibilities. The central result here is the generalization to multi-variant systems and the analysis of the arising microstructures. Also, we demonstrate how the proper coefficients of the Ising model can be obtained from general linear elastic calculations.

To illustrate the approach, we use a four variant per grain case, where each grain is represented by two Ising spins. We use a linear combination of shear and tetragonal deformations to demonstrate the methodology. As a result, the equilibrium microstructure depends on the applied external strains (or stresses), as well as on the strength of the distortions induced by the different variants. The observed patterns can largely be explained by computations of the anisotropy of laminar arrangements of the different variants, showing that the mismatch of neighboring domains dominates the overall elastic energy.

From a fundamental perspective, it is important to investigate whether QA is superior to classical global minimization strategies such as simulated annealing. The present example of long-range elastic interactions between misfitting variants falls into the class of random spin glass models, and it is plausible that — at least for small system sizes — the minimization directly benefits from multiqubit tunneling [268, 269]. From the perspective of the investigated application, suitable scenarios to study this effect could be constructed through specific arrangements of grains such that the underlying energy landscape has controlled “false minima”, similar to [269]. However, from a materials science perspective, large numbers of grains are usually more representative and desirable, and therefore it is less likely that the tunneling advantage can be detected in a straightforward way in the investigated examples. Moreover, beyond the order of 200 grains, the use of hybrid approaches is currently required and used in the present work, which changes the minimization dynamics. The results indicate that the ground state microstructural configuration is not always found, requiring repeated simulations, but in general the observed structures and interfaces are in agreement with the expected true minimum energy interface orientations, as demonstrated in this work.

For many applications in materials science, the formation of microstructures is critical and efficient simulation approaches to support experimental findings are highly desired. Our developed quantum annealing approach presents an efficient new technological opportunity for the determination of equilibrium microstructures with long-range elastic interactions, where multiple variants need to be considered.

4.3 Conclusions on Quantum Annealing for Batteries

Quantum technologies are only beginning to influence methodologies and modeling approaches in materials science. For batteries, the applications of QA remain in their infancy. Currently, the biggest limitation is the requirement to map the problem of interest as a minimization of an Ising Hamiltonian. Nonetheless, as discussed throughout this chapter, recent developments have demonstrated successful implementations [35, 36].

For Solid-State Batteries (SSBs), the mechanical behavior and microstructure of active components are central to performance. Consequently, the possibility of simulating these aspects via QA, which outputs results with remarkable speed, is compelling. Here, we have focused on the mechanics and microstructure question, mainly regarding the lithium metal anode. We have developed a modeling strategy that maps deformation twinning in BCC structures to the minimization of elastic energy, and solves it via a hybrid QA approach. To accurately capture twin formation and growth, interfacial energies were also incorporated. In addition, we extended the model to include multiple grain variants, which could reflect, e.g., the diversity of phases, twin configurations and deformation states found in microstructures.

Potentially, QA could also be used to extend the thermodynamics investigation from chapter 3. Atomistic simulations tend to suffer from slow convergence of ionic positions. This bottleneck had already been explored via QA to, e.g., optimize ionic configurations in battery materials [36] and high-entropy alloys [78]. This opens the door to similar approaches that could speed up the determination of positions of alloying atoms (as done in section 3.1 for sodium and lithium atoms) or of surface atoms (as done in section 3.2 for lithium and lithium-sodium carbonates). If generalized further, the possibilities are endless. Such models could support interface studies, a key point in SSBs. They could even dramatically enhance high-throughput screening across vast compositional spaces, a staple question in materials science.

Hence, in the context of QA for battery applications, our findings demonstrate that microstructure optimization via QA is not only feasible, but also promising. It is reasonable to expect that in the future, quantum technologies will have a strong influence on modeling and simulation of battery materials.

Chapter 5

Conclusions

As displayed throughout this thesis, Solid-State Batteries (SSBs) are regarded as promising candidate for the next-generation electrochemical cells. The market demands longer-range driving vehicles, safer cells and lighter consumer electronics, making this technology a valuable alternative to today's standard Li-ion batteries. However, the challenges surrounding these cells are non-trivial, and significant efforts are currently being made by both academia and industry to establish SSBs as top choice in electrochemical energy storage devices.

Here, we have investigated the mechanics and microstructure of lithium from both a fundamental and application perspective, merging experimental and computational methods to deliver a comprehensive study of this important anode material. Additionally, to complement the mechanics investigations and seeking to explain experimental observations in remarkable solid-state cells, we have tackled thermodynamics and surface effects, studying the interface between Lithium Metal Anode (LMA) and lithium lanthanum zirconium oxide - $Li_7La_3Zr_2O_{12}$ (LLZO) as Solid Electrolyte (SE). Finally, we have advanced our studies by developing novel quantum computing models that augment classical approaches.

In summary, the main conclusions and contributions of this work, as well as future research directions, are discussed below.

Research question 1: How does lithium behave mechanically? Do alloying and processing affect the mechanics of anode foils? Can we understand the correlation between processing, microstructure and mechanical properties?

It is thought that one of the main present issues with SSBs is the lack of understanding of the mechanics of the active components. Mainly the metal anodes were poorly characterized regarding its mechanical properties and microstructure. Furthermore, as the lithium filaments in SSBs appear on small length scales, understanding how these small lithium volumes behave can support future work in the battery field. Even though it could be theoretically assumed that lithium would purely behave as any other BCC metal, a detailed, focused and direct investigation was much needed. As it was shown

and discussed in this thesis, lithium is indeed intricate and challenging to characterize. Nevertheless, we succeeded to get a deep understanding into the underlying mechanics.

The atomistic simulations performed in this work show lithium as an extremely anisotropic material. The anisotropy is not only present in elasticity, but also in plasticity, with nanopillars of different orientations plastically deforming with different deformation mechanisms. This point had already been found in other BCC structures, but it had, until now, not been reported for lithium. Additionally, size effects are found at these nanopillars. The size effects arise from inherent plasticity constraints and are more significant for slip-based deformed pillars than for twinning-based deformed pillars. From the simulation results, these anisotropic and size effects are found in nanometer sized specimens, and we were able to map how the mechanical properties vary with strain rate, specimen size, orientation and load type.

Experimentally, it was found that alloying the lithium with sodium does not cause significant changes on the metal foil. However, the rolling of foils leads to important changes on hardness and microstructure of the metal anodes. Thus, even lithium possessing a low melting point and strong creep tendencies, rolled foils are still subjected to effects from the manufacturing processes. Most likely, rolled metal anodes will present a strong texture and strain hardening.

Future research work could be focused on the influence of these aforementioned mechanical aspects on electrochemical behavior, and subsequent inclusion in electrochemical models. Therefore, it would be beneficial to develop straightforward ways of accounting anisotropy and size effects in well-established formulations in both the mechanics and battery fields.

Research question 2: What are the main aspects influencing the solid-solid interface between LMA and LLZO? How to improve this interface to obtain longer-lasting cells?

The interface between LMA and SE is another challenge of these solid cells. Due to low lithium self diffusion, pores are generated at the interface, and frequently an external stack pressure is applied on the cell to close these pores. Nevertheless, this generates high mechanical loads and the whole pressure setup is not desired from an application point of view.

Here, we have worked towards obtaining solid-state cells that do not require stack pressure. We optimized the interface by alloying lithium with sodium, achieving stable cycling without the need for an external load. We found that, in this case, mechanics are not a central factor. Instead, the thermodynamics and chemistry of the system are more relevant. The mixture of lithium and sodium promotes a carbonate cleansing of

the interface, exchanging the lithiophobic lithium carbonate to the lithiophilic lithium-sodium carbonate. Besides, a beneficial 3D microstructure is formed thanks to the spinodal instability. To obtain theoretical predictions of the sodium concentration at which spinodal decomposition is expected to begin, we dived deeper into the thermodynamics of the lithium-sodium system. We highlight that even in a pure thermodynamic analysis, the inclusion of mechanical effects significantly alters the equilibrium of the system, and even though the mechanics are not the focal point, it should not be ignored.

Future work in this direction could be focused on including kinetics and electrochemical effects into the microstructure formation analysis. The mechanics are also assumed as isotropic and plasticity is not considered. We know from the mechanistic studies that these simplifications are not completely true for lithium. Therefore, these aspects could still be used to improve the current microstructure formation model. Regarding the carbonate formation, experimental validation measuring the surface energy of the carbonates and their affinity with lithium metal would support immensely the computational results hereby reported. Besides, more efficient ways of investigating surfaces via atomistic models, e.g., via quantum computing regarding the positioning of the adsorpted atoms, would be highly beneficial.

Research question 3: Is it possible to use quantum computing to simulate SSBs materials?

As demonstrated in this work, quantum computing technologies, particularly Quantum Annealing (QA), can already have a remarkable impact on materials science modeling. Elastic deformations and interface effects are formulated as Ising model and used to describe deformation twinning and microstructure formation in lithium metal. Large scale simulations with hybrid schemes are performed. Particularly, polycrystalline simulations are carried out, which are usually way beyond what atomistic methods can perform in reasonable computational times. The results can be benchmarked with atomistic simulations for single crystals and experiments for polycrystals. Hence, the QA simulations complement and expand the atomistic simulations on lithium mechanics. To pave the way to realistic microstructural equilibrium prediction, we have extended the shear-only description to include a multi-variant selection between different deformation possibilities, e.g., tetragonal transformations. It is clear that many more variants would have to be considered. In the lithium case, for instance, anti-twinning and slip cases are also relevant. Nevertheless, the current results show that it is possible to predict the behavior of complex systems within the defined physical models and constraints.

Future research could include the use of QA to optimize ionic configurations to accelerate the surface atomistic simulations performed in this work. SSBs interfaces and grain

boundaries studies could also strongly benefit from such approach. Besides, screening of the huge search materials space could be made even faster, moving past machine learning techniques.

Currently, the key challenge lies in translating physical problems into the strict QA formulations, while the main advantage is the acceleration of existing computational models. Pottentially, large systems could be studied in dramatically reduced time-frames. In summary, quantum computing serves today as a complementary tool that can substantially speed up discoveries and predictions, also for battery materials. Yet, its future trajectory and ultimate impact on computational materials science remains an open question.

Publications and Conferences

In this section, all publications and scientific conferences that I was a part of and contributed to during my PhD work are listed.

Published Peer Reviewed Journal Publications

Lara Caroline Pereira dos Santos, Antje Dollmann, Christian Greiner, Daniel Grüner, Yann Le Bouar, Robert Spatschek. **Discover Materials**. *Modeling of deformation twinning in bcc metals via quantum annealing*. 2026. https://doi.org/10.1007/s43939-026-00612-8.

Lara Caroline Pereira dos Santos, Daniel Grüner, Robert Spatschek. **Modelling and Simulation in Materials Science and Engineering**. *Atomistic modeling of the mechanical properties and deformation behavior of lithium*. 2025. https://doi.org/10.1088/1361-651X/ae0b9c.

Lara Caroline Pereira dos Santos, Markus Mann, Christian Schwab, Dina Fattakhova-Rohlfing, Martin Finsterbusch, Robert Spatschek. **Next Materials**. *Revisiting the Li-Na system: Ab initio based description of the low temperature thermodynamics for battery applications*. 2025. https://doi.org/10.1016/j.nxmate.2025.101202.

Markus Mann, Christian Schwab, **Lara Caroline Pereira dos Santos**, Robert Spatschek, Dina Fattakhova-Rohlfing, Martin Finsterbusch. **Energy Storage Materials**. *Improving the rate performance of lithium metal anodes: In-situ formation of 3D interface structures by mechanical mixing with sodium metal*. 2025. https://doi.org/10.1016/j.ensm.2024.103975.

Lara Caroline Pereira dos Santos, Tian Hang, Roland Sandt, Martin Finsterbusch, Yann Le Bouar, Robert Spatschek. **Physical Review Research**. *Elastic energy driven*

multivariant selection in martensites via quantum annealing. 2024. https://doi.org/10.1103/PhysRevResearch.6.023076.

Belen Celik, Roland Sandt, **Lara Caroline Pereira dos Santos**, Robert Spatschek. **Batteries**. *Prediction of battery cycle life using early-cycle data, machine learning and data management*. 2022. https://doi.org/10.3390/batteries8120266.

Oral Conference Presentations

Lara Caroline Pereira dos Santos, Robert Spatschek. **2024 MRS - Materials Research Society - Spring Meeting and Exhibit**. *Mechanical properties and deformation behavior of lithium metal*. https://www.mrs.org/meetings-events/annual-meetings/archive/meeting/presentations/view/2024-mrs-spring-meeting/2024-mrs-spring-meeting-4000307.

Lara Caroline Pereira dos Santos, Markus Mann, Martin Finsterbusch, Robert Spatschek. **2024 InMa - Characterization and Properties of Interface Dominated Materials**. *Understanding interface structure formation in solid-state batteries through ab initio simulations and thermodynamics*. https://events.hifis.net/event/1738/.

Poster Conference Presentation

Lara Caroline Pereira dos Santos, Robert Spatschek. **2025 ELECTRA Battery Symposium**. *Microstructure, mechanics and interfaces in solid-state batteries*. https://iffindico.fz-juelich.de/event/15/.

Bibliography

[1] B. Scrosati. History of lithium batteries. *Journal of solid state electrochemistry*, 15(7):1623–1630, 2011.

[2] P. Selinis and F. Farmakis. Review—a review on the anode and cathode materials for lithium-ion batteries with improved subzero temperature performance. *Journal of The Electrochemical Society*, 169(1):010526, jan 2022.

[3] S. He, S. Huang, S. Wang, I. Mizota, X. Liu, and X. Hou. Considering critical factors of silicon/graphite anode materials for practical high-energy lithium-ion battery applications. *Energy & Fuels*, 35(2):944–964, 2021.

[4] N. Boaretto, I. Garbayo, S. Valiyaveettil-SobhanRaj, A. Quintela, C. Li, M. Casas-Cabanas, and F. Aguesse. Lithium solid-state batteries: State-of-the-art and challenges for materials, interfaces and processing. *Journal of Power Sources*, 502:229919, 2021.

[5] P. Albertus, S. Babinec, S. Litzelman, and A. Newman. Status and challenges in enabling the lithium metal electrode for high-energy and low-cost rechargeable batteries. *Nature Energy*, 3:16–21, 2018.

[6] Z. Zhang, Y. Shao, B. Lotsch, Y.-S. Hu, H. Li, J. Janek, L. F. Nazar, C.-W. Nan, J. Maier, M. Armand, et al. New horizons for inorganic solid state ion conductors. *Energy & Environmental Science*, 11(8):1945–1976, 2018.

[7] B. Horstmann, J. Shi, R. Amine, M. Werres, X. He, H. Jia, F. Hausen, I. Cekic-Laskovic, S. Wiemers-Meyer, J. Lopez, D.o Galvez-Aranda, F. Baakes, D. Bresser, C. C. Su, Y. Xu, W. Xu, P. Jakes, R. A. Eichel, E. Figgemeier, U. Krewer, J. M. Seminario, P. B. Balbuena, C. Wang, S. Passerini, Y. Shao-Horn, M. Winter, K. Amine, R. Kostecki,

and A. Latz. Strategies towards enabling lithium metal in batteries: interphases and electrodes. *Energy Environ. Sci.*, 14:5289–5314, 2021.

[8] Y. Chen, K. Wen, T. Chen, X. Zhang, M. Armand, and S. Chen. Recent progress in all-solid-state lithium batteries: The emerging strategies for advanced electrolytes and their interfaces. *Energy Storage Materials*, 31:401–433, 2020.

[9] L. Bai, W. Xue, Y. Li, X. Liu, Y. Li, and J. Sun. The interfacial behaviours of all-solid-state lithium ion batteries. *Ceramics International*, 44(7):7319–7328, 2018.

[10] Y. Lu, L. Li, Q. Zhang, Z. Niu, and J. Chen. Electrolyte and interface engineering for solid-state sodium batteries. *Joule*, 2(9):1747–1770, 2018.

[11] A. Sakuda, A. Hayashi, and M. Tatsumisago. Recent progress on interface formation in all-solid-state batteries. *Current Opinion in Electrochemistry*, 6(1):108–114, 2017.

[12] C. Cao, Z. B. Li, X. L. Wang, X. B. Zhao, and W. Q. Han. Recent advances in inorganic solid electrolytes for lithium batteries. *Frontiers in Energy Research*, 2(Jun):1–10, 2014.

[13] A. Kim, S. Woo, M. Kang, H. Park, and B. Kang. Research progresses of garnet-type solid electrolytes for developing all-solid-state li batteries. *Frontiers in Chemistry*, 8(Jun):1–13, 2020.

[14] T. Krauskopf, F. H. Richter, W. G. Zeier, and J. Janek. Physicochemical concepts of the lithium metal anode in solid-state batteries. *Chemical Reviews*, 120(15):7745–7794, 2020. PMID: 32786669.

[15] J. Biao, C. Bai, J. Ma, M. Liu, F. Kang, Y. Cao, and Y.-B. He. Perspectives on li dendrite penetration in $Li_7La_3Zr_2O_{12}$-based solid-state electrolytes and batteries: Materials, interfaces, and charge transfer. *Advanced Energy Materials*, 14(10):2303128, 2024.

[16] J. Wang, L. Chen, H. Li, and F. Wu. Anode interfacial issues in solid-state li batteries: Mechanistic understanding and mitigating strategies. *ENERGY & ENVIRONMENTAL MATERIALS*, 6(4):e12613, 2023.

[17] J.-M. Doux, H. Nguyen, D. H. S. Tan, A. Banerjee, X. Wang, E. A. Wu, C. Jo, H. Yang, and Y. S. Meng. Stack pressure considerations for room-temperature all-solid-state lithium metal batteries. *Advanced Energy Materials*, 10(1):1903253, 2020.

[18] S. H. Kim, K. Kim, H. Choi, D. Im, S. Heo, and H. S. Choi. In situ observation of lithium metal plating in a sulfur-based solid electrolyte for all-solid-state batteries. *J. Mater. Chem. A*, 7:13650–13657, 2019.

[19] Y. Lu, C.-Z. Zhao, H. Yuan, X.-B. Cheng, J.-Q. Huang, and Q. Zhang. Critical current density in solid-state lithium metal batteries: Mechanism, influences, and strategies. *Advanced Functional Materials*, 31(18):2009925, 2021.

[20] S. E. Sandoval, C. G. Haslam, B. S. Vishnugopi, D. W. Liao, J. S. Yoon, S. H. Park, Y. Wang, D. Mitlin, K. B. Hatzell, D. J. Siegel, P. P. Mukherjee, N. P. Dasgupta, J. Sakamoto, and M. T. McDowell. Electro-chemo-mechanics of anode-free solid-state batteries. *Nature Materials*, 24(5):673–681, 2025.

[21] L. Porz, T. Swamy, B. W. Sheldon, D. Rettenwander, T. Frömling, H. L. Thaman, S. Berendts, R. Uecker, W. C. Carter, and Y. M. Chiang. Mechanism of lithium metal penetration through inorganic solid electrolytes. *Advanced Energy Materials*, 7(20):1701003, 2017.

[22] L. Xu, S. Tang, Y. Cheng, K. Wang, J. Liang, C. Liu, Y.-C. Cao, F. Wei, and L. Mai. Interfaces in solid-state lithium batteries. *Joule*, 2(10):1991–2015, 2018.

[23] B. Zhang, B. Yuan, X. Yan, X. Han, J. Zhang, H. Tan, C. Wang, P. Yan, H. Gao, and Y. Liu. Atomic mechanism of lithium dendrite penetration in solid electrolytes. *Nature Communications*, 16(1):1906, Feb 2025.

[24] B. Gao, R. Jalem, H.-K. Tian, and Y. Tateyama. Revealing atomic-scale ionic stability and transport around grain boundaries of garnet $Li_7La_3Zr_2O_{12}$ solid electrolyte. *Advanced Energy Materials*, 12(3):2102151, 2022.

[25] S. Monismith, J. Qu, and R. Dingreville. Grain-boundary fracture mechanisms in $Li_7La_3Zr_2O_{12}$ (llzo) solid electrolytes: When phase transformation acts as a temperature-dependent toughening mechanism. *Journal of the Mechanics and Physics of Solids*, 160:104791, 2022.

[26] N. Seitzman, H. Guthrey, D. B. Sulas, H. A. S. Platt, M. Al-Jassim, and S. Pylypenko. Toward all-solid-state lithium batteries: Three-dimensional visualization of lithium migration in β-Li_3PS_4 ceramic electrolyte. *Journal of The Electrochemical Society*, 165(16):A3732–A3737, 2018.

[27] Y. Shi, J. Wan, G.-X. Liu, T.-T. Zuo, Y.-X. Song, B. Liu, Y.-G. Guo, R. Wen, and L.-J. Wan. Interfacial evolution of lithium dendrites and their solid electrolyte interphase shells of quasi-solid-state lithium-metal batteries. *Angewandte Chemie International Edition*, 59(41):18120–18125, 2020.

[28] W. Ping, C. Wang, Z. Lin, E. Hitz, C. Yang, H. Wang, and L. Hu. Reversible short-circuit behaviors in garnet-based solid-state batteries. *Advanced Energy Materials*, 10(25), 2020.

[29] Y. Pang, J. Pan, J. Yang, S. Zheng, and C. Wang. Electrolyte/electrode interfaces in all-solid-state lithium batteries: A review. *Electrochemical Energy Reviews*, 4(2):169–193, 2021.

[30] R. H. Basappa, T. Ito, and H. Yamada. Contact between garnet-type solid electrolyte and lithium metal anode: Influence on charge transfer resistance and short circuit prevention. *Journal of The Electrochemical Society*, 164(4):A666, feb 2017.

[31] A. M. Nolan, Y. Zhu, X. He, Q. Bai, and Y. Mo. Computation-accelerated design of materials and interfaces for all-solid-state lithium-ion batteries. *Joule*, 2(10):2016–2046, 2018.

[32] R. Sandt, Y. Wang, and R. Spatschek. Investigation of mechanical properties of garnet structured $Li_7La_3Zr_2O_{12}$ under Al^{3+} and Ta^{5+} co-substitutions. *Solid State Ion.*, 402:116364, 2023.

[33] B. Celik, R. Sandt, L. C. P. dos Santos, and R. Spatschek. Prediction of battery cycle life using early-cycle data, machine learning and data management. *Batteries*, 8(12), 2022.

[34] Y. Zhao, R. Wang, and E. Martínez-Pañeda. A phase field electro-chemo-mechanical formulation for predicting void evolution at the Li–electrolyte interface in all-solid-state batteries. *Journal of the Mechanics and Physics of Solids*, 167:104999, 2022.

[35] R. Sandt, Y. Le Bouar, and R. Spatschek. Microstructure equilibration with consideration of elastic and interfacial interactions via quantum annealing with application to the solid electrolyte llzo. *Phys. Rev. Res.*, 6:033047, Jul 2024.

[36] T. Binninger, Y.-Y. Ting, P. M. Kowalski, and M. H. Eikerling. Optimization of ionic configurations in battery materials by quantum annealing. *Phys. Rev. B*, 110:L180202, Nov 2024.

[37] A. De Gol, K. B. Dermenci, L. Farkas, and M. Berecibar. Electro-chemo-mechanical degradation in solid-state batteries: A review of microscale and multiphysics modeling. *Advanced Energy Materials*, 14(47):2403255, 2024.

[38] T. H. Wan and F. Ciucci. Electro-chemo-mechanical modeling of solid-state batteries. *Electrochimica Acta*, 331:135355, 2020.

[39] Y. Wang and Y. T. Cheng. A nanoindentation study of the viscoplastic behavior of pure lithium. *Scripta Materialia*, 130:191–195, 2017.

[40] E. G. Herbert, S. A. Hackney, V. Thole, N. J. Dudney, and P. Sudharshan Phani. Nanoindentation of high-purity vapor deposited lithium films: A mechanistic rationalization of the transition from diffusion to dislocation-mediated flow. *Journal of Materials Research*, 33(10):1361–1368, 2018.

[41] E. G. Herbert, S. A. Hackney, N. J. Dudney, and P. Sudharshan Phani. Nanoindentation of high-purity vapor deposited lithium films: The elastic modulus. *Journal of Materials Research*, 33(10):1335–1346, 2018.

[42] A. Masias, N. Felten, R. Garcia-Mendez, J. Wolfenstine, and J. Sakamoto. Elastic, plastic, and creep mechanical properties of lithium metal. *Journal of Materials Science*, 54(3):2585–2600, 2019.

[43] A. Masias, N. Felten, and J. Sakamoto. Characterizing the mechanical behavior of lithium in compression. *Journal of Materials Research*, 36(3):729–739, 2021.

[44] C. D. Fincher, D. Ojeda, Y. Zhang, G. M. Pharr, and M. Pharr. Mechanical properties of metallic lithium: from nano to bulk scales. *Acta Materialia*, 186:215–222, 2020.

[45] J. Aspinall, D. E. J. Armstrong, and M. Pasta. EBSD-coupled indentation: nanoscale mechanics of lithium metal. *Materials Today Energy*, 30:101183, 2022.

[46] E. Darnbrough, J. Aspinall, M. Pasta, and D. E. J. Armstrong. Elastic and plastic mechanical properties of lithium measured by nanoindentation. *Materials & Design*, 233:112200, 2023.

[47] M. Lu, N. Kanazi, E. Lin, and S. Xia. Size- and temperature-dependent mechanical properties of metallic lithium. *Extreme Mechanics Letters*, 61:102022, 2023.

[48] S. Kalnaus, N. J. Dudney, A. S. Westover, E. Herbert, and S. Hackney. Solid-state batteries: The critical role of mechanics. *Science*, 381(6664):eabg5998, 2023.

[49] S. P. Timoshenko and J. N. Goodier. *Theory of Elasticity*. McGraw-Hill, New York, 2nd edition, 1951.

[50] S. Nemat-Nasser and M. Hori. *Micromechanics: Overall Properties of Heterogeneous Materials*. Elsevier Science Publishers B.V., 1993.

[51] L. D. Landau and E. M. Lifshitz. *Theory of Elasticity: Volume 7*. Pergamon Press, U.K., 1970.

[52] A. B. Finnila, M. A. Gomez, C. Sebenik, C. Stenson, and J. D. Doll. Quantum annealing: A new method for minimizing multidimensional functions. *Chemical Physics Letters*, 219(5-6):343–348, 1994.

[53] J. Brooke, D. Bitko, T. F. Rosenbaum, and G. Aeppli. Quantum Annealing of a Disordered Magnet. *Science*, 284:779–781, 1999.

[54] T. Kadowaki and H. Nishimori. Quantum annealing in the transverse Ising model. *Phys. Rev. E*, 58(5):5355–5363, 1998.

[55] S. Morita and H. Nishimori. Mathematical foundation of quantum annealing. *J. Math. Phys.*, 49:125210, 2008.

[56] A. Rajak, S. Suzuki, A. Dutta, and B. K. Chakrabarti. Quantum annealing: an overview. *Phil. Trans. R. Soc. A*, 381:20210417, 2023.

[57] R. H. Warren. Mathematical methods for a quantum annealing computer. *Adv. Appl. Math.*, 3(3):82–90, 2018.

[58] M. W. Johnson, M. H. Amin, S. Gildert, T. Lanting, F. Hamze, N. Dickson, R. Harris, A. J. Berkley, J. Johansson, P. Bunyk, E. M. Chapple, C. Enderud, J. P. Hilton, K. Karimi, E. Ladizinsky, N. Ladizinsky, T. Oh, I. Perminov, C. Rich, M. C. Thom, E. Tolkacheva, C. J. S. Truncik, S. Uchaikin, J. Wang, B. Wilson, and G. Rose. Quantum annealing with manufactured spins. *Nature*, 473:194–198, 2011.

[59] S. Boixo, T. F. Rønnow, S. V. Isakov, Z. Wang, D. Wecker, D. A. Lidar, J. M. Martinis, and M. Troyer. Evidence for quantum annealing with more than one hundred qubits. *Nat. Phys.*, 10:218–224, 2014.

[60] A. Lucas. Ising formulations of many NP problems. *Front. Phys.*, 2(5), 2014.

[61] T. Lanting, A. J. Przybysz, A. Yu. Smirnov, F. M. Spedalieri, M. H. Amin, A. J. Berkley, R. Harris, F. Altomare, S. Boixo, P. Bunyk, N. Dickson, C. Enderud, J. P. Hilton, E. Hoskinson, M. W. Johnson, E. Ladizinsky, R. Neufeld, T. Oh, I. Perminov, C. Rich, M. C. Thom, E. Tolkacheva, S. Uchaikin, A. B. Wilson, and G. Rose. Entanglement in a quantum annealing processor. *Physical Review X*, 4(2):021041, 2014.

[62] R. Sandt, Y. Le Bouar, and R. Spatschek. Quantum annealing for microstructure equilibration with long-range elastic interactions. *Sci. Rep.*, 13:6036, 2023.

[63] R. Sandt and R. Spatschek. Efficient low temperature Monte Carlo sampling using quantum annealing. *Sci. Rep.*, 13:6754, 2023.

[64] J. Raymond, R. Stevanovic, W. Bernoudy, K. Boothby, C. C. McGeoch, A. J. Berkley, P. Farré, and A. D. King. Hybrid quantum annealing for larger-than-QPU lattice-structured problems. *ACM Trans. Quantum Comput.*, 2023.

[65] J. J. Berwald. The Mathematics of Quantum-Enabled Applications on the D-Wave Quantum Computer. *Not. Am. Math. Soc.*, 66(6):832–841, 2019.

[66] D-Wave Leap quantum cloud service. https://cloud.dwavesys.com. [Online; accessed 6-December-2023].

[67] J. Nelson, M. Vuffray, A. Y. Lokhov, T. Albash, and C. Coffrin. High-Quality Thermal Gibbs Sampling with Quantum Annealing Hardware. *Phys. Rev. Appl.*, 17:044046, 2022.

[68] M. Vuffray, C. Coffrin, Y. A. Kharkov, and A. Y. Lokhov. Programmable Quantum Annealers as Noisy Gibbs Samplers. *PRX Quantum*, 3:020317, 2022.

[69] S. Mandrà, Z. Zhu, and H.G. Katzgraber. Exponentially Biased Ground-State Sampling of Quantum Annealing Machines with Transverse-Field Driving Hamiltonians. *Physical Review Letters*, 118:070502, 2017.

[70] M. S. Könz, G. Mazzola, A. J. Ochoa, H. G. Katzgraber, and M. Troyer. Uncertain fate of fair sampling in quantum annealing. *Phys. Rev. A*, 100:030303, 2019.

[71] S. Mukherjee and B. K. Chakrabarti. On the question of ergodicity in quantum spin glass phase and its role in quantum annealing. *J. Phys. Soc. Jpn.*, 88:061004, 2019.

[72] M. Yamamoto, M. Ohzeki, and K. Tanaka. Fair Sampling by Simulated Annealing on Quantum Annealer. *J. Phys. Soc. Jpn.*, 89:025002, 2020.

[73] R. Harris, Y. Sato, A. J. Berkley, M. Reis, F. Altomare, M. H. Amin, K. Boothby, P. Bunyk, C. Deng, C. Enderud, S. Huang, E. Hoskinson, M. W. Johnson, E. Ladizinsky, N. Ladizinsky, T. Lanting, R. Li, T. Medina, R. Molavi, R. Neufeld, T. Oh, I. Pavlov, I. Perminov, G. Poulin-Lamarre, C. Rich, A. Smirnov, L. Swenson, N. Tsai, M. Volkmann, J. Whittaker, and J. Yao. Phase transitions in a programmable quantum spin glass simulator. *Science*, 361:162–165, 2018.

[74] P. Kairys, A.D. King, I. Ozfidan, K. Boothby, J. Raymond, A. Banerjee, and T.S. Humble. Simulating the Shastry-Sutherland Ising Model Using Quantum Annealing. *PRX Quantum*, 1:020320, 2020.

[75] B. Camino, J. Buckeridge, P. A. Warburton, V. Kendon, and S. M. Woodley. Quantum computing and materials science: A practical guide to applying quantum annealing to the configurational analysis of materials. *J. Appl. Phys.*, 133:221102, 2023.

[76] K. Kitai, J. Guo, S. Ju, S. Tanaka, K. Tsuda, J. Shiomi, and R. Tamura. Designing metamaterials with quantum annealing and factorization machines. *Phys. Rev. Res.*, 2:013319, 2020.

[77] K. Hatakeyama-Sato, T. Kashikawa, K. Kimura, and K. Oyaizu. Tackling the challenge of a huge materials science search space with quantum-inspired annealing. *Advanced Intelligent Systems*, 3(4):2000209, 2021.

[78] Z. Xu, W. Shang, S. Kim, E. Lee, and T. Luo. Quantum annealing-assisted lattice optimization. *npj Computational Materials*, 11(1):4, 2025.

[79] M. Jünger, E. Lobe, P. Mutzel, G. Reinelt, F. Rendl, G. Rinaldi, and T. Stollenwerk. Quantum Annealing versus Digital Computing: An Experimental Comparison. *ACM J. Exp. Algorithms*, 26(1):1.9, 2021.

[80] O. Parekh, J. Wendt, L. Shulenburger, A. Landahl, J. Moussa, and J. Aidun. Benchmarking Adiabatic Quantum Optimization for Complex Network Analysis. https://www.osti.gov/biblio/1459086, 2015.

[81] B. Yan and N. A. Sinitsyn. Analytical solution for nonadiabatic quantum annealing to arbitrary Ising spin Hamiltonian. *Nat. Commun.*, 13:2212, 2022.

[82] A. D. King, J. Raymond, T. Lanting, R. Harris, A. Zucca, F. Altomare, A. J. Berkley, K. Boothby, S. Ejtemaee, C. Enderud, E. Hoskinson, S. Huang, E. Ladizinsky, A. J. R. MacDonald, G. Marsden, R. Molavi, T. Oh, G. Poulin-Lamarre, M. Reis, C. Rich, Y. Sato, N. Tsai, M. Volkmann, J. D. Whittaker, J. Yao, A. W. Sandvik, and M. H. Amin. Quantum critical dynamics in a 5,000-qubit programmable spin glass. *Nature*, 617:61–66, 2023.

[83] V. A. Buryachenko. *Micromechanics of Heterogeneous Materials*. Springer, 2007.

[84] W. Voigt. Über die beziehung zwischen den beiden elasticitätsconstanten isotroper körper. *Annalen der Physik*, 274(12):573–587, 1889.

[85] A. Reuss. Berechnung der fließgrenze von mischkristallen auf grund der plastizitätsbedingung für einkristalle. *Zeitschrift für Angewandte Mathematik und Mechanik*, 9(1):49–58, 1929.

[86] R. Hill. The elastic behaviour of a crystalline aggregate. *Proceedings of the Physical Society. Section A*, 65(5):349–354, 1952.

[87] P. Atkins and J. de Paula. *Physical Chemistry*. W. H. Freeman and Company, New York, NY, 8th edition, 2006.

[88] U. R. Kattner. The calphad method and its role in material and process development. *Tecnologia em Metalurgia, Materiais e Mineração*, 13(1):3–15, 2016.

[89] L. Kaufman and H. Bernstein. *Computer Calculation of Phase Diagrams*. Academic Press, New York, 1970.

[90] J. G. Lee. *Computational materials science: an introduction*. CRC press, 2016.

[91] G. Kresse and J. Furthmüller. Efficient iterative schemes for ab initio total-energy calculations using a plane-wave basis set. *Physical Review B*, 54:11169–11186, Oct 1996.

[92] A. P. Thompson, H. M. Aktulga, R. Berger, D. S. Bolintineanu, W. M. Brown, P. S. Crozier, P. J. in 't Veld, A. Kohlmeyer, S. G. Moore, T. D. Nguyen, R. Shan, M. J. Stevens, J. Tranchida, C. Trott, and S. J. Plimpton. LAMMPS - a flexible simulation tool for particle-based materials modeling at the atomic, meso, and continuum scales. *Computer Physics Communications*, 271:108171, 2022.

[93] G. F. Harrington and J. Santiso. Back-to-basics tutorial: X-ray diffraction of thin films. *Journal of Electroceramics*, 47(2):141–163, 2021.

[94] K. Nagao and E. Kagami. X-ray thin film measurement techniques vii. pole figure measurement. *Rigaku Journal*, 27(2):6–14, 2011.

[95] T. Fuchs, T. Ortmann, J. Becker, C. G. Haslam, M. Ziegler, V. K. Singh, M. Rohnke, B. Mogwitz, K. Peppler, L. F. Nazar, J. Sakamoto, and J. Janek. Imaging the microstructure of lithium and sodium metal in anode-free solid-state batteries using electron backscatter diffraction. *Nature Materials*, 23(12):1678–1685, 2024.

[96] W. C. Oliver and G. M. Pharr. An improved technique for determining hardness and elastic modulus using load and displacement sensing indentation experiments. *Journal of Materials Research*, 1992.

[97] H. R. Wilde and A. Wehrstedt. Introduction of martens hardness hm: An internationally accepted designation for "hardness under test force". *Materials Testing*, 42(11-12):468–470, 2000.

[98] W. C. Oliver and G. M. Pharr. Measurement of hardness and elastic modulus by instrumented indentation: Advances in understanding and refinements to methodology. *Journal of Materials Research*, 2004.

[99] H. Hertz. The contact of elastic solids. *J Reine Angew, Math*, 92:156–171, 1881.

[100] H. Hertz. On the contact of rigid elastic solids and on hardness, chapter 6: Assorted papers by h. hertz. *MacMillan, New York*, 1882.

[101] H. Hertz. On the contact of solids—on the contact of rigid elastic solids and on hardness. *Miscellaneous papers*, pages 146–183, 1896.

[102] I. N. Sneddon. The relation between load and penetration in the axisymmetric boussinesq problem for a punch of arbitrary profile. *International journal of engineering science*, 3(1):47–57, 1965.

[103] L. C. P. dos Santos, D. Gruener, and R. Spatschek. Atomistic modeling of the mechanical properties and deformation behavior of lithium. *Modelling and Simulation in Materials Science and Engineering*, 2025.

[104] M. Mann, C. Schwab, L. C. P. dos Santos, R. Spatschek, D. Fattakhova-Rohlfing, and M. Finsterbusch. Improving the rate performance of lithium metal anodes: In-situ formation of 3d interface structures by mechanical mixing with sodium metal. *Energy Storage Materials*, 74:103975, 2025.

[105] H. Nash and C. Smith. Single-crystal elastic constants of lithium. *Journal of Physics and Chemistry of Solids*, 9(2):113–118, 1959.

[106] M. M. Beg and M. Nielsen. Temperature dependence of lattice dynamics of lithium 7. *Physical Review B*, 14:4266–4273, Nov 1976.

[107] C. A. Swenson. Lithium metal: An experimental equation of state. *Journal of Physics and Chemistry of Solids*, 27(1):33–38, 1966.

[108] W. Pichl. Recrystallization of partially transformed lithium single crystals. *Physica Status Solidi*, 158:101–106, 1996.

[109] T. Slotwinski and J. Trivisonno. Temperature dependence of the elastic constants of single crystal lithium. *Journal of Physics and Chemistry of Solids*, 30(5):1276–1278, 1969.

[110] R. A. Felice, J. Trivisonno, and D. E. Schuele. Temperature and pressure dependence of the single-crystal elastic constants of ^{6}Li and natural lithium. *Phys. Rev. B*, 16:5173–5184, Dec 1977.

[111] C. Xu, Z. Ahmad, A. Aryanfar, V. Viswanathan, and J. R. Greer. Enhanced strength and temperature dependence of mechanical properties of Li at small scales and its implications for Li metal anodes. *Proceedings of the National Academy of Sciences of the United States of America*, 114(1):57–61, 2017.

[112] J. R. Greer and W. D. Nix. Nanoscale gold pillars strengthened through dislocation starvation. *Phys. Rev. B*, 73:245410, Jun 2006.

[113] W. S. LePage, Y. Chen, E. Kazyak, K. H. Chen, A. J. Sanchez, A. Poli, E. M. Arruda, M. D. Thouless, and N. P. Dasgupta. Lithium Mechanics: Roles of Strain Rate and Temperature and Implications for Lithium Metal Batteries. *Journal of The Electrochemical Society*, 166(2):A89–A97, 2019.

[114] S. Ding, L. Fairgrieve-Park, O. Sendetskyi, and M. Fleischauer. Compressive creep deformation of lithium foil at varied cell conditions. *Journal of Power Sources*, 488(229404), 2021.

[115] T. Sedlatschek, J. Lian, W. Li, M. Jiang, T. Wierzbicki, M. Z. Bazant, and J. Zhu. Large-deformation plasticity and fracture behavior of pure lithium under various stress states. *Acta Materialia*, 208, 4 2021.

[116] M. A. Citrin, H. Yang, S. K. Nieh, J. Berry, W. Gao, X. Pan, D. J. Srolovitz, and J. R. Greer. From ion to atom to dendrite: Formation and nanomechanical behavior of electrodeposited lithium. *MRS Bulletin*, 45, 2020.

[117] L. Zhang, T. Yang, C. Du, Q. Liu, Y. Tang, J. Zhao, B. Wang, T. Chen, Y. Sun, P. Jia, H. Li, L. Geng, J. Chen, H. Ye, Z. Wang, Y. Li, H. Sun, X. Li, Q. Dai, Y. Tang, Q. Peng, T. Shen, S. Zhang, T. Zhu, and J. Huang. Lithium whisker growth and stress generation in an in situ atomic force microscope–environmental transmission electron microscope set-up. *Nature Nanotechnology*, 15, 2020.

[118] W. D. Nix and H. Gao. Indentation size effects in crystalline materials: A law for strain gradient plasticity. *Journal of the Mechanics and Physics of Solids*, 46(3):411–425, 1998.

[119] Y. Wang, D. Dang, M. Wang, X. Xiao, and Y.-T. Cheng. Mechanical behavior of electroplated mossy lithium at room temperature studied by flat punch indentation. *Applied Physics Letters*, 115(4):043903, 2019.

[120] C. G. Haslam, J. B. Wolfenstine, and J. Sakamoto. The effect of aspect ratio on the mechanical behavior of li metal in solid-state cells. *Journal of Power Sources*, 520:230831, 2022.

[121] K. S. Nagy and D. J. Siegel. Anisotropic Elastic Properties of Battery Anodes. *Journal of The Electrochemical Society*, 167(11):110550, 2020.

[122] S. Narayan and L. Anand. A large deformation elastic-viscoplastic model for lithium. *Extreme Mechanics Letters*, 24:21–29, 2018.

[123] L. Anand and S. Narayan. An elastic-viscoplastic model for lithium. *Journal of The Electrochemical Society*, 166:A1092–A1095, 2019.

[124] S. Narayan and L. Anand. On modeling the detrimental effects of inhomogeneous plating-and-stripping at a lithium-metal/solid-electrolyte interface in a solid-state-battery. *Journal of The Electrochemical Society*, 167:040525, 3 2020.

[125] R. F. Cook and M. L. Oyen. Nanoindentation behavior and mechanical properties measurement of polymeric materials. *International Journal of Materials Research*, 98:370–378, 2007.

[126] A. J. Gayle and R. F. Cook. Mapping viscoelastic and plastic properties of polymers and polymer-nanotube composites using instrumented indentation. *Journal of materials research*, 31(15):2347–2360, 2016.

[127] R. F. Cook. A flexible model for instrumented indentation of viscoelastic-plastic materials. *MRS Communications*, 8:586–590, 6 2018.

[128] R. S. Ginder, W. D. Nix, and G. M. Pharr. A simple model for indentation creep. *Journal of Mechanics Physics of Solids*, 112:552–562, 2018.

[129] A. H. W. Ngan, H. T. Wang, B. Tang, and K. Y. Sze. Correcting power-law viscoelastic effects in elastic modulus measurement using depth-sensing indentation. *International Journal of Solids and Structures*, 42:1831–1846, 3 2005.

[130] D. Saraev and R. E. Miller. Atomic-scale simulations of nanoindentation-induced plasticity in copper crystals with nanometer-sized nickel coatings. *Acta Materialia*, 54(1):33–45, 2006.

[131] Y. Zhu, L. Zhou, Y. X. Yao, and G. W. Kang. Molecular dynamics simulation for single crystal aluminum nano-indentation effect by indenter radius. *Applied Mechanics and Materials*, 10:401–405, 2008.

[132] V. Dupont and F. Sansoz. Molecular dynamics study of crystal plasticity during nanoindentation in ni nanowires. *Journal of Materials Research*, 24(3):948–956, 2009.

[133] Y. Gao, C. J. Ruestes, D. R. Tramontina, and H. M. Urbassek. Comparative simulation study of the structure of the plastic zone produced by nanoindentation. *Journal of the Mechanics and Physics of Solids*, 75:58–75, 2015.

[134] M. Yaghoobi and G. Z. Voyiadjis. Atomistic simulation of size effects in single-crystalline metals of confined volumes during nanoindentation. *Computational Materials Science*, 111:64–73, 2016.

[135] C. J. Ruestes, E. M. Bringa, Y. Gao, and H. M. Urbassek. Molecular dynamics modeling of nanoindentation. *Applied nanoindentation in advanced materials*, pages 313–345, 2017.

[136] H. T. Luu, S. L. Dang, T. V. Hoang, and N. Gunkelmann. Molecular dynamics simulation of nanoindentation in al and fe: On the influence of system characteristics. *Applied Surface Science*, 551:149221, 2021.

[137] C. Su, E. G. Herbert, S. Sohn, J. A. LaManna, W. C. Oliver, and G. M. Pharr. Measurement of power-law creep parameters by instrumented indentation methods. *Journal of the Mechanics and Physics of Solids*, 61(2):517–536, 2013.

[138] Y. Tang, L. Zhang, J. Chen, H. Sun, T. Yang, Q. Liu, Q. Huang, T. Zhu, and J. Huang. Electro-chemo-mechanics of lithium in solid state lithium metal batteries. *Energy and Environmental Science*, 14:602–642, 2 2021.

[139] S. Esmizadeh, L. Cabras, M. Serpelloni, T. Dev, V. Oancea, E. Knobbe, M. Lachner, and A. Salvadori. A review on modeling of nucleation and growth of li dendrites in solid electrolytes. *Journal of Energy Storage*, 97:112897, 2024.

[140] P. Sudharshan Phani and W. C. Oliver. A critical assessment of the effect of indentation spacing on the measurement of hardness and modulus using instrumented indentation testing. *Materials and Design*, 164, 2 2019.

[141] A. Mokhtari, N. Tala-Ighil, and Y. A. Masmoudi. Nanoindentation to determine young's modulus for thermoplastic polymers. *Journal of Materials Engineering and Performance*, 31, 2022.

[142] P. E. Blöchl. Projector augmented-wave method. *Physical Review B*, 50:17953–17979, Dec 1994.

[143] G. Kresse and D. Joubert. From ultrasoft pseudopotentials to the projector augmented-wave method. *Physical Review B*, 59:1758–1775, Jan 1999.

[144] J. P. Perdew, K. Burke, and M. Ernzerhof. Generalized gradient approximation made simple. *Physical Review Letters*, 77:3865–3868, Oct 1996.

[145] H. J. Monkhorst and J. D. Pack. Special points for brillouin-zone integrations. *Physical Review B*, 13:5188–5192, Jun 1976.

[146] S. Yu, R. D. Schmidt, R. Garcia-Mendez, E. Herbert, N. J. Dudney, J. B. Wolfenstine, J. Sakamoto, and D. J. Siegel. Elastic properties of the solid electrolyte $li_7la_3zr_2o_{12}$ (llzo). *Chemistry of Materials*, 28(1):197–206, 2015.

[147] P. Söderlind, O. Eriksson, J. M. Wills, and A. M. Boring. Theory of elastic constants of cubic transition metals and alloys. *Physical Review B*, 48:5844–5851, 1993.

[148] M. Jamal, S. Jalali Asadabadi, I. Ahmad, and H.A. Rahnamaye Aliabad. Elastic constants of cubic crystals. *Computational Materials Science*, 95:592–599, 2014.

[149] W. Voigt. *Lehrbuch der Kristallphysik*. B. B. Teubner, 1928.

[150] A. Nichol and G. J. Ackland. Property trends in simple metals: An empirical potential approach. *Physical Review B*, 93:184101, May 2016.

[151] A. Stukowski. Visualization and analysis of atomistic simulation data with OVITO-the Open Visualization Tool. *Modelling and Simulation in Materials Science and Engineering*, 18(1), JAN 2010.

[152] T. Williams, C. Kelley, and “many others". Gnuplot 4.6: an interactive plotting program, April 2013.

[153] G. Clavier, N. Desbiens, E. Bourasseau, V. Lachet, N. Brusselle-Dupend, and B. Rousseau. Computation of elastic constants of solids using molecular simulation: comparison of constant volume and constant pressure ensemble methods. *Molecular Simulation*, 43(17):1413–1422, 2017.

[154] G. Sainath and B. K. Choudhary. Molecular dynamics simulations on size dependent tensile deformation behaviour of [110] oriented body centred cubic iron nanowires. *Materials Science and Engineering: A*, 640:98–105, 2015.

[155] G. Sainath and B. K. Choudhary. Orientation dependent deformation behaviour of bcc iron nanowires. *Computational Materials Science*, 111:406–415, 2016.

[156] P. Hirel. Atomsk: A tool for manipulating and converting atomic data files. *Computer Physics Communications*, 197:212–219, 2015.

[157] A. R. Natarajan and A. V. d. Ven. Toward an understanding of deformation mechanisms in metallic lithium and sodium from first-principles. *Chemistry of Materials*, 31:8222–8229, 2019.

[158] J. Dorrell and L. B. Pártay. Pressure-temperature phase diagram of lithium, predicted by embedded atom model potentials. *The Journal of Physical Chemistry B*, pages 6015–6023, 2020.

[159] W. B. Pearson. Thermal expansion of lithium, 77° to 300° k. *Canadian Journal of Physics*, 32(11):708–713, 1954.

[160] R. H. Schumm, D. D. Wagman, S. Bailey, W. H. Evans, and V. B. Parker. Technical notes 270-1 to 270-8. Technical report, National Bureau of Standards (USA), 1973.

[161] P. M. Larsen, S. Schmidt, and J. Schiøtz. Robust structural identification via polyhedral template matching. *Modelling and Simulation in Materials Science and Engineering*, 24(5):055007, may 2016.

[162] Y. Zhang, J. P. Liu, S. Y. Chen, X. Xie, P. K. Liaw, K. A. Dahmen, J. W. Qiao, and Y. L. Wang. Serration and noise behaviors in materials. *Progress in Materials Science*, 90:358–460, 2017.

[163] J. Y. Kim, D. Jang, and J. R. Greer. Insight into the deformation behavior of niobium single crystals under uniaxial compression and tension at the nanoscale. *Scripta Materialia*, 61(3):300–303, 2009.

[164] M. J. Mills and T. Neeraj. Dislocations in metals and metallic alloys. *Encyclopedia of Materials: Science and Technology*, pages 2278–2291, 2001.

[165] L. Dezerald, D. Rodney, E. Clouet, L. Ventelon, and F. Willaime. Plastic anisotropy and dislocation trajectory in bcc metals. *Nature Communications*, 2016.

[166] A. Stukowski and K. Albe. Extracting dislocations and non-dislocation crystal defects from atomistic simulation data. *Modelling and Simulation in Materials Science and Engineering*, 18(8):085001, sep 2010.

[167] A. Stukowski, V. V Bulatov, and A. Arsenlis. Automated identification and indexing of dislocations in crystal interfaces. *Modelling and Simulation in Materials Science and Engineering*, 20(8):085007, oct 2012.

[168] F. Bachmann, R. Hielscher, and H. Schaeben. Texture analysis with mtex – free and open source software toolbox. In *Texture and Anisotropy of Polycrystals III*, volume 160 of *Solid State Phenomena*, pages 63–68. Trans Tech Publications Ltd, 3 2010.

[169] R. Gröger, J. Holzer, and T. Kruml. Twinning and antitwinning in body-centered cubic metals. *Computational Materials Science*, 216:111874, 2023.

[170] X. Li, Z. Zhang, and J. Wang. Deformation twinning in body-centered cubic metals and alloys. *Progress in Materials Science*, 139:101160, 2023.

[171] S. Li, X. Ding, J. Deng, T. Lookman, J. Li, X. Ren, J. Sun, and A. Saxena. Superelasticity in bcc nanowires by a reversible twinning mechanism. *Physical Review B*, 82:205435, Nov 2010.

[172] G. Sainath and B. K. Choudhary. Twinning to slip transition in ultrathin bcc fe nanowires. *Physics Letters A*, 382(15):1047–1051, 2018.

[173] G. Sainath, S. Goyal, and A. Nagesha. Plasticity through de-twinning in twinned bcc nanowires. *Crystals*, 10(5), 2020.

[174] J. Veerababu, G. Sainath, and A. Nagesha. Twin boundary reversibility characteristics in alpha-fe. *Materials Today Communications*, 29:102970, 2021.

[175] I. J. Beyerlein R. F. Zhang, J. Wang and T. C. Germann. Twinning in bcc metals under shock loading: a challenge to empirical potentials. *Philosophical Magazine Letters*, 91(12):731–740, 2011.

[176] M. A. Meyers, O. Vöhringer, and V. A. Lubarda. The onset of twinning in metals: a constitutive description. *Acta Materialia*, 49(19):4025–4039, 2001.

[177] N. Brodusch, K. Zaghib, and R. Gauvin. Electron backscatter diffraction applied to lithium sheets prepared by broad ion beam milling. *Microscopy Research and Technique*, 78(1):30–39, 2015.

[178] M. Paggi and P. Wriggers. Stiffness and strength of hierarchical polycrystalline materials with imperfect interfaces. *Journal of the Mechanics and Physics of Solids*, 60(4):557–572, 2012.

[179] A. H. Chokshi, A. Rosen, J. Karch, and H. Gleiter. On the validity of the hall-petch relationship in nanocrystalline materials. *Scripta Metallurgica*, 23(10):1679–1683, 1989.

[180] A. Husain, P. La, Y. Hongzheng, and S. Jie. Molecular dynamics as a means to investigate grain size and strain rate effect on plastic deformation of 316 l nanocrystalline stainless-steel. *Materials*, 13(14), 2020.

[181] A. V. Bolesta and V. M. Fomin. Molecular dynamics simulation of polycrystalline copper. *Journal of Applied Mechanics and Technical Physics*, 2014.

[182] C. E. Carlton and P. J. Ferreira. What is behind the inverse hall–petch effect in nanocrystalline materials? *Acta Materialia*, 55(11):3749–3756, 2007.

[183] H. Zhang, F. Liu, G. Ungar, Z. Zheng, Q. Sun, and Y. Han. A regime beyond the hall–petch and inverse-hall–petch regimes in ultrafine-grained solids. *Communications Physics*, 5, 2022.

[184] W. Hou, X. Guo, X. Shen, K. Amine, H. Yu, and J. Lu. Solid electrolytes and interfaces in all-solid-state sodium batteries: Progress and perspective. *Nano Energy*, 52:279–291, 2018.

[185] Y. Lu, L. Li, Q. Zhang, Z. Niu, and J. Chen. Electrolyte and interface engineering for solid-state sodium batteries. *Joule*, 2(9):1747–1770, 2018.

[186] C. D. Fincher, Y. Zhang, G. M. Pharr, and M. Pharr. Elastic and plastic characteristics of sodium metal. *ACS Applied Energy Materials*, 3(2):1759–1767, 2020.

[187] M. E. Diederich and J. Trivisonno. Temperature dependence of the elastic constants of sodium. *Journal of Physics and Chemistry of Solids*, 27(4):637–642, 1966.

[188] R. H. Martinson. Variation of the elastic constants of sodium with temperature and pressure. *Physical Review*, 178(3):902, 1969.

[189] M. J. Wang, J.-Y. Chang, J. B. Wolfenstine, and J. Sakamoto. Analysis of elastic, plastic, and creep properties of sodium metal and implications for solid-state batteries. *Materialia*, 12:100792, 2020.

[190] C. W. Bale. The Li-Na (Lithium-Sodium) System. *Bulletin of Alloy Phase Diagrams*, 10(3):265–268, 1989.

[191] Y. Zhang, J. Meng, K. Chen, H. Wu, J. Hu, and C. Li. Garnet-based solid-state lithium fluoride conversion batteries benefiting from eutectic interlayer of superior wettability. *ACS Energy Lett.*, 5(4):1167–1176, 2020.

[192] X. Fu, T. Wang, W. Shen, M. Jiang, Y. Wang, Q. Dai, D. Wang, Z. Qiu, Y. Zhang, K. Deng, Q. Zeng, N. Zhao, X. Guo, Z. Liu, J. Liu, and Z. Peng. A high-performance carbonate-free lithium | garnet interface enabled by a trace amount of sodium. *Advanced Materials*, 32, 7 2020.

[193] L. C. P. dos Santos, M. Mann, C. Schwab, D. Fattakhova-Rohlfing, M. Finsterbusch, and R. Spatschek. Revisiting the Li–Na system: Ab initio based description of the low-temperature thermodynamics for battery applications. *Next Materials*, 9:101202, 2025.

[194] S. Zhang, D. Shin, and Z. Liu. Thermodynamic modeling of the Ca–Li–Na system. *Calphad*, 27(2):235–241, 2003.

[195] A. D. Pelton. Calculation of phase equilibria and thermodynamic properties of the Li-Na-H system. *Int. J. Mater. Res.*, 84(11):767–772, 1993.

[196] A. T. Dinsdale. SGTE data for pure elements. *Calphad*, 15(4):317–425, 1991.

[197] F. C. Campbell. *Phase diagrams: understanding the basics*. ASM international, 2012.

[198] H. K. Schürmann and R. D. Parks. Paraconductivity in binary metallic liquids above the critical point. *Physical Review Letters*, 27(26):1790, 1971.

[199] P. D. Feitsma, J. J. Hallers, F. V. D. Werff, and W. Van der Lugt. Electrical resistivities and phase separation of liquid lithium-sodium alloys. *Physica B+C*, 79(1):35–52, 1975.

[200] M. G. Down, P. Hubberstey, and R. J. Pulham. Sodium–lithium phase diagram: redetermination of the liquid immiscibility system by resistance measurement. *J. Chem. Soc., Dalton Trans.*, pages 1490–1492, 1975.

[201] M. G. Down, P. Hubberstey, and R. J. Pulham. Electrical resistivity of liquid sodium + lithium mixtures. evidence for incipient immiscibility? *J. Chem. Soc., Faraday Trans. 1*, 71:1387–1391, 1975.

[202] H. Endo, H. Hoshino, K. Tamura, and M. Mushiage. Phase separation of liquid binary mixtures containing metals under pressure. *Solid State Commun.*, 32(12):1243–1246, 1979.

[203] R. C. Faxon F. A. Kanda and D. V. Keller. The determination of the liquid immiscibility boundaries of the lithium-sodium and thallium-selenium systems by the liquid density method. *Phys. Chem. Liq.*, 1(1):61–72, 1968.

[204] E. S. Wu and H. Brumberger. Critical small-angle x-ray scattering of the liquid sodium-lithium system. *Phys. Lett. A*, 53(6):475–477, 1975.

[205] W. H. Howland and L. F. Epstein. *The Binary System Sodium-Lithium*, chapter 5, pages 34–41. American Chemical Society, 1957.

[206] O. N. Salmon and D. H. Ahmann. The lithiuim–sodium liquid metal system. *J. Phys. Chem.*, 60:13–16, 1956.

[207] P. H. Mayrhofer, D. Music, and J. M. Schneider. Ab initio calculated binodal and spinodal of cubic ti1-xalxn. *Appl. Phys. Lett.*, 88(7):071922, 02 2006.

[208] A. Zunger, S.-H. Wei, L. G. Ferreira, and J. E. Bernard. Special quasirandom structures. *Physical Review Letters*, 65:353–356, Jul 1990.

[209] N. D. Tripathi and S. K. Pandey. Study of the effective debye temperature in alkali metals and their halides. *Acust.*, 35:278, 1976.

[210] B. Grabowski, T. Hickel, and J. Neugebauer. Ab initio study of the thermodynamic properties of nonmagnetic elementary fcc metals: Exchange-correlation-related error bars and chemical trends. *Phys. Rev. B*, 76:024309, Jul 2007.

[211] R. Spatschek, G. Gobbi, C. Hüter, A. Chakrabarty, U. Aydin, S. Brinckmann, and J. Neugebauer. Scale bridging description of coherent phase equilibria in the presence of surfaces and interfaces. *Phys. Rev. B*, 94:134106, Oct 2016.

[212] P. H. Mayrhofer, F. D. Fischer, H. J. Böhm, C. Mitterer, and J. M. Schneider. Energetic balance and kinetics for the decomposition of supersaturated ti1-xalxn. *Acta Materialia*, 55(4):1441–1446, 2007.

[213] P. H. Mayrhofer, L. Hultman, J. M. Schneider, P. Staron, and H. Clemens. Spinodal decomposition of cubic ti1-xalxn: Comparison between experiments and modeling. *Int. J. Mater. Res.*, 98(11):1054–1059, 2007.

[214] J. Weissmüller. Coherent phase change in interstitial solutions: A hierarchy of instabilities. *Adv. Sci.*, 11(21):2308554, 2024.

[215] P. Fratzl, O. Penrose, and J. Lebowitz. Modeling of phase separation in alloys with coherent elastic misfit. *J. Stat. Phys.*, 95:1429–1503, 1999.

[216] J. W. Cahn. Coherent fluctuations and nucleation in isotropic solids. *Acta Metall.*, 10:907, 1962.

[217] T. Krauskopf, B. Mogwitz, C. Rosenbach, W. G. Zeier, and J. Janek. Diffusion limitation of lithium metal and Li–Mg alloy anodes on LLZO type solid electrolytes as a function of temperature and pressure. *Adv. Energy Mater.*, 9(44):1902568, 2019.

[218] C. Hüter, G. Boussinot, E. A. Brener, and R. Spatschek. Solidification in syntectic and monotectic systems. *Phys. Rev. E*, 86:021603, Aug 2012.

[219] M. Hillert. A solid-solution model for inhomogeneous systems. *Acta Metall.*, 9(6):525–535, 1961.

[220] J. Zhu, L. Chen, J. Shen, and V. Tikare. Coarsening kinetics from a variable-mobility cahn-hilliard equation: Application of a semi-implicit fourier spectral method. *Phys. Rev. E*, 60:3564–3572, Oct 1999.

[221] C. Wagner. Theorie der alterung von niederschlägen durch umlösen (ostwald-reifung). *Z. Elektrochem., Ber. der Bunsenges. Phys. Chem.*, 65(7-8):581–591, 1961.

[222] I. M. Lifshitz and V. V. Slyozov. The kinetics of precipitation from supersaturated solid solutions. *J. Phys. Chem. Solids*, 19(1-2):35–50, 1961.

[223] Y. Li, X. Chen, A. Dolocan, Z. Cui, S. Xin, L. Xue, H. Xu, K. Park, and J. B. Goodenough. Garnet electrolyte with an ultralow interfacial resistance for li-metal batteries. *Journal of the American Chemical Society*, 140:6448–6455, 5 2018.

[224] A. Sharafi, S. Yu, M. Naguib, M. Lee, C. Ma, H. M. Meyer, J. Nanda, M. Chi, D. J. Siegel, and J. Sakamoto. Impact of air exposure and surface chemistry on $Li - Li_7La_3Zr_2O_{12}$ interfacial resistance. *Journal of Materials Chemistry A*, 5:13475–13487, 2017.

[225] M. M. Markowitz and D. A. Boryta. Lithium metal-gas reactions. *Journal of Chemical & Engineering Data*, 7(4):586–591, 1962.

[226] D. W. Jeppson, J. L. Ballif, W. W. Yuan, and B. E. Chou. Lithium literature review: lithium's properties and interactions. Technical report, Hanford Engineering Development Lab., Richland, Wash. (USA), 1978.

[227] V. A. D'yakov, C. A. Ebbers, M. V. Pchelkin, and V. I. Pryalkin. Lithium sodium carbonate: a new nonlinear-optics crystal. *Journal of Russian Laser Research*, 17:489–494, 1996.

[228] A. V. Yatsenko, S. G. Zhukov, V. A. D'yakov, A. Etz, W. Molleman, and H. Schenk. X-ray study of low and high symmetry phases of linaco3. *Materials Research Bulletin*, 30:739–744, 1995.

[229] A. V. Yatsenko, S. G. Zhukov, V. A. D'yakov, and H. Schenk. Triclinic alpha - linaco3. *Acta Crystallographica*, 52:1–3, 1996.

[230] C. Ricca, A. Ringuedé, M. Cassir, C. Adamo, and F. Labat. Mixed lithium-sodium (linaco3) and lithium-potassium (likco3) carbonates for low temperature electrochemical applications: Structure, electronic properties and surface reconstruction from ab-initio calculations. *Surface Science*, 647:66–77, 5 2016.

[231] M. Bruno and M. Prencipe. Ab initio quantum-mechanical modeling of the (0 0 1), (-1 0 1) and (1 1 0) surfaces of zabuyelite (li2co3). *Surface Science*, 601:3012–3019, 7 2007.

[232] J. Qi. *Thermodynamics of salt system: $Li^+, K^+, Na^+ \parallel Cl^-, CO_3^{2-}$*. PhD thesis, RWTH Aachen University - Faculty of Georesources and Materials Engineering, 2024.

[233] DIN EN ISO 14175: Welding consumables – Gases and gas mixtures for fusion welding and allied processes, 2008. ISO 14175:2008.

[234] V. Fiorentini and M. Methfessel. Extracting convergent surface energies from slab calculations. *Journal of Physics: Condensed Matter*, 8:6525–6529, 1996.

[235] S. P. Kaur, V. Mishra, and B. Chakraborty. 6 - transition metal dichalcogenides and hybrids for electrochemical sensing. In C. S. Rout, editor, *2D Materials-Based Electrochemical Sensors*, pages 199–224. Elsevier, 2023.

[236] D. Sherrington. A simple spin glass perspective on martensitic shape-memory alloys. *J. Phys.: Condens. Matter*, 20:304213, 2008.

[237] S. Kartha, T. Castán, J. A. Krumhansl, and J. P. Sethna. Spin-Glass Nature of Tweed Precursors in Martensitic Transformations. *Physical Review Letters*, 67:3630, 1991.

[238] J. P. Sethna, S. Kartha, T. Castán, and J. A. Krumhansl. Tweed in Martensites: A Potential New Spin Glass. *Phys. Scr.*, 1992:214–219, 1992.

[239] R. Vasseur and T. Lookman. Spin Models for Ferroelastics: Towards a Spin Glass Description of Strain Glass. *Solid State Phenom.*, 172-174:1078–1083, 2011.

[240] E. Polatidis, M. Šmíd, I. Kuběna, W.-N. Hsu, G. Laplanche, and H. Van Swygenhoven. Deformation mechanisms in a superelastic NiTi alloy: An in-situ high resolution digital image correlation study. *Mater. Des.*, 191:108622, 2020.

[241] Z. Wang, J. Chen, R. Kocich, I. P. Dolbnya S. Tardif, L. Kunčická, J.-S. Micha, K. Liogas, O. V. Magdysyuk, I. Szurman, and A. M. Korsunsky. Grain Structure Engineering of NiTi Shape Memory Alloys by Intensive Plastic Deformation. *ACS Appl. Mater. Interfaces*, 14:31396–31410, 2022.

[242] L. Mañosa and A. Planes. Mechanocaloric effects in shape memory alloys. *Phil. Trans. R. Soc. A*, 374:20150310, 2016.

[243] K. Otsuka and X. Ren. Physical metallurgy of Ti–Ni-based shape memory alloys. *Prog. Mater. Sci.*, 50:511, 2005.

[244] L. C. P. dos Santos, A. Dollmann, C. Greiner, D. Gruener, Y. Le Bouar, and R. Spatschek. Modeling of deformation twinning in BCC metals via quantum annealing. *Discover Materials*, 6(1):129, March 2026.

[245] L. C. P. dos Santos, T. Hang, R. Sandt, M. Finsterbusch, Y. Le Bouar, and R. Spatschek. Elastic energy driven multivariant selection in martensites via quantum annealing. *Phys. Rev. Res.*, 6:023076, Apr 2024.

[246] S. A. Kotrechko, A. V. Filatov, and A. V. Ovsjannikov. Molecular dynamics simulation of deformation and failure of nanocrystals of bcc metals. *Theoretical and Applied Fracture Mechanics*, 45(2):92–99, 2006.

[247] A. Ojha, H. Sehitoglu, L. Patriarca, and H. J. Maier. Twin nucleation in fe-based bcc alloys - modeling and experiments. *Modelling and Simulation in Materials Science and Engineering*, 22, 10 2014.

[248] Z. Shi and C. V. Singh. Competing twinning mechanisms in body-centered cubic metallic nanowires. *Scripta Materialia*, 113:214–217, 2016.

[249] K. Anten and B. Scholtes. Formation of macroscopic twin bands and inhomogeneous deformation during cyclic tension-compression loading of the mg-wrought alloy az31. *Materials Science and Engineering: A*, 746:217–228, 2 2019.

[250] J. Zhang, S. Du, and S. Ding. Crystal plasticity finite element modeling of twin band formation and evolution together with the macroscale mechanical responses of hexagonal metals. *Materials Science and Engineering: A*, 855, 10 2022.

[251] J. Wang and X. Zhang. Twinning effects on strength and plasticity of metallic materials. *MRS Bulletin*, 41:274–281, 2016.

[252] S. Mahajan. Critique of mechanisms of formation of deformation, annealing and growth twins: Face-centered cubic metals and alloys. *Scripta Materialia*, 68(2):95–99, 2013.

[253] H. K. D. H. Bhadeshia. *Worked Examples in the Geometry of Crystals*. Institute of Materials, London, 2nd edition, 2001. Updated 2006; available online.

[254] D. P. Field, L. T. Bradford, M. M. Nowell, and T. M. Lillo. The role of annealing twins during recrystallization of cu. *Acta Materialia*, 55(12):4233–4241, 2007.

[255] S. L. Wong, M. Madivala, U. Prahl, F. Roters, and D. Raabe. A crystal plasticity model for twinning- and transformation-induced plasticity. *Acta Materialia*, 118:140–151, 2016.

[256] B. Huang, J. Yang, Z. Luo, Y. Wang, and N. Wang. Formation of twin boundaries in rapidly solidified metals through deformation twinning. *Materials*, 16(13), 2023.

[257] A. G. Khachaturyan. *Theory of Structural Transformations in Solids*. Dover Publications, Inc., Mineola, New York, 2008.

[258] A. Authier. *International tables for crystallography. D. Physical properties of crystals*. Wiley, Chichester, West Sussex, second online edition, 2013.

[259] T. W. Heo, Y. Wang, S. Bhattacharya, X. Sun, S. Hu, and L.-Q. Chen. A phase-field model for deformation twinning. *Philosophical Magazine Letters*, 91(2):110–121, 2011.

[260] E. O. Hall. The deformation and ageing of mild steel: Iii discussion of results. *Proceedings of the Physical Society. Section B*, 64(9):747, sep 1951.

[261] N. J. Petch. The cleavage strength of polycrystals. *Journal of the Iron and Steel Institute*, 174:25–28, 1953.

[262] G. F. Bolling and R. H. Richman. Mechanical twinning of polycrystalline b.c.c. metals. *The Canadian Journal of Metallurgy and Materials Science, Canadian Metallurgical Quarterly*, 5(2):143–160, 1966.

[263] J. N. Florando, B. S. El-Dasher, C. Chen, D. C. Swift, N. R. Barton, J. M. McNaney, K. T. Ramesh, Kevin J. Hemker, and M. Kumar. Effect of strain rate and dislocation density on the twinning behavior in tantalum. *AIP Advances*, 6(4):045120, 04 2016.

[264] M. A. Kumar and I. J. Beyerlein. Local microstructure and micromechanical stress evolution during deformation twinning in hexagonal polycrystals. *Journal of Materials Research*, 35(3):217–241, 2020.

[265] Y. Wang, D. Banerjee, C. C. Su, and A. G. Khachaturyan. Field kinetic model and computer simulation of precipitation of $L1_2$ ordered intermetallics from f.c.c. solid solution. *Acta Materialia*, 46:2983, 1998.

[266] H. Lebbad, B. Appolaire, Y. Le Bouar, and A. Finel. Insights into the selection mechanism of Widmanstätten growth by phase-field calculations. *Acta Materialia*, 217:117148, 2021.

[267] Y. Le Bouar, A. Loiseau, and A. G. Khachaturyan. Origin of chessboard-like structures in decomposing alloys. Theoretical model and computer simulation. *Acta Materialia*, 46:2777, 1998.

[268] S. Mukherjee and B. K. Chakrabarti. Multivariable optimization: Quantum annealing and computation. *The European Physical Journal Special Topics*, 224(1):17–24, 2015.

[269] S. Boixo, V. N. Smelyanskiy, A. Shabani, S. V. Isakov, M. Dykman, V. S. Denchev, M. H. Amin, A. Y. Smirnov, M. Mohseni, and H. Neven. Computational multiqubit tunnelling in programmable quantum annealers. *Nat. Commun.*, 7(1):10327, 2016.